Modeling, Analysis and Control of Single and Multiple Micro-grid-Based Active Distribution Grids

by

Alireza Kahrobaeian

A thesis submitted in partial fulfillment of the requirements for the degree of

Doctor of Philosophy

in

Energy Systems

Department of Electrical and Computer Engineering
University of Alberta

Abstract

Derived by economic, technical and environmental reasons, the energy sector is moving towards a new era of "*Smart Active Distribution Systems*" where clusters of converter-based distributed generation (DG) units, local loads and other filtering devices form micro-grids (MG), which can be regarded as the building blocks of future active distribution grids. However, several undesirable interaction dynamics could occur between the DG converters, which are usually equipped with high-order LC or LCL filters and system components such as power-factor correction capacitors, static and dynamic loads. Moreover, the lack of coordination between DG entities in single and multiple micro-grid systems results in inaccurate power sharing, frequency deviation and system instabilities.

To solve these problems, this thesis provides detailed modeling, analysis and control of micro-grid systems with compromised voltage or power stability issues due to system uncertainties in presence of different types of loads, electronic devices or line parameter variation. Several robust converter-level control interfaces are proposed to mitigate such stability challenges in both voltage-controlled and current-controlled converters. Furthermore, accurate power sharing and coordinated control of multiple micro-grids is achieved by developing a new system-level hierarchical distributed networked-based control strategy which can provide active synchronization and power-tie regulation between multiple micro-grid entities in large active distribution systems. Simulation and experimental results validate the effectiveness of the proposed control schemes.

Preface

This thesis, including the literature review, data analysis and concluding analysis are my original work. The following parts of this thesis have been published or accepted for publication in which Y.A.-R. I. Mohamed was the supervisory author and was involved with concept formation and manuscript composition:

Chapter 2 of this thesis has been published as A. Kahrobaeian, and Y. A.-R. I. Mohamed, "Interactive Distributed Generation Interface for Flexible MG Operation in Smart Distribution Systems", *IEEE Trans. on Sustainable Energy*, vol. 3, no. 2, pp. 295-305, April 2012.

Chapter 3 of this thesis has been published as A. Kahrobaeian, and Y. A.-R. I. Mohamed, "Suppression of Interaction Dynamics in Distributed Generation MGs Via Robust System-oriented Control Approach", *IEEE Trans. on Smart Grids*, vol. 3 no. 4, pp. 1800-1811, December 2012.

Chapter 4 of this thesis has been published as A. Kahrobaeian, and Y. A.-R. I. Mohamed, , "Direct Single-Loop μ-Synthesis Voltage Control for Suppression of Multiple Resonances in MGs with PFC Capacitors", *IEEE Trans. on Smart Grids,* vol. 4 no. 2, pp. 1151-1161, June 2013.

Chapter 5 of this thesis has been accepted for publication as A. Kahrobaeian, and Y. A.-R. I. Mohamed, "Robust Single-Loop Direct Current Control of LCL-Filtered Converter-based DG Units in Grid-Connected and Autonomous MG Modes", accepted in *IEEE Trans. on Power Electronics*, in press.

Chapter 6 of this thesis has been published as A. Kahrobaeian, and Y. A.-R. I. Mohamed, "Analysis and Mitigation of Low-Frequency Instabilities in Autonomous Medium-Voltage Converter-Based MGs With Dynamic Loads", *IEEE Trans. on Industrial Electronics*, vol.61, no.4, pp.1643,1658, April 2014.

Chapter 7 of this thesis has been accepted for publication as A. Kahrobaeian, and Y. A.-R. I. Mohamed, "Networked-based Hybrid Distributed Power sharing and Control for Islanded MG Systems", *IEEE Trans. on Power Electronics*, in press.

Also, Chapter 8 of this thesis has been submitted for publication to *IEEE Trans. on Power Systems*.

Acknowledgement

I would like to express my sincere appreciation to Dr. Yasser Abdel-Rady I. Mohamed for his kind support and excellent supervision during this research project. This research and dissertation would not have been possible without his continuing guidance.

I would also like to acknowledge the financial support provided by the Alberta Innovates Graduate Student Scholarship.

Finally, I would like to extend a special thank you to Dr. Reza Iravani and other examining committee members including Dr. Yasser Mohamed , Dr. Venkata Dinavahi, Dr. Mahdi Tavakoli and Dr. Jinfeng Liu for taking the time to review this thesis. I am also thankful to all the faculty and staff members in the Department of Electrical and Computer Engineering at the University of Alberta who provided a pleasant working atmosphere for me during the past four years.

Table of Contents

List of Tables

List of Figures

List of Acronyms

DC	Direct Current
DG	Distributed Generation
DOF	Degree-of-Freedom
DPR	Distributed Power Regulator
EMU	Energy Management Unit
HC	Harmonic Compensator
IM	Induction Motor
IMC	Internal Model Control
LHP	Left Half Plane
MG	Micro-grid
MV	Medium Voltage
PCC	Point of Common Coupling
PFC	Power Factor Correction
P-HERES	Proportional-Resonant with Harmonic Compensator
PI	Proportional-Integral
PLL	Phase Locked Loop
PQ-Bus	Active and Reactive Power Regulated Bus
PR	Proportional and Resonant
PV	Photovoltaic
PV-Bus	Active Power and Voltage Regulated Bus
PWM	Pulse Width Modulation
RHP	Right Half Plane
THD	Total Harmonic Distortion
UPS	Uninterruptable Power Supply
VSI	Voltage Source Inverter

Chapter 1

Introduction

The everyday increasing demand for energy on one hand and the economic and environmental issues associated with large power generating plants run on fossil fuels on the other hand, have made distributed generation an appealing option for the future power system structure. According to the IEEE standard 1547.4 [1] in the new vision of power systems, the conventional distribution system is going to be reshaped into multiple modern, interconnected subsystems so called micro-grids (MG) forming a large active distribution system.

MGs, as the future building blocks of the power distribution systems, can be considered as small electrical distribution systems which consist of consumers and several locally-connected DG units. Clustering the large scale distribution system into a set of smaller MG subsystems has several benefits to the utility as well as the consumers. The interactive nature of MGs, which enables them to operate in both grid-connected and islanded modes, would enhance system reliability. Moreover, due to the fast response of the converter-based interface of MG generators, faster and more effective control strategies can be adopted to improve the power quality. Distributed control, easier integration of renewable energy systems and the optimal load sharing are among some of the other advantages of the adoption of MG based active distribution systems. Note that having such self-sufficient islands would help maintain the system stability in the event of propagated faults that may cause cascaded blackouts.

Figure 1-1 shows a schematic of the future active distribution system where a large number of inverter-based DG units and other electronically-coupled devices form several interconnected MGs which can be actively connected to or disconnected from one another. Note that unlike the traditional concept, the power can flow from each entity to another; thus providing a multidirectional flow of energy yielding higher reliability.

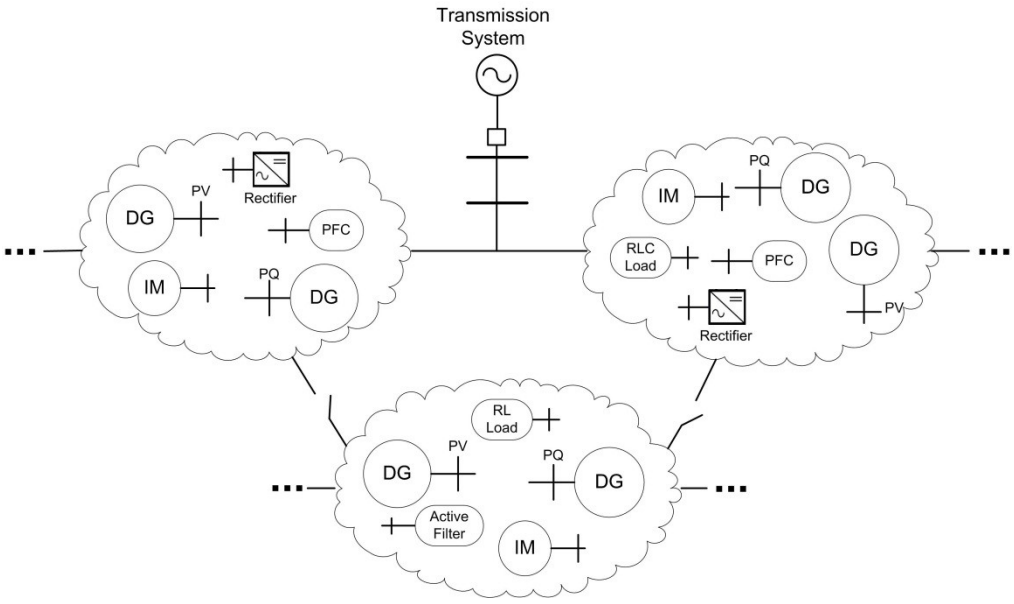

Figure 1-1: Future active distribution system consisting of multiple interactive MGs.

1.1 Background and Motivation

Research on active distribution systems is still in its infancy. Several modeling, analysis and control problems should be addressed to realize this vision. The challenges this research is seeking to address can be categorized into two main categories: converter- and system-level interactions.

At the converter-level, several undesirable converter-MG interactions can occur due to 1) switching between different operational modes (i.e. grid-connected/islanded, PV-Bus/PQ-Bus modes; 2) power-angle interactions between mutual converters and between converters and dynamic loads (e.g. line-start induction motors); and 3) uncertain multiple resonances due to the interfacing filter parameter uncertainties in both voltage-controlled dispatchable and current-controlled non-dispatchable entities. In this context, detailed modeling and analysis is required to quantify the impact of such interactions on converter stability and performance. New control design approaches, which avoid the use of the complete MG dynamics, are therefore needed in order to develop novel control interfaces that can mitigate the aforementioned undesirable interaction dynamics within a MG system. Such control interfaces should offer simplicity, robustness and efficient implementation, which make them attractive for industrial implementation.

Secondly, ***at the system-level***, the lack of coordinated control in MG systems, calls for system level controllers that can coordinate the control action of individual entities. In

this context, several control issues need to be investigated. Important among these are: 1) frequency and voltage deviations in islanded MG systems; 2) accuracy of active and reactive power sharing in large MGs; 3) power flow control and synchronization of multiple MGs. To satisfy these essential control functions, supervisory communication-based control approaches are needed.

The rest of this section elaborates on the challenges that have motivated this research, and helped in identifying its objectives.

1.1.1 Flexible Interactive DG Interface for Smart-grid Application

Flexible operation and seamless integration of DG units are major objectives in future smart power grids [2-5]. The majority of DG units are interfaced to the grid/load via power electronics converters. Current-controlled voltage-sourced inverters (VSIs) are commonly used for grid connection [6]. Within the smart grid environment, DG units should be included in the system operational control framework, where they can be used to enhance system reliability by providing backup generation in isolated mode, and to provide ancillary services (e.g. voltage support and reactive power control) in the grid-connected mode. These operational control actions are dynamic in nature as they depend on the load/generation profile, demand-side management control and overall network optimization controllers (e.g. grid reconfiguration and supervisory control actions) [5]. To achieve this vision, the DG interface should offer high flexibility and robustness in meeting a wide range of control functions, such as seamless transition between grid-connected operation and islanded mode; seamless transition between PV-Bus or PQ-Bus modes of operation in the grid connected mode; robustness against islanding detection delays; offer minimal control-function switching during mode transition; and maintaining a standard hierarchical control structure, which is widely adopted in the power converter industry.

Several control system improvements have been made to the hierarchical control structure to enhance the control performance of DG units either in grid-connected or isolated MG systems [6-12]. However, subsequent to an islanding event, changing the controlling strategy from current to voltage control, may result in serious voltage deviations especially when the islanding detection is delayed [13]. Further, mode transition transients will be imposed on the output voltage vector, where both the magnitude of the output voltage and the power angle will be subjected to disturbances.

Few studies addressed the extended nature of MG operation during mode transition and flexible operation. Seamless voltage control while transitioning between grid-connected and isolated local-voltage controlled modes is reported in [14]. Indirect current control technique is proposed in [13] to mitigate voltage transients in mode transition. In [15], a direct control structure that mimics synchronous generator operation is proposed to provide seamless transfer characteristics. These control schemes, however, do not cope with the standard hierarchical control structure in modern power converters. A nonlinear sliding-mode voltage controller and adaptive power sharing controller are proposed in [16] to achieve seamless mode transfer in MGs. These controllers adopt complicated control structures. Further, the robustness against islanding detection delays is not tested in previously developed controllers. Therefore, there is a great need to develop a robust and flexible hierarchical control structure with simple linear control design that provides a powerful control platform for high-level controllers in the smart grid environment.

1.1.2 Voltage and Power-Angle Dynamic Interactions in MGs

One of the popular operating regimes possible for DG units is the islanded MG [17-19] operation, in which a cluster of DG units, served by a distribution system, is formed to maintain the reliability of critical loads, mainly when the utility supply is not available. In autonomous MGs, the basic control objective is to achieve accurate power sharing while maintaining close regulation of the MG voltage magnitude and frequency. The stability and robustness of MG operation depend mainly on the power sharing and voltage controllers adopted in DG units.

To realize autonomous power sharing function among parallel converters, droop controllers are widely adopted for power sharing control. The stability and robustness of autonomous MG operation depend mainly on the power sharing and voltage controllers adopted in DG units. Several droop control schemes are reported to enhance the power sharing dynamics in MGs; these schemes include transient droop controller, angle droop functions, resistive output impedance droop controllers, complex impedance droop controllers, and adaptive droop controllers [7, 17-25]. Further, several voltage control methods are adopted for output voltage regulation in MG converters. These methods include robust servo-mechanism, harmonic resonant, sliding mode, linear with variable structure, adaptive and deadbeat controllers [26-31].

Existing power sharing and voltage control schemes, however, are designed at the single converter level, where interactions among MG converters are usually neglected. This is motivated by the difficulty of designing converter control schemes that consider the overall MG dynamics, which demands accurate modeling of the complete MG dynamics. In a converter-dominated MG system where the converter ratings are comparable and the physical inertia is quite small as compared to typical synchronous generators, two main types of interactions imposed on a DG unit are: 1) voltage interactions, and 2) power angle interactions.

The small-signal stability analysis of typical MGs in [18, 19] indicates that there is a frequency-scale separation between the modes associated with each of these two kind of interactions. The power angle interaction dynamics are associated with the low-frequency modes in the overall MG linearized state-space model whereas the voltage interactions are associated with the medium-frequency modes. Eigen participation analysis in [18] confirms that the low-frequency modes are mainly dictated by the power sharing droop controller state (i.e. power angle) while the medium-frequency modes are largely sensitive to the state variables of the voltage controller. The remaining high-frequency cluster of modes are dictated by the output LCL filters and since they are already highly damped, as long as they are properly designed, their effect on the system stability is minimal. This indicates that both the power sharing and voltage control loops should be designed with a robust mechanism to mitigate possible interactions among DG units.

Dynamic interactions and disturbances might occur due to several reasons. Important among these are:

1) Conventional droop controllers are designed under the conventional infinite-bus assumption; which is not valid in a typical MG system, where converter ratings are quite similar. Further, the absence of physical inertia in converter-dominated MGs remarkably affects the disturbance rejection performance against power angle disturbances. Therefore, network-, converter- or load-induced disturbances lead to a power-angle disturbance at one location within the MG, which might propagate over the network affecting the relative angle stability of different DG units. Such power angle interaction dynamics are associated with low-damping modes in the overall MG linearized dynamics [18].

2) For optimized economic operation of a typical MG system, static droop coefficients of MG generators can be varied over wide range. Interactions among

micro-generators are remarkably affected by the droop gains due to their direct effect on the low-frequency modes of a MG system [19].

3) Stability analysis of typical MGs indicates the presence of medium-frequency modes, which are associated with the voltage control dynamics [18, 19]. The relative stability of medium-frequency modes is affected by the operating condition of the MG system (e.g. output power) and load types. Interaction dynamics at these modes can be yielded due to possible mode excitation by MG low-order harmonics.

4) Local and remote nonlinear loads induce harmonic disturbances that should be rejected by the DG interface [26, 27].

5) Variation in system topology due to MG-reconfiguration (for self-healing control or loss minimization, connection/disconnection of sub MGs and connection/disconnection to the main utility grid) affects the impedance parameters as seen by DG units, and might induce instabilities or control performance degradation [10].

1.1.3 Uncertain Resonance Modes in MGs with PFC Capacitors

Robust control and stability of MGs can be a challenging task when different types of loads and power system devices are connected within the vicinity of each DG unit. One of the devices that is widely used in power systems to improve their efficiency and power quality is power factor correction (PFC) capacitors. PFC capacitors are mainly used on customer's side to avoid utility power factor penalties. They are also used by utilities for Volt/VAr control. Reactive power compensation results in reduced losses in transmission lines as well as transformer heating. Moreover, in long distribution lines, they are often used in order to increase the supply voltage at the load side. However, switching of PFC capacitors within a MG can cause performance degradation and even instability of the system [32-35]. This is due to 1) PFC capacitors affect the effective value of the capacitor filter of DG units; and 2) PFC capacitors introduce additional uncertain resonant dynamics reflected to DG units. On the other hand, capacitive loads (e.g. residential capacitive loads) might generate uncertain resonant modes reflected to DG converter control dynamics [36]. Accordingly, PFC capacitors and capacitive loads in DG MGs directly affect the closed loop voltage control stability and might yield high resonant voltage and current disturbances.

Several hierarchical control strategies have been reported for DG units in grid connected and autonomous MG modes [18, 26-28]. However, these methods do not incorporate the effects of filter parameter variations and the system uncertainties along with the effect of the connection of PFC capacitor banks in the vicinity of DG units.

One of the well-established robust control approaches that is reported in many converter-based robust applications is H_∞ control [27, 36-38]. A conventional multi-loop control scheme composed of a robust H_∞ outer voltage controller is proposed in [35] to increase MG robustness against effective filter capacitance variations in presence of PFC capacitors. However, in [35] the uncertainty over the effective filter capacitance caused by connection of PFC capacitor has been only modeled as a lumped unstructured uncertainty. This is usually obtained by comparing the nominal open loop transfer function and the transfer function with the worst case filter capacitor variations. The proposed controller succeeds in maintaining the system stability in the presence of PFC capacitors; however, the robust performance of the system is compromised due to the inherent conservative nature of a robust H_∞ controller synthesized for unstructured uncertainties [39, 40]. Therefore, possible instabilities can be yielded under parameter variation; and the voltage quality is highly affected as the PFC capacitor is connected. It should be noted that this limitation is inherently related to the fundamental concept behind the H_∞ control approach, which is the optimum loop shaping under unstructured uncertainty model. Unstructured uncertainty modeling can be used in large control systems, where there is difficulty in modeling uncertainties in each subsystem. For converter-based DG units, the system order is generally low. Therefore, the conservative unstructured uncertainty assumption is not really needed in such application. On the other hand, conventional H_∞ control is applied with inductor current feedback control and inner capacitor current loop to dampen the resonant peak of the ac-side filter [35]; without damping the filter resonance peak, the perturbed closed loop system cannot remain stable with conventional H_∞ control. However, in MG applications, it has been shown recently that direct voltage control enables simpler implementation and more importantly, high bandwidth voltage control performance, which helps in realizing seamless transition between grid connected and autonomous MGs [41].

1.1.4 Stability of LCL-Filtered Current-Controlled Converters in Grid-Connected and Isolated MGs

Renewable DG units, such as photovoltaic (PV) arrays and wind turbines, are often operated in current control mode in order to control both the power factor and the harmonic content of the injected current. The current control mode is suitable for grid-connected application and it can be used in isolated MGs with appropriate energy management strategy. Currently, there is a growing interest in using inductor-capacitor-inductor (LCL) ac-side filters in grid-connected inverters, which yield better attenuation of switching harmonics. Accordingly, an LCL-filtered inverter is suitable for high power DG applications, which are characterized by low switching frequencies (few kHz) [10, 42-45]. However, low- and high-frequency instabilities can occur due to the resonance frequency introduced by the LCL filter and the interactions between the current controller and the grid impedance [10, 42-45]. The associated undamped resonance peak also limits the open loop gain; thus compromising the controller's bandwidth yielding very slow response times [10]. Further, without resonance damping, the resonance mode can be excited during network or converter disturbance. Different damping solutions are proposed in order to remove the LCL filter resonance where the active methods are preferred over the passive ones due to their minimized power losses [42, 46-56]. Active resonance damping can generally be achieved by utilizing a multi-loop control system or full-state feedback control. The inner feedback loops can be from the inverter-side inductor current [48, 49], the filter capacitor current [50, 51] or the filter capacitor voltage [42, 52]. Full-state feedback control is adopted in [53, 54] to provide resonance damping and achiev complete system controllability. However these methods require an additional number of sensors which might not be considered an optimized solution. Other resonance damping techniques include the use of special filter and/or sensor arrangement such as split capacitor or two-sensor feedback control [49, 55]. A filter-based approach is presented in [56] where a notch filter is added to dampen the resonance peak.

Single-loop control structure without the adoption of extra damping loops is investigated in [44], [57-59]. The stability of the single-loop LCL-interfaced system for different control bandwidth frequencies is investigated in [44]. The analysis suggests that the presence of the LCL resonance peak limits the control bandwidth of the PI controller. Therefore, the closed-loop system dynamics should be chosen to be slower in order to avoid instability. It is shown that stable system operation can be achieved by a careful

choice of filter parameters using PI control [57]. The study in [58] confirms the necessity of small loop gains in order to avoid instability. Note that the limited controller dynamics in [44, 57-59] makes the adoption of harmonic compensation [43], which is a necessary feature especially in active filter applications, impossible. Moreover, the effect of line parameter uncertainty over system stability has not been addressed in the preceding works reporting single-loop structure. This is especially important considering the fact that even in the multi-loop active damping structure, when adopting harmonic compensators, the line inductance uncertainty can easily shift the open-loop cross-over frequency; therefore, bringing the frequencies of the harmonic compensators outside the bandwidth of the system leading to instability [10, 43]. A single-loop frequency domain stabilizing controller is provided in [59] that follows the norm minimization method through convex optimization similar to H_∞. Although the proposed controller is proven to stabilize the nominal plant by introducing inherent active damping; however it fails to verify its robust stability for a high range of system uncertainty as plant uncertainties are not considered in the design procedure. Moreover, no control effort is used to reject the harmonic disturbances, yielding a compromised current quality in the presence of voltage harmonics. Note that deadbeat and predictive current controllers, which provide fast dynamics, also are highly-dependent on system modeling, which makes them sensitive towards parameter variation and demand robust or adaptive control design [43].

1.1.5 Low-Frequency MG Instability with Dynamic-Type Loads

As mentioned earlier, the stability of autonomous MGs is a critical issue considering the low-inertia nature of such converter-dominated systems. Small-signal-based stability analysis, reported in [17-19, 60], are used to study the stability of the autonomous droop-controlled MG systems where the state-space analysis indicates that the dominant low-frequency modes are very sensitive to the load demand and power sharing controller parameters. Moreover, [61] shows that proper load sharing especially under weak grids (with low line reactance/resistance ratio) requires higher frequency droop gains in order to avoid the coupling issue between active and reactive power generation. On the other hand, the stability analysis reveals that higher droop gains, would compromise system stability by shifting its dominant poles to the right-hand-plane (RHP) yielding oscillatory responses. Reference [62] suggests that, therefore, a stability margin can be identified for the droop gains and proposes a method on updating the system droop gains for each operating point in order to meet the desired damping. In all of the previous studies

addressing MG stability issues, static (RL-type) loads are considered to simplify the modeling and analysis tasks. The static load modeling approach is suitable in low-voltage MG applications (e.g. residential loads and/or small induction motors). For small induction motors (IMs), the rotor-circuit time-constant is small, which yields a fast decay of rotor electrical dynamics as compared to rotor mechanical dynamics (flux-angle and slip decoupled dynamics) [63]. Therefore, the electromechanical rotor dynamics are decoupled and, accordingly, small IM loads can be modeled by its equivalent steady-state circuit or active and reactive power demand. In this case, the circuit behavior of the induction motor dominates its dynamics. This justifies the use of static load models in previous low-voltage low-power MG stability studies.

However, with the expected high penetration level of MGs in future power networks and recent advances in power converter ratings and topologies, medium voltage multi-MW MG systems will be created and they will be subjected to a wide pattern of both static and dynamic loads. Electromechanical rotor oscillation phenomenon occurs in an obvious way in large MW range motors [64], which are directly connected to medium voltage systems (1.0kV to 20kV). These motors account for approximately 23% of energy usage [65]. Therefore, ignoring this type of load in stability analysis of MG systems results in a rather unrealistically large stability operating region due to the highly nonlinear load dynamics, which couples the active power, reactive power, voltage and supply frequency dynamics in a MG system.

In conventional power system analysis, several studies are reported to analyze the impact of large IM loads on power system dynamics. In addition to the well-known impact of IMs on voltage stability, it has been shown that large IMs might interact with synchronous generator rotor dynamics and excitation systems leading to modal resonances, limit cycles and voltage oscillations [64]. In power system small-signal studies, conventional line-star motors are used for stability analysis around their operating point [64, 66-70]. The linearized small-signal-based state-space model of the induction motor is adopted in [64, 66-70] where the system eigenvalue spectrum is derived for the purpose of stability analysis. In the context of MGs, the impact of IMs on load margins is studied in [70]. Impedance mismatch between IM loads and VSIs in MGs is recently addressed in [71], where it is shown that medium-frequency instabilities (in the range of tens of Hz to few hundreds of Hz) can occur in converter-based MGs with IM loads. However, even if the impedance-ratio stability criterion is maintained, a MG

system with dynamic loads can still be subjected to low-frequency instabilities due to the time-scale separation between the corresponding modes. A literature survey indicates that a detailed analysis, and more importantly, stabilization of MW droop-controlled MGs with IM loads are not reported and demand special attention.

1.1.6 Coordinated Control of Multiple MGs

In the smart active distribution paradigm, MG systems are considered to be the building blocks of the distribution grids [2]. In this paradigm, clustering a large scale distribution system into a set of smaller supply-adequate MGs can provide higher reliability and efficiency as well as enhanced distributed control strategies [72]. Therefore, bidirectional power-flow control between MGs is essential. In this way, each MG can actively participate in shaping the supply/demand balance resulting in more optimized performance. Energy optimization or generation/demand estimation can be adopted to control the amount and direction of the power flow between MGs entities. Each MG cluster may consist of both dispatchable (i.e. diesel generators, fuel cells, micro-turbines, etc.) and non-dispatchable (i.e. photovoltaic arrays, wind, etc.) DG entities. Although the clusters can be designed to provide adequate supply for their local demands, the intermittent nature of the renewable energy resources, load uncertainties and the economic criteria imposed on dispatchable DG units (like the fuel price and the energy storage levels) make the interaction among different MGs an absolute necessity. In addition to controlling the power transfer between MGs (tie-line power control), the energy flow in each MG can also be optimized by ensuring that certain local-level power sharing objectives are met. Therefore, the power demand can be shared among dispatchable units based on their size or other energy management objectives depending on the customer and utility needs. For example, these objectives include minimizing the fuel cost, minimizing the emissions and maximizing the network security [62, 73-77] .Therefore, utilization of a dispatch centre in each MG brings more intelligence and efficiency to the MG system where more flexible operation is needed [31]. However, one of the challenges associated with the operation of multiple MG systems is their synchronization prior to their connection. Any synchronization algorithm should minimize the voltage and angle differences at the point of common coupling without violating the power sharing criteria. Therefore, all dispatchable DG units should contribute to the synchronization effort according to their share decided by the local dispatch centre.

The majority of MG control structures available in the literature are based on autonomous droop controllers, which eliminate the communication requirements between individual DG units [17-19, 78-80]. However, droop-based MGs suffer from permanent frequency/voltage offset, inaccurate reactive power sharing, poor dynamic performance and possible instability under high droop gains which are needed to enhance the power sharing performance. Although cost-optimization algorithms can be applied in a droop-based control system via changing their droop gain ratios, however as suggested in [62], [81] system stability is highly sensitive to the selected droop gains and one should consider this criteria in an online/offline manner prior to adopt any energy management strategy. Networked-based secondary and tertiary control schemes are therefore proposed in [7, 21, 82-85] to remove the frequency and voltage deviations as well as to regulate the power flow between the MG and the main grid, respectively. However at the secondary control level, most of the proposed schemes provide a centralized structure which increases the communication cost and compromises its reliability in the presence of delay and network failures. A distributed networked-based control structure is proposed in [84, 85] to minimize the power sharing error as well as maintaining frequency and voltage levels in parallel inverters using secondary level auxiliary voltage and frequency signals. However, the synchronization and power-tie regulation are not studied in these previous works, and a general framework that includes these functions is not developed. In [7, 84, 85], the secondary level control effort is not allocated based on the primary level power sharing objectives. Therefore, the secondary control loops are needed to be designed much slower than the primary droop controllers to avoid violating the power sharing objectives [86]. An active synchronization scheme is presented in [87] which acts as a centralized secondary control scheme. The synchronization effort is shared between DG units by introducing weighting functions to comply with the primary level power sharing objectives. However, a clear procedure on designing the weighting functions is not provided and the effect of such a synchronization process on the power sharing dynamics is not studied.

1.2 Research Objectives

Motivated by the limitations mentioned in Section 1.1, this research aims to provide a comprehensive study of these limitations leading to the development of new converter- and system-level control interfaces that can enhance stability and performance of MG

systems in both grid-connected and islanded modes. Therefore the following research objectives are defined in order to enhance the flexibility, stable operation and plug-and-play features of MG systems:

1. The development of a flexible DG interface that provides minimal transition between different operational modes with minimal control-function switching.
2. The development of robust DG control interfaces to mitigate undesirable interaction dynamics in MG systems; including converter-MG voltage and angle interactions, uncertain resonant modes in MG systems and interaction dynamics with IM loads.
3. The development of coordinated control frameworks for optimization and stabilization of MG systems using networked-based supervisory control and conducting delay-dependent stability analysis of such systems.
4. The development of auxiliary supervisory control units for the purpose of active synchronization and power-tie control in multiple MG systems.

1.3 Thesis Overview and Summary

A flexible DG interface that can operate in both grid-connected and islanded modes is proposed in Chapter 2 where a fixed hierarchical structure is utilized to minimize control function switching yielding robust control performance under islanding detection delays. A two-degree-of-freedom internal-model-based control structure is proposed to maximize the disturbance rejection performance within the DG interface in order to maintain voltage quality. In Chapter 3 the effect of voltage and power-angle interaction dynamics in the stability of frequency and voltage droop controlled DG entities is studied. A novel system-oriented design approach for DG converters in MGs is then presented to provide system robustness against system-level interactions without a strict knowledge of the complete MG system dynamics. An H_∞ voltage controller as well as an angle feed-forward method are adopted to account for both voltage and angle interaction dynamics. The effect of connecting PFC capacitors that introduce undamped resonance modes in MG systems is studied in Chapter 4 where, in order to preserve the stability in a wide range of capacitive uncertainties imposed on the DG interfacing filters, the conventional uncertainty modeling approach is enhanced by capturing the structure of the uncertainties. This facilitates the realization of a robust controller based on structured singular values (μ) minimization. The resultant controller is used as a direct voltage controller where no additional damping technique, either passive or active, is required. The new structured uncertainty modeling and the μ-synthesis approach introduced in Chapter 4 is also adopted for LCL-filtered current controlled DG units in grid-connected and islanded MG modes in order to maintain their stability in presence of line inductance uncertainties as explained in Chapter 5. Unlike the conventional H_∞-based approach, the proposed interface is proven to maintain both robust stability and robust performance for a wide range of line parameter variations. Chapter 6 studies the effects of high integration of dynamic loads in MV MGs. In this chapter, unlike the conventional MG stability analysis methods in which only static type loads are adopted, the detailed small-signal model of a typical MV droop-controlled MG system is developed to capture the dynamics of IM loads in compromising system's stability. A supplementary active damping control method is then suggested to mitigate the associated low frequency dynamics via participation factor analysis. In Chapter 7 a new hybrid distributed networked-based power control scheme is proposed in order to address the remaining challenges associated with the conventional autonomous frequency- and voltage-droop control structure. The

proposed scheme provides improved MG dynamic performance, minimized active/reactive power sharing errors under unknown line impedances, and high reliability and robustness against network failures or communication delays. The proposed distributed networked-based control scheme of Chapter 7 is completed in Chapter 8 by developing a comprehensive hierarchical framework that can not only provide accurate active and reactive power sharing with minimal frequency deviations but also actively engages the DG units in active synchronization and power-flow control among multiple interconnected MGs without interfering with the inner power sharing loops. The thesis summary, contributions and some directions for future works are presented in Chapter 9.

Chapter 2

Interactive DG Interface for Flexible MG Operation[1]

Motivated by the difficulties mentioned in subsection 1.1.1, this chapter presents an interactive DG interface for flexible MG operation in smart distribution systems. The proposed control scheme utilizes a fixed hierarchical power-voltage-current control structure, which is used under different modes of operation. Therefore, only the magnitude of the reference voltage vector is subjected to variation, which minimizes the internal disturbances generated by switching a current-controlled interface to a voltage-controlled interface in conventional control techniques. The voltage controller is robustly designed to offer internal model control characteristics against random disturbances associated with mode transfer and harmonic and unbalanced voltage disturbances associated with DG operation under unbalanced voltages and nonlinear loads. Further, the proposed controller offers robustness against islanding detection delays due to the fixed control structure. Theoretical analysis and evaluation results verify the effectiveness of the proposed control scheme [31].

2.1 System Configuration

Figure 2-1 shows the 3-DG under study MG system, which is adapted from IEEE 399 standard for low to medium voltage applications [88]. The adopted test system represents a general distribution system, where different types of loads and different numbers of DG units can be considered to be connected to the main feeder. The DG units can be employed to work either in parallel to the utility grid; or in isolated mode to serve sensitive loads connected to the main feeder when the main breaker (SW) is open. Without the loss of generality in Chapter 2 through Chapter 4, the performance of the MG system is studied when only the first two DG units are connected. However as will be seen in the future chapters this structure is expanded in order to capture different types of low- and medium- frequency interaction dynamics in a MG system by connecting more DG units as well as introducing new components to the existing system.

[1] A version of this chapter has been published: A. Kahrobaeian, and Y. A.-R. I. Mohamed, "Interactive Distributed Generation Interface for Flexible MG Operation in Smart Distribution Systems", *IEEE Trans. on Sustainable Energy*, vol. 3, no. 2, pp. 295-305, April 2012.

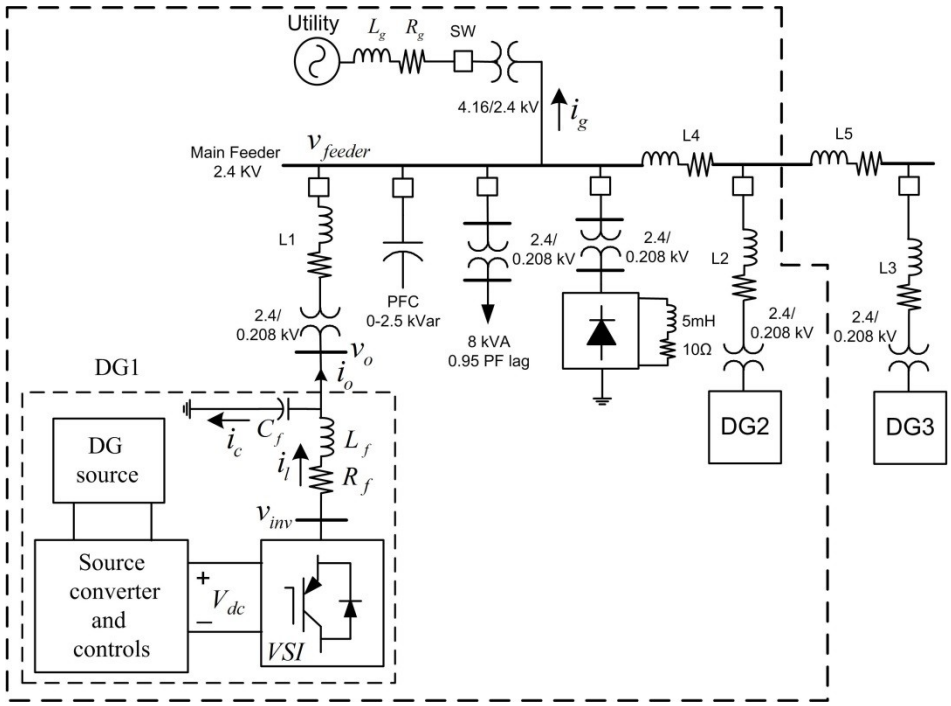

Figure 2-1: Single line diagram of the MG test system

In Figure 2-1 the load on the main feeder is an inductive load where a 2.5KVAr power factor correction capacitor bank is also considered to be connected to the main feeder. The adopted load model is in line with the IEEE 1547 test load used in DG applications [89]. The nonlinear load is a three-phase diode rectifier with an *R-L* load at the dc-side. The addition of the diode rectifier helps in assessing the effectiveness of the proposed controller in rejecting voltage harmonics associated with nonlinear loading, and rejecting load-DG-unit-grid interactions at harmonic frequencies. The line and DG circuit parameters are as follow: S_{base}=10 kVA, $V(L\text{-}L)_{base}$= 208 V, DG1, DG2= 15 kVA, 60 Hz V_{dc}=400V , L_f =1.2 mH, R_f=0.1 Ω, C_f=50 μF, f_{sw}=10 kHz, L1=(1+3.2j)%, L2=(1+3.2j)%, L4= (0.5+0.53)%.

The schematic diagram of a single DG unit as the building block of the sample MG system is also shown in Figure 2-1. When the DG unit is connected to the grid, the voltage and frequency at the point of common coupling are dominantly dictated by the grid. However, in case of weak grids, the voltage is prone to voltage sags and disturbances. In this case, the DG unit can be controlled to support the grid voltage. Therefore, the voltage regulation-mode (PV-Bus mode) can be adopted in the grid-connected mode to support the weak grid. Moreover, the output reactive power generated

by each DG can be controlled if the DG is assumed to operate in PQ-Bus mode. Subsequent to an islanding event, DG units can form an autonomous MG system to enhance the reliability of sensitive loads. However, this flexible operation requires robust control infrastructure, which is essential for system operators and supervisory controllers in the smart grid environment.

In both grid-connected and isolated modes, the state space presentation of the DG interface dynamics can be given in the stationary $\alpha\beta$ reference frame by (2-1)-(2-2).

$$v_{inv,\alpha\beta} = L_f . \frac{di_{l,\alpha\beta}}{dt} + R_f . i_{l,\alpha\beta} + v_{o,\alpha\beta} \tag{2-1}$$

$$i_{l,\alpha\beta} = i_{o,\alpha\beta} + C_f \frac{dv_{o,\alpha\beta}}{dt} \tag{2-2}$$

where L_f and C_f are the filter inductance and capacitance, v_{inv} is the inverter output voltage, i_l is the inverter output current, v_o is the voltage at the point of common coupling, and i_o is the network-side current. Note that the small filter-inductor resistance is represented by R_f. (2-1)-(2-2) suggests that the output current (i.e. i_o) can be regarded as an external disturbance caused by unknown load or grid behavior either in islanded or grid connected mode. Along with these exogenous disturbances, control mode switching in conventional DG controllers (e.g. from current control to voltage control) generates internal disturbances within the control structure.

2.2 Proposed Control Scheme

2.2.1 Control Structure

External disturbances will be imposed on the DG interface during mode transition and in the presence of network/load disturbances. On the other hand, internal disturbances will be generated due to the control function switching between different modes in the conventional hierarchical control structure.

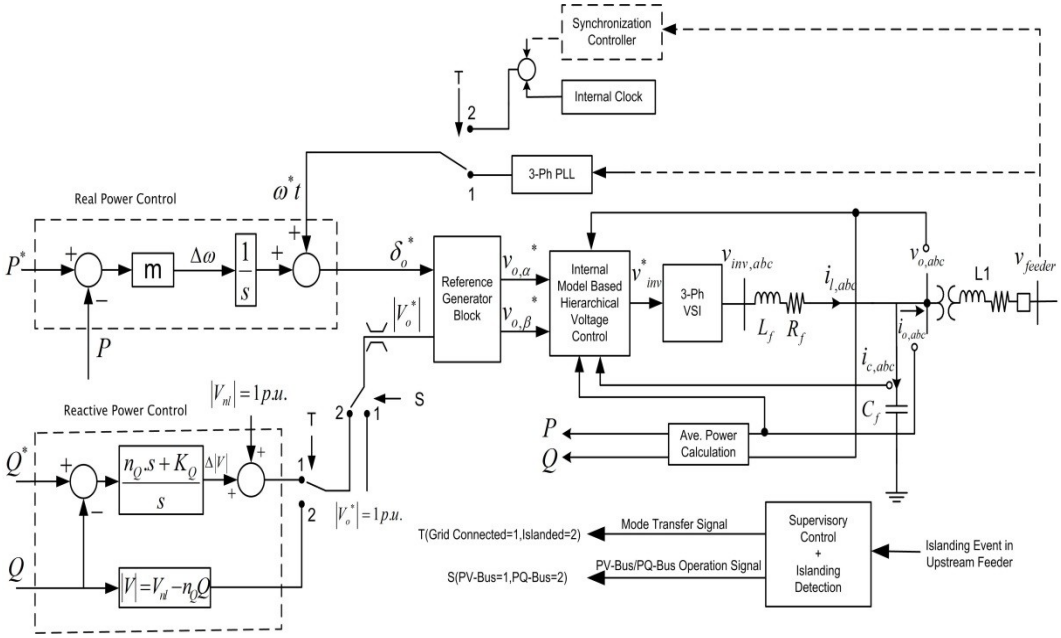

Figure 2-2: Proposed control scheme.

To overcome these issues and to achieve a flexible and robust operation of DG units under the smart grid environment whilst maintaining the hierarchical control structure, the proposed control scheme, shown in Figure 2-2, utilizes a fixed hierarchical power-voltage-current control structure in both grid-connected and isolated modes. This will minimize the undesired voltage transients generated by switching from a current-controlled interface to a voltage-controlled interface in conventional control techniques. Further, the proposed power controller works under grid-connected and isolated MG modes; this feature provides a flexible interface for the DG unit to be used in different operational modes with minimal switching. Due to the proposed design strategy, both the external and the internal disturbances can be eliminated or remarkably attenuated within the DG interface. Moreover, the fixed control structure increases the robustness of the control structure to islanding detection delays. The voltage control is designed by considering an augmented model that includes the *LC*-filter active damping and inner current control loop dynamics to ensure robustness and coordinated control design. Theoretical analysis and design procedure of the proposed control scheme are described in the following sections.

2.2.2 Augmented Internal Model-Based Voltage Control

The main objective of the proposed voltage control scheme is to maximize the disturbance rejection performance for a wide band of disturbances; and to meet the voltage tracking requirements. Towards this goal, a newly designed augmented internal model control (IMC) structure is proposed to provide internal model dynamics for harmonic, unbalanced and random voltage disturbances. Figure 2-3 shows a general two degree of freedom internal model control (IMC) structure [90]. In Figure 2-3, $G_m(s)$ represents a nominal model for the actual plant of $G(s)$, whereas $Q_r(s)$ and $Q_d(s)$ are feed-forward and feedback compensators, respectively and d can be regarded as the exogenous disturbance.

Under exact model matching (i.e. $G_m(s)=G(s)$) and the absence of system disturbances, the feedback signal, which is influenced by the disturbance or any model uncertainties, would be zero. In this case, the IMC structure, shown in Figure 2-3, can be regarded as an open loop system where the feed-forward compensator should be designed to ensure close tracking performance. On the other hand, disturbance rejection can be achieved via the feedback compensator design. Because the tracking and disturbance rejection performances can be designed independently, the IMC control scheme can be considered as a two-degree-of-freedom controller.

The sensitivity function (S) and the complementary sensitivity function (T), which represent tracking and disturbance rejection capabilities of the system respectively, can be derived as in (2-3)-(2-4):

$$S(s) = \frac{y(s)}{d(s)}\Big|_{r=0} = \frac{1}{1+G(s)Q_d(s)} \tag{2-3}$$

$$T(s) = \frac{y(s)}{r(s)}\Big|_{d=0} = \frac{Q_r(s)G(s)(1+G_m(s)Q_d(s))}{1+G(s)Q_d(s)} \tag{2-4}$$

.

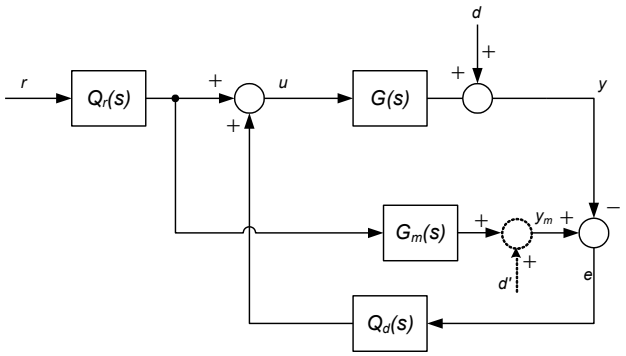

Figure 2-3: Two degree of freedom internal model control scheme.

The design goal is then to propose Q_d and Q_r such that $S(s)=0$ and $T(s)=1$ within a reasonably large range of frequencies of interest. This will ensure both disturbance rejection and tracking ability of the system. Assuming $G_m(s)=G(s)$ and $d(s)=0$, then the model following error (e) is zero and the control scheme is reduced to an open loop with $T(s)=Q_r(s)G(s)$. In this case, $Q_r(s)=G_m^{-1}(s)$ can provide perfect tracking performance. Stability constraints require $G_m(s)$ to be minimum phase. Besides $G_m^{-1}(s)$ can be an improper transfer function and cannot be realized practically. Therefore, a low pass filter is used to yield a proper feed forward compensator in form of (2-5) where τ corresponds to the bandwidth of the filter, and n is an integer selected in such a way that $Q_r(s)$ is a proper or strictly proper function

$$Q_r(s) = \frac{1}{(\tau s+1)^n}.G_m^{-1}(s) \tag{2-5}$$

The disturbance rejection is achieved via $Q_d(s)$ that produces a compensating input to cancel out disturbances. To overcome the computational burden associated with frame transformations, the proposed controller is performed in Clark's αβ-frame. Proportional resonant controllers with harmonic compensators are proposed to realize $Q_d(s)$ as in (2-6):

$$Q_d = \underbrace{K_p + \frac{2\omega_c K_I s}{\quad}}_{PR(s)} + \underbrace{\sum_{\quad} \frac{2\omega_c K_{Ih} s}{\quad}}_{HC(s)} \tag{2-6}$$

In (2-6), the first term, $PR(s)$, is the proportional resonant compensator with a proportional gain K_p, and resonant gain K_I, which is tuned at the fundamental angular frequency. The second term, $HC(s)$, is the harmonic compensator, where h denotes the harmonic order to be compensated and K_{Ih} is the corresponding resonant filter gain. In

$PR(s)$ and $HC(s)$, ω_c is the cut-off frequency, which is introduced to facilitate practical implementation of resonant controllers under variation in the fundamental angular frequency (e.g. under isolated MG operation). The PR+HC provides high disturbance rejection gains at the fundamental and selected harmonic frequencies of the tracking error. Therefore, a wide range of disturbances can be effectively rejected.

Applying an *LC* filter at the output stage introduces a resonance peak to the frequency response of the system, which can limit the achievable bandwidth of the current controller in a multi-loop hierarchical control approach. Therefore, converter resonance damping is essential to maintain stability and facilitate high bandwidth current control design. Active resonance damping can be a viable option, particularly in DG applications where losses associated with passive damping can reduce the generation efficiency. Therefore, in order to cope with the hierarchical control structure, which inherently provides active damping and enhanced system stability, the inductor and capacitor inner current loops are augmented in the voltage control design. The augmented model with both current loop dynamics is shown in Figure 2-4, where i_L and i_c are used as feedback signals, respectively.

Due to the presence of the voltage controller in all modes of operation, a simple proportional current controller K_c can be adopted as shown in Figure 2-4. Note that the reference current, i_l^*, in Figure 2-4, is generated by the outer IMC-based voltage controller. The augmented model can be simplified and the output/input transfer function is given in (2-7). The capacitor current feedback gain is assumed to be K_d.

$$\frac{v_o}{i_l^*} = G_m(s) = \frac{K_c L_f}{L_f{}^2 C_f s^2 + (K_c L_f C_f + (K_d + R_f) L_f C_f) s + (L_f + (K_d + R_f) K_c C_f)} \tag{2-7}$$

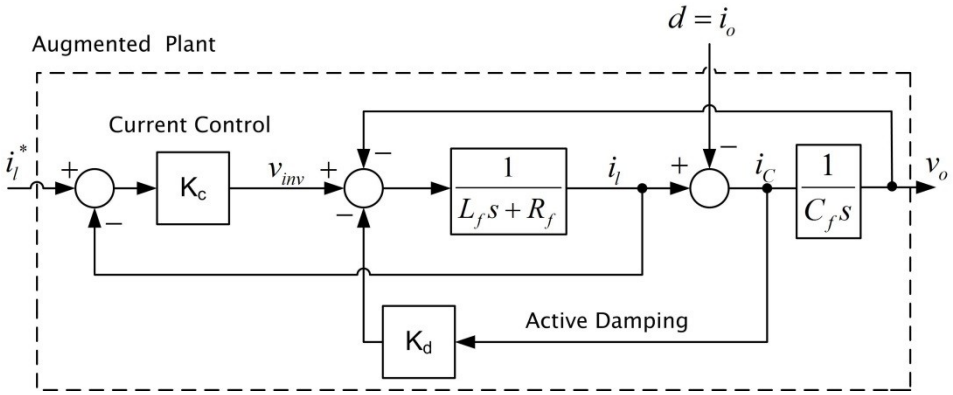

Figure 2-4: Augmented plant model including inner current control loops.

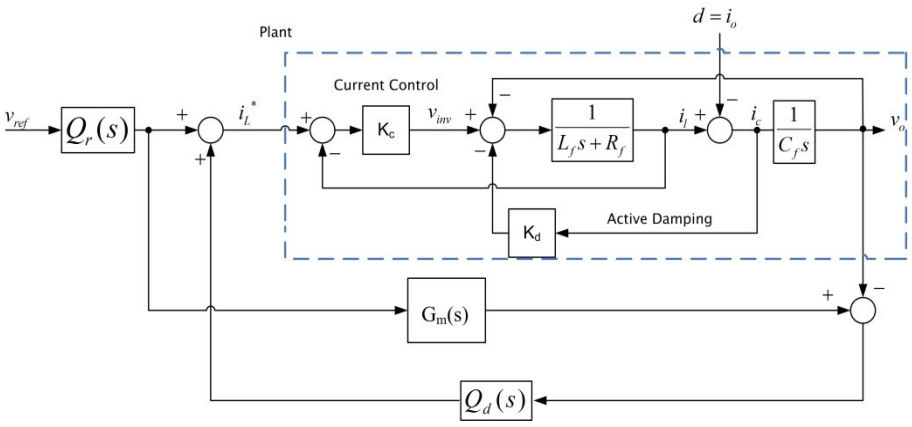

Figure 2-5: Hierarchical voltage control of the DG unit based on IMC scheme.

Figure 2-5 depicts the proposed IMC-based multi-loop voltage control structure. In Figure 2-5, $Q_r(s)$ can be calculated as in (2-8) by substituting the nominal transfer function of (2-7).

$$Q_r(s) = \frac{G_m^{-1}(s)}{(\tau s + 1)^2} \tag{2-8}$$

It can be noted that the feed-forward compensator is both stable and proper. The time constant τ dictates the tracking bandwidth of the system and it should be designed to provide, at least, half the inner current loop bandwidth. It can be also noted that mismatch in system parameters can be considered as disturbances and will be attenuated by the feedback compensators. Therefore, robustness against parameter variation and disturbances can be yielded. The sensitivity transfer function of the proposed system, which represents the frequency response of the v_o/i_o ratio can also be obtained from Figure 2-5 as (2-9) where $Q_d(s)$ is the feedback compensator defined in (2-6)

$$\frac{v_o}{i_o} = \frac{L_f s}{K_c Q_d(s) + L_f C_f s^2 + (K_d + R_f + K_c) C_f s + 1}. \tag{2-9}$$

The following control parameters are suggested to be substituted in (2-7)-(2-9) following the aforementioned design procedure: L_f =1.2 mH, R_f=0.1Ω, C_f=50μF, K_c =10, K_d=6, K_p =0.5, $K_I = K_{Ih}$ =15, τ=1e-4, ω_0=120π rad/s, ω_c= 2 rad/s.

Using the above circuit and control system parameters, the tracking and disturbance rejection characteristics of the suggested controller are demonstrated in Figure 2-6 (a) and Figure 2-6(b) respectively.

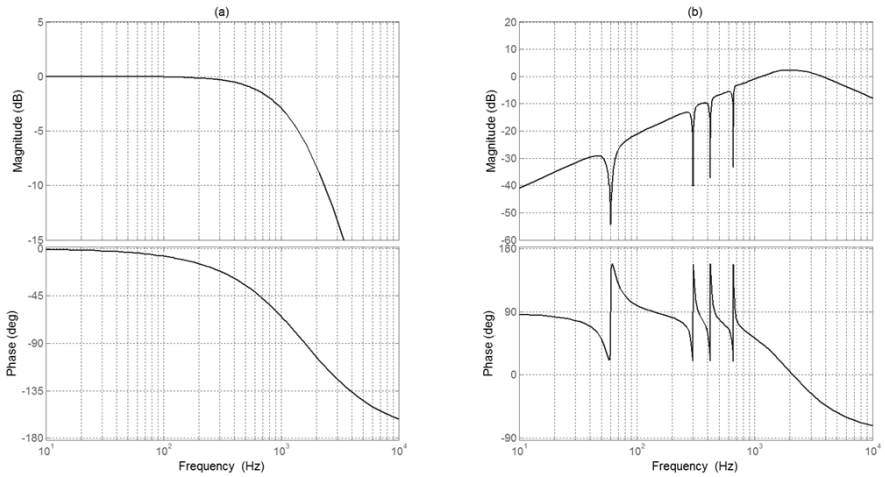

Figure 2-6: Frequency response for the (a) tracking and (b) disturbance rejection performances.

Figure 2-6(a) implies that the proposed feed-forward compensator provides a very good tracking performance, which ensures minimum voltage tracking error. Figure 2-6 (b) shows that the proposed control structure can attenuate a wide range of random disturbances associated with the output current (e.g. voltage disturbances associated with mode transition). Further, due to the presence of the internal models tuned at harmonic frequencies, the proposed controller provides very high attenuation around the fundamental and selective harmonics (i.e. 5^{th}, 7th and 11^{th}).

2.2.3 Power Flow Control

The adopted hierarchical design approach provides flexible operation of the DG unit in grid-connected mode. To minimize the control switching actions between grid-connected and isolated modes, a single active power control structure is used in both modes. The proposed active power controller, shown in Figure 2-2, consists of a slow integrator, which generates frequency deviations $\Delta\omega$ according to the power-frequency characteristics presented in (2-10) where P is the averaged active power and P^* is the nominal power value.

$$\Delta\omega = m(P^* - P) \tag{2-10}$$

Note that (2-10) is similar to the frequency-power droop equation in autonomous MG system [7] and therefore, by adopting an appropriate slope coefficient (i.e. m) based on a reasonably small frequency deviation range, the proposed real power controller can be used both in grid connected and islanded modes. Even if it is required to have different slopes at different modes, the control structure remains the same to minimize the

generation of internal disturbances within the control structure. As shown in Figure 2-2, in the grid-connected mode, the phase angle of the grid ω^*t, is generated via a *dq* three phase phase-locked loop (PLL). A resonant filter tuned at the fundamental grid frequency is used along with the PLL to make it more robust in presence of voltage harmonics or unbalances [91]. On the other hand, during islanded operation, the processor internal clock is used to generate the aforementioned signal while ω^* is assumed to be 120π. Considering the voltage and reactive power controller, the voltage amplitude can be either set to 1.0 p.u. for PV-Bus operation, or it can be adjusted through a reactive power controller for PQ-Bus operation. In the grid-connected mode, a proportional integral (PI) controller is adopted to provide the magnitude of the output voltage $|V_o|$. Therefore, the voltage control signal can be generated as in (2-11):

$$\Delta V = (\frac{n_Q.s + K_Q}{s})(Q^* - Q). \tag{2-11}$$

where n_Q, K_Q are the proportional and integral gains, respectively, Q^* is the reference reactive power, and Q is the averaged reactive power. In islanded operation, however, a voltage droop function is adopted to share the reactive power among different DG units. Accordingly, the voltage magnitude is generated according to (2-12) where n is the reactive power droop gain and V_{nl} is the no-load voltage.

$$|V_o| = V_{nl} - nQ \tag{2-12}$$

The suggested power controller gains are as follow: m=5e-5 rad/W, n_Q=1e-3 V/VAr, K_Q=1.

2.2.4 PLL Configuration and Synchronization

Figure 2-7 shows the configuration of the adopted pre-filtered three phase *dq*-PLL for synchronization purpose in grid connected mode [91]. This is a standard *dq*-PLL where a resonant filter has also been used to make it more robust in the presence of voltage harmonics and voltage unbalances.

The islanded operation is inevitable when there is a grid failure or blackout, however when the grid voltage is back to its normal condition, a synchronization process is required before transitioning to the grid connected mode. In order to bring the output voltage angle to the grid angle, which is estimated by the adopted PLL of Figure 2-7, a synchronization controller, shown in Figure 2-8, can be realized by applying small

frequency deviations in the voltage command to decrease the phase mismatching between the two voltages. The DG unit would connect to the grid when the angle difference is lower than a threshold tolerance ε to ensure seamless connection with respect to the phase angle.

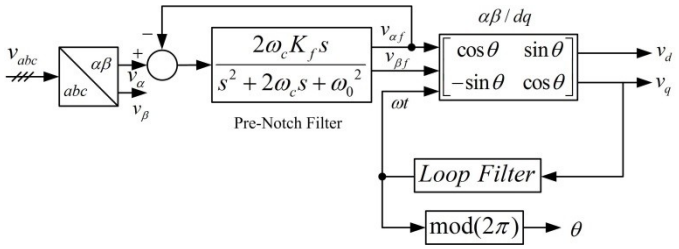

Figure 2-7: Three phase *dq*-PLL with pre-notch resonant filter.

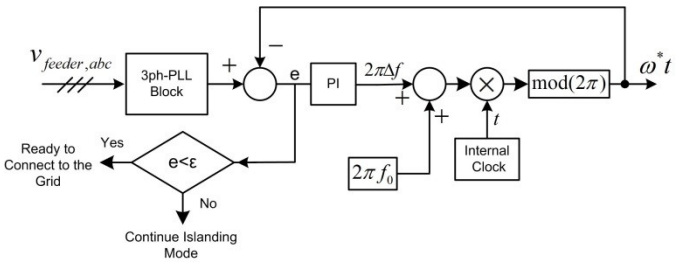

Figure 2-8: Synchronization controller.

2.3 Sample Evaluation Results

To evaluate the performance of the proposed control scheme, the test system depicted in Figure 2-1 is implemented for time domain simulation under Matlab/Simulink® environment. The MG system employs two DG units, which can work in parallel to the utility grid; or in isolated mode when the grid is not available to serve as a sensitive load. The proposed flexible control structure makes it possible for the DG unit to support the grid in different scenarios. Different scenarios are tested. Key results are presented as follows.

2.3.1 Grid-Connected Mode

Figure 2-9 shows the control performance under PQ-Bus operation mode for one of the DG units. The inductive load and the capacitor bank are activated in this scenario. The reactive power command is set to zero, whereas the active power command experiences a step change from 5 kW to 10 kW at t=1s. Figure 2-9 (a),(b) shows the active and reactive powers generated by the unit. Close active power tracking performance is yielded.

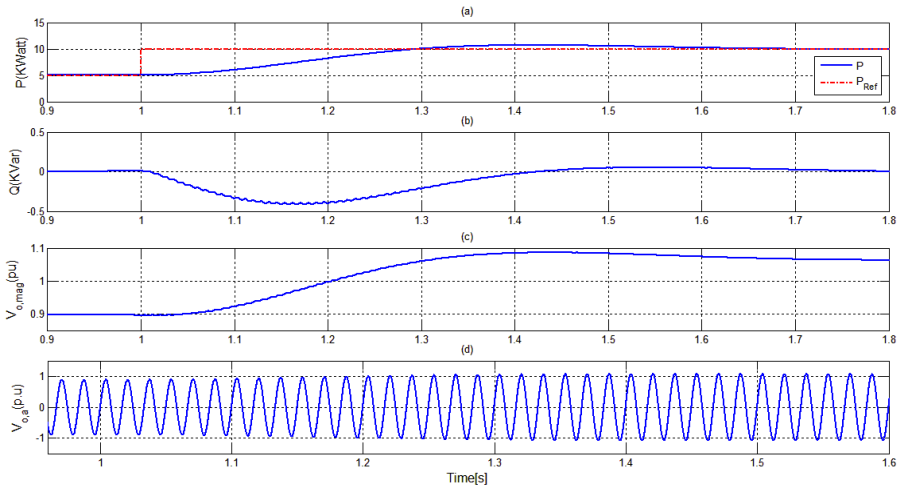

Figure 2-9: Dynamic response of the system to an active power command step change in grid connected mode and PQ-Bus operation. (a) Converter active power (b) Converter reactive power. (c) Output voltage magnitude. (d) Instantaneous phase-a output voltage.

Figure 2-9 (c) depicts how the output voltage amplitude changes to maintain the unity power factor condition while increasing the active power injection. Voltage fluctuation in this mode is that natural result of the absence of voltage control at the point of common coupling. The instantaneous phase-*a* output voltage is shown in Figure 2-9 (d).

In addition to active power regulation, the DG unit can contribute to the voltage reliability at the point of common coupling by allowing bus voltage control (i.e. PV-Bus mode). This mode can be activated once voltage sags (e.g. due to upstream faults) are detected. Under these conditions, the voltage control mode is activated to inject reactive power during the sag period to provide fault-ride-through performance. Accordingly, the economic operation of the DG unit will not be compromised. On the other hand, in long radial feeders and weak grids, existing DG units can be used for continuous voltage support. Figure 2-10 shows the effectiveness of the proposed control strategy in terms of providing the DG unit with the fault ride through capability. The grid voltage encounters a 10% sag from t = 1s to t = 1.25s due to an up-stream fault in the main feeder. The *R-L-C* load is assumed to be the locally connected load. Figure 2-10 (a) shows the phase-*a* voltage during the voltage disturbance. Figure 2-10 (b) shows the magnitude of the output voltage of the DG unit and the main feeder. Figure 2-10 (c) shows the reactive power injected by the unit during the fault period. Provided that there is enough reactive power rating, larger voltage sags can be mitigated by the DG interface.

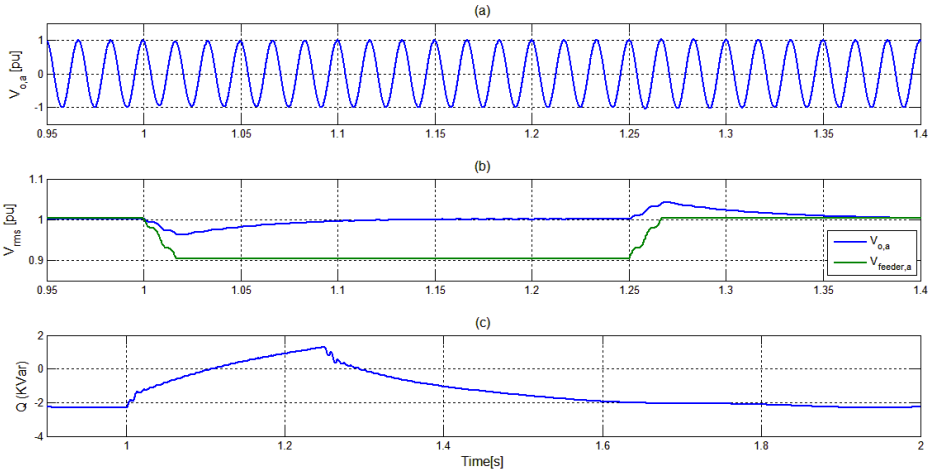

Figure 2-10: Dynamic response of the system under 10% grid voltage sag under PV-Bus operation. (a) Instantaneous phase-*a* output voltage. (b) DG output voltage (blue) and feeder voltage in p.u. (c) Converter reactive power.

To test the disturbance rejection against loading transients and harmonic loading, the nonlinear load is switched on at t = 0.5 s. The controller response to the addition of the nonlinear load is shown in Figure 2-11. Figure 2-11 (a) shows the output voltage waveform of phase-*a*, whereas Figure 2-11 (b) shows the load current. The proposed controller acts fast enough to reject the sudden loading disturbance yielding close voltage regulation at the local ac bus voltage. On the other hand, the harmonic disturbance rejection ability of the proposed controller is obvious. In spite of the heavily distorted load current, the total harmonic distortion (THD) of the phase-*a* voltage is 0.67% and 0.81% before and after adding the nonlinear load, respectively. The PLL output in presence of harmonics is also shown in Figure 2-11 (c). Note that the PLL output is robust even after adding the rectifier load to the system. This is because of the resonant filter which provides robust phase tracking in presence of harmonics. The results confirm the high disturbance rejection performance of the proposed controller.

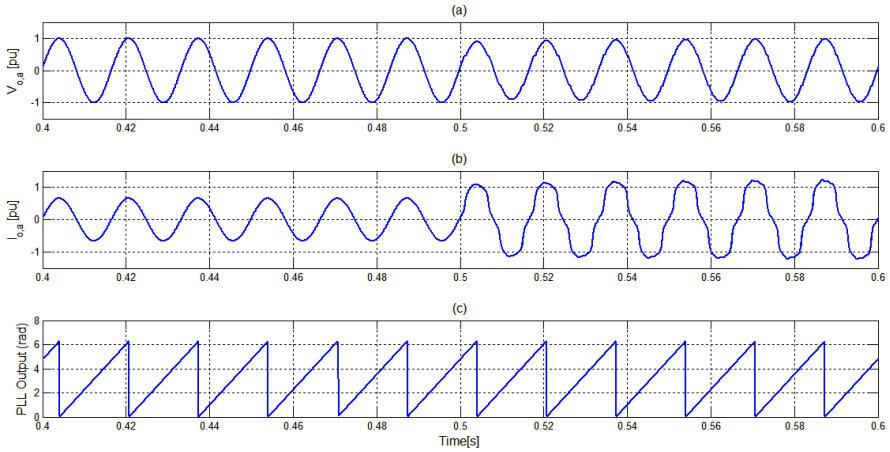

Figure 2-11: Dynamic response of the system when a nonlinear load is added in grid connected mode. (a) Phase-*a* output voltage. (b) Phase-*a* load current (c) PLL output

2.3.2 Isolated Mode

The transitional performance of the study system under the proposed control scheme from grid connected to islanded mode is evaluated by emulating an islanding event via opening the switch (SW) at the upstream feeder in Figure 2-1. Initially, the MG system is connected to the grid and both DG units are working in the PV-Bus mode. The study system is islanded at t=0.8 s by opening SW. In this chapter, the smart distribution study system is assumed to be equipped with power line communication-based islanding detection scheme [92, 93] where, the islanding event is detected with some communication delays after the upstream feeder breaker goes open and this event is signaled to the supervisory control unit shown in Figure 2-2. The detection delay is assumed to be 20ms; therefore the islanding event is detected at t = 0.82s. Figure 2-12 depicts the dynamic response of the system prior and after the islanding event. DG units utilize the same control structure, which is applied for both grid connected and islanded modes. Reactive power sharing is adopted in the isolated mode. The load voltage waveform and magnitude are shown in Figure 2-12 (a), (b), respectively. In Figure 2-12 (a) the voltage response associated with the conventional method (i.e. switching from current controlled to voltage controlled interface) is also shown. As it can be seen, without applying the proposed method, the system is experiencing much higher over voltages due to the internal disturbance generated by switching from current-controlled interface to a voltage-controlled one; and thus implying the effectiveness of the adopted control scheme. Figure 2-12 confirms that the proposed controller is well capable of maintaining the load voltage subsequent to an islanding event.

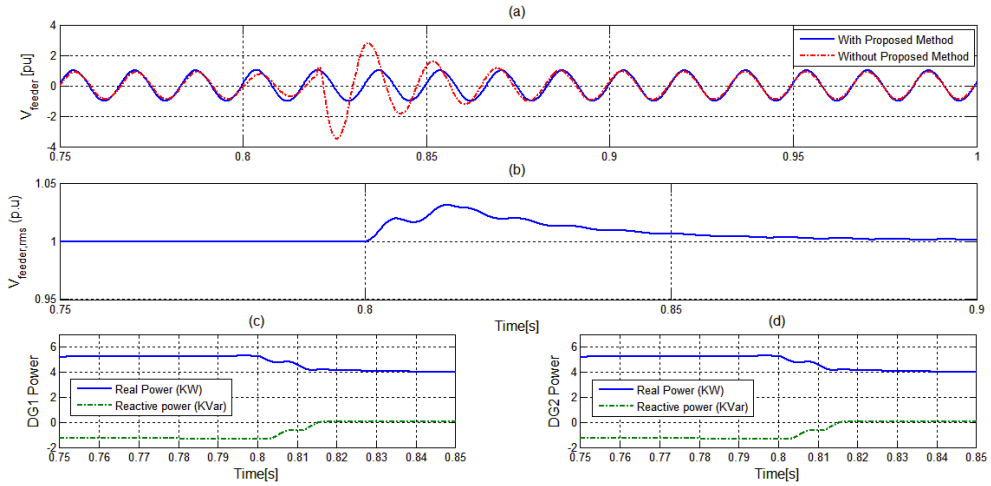

Figure 2-12: Dynamic response of the two-DG MG system due to an islanding event while units are acting as PV-Buses. (a) Instantaneous phase-*a* grid voltage with and without proposed controller. (b) RMS feeder voltage with proposed controller. (c),(d) Active and reactive converter powers for each DG unit.

The dynamics of the active and reactive power components for each DG unit is shown in Figure 2-12 (c), (d) where the initial active power generated by each DG is 5 kW, dictated by the power controller in grid connected mode. However, subsequent to the islanding event, the generated active power is decreased in order to meet the load consumption (i.e. 8.0 kW). The robustness of the proposed controller under MG operation is obvious.

For further performance evaluation, the MG system is connected to the grid and both DG units are working in the PQ-Bus mode (with unity power factor). The utility supply is lost at t = 0.8 s. The islanding is detected after 20ms by the supervisory control unit at t = 0.82s. Figure 2-13 depicts the dynamic response of the system prior and after the islanding event. The load voltage waveform and magnitude are shown in Figure 2-13 (a), (b), respectively. Close voltage control characteristics are yielded subsequent to the islanding event. Once again the system response in the absence of the proposed scheme is shown in Figure 2-13 (a) where the higher transient over-voltage is obvious. The active and reactive power responses for each DG unit are shown in Figure 2-13 (c), (d) where the initial active power generated by each DG is 6.0 kW at unity power factor. Subsequent to the islanding event, the generated active power decreases in order to meet the load consumption.

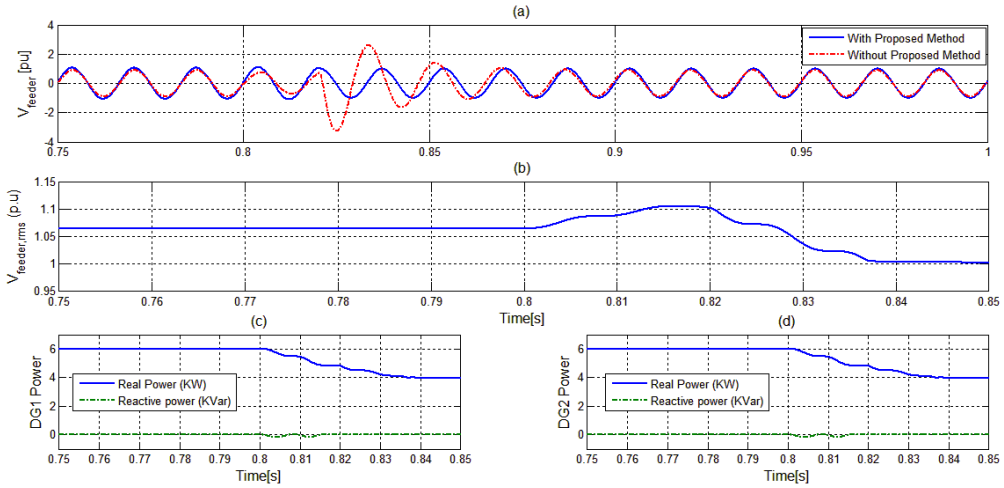

Figure 2-13: Dynamic response of the two-DG MG system due to an islanding event while units are acting as PQ-Bus buses. (a) Instantaneous phase-a grid voltage with and without proposed controller. (b) RMS feeder voltage with proposed controller. (c),(d) Active and reactive converter powers for each DG unit.

Figure 2-14 shows the load voltage and current responses of the islanded system when the nonlinear load is added at t = 0.5 s. Figure 2-14 (a) shows the load voltage, whereas Figure 2-14 (b) shows the load current. It can be seen that the controller is well capable of maintaining the output voltage quality despite of the highly distorted current going through the load. The THD of the load voltage is 2.7%. Figure 2-14 (c)-(f) show the active and reactive power profiles of both DG units. Accurate power sharing performance is yielded even in the presence of harmonic loading, which demands reactive power injection by both DG units.

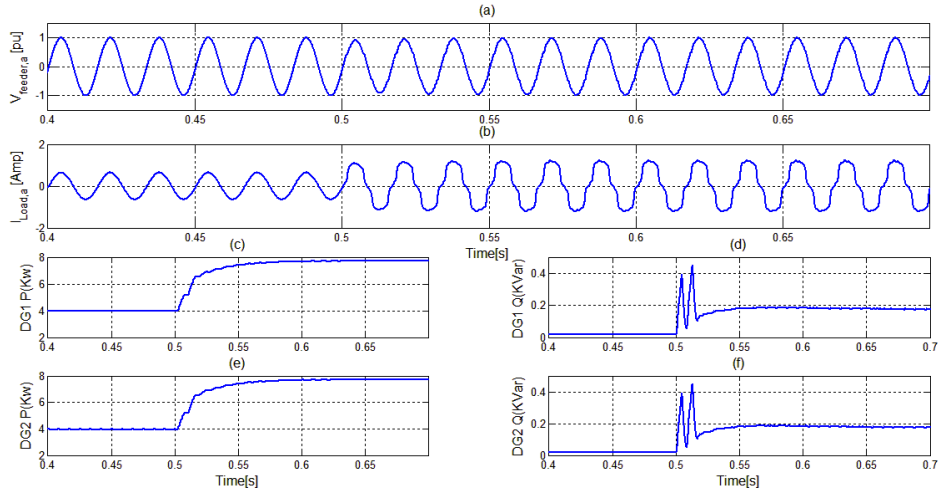

Figure 2-14: Dynamic response of the system when a nonlinear load is added in islanded mode. (a) Instantaneous phase-*a* output voltage (b) Phase-*a* load current. Instantaneous phase-*a* grid current (c), (d) Active and reactive converter powers for DG1. (e),(f) Active and reactive converter powers for DG2.

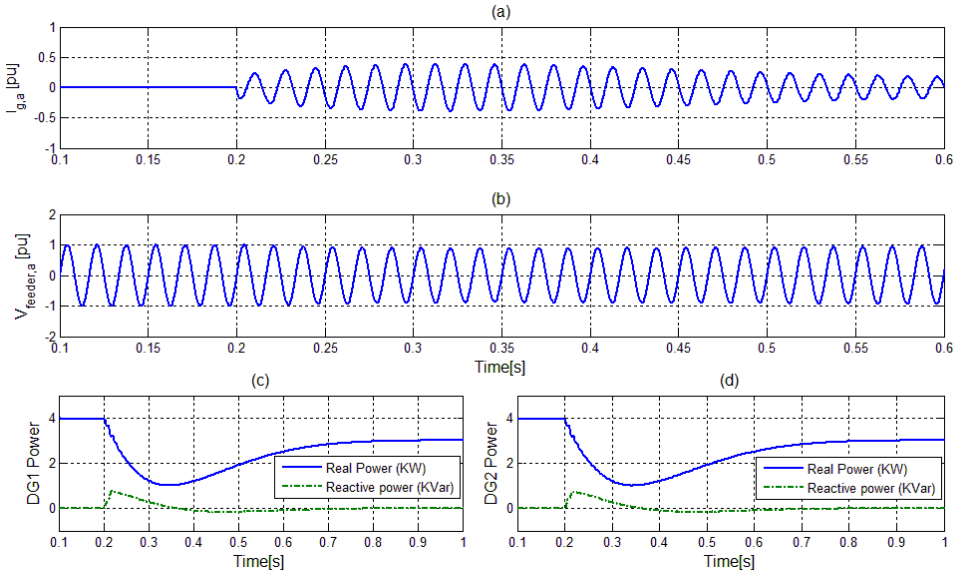

Figure 2-15: Dynamic response of the two-DG MG system when reconnecting to the utility as PQ-buses. (a) Instantaneous phase-*a* grid current. (b) Instantaneous phase-*a* output voltage. (c),(d) Active and reactive converter powers for each DG unit.

Figure 2-15 shows the grid current, the load voltage and power responses during a supply restoration scenario at $t = 0.2$ s. Once the utility supply is restored, both DG units operate as a PQ-Bus with unity power factor and with a power command of 3.0 kW for each unit. In spite of grid-current transients, the load voltage is closely controlled to facilitate seamless restoration. Similar to the MG formation event, the proposed control scheme yields seamless connection performance under the supply restoration event by rejection of the disturbances generated internally and externally to the control structure.

2.4 Summary and Conclusions

An interactive DG interface for flexible MG operation in the smart distribution system environment has been presented in this chapter. The proposed control scheme utilizes a fixed power-voltage-current cascaded control structure with a robust internal model voltage controller to maximize the disturbance rejection performance within the DG interface; and to minimize control function switching. The proposed control scheme has a simple and linear control structure that facilitates flexible DG operation in the grid-connected mode and autonomous MGs, yields robust transition between grid-connected and islanded modes either in PQ-Bus or PV-Bus operational modes; and provides robustness against islanding detection delays due to the fixed control structure.

Chapter 3

Suppression of Voltage and Power-Angle Interaction Dynamics in MGs [2]

The cascaded power-voltage-current control structure, presented in Chapter 2 provides means to achieve seamless operation in both grid-connected and islanded modes. However the proposed scheme is designed at the single converter level, where the voltage and power-angle interaction dynamics between the DG converters and the rest of a MG system are not accounted for in the design procedure. Note that as mentioned in section 1.1.2, suppression of angle and voltage interaction dynamics in a MG system is crucial to improve its stability and increase the safe penetration limit of DG MGs. Therefore unlike conventional converter control design techniques, where interaction dynamics are completely ignored or assumed as lump-sum external disturbance, a design approach that is more robust to MG interaction dynamics should be synthesized when interaction dynamics are qualitatively considered in the design process without strict use of overall MG dynamics (i.e. using a gray-box model of the MG system as reflected to each DG interface). Moreover, most of the voltage control schemes provided in the literature [26-31] including the one presented in Chapter 2, fail to provide a direct loop voltage control solution due to the active damping requirements yielding a higher number of required sensors as well as a limited bandwidth.

Motivated by the aforementioned difficulties, this chapter presents a comprehensive control system of DG converters featuring effective suppression of typical interaction dynamics in MGs. The conceptual design of the proposed control scheme is to provide control system robustness against system level interactions without a strict knowledge of the complete system dynamics. To increase the robustness against converter-MG interactions, the MG system is modeled by a dynamic equivalent circuit with uncertain parameters, which might include uncertainties induced due to the MG impedance variation and interactions with the equivalent MG bus-voltage. The equivalent MG model

[2] A version of this chapter has been published: A. Kahrobaeian, and Y. A.-R. I. Mohamed, "Suppression of Interaction Dynamics in Distributed Generation MGs Via Robust System-oriented Control Approach", *IEEE Trans. on Smart Grids*, vol. 3 no. 4, pp. 1800-1811, December 2012.

is augmented with the DG interface power circuit model to develop a robust H_∞ voltage controller [94]. Local load interactions and uncertainties in the ac-side filter parameters are also modeled in the augmented converter- network model. H_∞ optimization control approach is adopted to reject uncertainties and disturbances imposed on the augmented model. The proposed method offers a single-loop structure eliminating the need for extra current sensors, yielding a simpler implementation and more importantly a higher control bandwidth. Note that recent studies suggest that the advantages of direct-voltage control have made this approach an interesting option for MG applications [41].

To account for power angle interaction dynamics, an angle feed-forward control approach is adopted, where the angle of the equivalent MG bus, as seen by each DG unit, is estimated and used for feed-forward control in each DG unit. Using this approach, the sensitivity of the power injection with respect to the remote-bus angle of each DG unit is remarkably decreased; and accordingly, power sharing design of each DG unit can be synthesized in the sense of the infinite bus model. Further, the angle feed-forward controller transforms the conventional power sharing controller into a two-degree-of-freedom (2-DOF) controller. Therefore, the static droop gain can be changed over a wide range to meet the economic operational constraints without noticeable effect on the power sharing stability. Theoretical analysis and comparative simulation and experimental results are presented to demonstrate the effectiveness of the proposed control scheme [95].

3.1 Voltage and Power-Angle Dynamics Modeling

As discussed in section 2.2.3 when the MG is connected to the utility grid, the demanded power is supplied by both the utility and the DG units, however once disconnected from the utility, the DG units are supposed to supply the total connected load with high power quality and minimum interaction dynamics among power converters and MG entities. The same MG setup as in Figure 2-1 is studied in this chapter and without loss of generality, a MG building block is shown in Figure 3-1, where an equivalent MG dynamic model with unknown parameters is also included to account for possible interactions between a DG unit and the rest of MG.

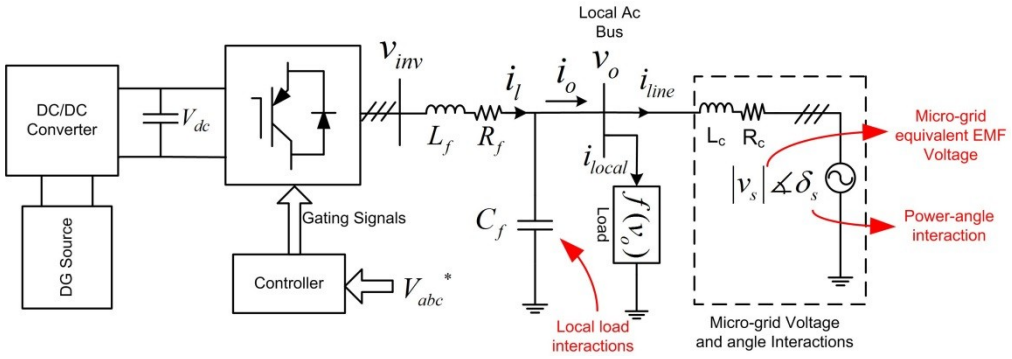

Figure 3-1: DG interface and interactions imposed on the output voltage.

Using Figure 3-1, the DG interface dynamics presented in (3-1) - (3-3) are obtained. Note that the parameters in (3-1) are already introduced in 2.1. However in (3-3) v_s and i_{line} are introduced to account for the voltage dynamics imposed by the rest of the MG.

$$v_{inv,\alpha\beta} = L_f . \frac{di_{l,\alpha\beta}}{dt} + R_f . i_{l,\alpha\beta} + v_{o,\alpha\beta} \tag{3-1}$$

$$i_{l,\alpha\beta} = i_{local,\alpha\beta} + i_{line,\alpha\beta} + C_f \frac{dv_{o,\alpha\beta}}{dt} \tag{3-2}$$

$$v_{o,\alpha\beta} = R_c . i_{line,\alpha\beta} + L_c . \frac{di_{line,\alpha\beta}}{dt} + v_{s,\alpha\beta} \tag{3-3}$$

As suggested earlier in 2.2.3, in the autonomous MG operation, the frequency and voltage droop characteristics can be written as (3-4) and (3-5) respectively to provide the frequency and the amplitude of the output voltage.

$$\omega_o = \omega_{nl} - mP \tag{3-4}$$

$$|V_o| = V_{od} = V_{nl} - nQ \tag{3-5}$$

where ω_{nl} and V_{nl} are the nominal frequency and voltage set-points, respectively, and m and n are the static droop gains, and they can be calculated for a given range of frequency and voltage magnitude as (3-6) and (3-7):

$$m = \frac{\omega_{\max} - \omega_{\min}}{P_{\max}} \tag{3-6}$$

$$n = \frac{V_{od\max} - V_{od\min}}{Q_{\max}}. \tag{3-7}$$

The set points in (3-4) and (3-5) act as a virtual communication agent for different inverters for autonomous operation. Also, the *d*-component of the output voltage is used in (3-5); as per the voltage-oriented control, the reference of the output voltage magnitude is aligned with the *d*-axis of the inverter reference frame. The static droop gains are selected to achieve correct power-sharing performance under different unit ratings according to (3-8) and (3-9) where *S* is the rated apparent power, and subscripts *i,j* denote two MG-connected units.

$$m_i S_i = m_j S_j \quad \forall \mathrm{i,j} \tag{3-8}$$

$$n_i S_i = n_j S_j \quad \forall \mathrm{i,j} \tag{3-9}$$

To allow sufficient time-scale separation between the power and current control loops and to achieve high power quality injection [19], the average active and reactive powers corresponding to the fundamental components are subjected to the control action, and they are obtained by means of a low pass filter (LPF) in (3-10) and (3-11) in which ω_c is the filter cut-off frequency.

$$P = \frac{\omega_c}{s + \omega_c} p \tag{3-10}$$

$$Q = \frac{\omega_c}{s + \omega_c} q \tag{3-11}$$

The steady-state active and reactive powers injected by a DG unit to the MG system can be expressed as

$$p = \frac{X_s V_o V_s \sin(\delta_o - \delta_s) - R_s V_o V_s \cos(\delta_o - \delta_s)}{R_s^2 + X_s^2} \tag{3-12}$$

$$q = \frac{X_s \left(V_s^2 - V_o V_s \cos(\delta_o - \delta_s)\right) - R_s V_o V_s \sin(\delta_o - \delta_s)}{R_s^2 + X_s^2}. \tag{3-13}$$

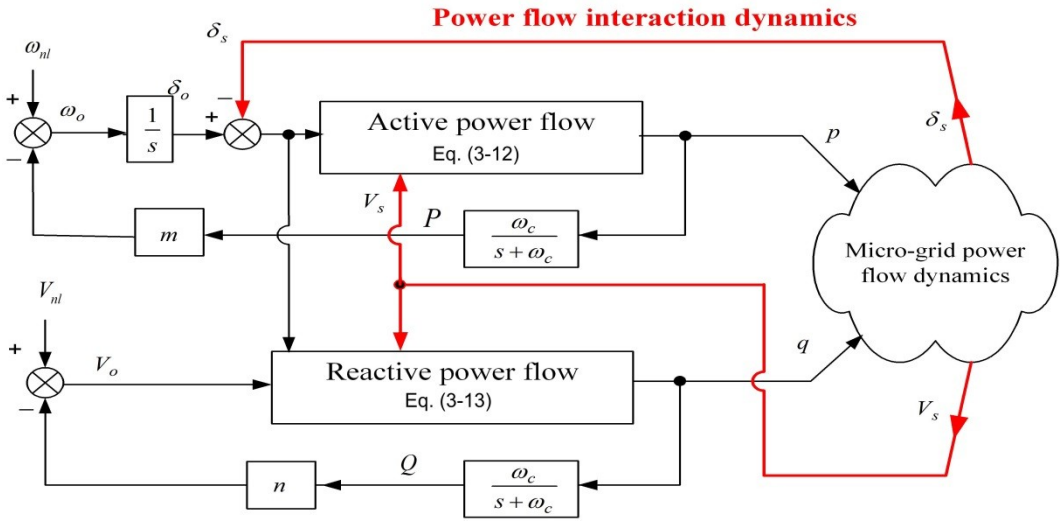

Figure 3-2: Power angle interactions imposed on a DG interface in a MG system.

In (3-12) and (3-13), δ_o-δ_s is the phase angle difference between the sending and receiving end voltages, V_o and V_s, respectively. The angle difference is changed dynamically according to the corresponding angular-frequency difference ω_o- ω_s by (3-14).

$$\delta_o - \delta_s = \int (\omega_o - \omega_s) dt \tag{3-14}$$

Note that equations (3-12)-(3-14) form the quasi-static power flow model between a DG unit and the rest of the MG system. Figure 3-2 illustrates the mechanism of power flow interaction dynamics between a DG unit and the rest of the MG system based on these equations.

3.1.1 Conceptual Design

The external disturbances, either locally generated within the DG interface or generated due to converter-MG interactions, will be imposed on the DG interface in both grid-connected and islanded modes of operation. The proposed controller should, therefore, maximize the disturbance rejection performance of the DG interface not only against local disturbances but also against disturbances associated with possible converter-MG interactions. As the control theory is mainly a model-based theory, better modeling approaches yield better control performance. However, using a complete MG model to design converter controllers is not a practical approach due to 1) the absence of

a priori knowledge of MG dynamics and connection topologies; and 2) the computational burden associated with complete MG modeling. To overcome these difficulties, the proposed control system adopts a robust system-oriented control approach, where system-level interactions, imposed on the output voltage magnitude and the power angle, are quantified and modeled in a computationally efficient way. First, an equivalent dynamic model of the MG system as seen by each DG unit is augmented in the voltage control structure to account for parametric uncertainties associated with topological changes in the network impedance and to suppress the interaction effects associated of the equivalent MG bus-voltage (e.g. harmonic voltage disturbances associated with remote loads, and transients associated with remote DG units). Using the augmented converter-network model, a robust multi-objective H_∞ voltage controller is designed to reject uncertainties and disturbances imposed on the augmented model; therefore, a wide band of interaction dynamics and disturbances can be effectively rejected by the proposed system-oriented modeling and control approach. The H_∞ optimization method has been adopted in order to design an optimal voltage controller, which guarantees system stability of the augmented converter-network model in the presence of parameter and modeling uncertainties with high disturbance rejection performance. The proposed H_∞ controller offers direct voltage control performance, which offers high bandwidth characteristics and wide-band disturbance rejection. Further, inherent LC filter active damping performance is yielded by the proposed augmented modeling and robust control design.

Second, the absence of the infinite-bus concept in MGs with comparable-size DG units, and the absence of physical inertia in converter-dominated networks induce power angle-interaction dynamics. Such interactions are associated with the power angle of the equivalent MG bus as seen by each DG unit. To reject these disturbances, the remote bus angle is estimated and used for angle feed-forward control. The output power of each DG unit depends on both the local and remote angles; therefore, the average power of each DG unit is processed by a linear compensator to provide a smooth estimate of the disturbing power angle. Using this approach, a 2-DOF power sharing controller is created, which remarkably reduces the impact of MG dynamics on the power sharing stability of the DG unit.

Figure 3-3 shows the block diagram of the proposed control scheme, which is designed to address the aforementioned voltage and power control problems.

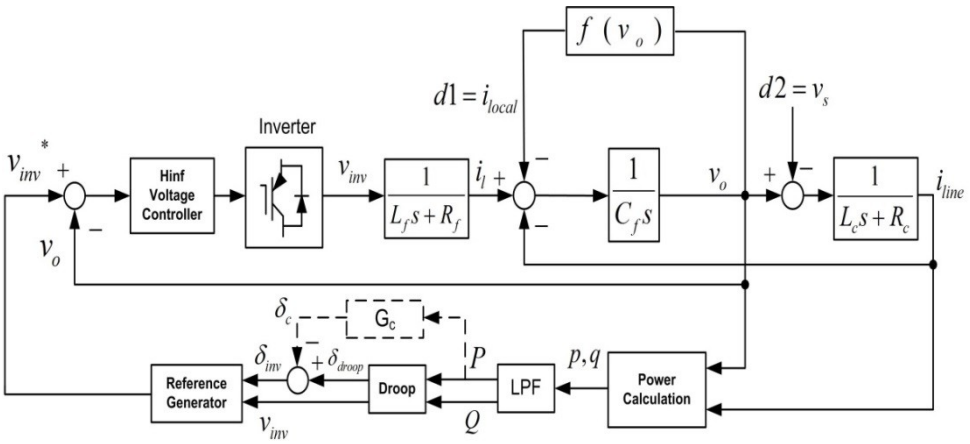

Figure 3-3: Proposed control scheme for rejecting voltage and power angle interactions.

3.2 Robust Voltage Control

To satisfy the aforementioned design requirement, a robust H_∞-based voltage controller is proposed for MG converters based on the augmented model of Figure 3-3. Therefore, a fixed-order controller $K(s)$ is required to reject dynamic perturbations and parameter uncertainties due to converter-MG interactions.

Figure 3-4 shows the block diagram of the closed-loop MG interface model based on the system dynamic equations presented in Figure 3-1. As shown in Figure 3-4, the effect of the local load and voltage disturbances generated due to the equivalent back EMF voltage, v_s, are taken into account as exogenous disturbances, whereas all possible parametric uncertainties have also been considered in the proposed model. In Figure 3-4, G_{LN} and G_{CN} are the nominal transfer functions associated with the DG interface filter components and the local load parameters as reflected to the DG interface, whereas G_{SN} represents the nominal transfer function for the equivalent MG model, and they are given by (3-15).

$$G_{LN} = \frac{1}{L_f s + R_f},\ G_{CN} = \frac{1}{C_f s}\ ,\ G_{SN} = \frac{1}{L_c s + R_c} \tag{3-15}$$

Note that the system parameters are the same as the ones listed earlier in section 2.1.

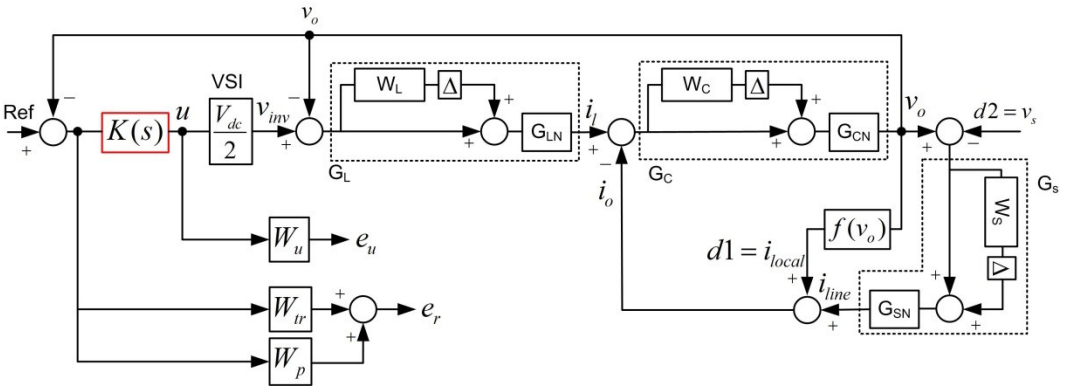

Figure 3-4: Closed-loop block diagram of the DG unit building block with uncertain parameters and exogenous disturbances.

It can be noted that that the selection of the nominal transfer functions is not restrictive. Usually, the nominal values of the filter parameters are known; whereas the nominal impedance of the interfacing transformer can be used as a nominal value of the equivalent MG impedance model. Deviations in model parameters are inherently considered in the robust control design process and can be rejected over a certain band of possible variation by appropriate design of the weighting functions of the H_∞ controller. The uncertainty weights W_L, W_C and W_S are chosen so that inequalities in (3-16) to (3-18)are satisfied:

$$|W_L(j\omega)| \geq \max \left| \frac{G_L(j\omega) - G_{LN}(j\omega)}{G_{LN}(j\omega)} \right| \quad \forall \omega \tag{3-16}$$

$$|W_C(j\omega)| \geq \max \left| \frac{G_C(j\omega) - G_{CN}(j\omega)}{G_{CN}(j\omega)} \right| \quad \forall \omega \tag{3-17}$$

$$|W_S(j\omega)| \geq \max \left| \frac{G_S(j\omega) - G_{SN}(j\omega)}{G_{SN}(j\omega)} \right| \quad \forall \omega \tag{3-18}$$

The parameter variation range for G_L, G_C and G_S are assumed to be 10%, 50% and 500% of their nominal values respectively.

In order to adopt a unified and systematic design procedure, the open-loop block diagram can be formulated into a standard configuration using the linear fractional transformation (LFT) technique [94] and by building a connection between known and uncertain matrices of the augmented system model. The closed-loop block diagram of the DG unit building block with uncertain parameters and exogenous disturbances is shown in Figure 3-4; where "*Ref*" is the reference signal; and $d1$ and $d2$ are the external disturbances and although they are not exactly known, their effect on performance

specification must be minimized (i.e. tracking): e_u is the weighted control effort and e_r is the weighted error signal. The design problem can be regarded as an optimization problem in which, over the set of all stabilizing controllers, the optimal controller that minimizes the infinity norm of the matrix transfer function from all external inputs (r, $d1$ and $d2$) to the outputs e_r and e_u should be found. The following weighting functions W_P, W_{tr} and W_u are proposed to satisfy the design specifications:

$$W_{tr}(s) = \frac{k_0 \omega_0^2}{s^2 + \zeta_0 \omega_0 s + \omega_0^2} \tag{3-19}$$

$$W_P(s) = \sum_{n=5,7,11} \frac{k_n (n\omega_0)^2}{s^2 + \zeta_n (n\omega_0) s + (n\omega_0)^2} \tag{3-20}$$

$$W_u(s) = \beta \tag{3-21}$$

where ω_0 is the fundamental angular frequency, k_0, k_n and β are constants, ζ_0 and ζ_n are damping coefficient, and n is the harmonic order.

The selection criterion of the weighting functions W_P, W_{tr} and W_u is as follows. W_{tr} is selected in the form of a resonant compensator to ensure both good tracking and disturbance attenuation at the fundamental frequency. The width of the resonant peak is shaped by the damping coefficient to ensure stability under mismatches in the angular frequency, which is the case in autonomous operation of MGs (due to the droop controller). W_P is added to generate internal models for further attenuation of the exogenous disturbances of $d1$ and $d2$ at selected harmonic frequencies (i.e. 5^{th}, 7^{th} and 11^{th}), which are commonly generated due to nonlinear loads. The control weighting function W_u is chosen simply as a scalar to penalize the control effort, which is essential to ensure a control effort within the capabilities of the pulse-width-modulated converter interface. Using this design criterion, the following parameters are used: k_0=k_n=2, ζ_0=ζ_n=0.1, and β=0.001. The weighted closed loop system has been recast in the standard M-Δ configuration form [94], as shown in Figure 3-5 where the optimal controller, K, is augmented in the interconnection matrix M. Note that M can be obtained using the lower Linear Fractional Transformation (LFT) of P(s) and K(s) [94].

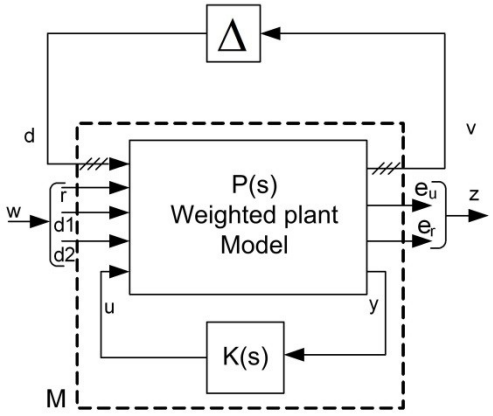

Figure 3-5: Standard closed loop M-Δ configuration for robust stability analysis.

The variables *w*, *z*, *v* and *d* are vector signals, where *w* denotes the exogenous input including reference command and disturbances; *z* denotes the error output; and *v* and *d* are the input and output signals of the dynamic uncertainties. The performance requirements are equivalent to the minimization of the H_∞ norm of the transfer function from *w* to *z*. Based on the 2-input, 2-output structure of Figure 3-5, *M* can be partitioned as in (3-22). It can be concluded that the stabilizing controller *K* should be designed in a way that not only the closed loop system is internally stable for all possible plant uncertainties of Δ, but also the optimized performance requirements with respect to tracking and disturbance rejection are met.

$$\begin{bmatrix} v \\ z \end{bmatrix} = \underbrace{\begin{bmatrix} M_{11}(s) & M_{12}(s) \\ \cdots & \cdots \end{bmatrix}}_{M(s)} \times \begin{bmatrix} d \\ \cdots \end{bmatrix} \tag{3-22}$$

According to the robust control theory [94], the standard configuration of Figure 3-5 is robustly stable if M_{11} is stable and $\|M_{11}\|_\infty$ is less than one. The performance criterion is met when the H_∞ norm of M_{22} is less than one. Considering system parameters provided in section 2.1, and by following the above-mentioned design procedure, the optimal robust H_∞ controller, *K*(s) is synthesized using the Matlab® Robust Control Toolbox [96]. Figure 3-6 shows the frequency response of the designed 11^{th} order controller. Due to the extended modeling approach and multi-objective control performance requirements, the order of the controller is relatively high. However, the computational burden is low for commercial grade digital signal processors.

Figure 3-7 shows that the robust stability criterion is satisfied by being maintained under unity. This implies that the proposed controller ensures system stability despite of parameter variation. It should be noted that this has been achieved via a single loop

control structure where no active/passive damping technique or inner current loop have been applied for stabilization purposes. This feature inherently mitigates network-converter resonance even under large variations in the network-side parameter and/or filter or power-factor correction capacitor parameters. Figure 3-8 shows the H_∞ norm of the closed loop system with the controller $K(s)$, and indicates that the nominal performance criterion is also satisfied over wide band of frequencies, which implies robust control performance under the occurrence of local and system-level disturbances and parameter variation.

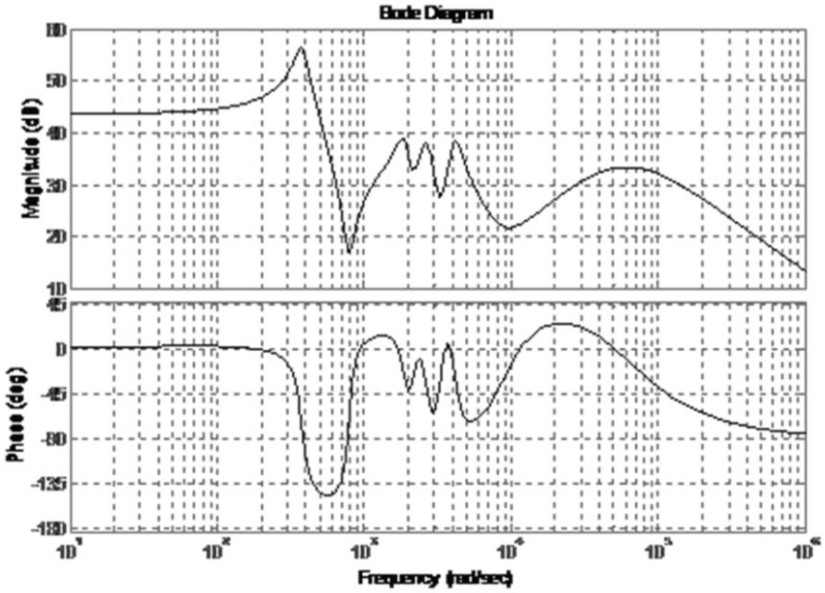

Figure 3-6: Bode diagram of the voltage controller.

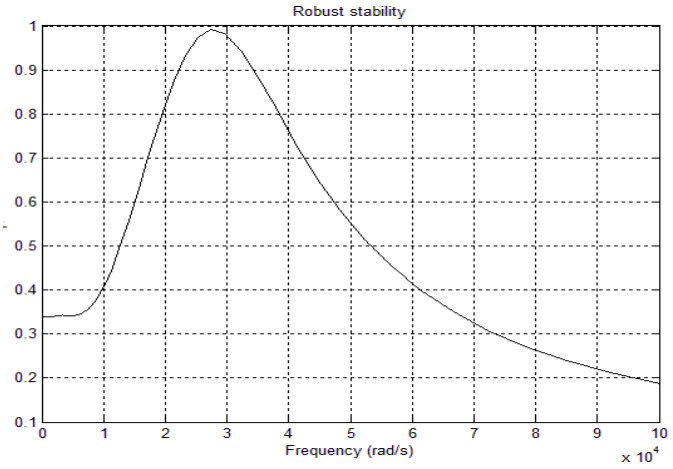

Figure 3-7: Robust stability analysis of the proposed controller.

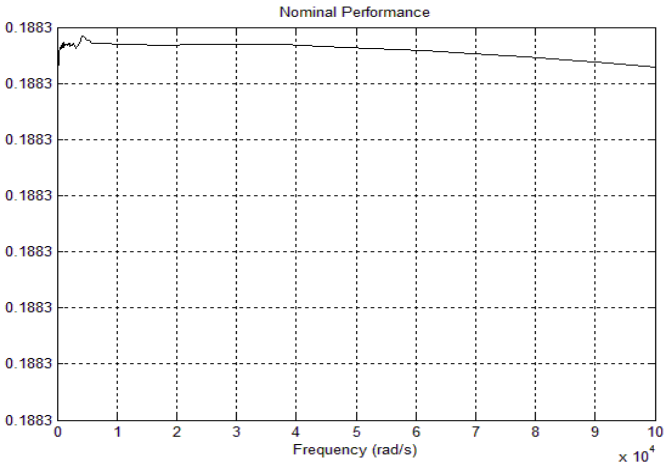

Figure 3-8: Nominal performance analysis of the proposed controler.

3.2.1 Robust Power Sharing Control

The dominant dynamics of a droop-controlled MG system are mainly dictated by the power sharing states. Figure 3-9 shows the linearized power transfer dynamics between a DG unit and the rest of the MG in small-signal sense. Depending on the power flow dynamics within the MG, the remote bus voltage magnitude V_s and its angle δ_s are dictated. These variables cannot be controlled by the DG unit. Voltage disturbances associated with V_s can be rejected via the robustly-designed voltage control loop. However, power angle interaction dynamics are yielded as input disturbances to the voltage controller via the angle δ_s. With high bandwidth direct voltage control, the converter can be regarded as a low-pass filter, where it behaves as a unity transfer function for the slow power sharing and power angle interaction dynamics. To suppress the effect of power angle interaction dynamics, a feed-forward compensating angle δ_c is estimated and injected at the reference angle generation stage as shown in Figure 3-9. As the power injection depends on the angle differences between the sending and receiving bus voltages (i.e. DG bus and equivalent MG voltage bus), the average power of each DG unit inherently contains the disturbance angle information via direct proportionality. Therefore, δ_c is estimated by processing the average power by a compensator with a transfer function $G_c(s)$. Due to direct angle feed-forward control, the compensator $G_c(s)$ can take the form of a low-pass filter. Therefore, the proposed technique offers simple implementation, and a smooth compensation signal even in the presence of harmonic power injection due to nonlinear loads.

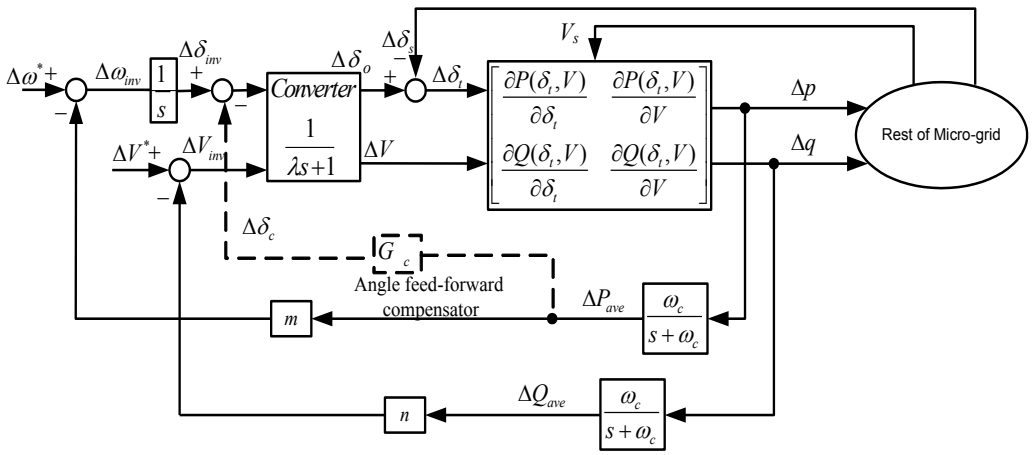

Figure 3-9:. Linearized power transfer dynamics between the DG unit and the rest of MG and proposed angle feed-forward comepnsator.

Accordingly, the compensator dynamics can be given in the form of (3-23) where k and a are positive constants.

$$G_c(s) = \frac{k}{s+a} \tag{3-23}$$

To show the effect of the proposed angle compensator on the closed loop power sharing dynamics, the small-signal dynamics of the power sharing characteristics with angle feed-forward control can be given around an operating point "$_o$" in (3-24)-(3-25).

$$\Delta\omega_o(s) = -\left(m + \frac{sk}{s+a}\right)\left(\frac{\omega_c}{s+\omega_c}\right)\times\left[\left(\frac{\partial p}{\partial(\delta_o-\delta_s)}\right)_o \Delta(\delta_o-\delta_s)(s) + \left(\frac{\partial p}{\partial V_o}\right)_o \Delta V_o(s)\right] \tag{3-24}$$

$$\Delta V_o(s) = \frac{-n\omega_c}{s+\omega_c}\left\{\left(\frac{\partial q}{\partial(\delta_o-\delta_s)}\right)_o \Delta(\delta_o-\delta_s)(s) + \left(\frac{\partial q}{\partial V_o}\right)_o \Delta V_o(s)\right\} \tag{3-25}$$

where the Jacobian elements can be derived from the power flow equations in (3-12) and (3-13). By solving (3-24) and (3-25), the power sharing dynamics of a DG unit is seen to be dictated by the characteristic equation listed in (3-26).

$$s^4\Delta\omega_o(s)+\alpha s^3\Delta\omega_o(s)+\beta s^2\Delta\omega_o(s)+\gamma s\Delta\omega_o(s)+\lambda=0 \tag{3-26}$$

$$\alpha = a+2\omega_c+n\omega_c\left(\frac{\partial q}{\partial V_o}\right)_o$$

$$\beta = \omega_c\{2a+n(\omega_c+a)\left(\frac{\partial q}{\partial V_o}\right)_o+(m+k)\left(\frac{\partial p}{\partial(\delta_o-\delta_s)}\right)_o+\omega_c\}$$

$$\gamma = \omega_c\{a\omega_c+na\omega_c\left(\frac{\partial q}{\partial V_o}\right)_o+(ma+k\omega_c+m\omega_c)\left(\frac{\partial p}{\partial(\delta_o-\delta_s)}\right)_o$$
$$+(n\omega_c(m+k)\left(\frac{\partial p}{\partial(\delta_o-\delta_s)}\right)_o\left(\frac{\partial q}{\partial V_o}\right)_o)$$
$$+(n\omega_c(k-m)\left(\frac{\partial q}{\partial(\delta_o-\delta_s)}\right)_o\left(\frac{\partial p}{\partial V_o}\right)_o)\}$$

$$\lambda = a\omega_c^2 m\{\left(\frac{\partial p}{\partial(\delta_o-\delta_s)}\right)_o+n\left(\frac{\partial p}{\partial(\delta_o-\delta_s)}\right)_o\left(\frac{\partial q}{\partial V_o}\right)_o$$
$$-n\left(\frac{\partial q}{\partial(\delta_o-\delta_s)}\right)_o\left(\frac{\partial p}{\partial V_o}\right)_o$$

Using the system parameters presented in section 2.1 and assuming k=0.01, a=0.002, Figure 3-10 shows the dominant eigenvalues associated with the coupled power sharing dynamics in (3-26) for conventional (k=0) and compensated power sharing loops of DG1 as the droop gain m changes from $m = 6\text{x}10^{-4}$ rad/s/W to $100\text{x}10^{-4}$ rad/s/W. It can be seen that the proposed angle compensation technique shifts the dominant eigenvalues to the left side of the s-plane resulting in a more damped performance of the system under a wide range of static droop gains.

The effect of changing the operating point (output power) on the relative stability of the system is also investigated through eigenvalue analysis. Figure 3-11 shows that the system can be unstable by increasing the output power of the DG unit when the conventional droop strategy is applied. The relative stability is remarkably increased by adding the proposed angle compensation loop, which stabilizes the power sharing dynamics along the whole loading trajectory.

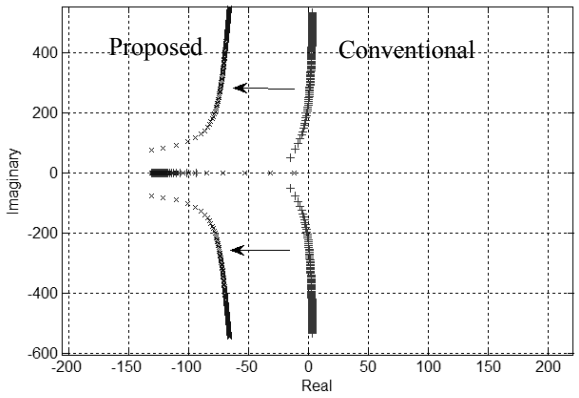

Figure 3-10. Dominant power sharing dynamic modes of DG1 with and without angle compensation loop when *m* is increased.

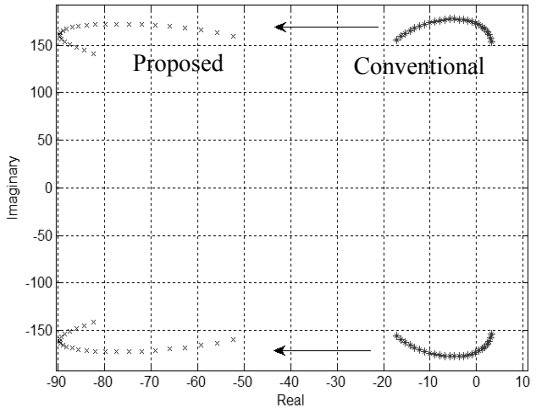

Figure 3-11: Dominant power sharing dynamic modes of the DG unit interface with and without angle compensation loop when output active power is increased.

Using the small-signal model of Figure 3-9, the sensitivity transfer functions from the external disturbance, δ_s, to the output power are obtained with and without the angle compensation loop and are presented in (3-27) and (3-28), respectively:

$$S_w(s) = \frac{\left(\frac{\partial p}{\partial(\delta_o - \delta_s)}\right)_o}{1 + \frac{m\omega_c}{s(s+\omega_c)}\left(\frac{\partial p}{\partial(\delta_o - \delta_s)}\right)_o} \tag{3-27}$$

$$S_c(s) = \frac{\left(\frac{\partial p}{\partial(\delta_o - \delta_s)}\right)_o}{1 + \frac{m\omega_c}{s(s+\omega_c)}\left(\frac{\partial p}{\partial(\delta_o - \delta_s)}\right)_o + \frac{\omega_c G_c(s)}{(s+\omega_c)}\left(\frac{\partial p}{\partial(\delta_o - \delta_s)}\right)_o}. \tag{3-28}$$

The sensitivity functions $S_w(s)$ and $S_c(s)$ can be used as an effective tool to investigate the effect of the proposed compensator on rejecting power-flow-induced disturbances. Figure 3-12 shows the magnitude responses of $S_w(s)$ and $S_c(s)$ at $V_o \sim V_s = 311\text{V}$, $\delta_o - \delta_s = \pi/3$.

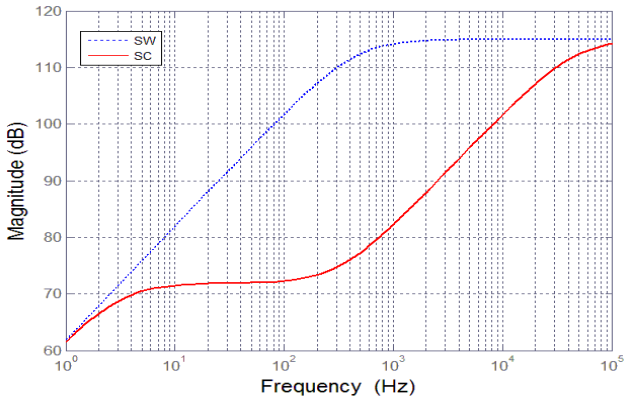

Figure 3-12: Frequency response for Sw (dashed) and Sc (solid).

The magnitude responses indicate the effectiveness of the proposed strategy in attenuating the amplitude of the sensitivity transfer function over the low- and high-frequency regions. The accumulative effect of the reduction in the sensitivity function at such frequencies implies that using the angle compensation strategy helps in suppressing power angle interaction dynamics in MGs.

3.3 Evaluation Results

The effectiveness of the designed control interface is verified via both simulation and experimental results. Time-domain simulation in the Matlab/Simulink environment is carried out for the test system of Figure 2-1 while a laboratory-scale MG system is used to evaluate system performance experimentally.

3.3.1 Sample Simulation Results

In order to have a better evaluation of the robustness of the designed H_∞ voltage controller in terms of rejecting disturbances caused by either parameter variation, loading transients, faults or harmonic loads, the performance of the understudy system has been investigated when the PFC capacitor bank and the nonlinear load (presented earlier in Figure 2-1) are added at t = 0.4 s and t = 0.45 s respectively. Figure 3-13 (a) shows the output voltage waveform of DG1 (phase-a), whereas Figure 3-13 (b) shows the load current. The proposed controller shows robust performance when the effective filter capacitor is experiencing a 50% increase due to the connection of a 500 Var PFC. It also acts fast enough to reject the sudden loading disturbance with minimal variation in the local ac-bus voltage when the nonlinear load is added.

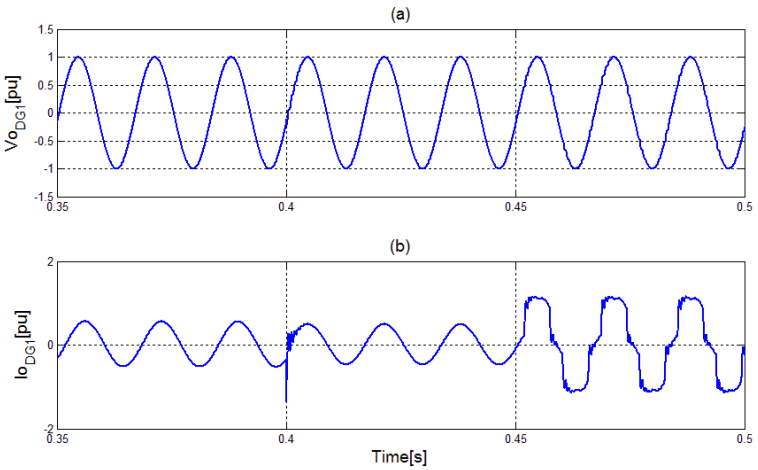

Figure 3-13: Instantaneous local phase-a voltage (a) and current (b) for DG1 when the PFC capacitor and the nonlinear load are added

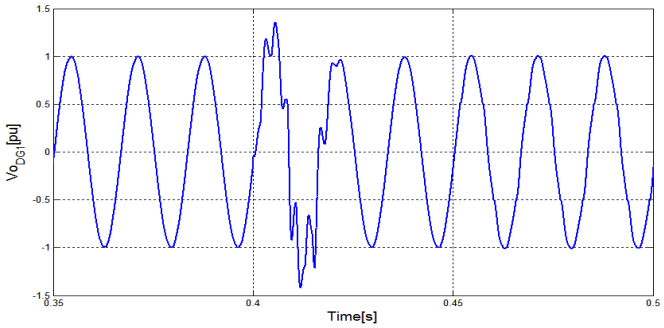

Figure 3-14: Instantaneous local phase-a voltage for DG1 when the PFC capacitor and the nonlinear load are added with a conventional PI controller.

This confirms the harmonic disturbance rejection ability of the proposed controller as well as its guaranteed stability for the limited capacitive filter variations. The THD of the phase-*a* voltage is 0.8% and 0.5% before and after adding the PFC capacitor, whereas the THD when the nonlinear load is added is 1.4%. The same scenario has been tested with the conventional PI voltage control scheme and the result is shown in Figure 3-14. The voltage quality is obviously degraded when the PFC capacitor is connected. As the nonlinear load is added at t = 0.45s, the THD is increased to 4.5% from the initial value of 0.8%. The excellent performance of the proposed control is due to considering the effect of all possible internal and external disturbances, imposed by parameter uncertainties or the local load, in the system model adopted for the H_∞ controller design.

3.3.2 Sample Experimental Results

Figure 3-15 shows the 1 kW, 208 V, 60 Hz laboratory-scale setup used to evaluate the proposed interface.

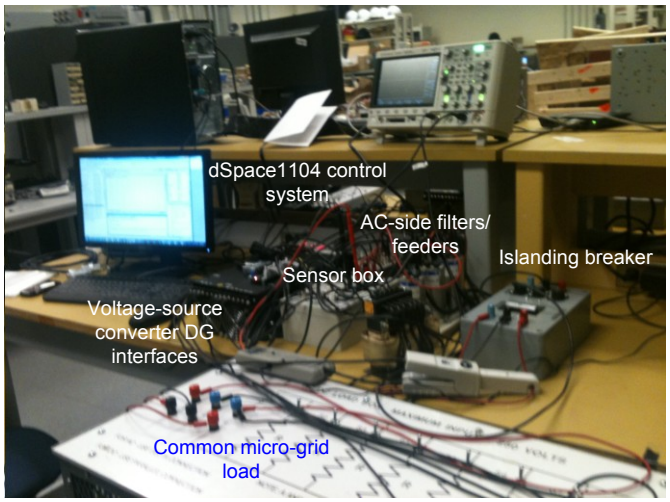

Figure 3-15: a view of the laboratory prototype

A Semistack IGBT voltage-source converter is used to interface a DG unit to the MG system. The dSpace1104 control system is used to implement the proposed control scheme in real-time. The pulse-width modulation algorithm is implemented on the slave-processor (TMS320F240-DSP) of the dSPACE controller. The sampling/switching frequency is 10 kHz, which indicates that the proposed control scheme (voltage and angle controllers) is computationally efficient and can be effectively implemented under high sampling frequency. Two phase currents as measured and used for feedback control as the neutral point is isolated. The voltage and current sensors used are LEM V 25-400 and HASS 50-S, respectively. The LC ac-side filter parameters are L_f= 1.2mH and C_f= 50μF S_{base}=1.0 kVA, $V(L\text{-}L)_{base}$ = 208 V, V_{DC} = 400V. Several experiments are conducted to evaluate the robustness of the proposed control scheme. Key results are presented in the following.

Figure 3-16 shows the output power of a single DG when the droop gain is subjected to a step change to increase the power injection to the MG. Figure 3-16 (a) shows the power response with the conventional droop controller. As shown by theoretical analysis in Figure 3-10, the power sharing loop generates lightly-damped mode under changes in the droop gain, which yields considerable power oscillations. Figure 3-16 (b) shows the power response with the proposed controller. The power response is perfectly damped due to the damping effect added by the proposed angle compensator. This feature enables effective mitigation of circulating currents among converters and converter overload during transients.

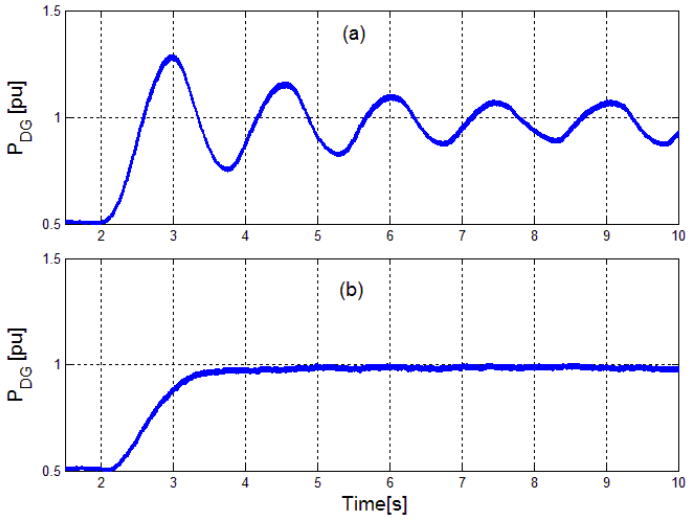

Figure 3-16: Power response during a step change in the droop gain. (a) With a conventional droop controller. (b) With proposed angle feed-forward control.

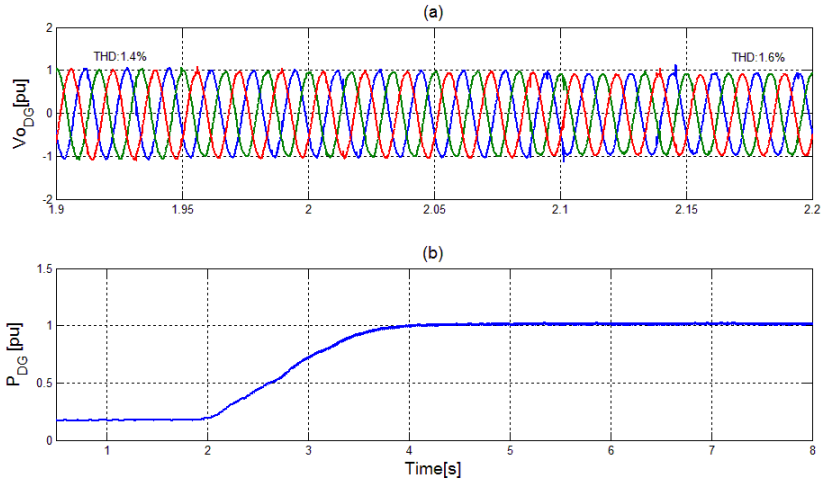

Figure 3-17: Voltage response with the proposed controller during an output power change. (a) Output voltage. (b) Output power.

Figure 3-17 shows the voltage dynamics when the output power changes from 0.2 to 1 p.u. The proposed voltage controller maintains robust voltage control performance during large changes in the output power.

Figure 3-18 shows the output voltage control performance under linear resistive load (Figure 3-18 (a)) and the nonlinear load (Figure 3-18 (b)). The voltage quality is slightly degraded under the nonlinear load conditions (3-phase full-wave bridge rectifier with inductive dc-side load). However, the THD in the output voltage is around 3%, which is below the standard limits [28].

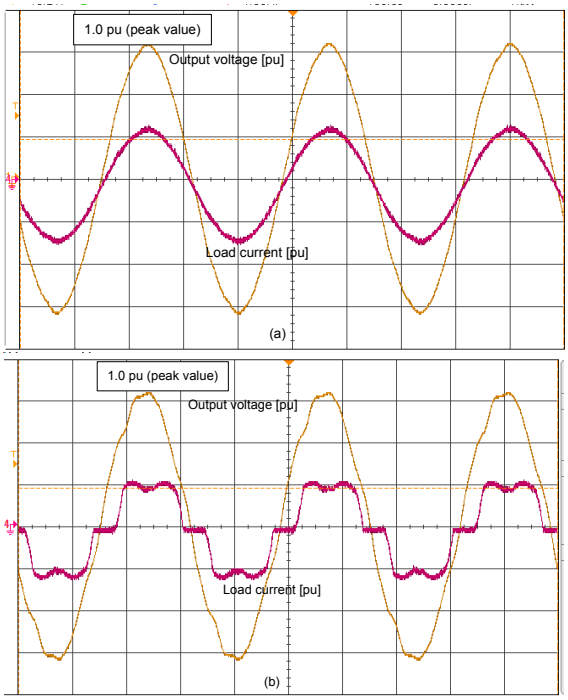

Figure 3-18: Voltage response with the proposed controller under (a) linear load (b) highly nonlinear load.

Figure 3-19 shows the output voltage performance under highly unbalanced load conditions (phase-a load resistance R_a=4.9Ω, phase-b load resistance R_b=41.6Ω, and phase-c load resistance R_c=∞ (open circuit)). The proposed voltage controller maintains high voltage quality under such highly unbalanced load conditions.

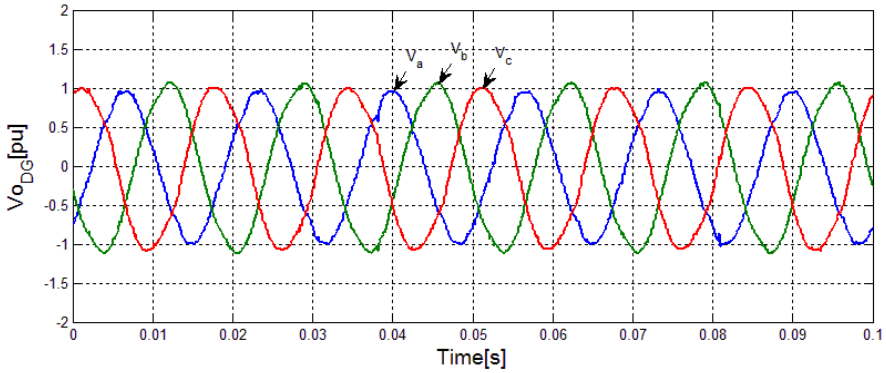

Figure 3-19: Voltage response with the proposed controller under highly unbalanced load conditions.

3.4 Summary and Conclusions

A robust system-oriented control approach has been presented in this chapter to improve the voltage and power dynamics in DG MGs. The proposed control scheme utilizes a robust H_∞ voltage controller, which is designed under an augmented model including different converter-network interactions imposed on the output voltage. Therefore, the controller provides effective mitigation of interaction dynamics either with the local load or with the rest of the MG system. In order to reject external disturbances caused by power angle-interaction dynamics, an angle feed-forward compensation method has been developed. The angle feed-forward controller provides a 2-DOF controller where the static droop gain can be changed over a wide range to meet the economic operation constraints without noticeable effect on the power sharing stability. The overall control scheme provides a comprehensive solution to enhance the dynamic performance of DG MGs under typical system level interaction and uncertainties. Simulation and experimental results have been presented to show the robustness and effectiveness of the proposed control scheme under a wideband of typical MG disturbances and interactions.

Chapter 4

Suppression of Uncertain Resonant Modes in Voltage-Controlled DG Units in MGs[3]

The H_∞-based control design introduced in Chapter 3 provided a useful framework to reject the undesirable voltage and angle interactions; However the conservative nature of H_∞ control synthesis, greatly compromises its performance in the presence of high capacitive uncertainties, yielding limited robust stability when high filter parameter variations are introduced. (Note only 50% capacitive uncertainty was tolerated in Chapter 3.) PFC capacitors and local capacitive loads are considered to cause high capacitive filter uncertainties as well as introducing new undamped resonance modes which would lead to instability. Therefore, motivated by the limitations of the conventional H_∞-based control algorithm in maintaining the system's voltage robust stability and robust performance in the presence of high capacitive uncertainties, this chapter presents a detailed modeling approach and a single-loop direct voltage control scheme based on the robust structured singular values (μ)-synthesis control approach. Unlike the augmented unstructured uncertainty modeling approach used with conventional H_∞ control, unstructured uncertainty modeling is adopted to enable the realization of a less conservative robust μ-synthesis [39, 40] controller. The resultant controller is used as a direct voltage controller where no additional damping technique, either passive or active, is required. Mathematical and comparative analysis are provided to show the advantages of proposed μ-synthesis approach over the conventional H_∞ controller in maintaining robust stability as well as robust performance of the MGs in presence of parameter uncertainties and uncertain resonant peaks caused by PFC capacitors connection. A systematic design approach for the proposed controller is presented. The performance of the proposed controller in mitigating uncertain resonant modes in DG MGs is investigated by simulation and experimental results [97].

[3] A version of this chapter has been published: A. Kahrobaeian, and Y. A.-R. I. Mohamed, , "Direct Single-Loop μ-Synthesis Voltage Control for Suppression of Multiple Resonances in MGs with PFC Capacitors", *IEEE Trans. on Smart Grids,* vol. 4 no. 2, pp. 1151-1161, June 2013.

4.1 Problem Statement

As stated in 3.1, the voltage reference provided by the droop controller dynamics in (3-4),(3-5) is applied to the voltage controller in order to regulate the inverter's output voltage. However, the relative stability of the medium-frequency modes, associated with the voltage control dynamics [37, 38], is mainly affected by the interaction dynamics between the filter parameters and other MG entities. Note that the interaction dynamics at these modes can be yielded due to possible mode excitation by MG low-order harmonics. PFC capacitor banks can affect those medium-frequency modes, yielding MG instability and performance degradation. The sample DG unit shown in Figure 4-1 (DG1) is connected to the main feeder through a LC filter and the line impedance (L1), supplying common loads connected to the feeder. Note that the same line and filter parameters used in Figure 2-1 are adopted for the understudy system. However a higher PFC capacitor unit and a highly capacitive local load are adopted in order to investigate their effect over the system's voltage stability. In order to comply with the new load rating, the DG1 and DG2 ratings are increased to 40 kVA and 20 kVA respectively; therefore higher output DG voltages are adopted while the dc link voltages are also increased to 800V. Note that the adoption of the PFC capacitor would increase the effective voltage-source inverter (VSI) filter capacitance, changing the LC filter cut-off frequency and subsequently affecting the stability of the VSI controller. Moreover, the additional capacitor located after the line impedance introduces new resonance frequencies which can cause resonant excitations if a disturbance near those resonances occur.

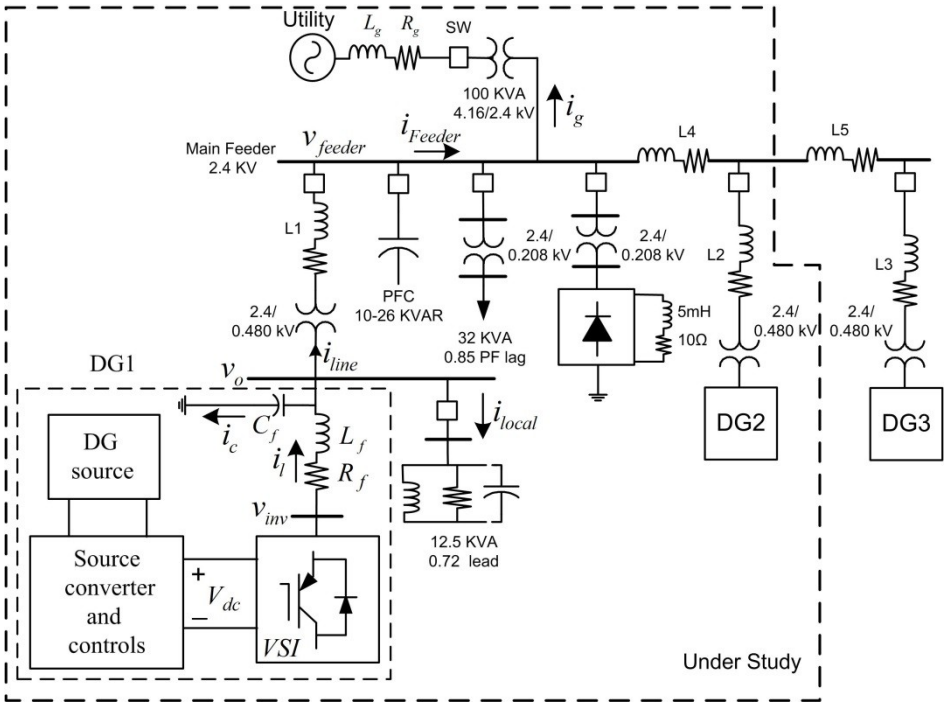

Figure 4-1: MG test system to investigate capacitive uncertainty.

Figure 4-2 demonstrates the effect of a PFC capacitor-connection on the open loop system as part of the interaction dynamics between the DG unit and the rest of the MG. Note that in the model on Figure 4-2, i_{local}, i_{line} and i_{Feeder} are all considered as external disturbances modeling the interactions between a DG unit and the network.

When the PFC capacitor is not connected, the open-loop transfer function can be obtained as in (4-1). When the PFC capacitor is connected, the new open-loop transfer function from the inverter voltage v_{inv} to the bus voltage v_{feeder} can be obtained by (4-2). Note that the inner capacitor current feedback loop, with gain K_d, is also considered in Figure 4-2 in order to account for the active damping feature.

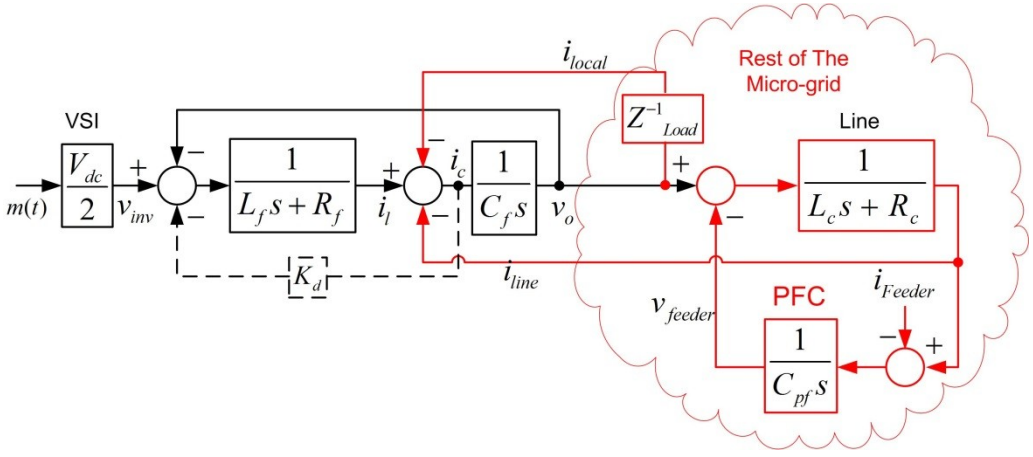

Figure 4-2: The effect of PFC capacitor on the open loop system dynamics.

$$G_{open,1}(s) = \frac{1}{C_f L_f s^2 + C_f (R_f + K_d) s + 1} \tag{4-1}$$

$$\begin{aligned} G_{open,2}(s) = 1 / \{ & C_f C_{pf} L_f L_c s^4 + C_f C_{pf} (R_c L_f + R_f L_c + K_d L_c) s^3 + \\ & (C_{pf} L_c + K_d C_f C_{pf} R_c + C_f L_f + C_{pf} L_f + C_{pf} C_f R_c R_f) s^2 + \\ & (C_{pf} R_f + C_{pf} R_c + K_d C_f + C_f R_f) s + 1 \} \end{aligned} \tag{4-2}$$

Considering the same filter parameters presented in 2.1, Figure 4-3(a) compares the frequency response of the open loop resonance transfer functions with and without the PFC capacitor. As shown in Figure 4-3 (a), connecting the PFC capacitor, not only causes the original resonance peak associated with the LC filter to drift, but also forms a new resonant frequency which can affect system stability and performance in the case of harmonic excitations. Multiple uncertain resonances can be easily created under different values of the PFC capacitor (e.g. switched capacitors).

As shown by the solid-curve in Figure 4-3 (b), when the PFC capacitor is not connected, applying current feedback from the filter capacitor current effectively damps the resonance peak of the LC filter. However, since there is no access to the current going through the PFC capacitor, C_{pf}, the resonance peaks caused by its connection cannot be fully mitigated; and therefore, affecting system stability and performance. As shown in , Figure 4-3 (b), this effect gets even more obvious as the capacitor value increases, which increases the low-frequency resonance peak. The uncertain low-frequency resonant mode matches the bandwidth of low-order harmonics; therefore harmonic excitation and harmonic instabilities can easily occur even if the converter-side LC filter resonance is damped. Figure 4-3 implies that the system stability and performance can be affected by the uncertainties imposed on the open loop by connecting the PFC capacitor even when active damping methods are used. This motivates the necessity of designing a robust voltage control strategy that maintains system stability and provides acceptable performance in a reasonably wide range of parameter variations that might be imposed by the un-modeled dynamics of the rest of the MG.

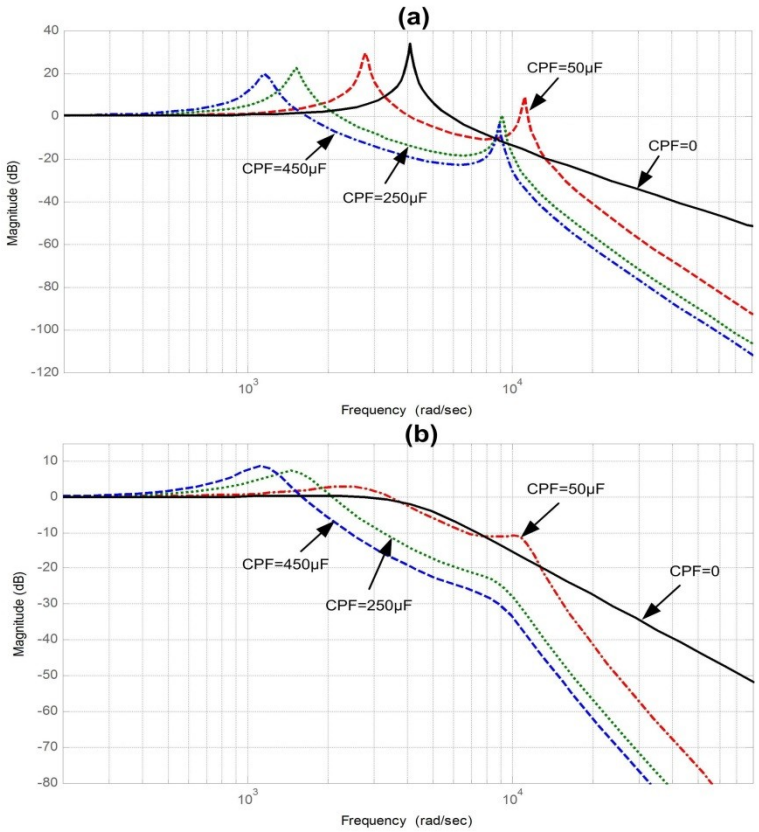

Figure 4-3: The effect of adding a PFC capacitor to the system open-loop frequency response (a) without active damping ($K_d = 0$) (b) with active damping $K_d = 6$

4.2 Robust Control of Systems with Unstructured Uncertainty

As stated in 3.2 any linear interconnection of inputs, outputs, system perturbations and the controller can be rearranged to match the standard closed loop M-Δ configuration represented in Figure 4-4 using a linear fractional transformation [94]. Where P(s) represents the open loop plant, Δ(s) models the perturbation and K(s) is the controller.

Ignoring the effect of the perturbation block, [39] suggests that the nominal performance is achieved when $||M_{22}||_\infty<1$. Note that $\|G\|_\infty = \sup_\omega \sigma[G(j\omega)]$ and $\sigma[.]$ stands for the singular value. The robust stability of the closed loop system can be studied based on Theorem 1.

***Theorem 1*:** Let $M_{11}(s)$ be stable, for all Δ , $||\Delta||_\infty<1$, the perturbed system of Figure 4-5 is robustly stable if $||M_{11}||_\infty<1$.

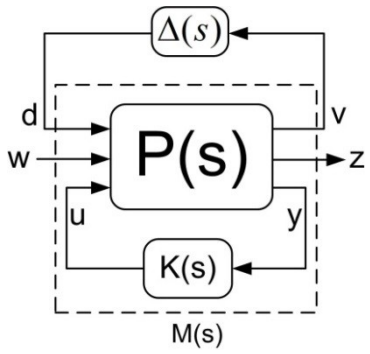

Figure 4-4: Standard closed loop M-Δ configuration for robust stability analysis.

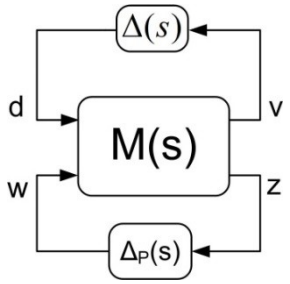

Figure 4-5: Standard M-Δ configuration for robust performance analysis.

Although adopting the H_∞ optimization approach, based on singular values minimization, provides stable operation of the perturbed system based on Theorem 1, the lack of information on the structure of Δ leads to conservative solutions in many practical problems where the uncertainty consist of multiple norm-bounded perturbations. In this case, the performance of the closed-loop perturbed system maybe degraded [39].

4.3 Robust Control of Systems with Structured Uncertainty

According to [39], having more knowledge on the uncertainty structure provides less conservative solutions on "structured singular values (μ) analysis. Using μ-analysis, not only can it provide robust stability, but the system performance under uncertainties would also improve. Once again consider the M-Δ configuration shown in Figure 4-4, the structure of the uncertainty block, Δ(s), is assumed to be known as in (4-3) this time.

$$\Delta = \{diag[\Delta_1,...,\Delta_f]\ ,\ \Delta_j \in C^{mj\times mj}\} \tag{4-3}$$

Where $\sum_{j=1}^{f} m_j = n$ with n is the dimension of the block Δ.

Definition 1: When M(s) is an interconnected transfer matrix as in Figure 4-4, the structured singular value with respect to Δ is defined by (4-4) where $\mu_\Delta^{-1}(M)$ is the smallest singular value of Δ (i.e. σ(Δ)) that makes $\det(I - M\Delta) = 0$.

$$\mu_\Delta(M(s)) = \sup_{\omega\in R} \mu_\Delta(M(j\omega)) \tag{4-4}$$

The above definition indicates a frequency dependent stability margin [39, 40]. The robust stability result with regards to structured uncertainties is given in Theorem 2.

Theorem 2: Let $M_{11}(s)$ be stable, and $\|\Delta\|_\infty<1$, the perturbed system of Figure 4-4 is robustly stable with respect to Δ, if and only if $\mu_\Delta(M_{11}(s))<1$.

Theorem 2 gives a sufficient and necessary condition for robust stabilization. It can be shown that it gives a less conservative stabilization measure as compared to H_∞ norm minimization. This can be shown in (4-5) where the equality only holds when Δ is unstructured.

$$\mu_\Delta(M_{11}) \le \sigma_{11}(M) \tag{4-5}$$

Therefore, in case of structured uncertainties, (4-5) clearly shows that the H_∞ norm optimization approach leads to more conservative controllers as compared to the controller designed based on minimizing structured singular values (i.e. $\mu_\Delta(M)$).

In addition to robust stability, it is desired that the designed control system can maintain a satisfactory performance level even in presence of plant dynamic uncertainties and disturbances. Using μ-analysis provides a measure to analyze the performance of the closed loop system with perturbations. The robust performance requirement can be set as (4-6) for all Δ [39, 40].

$$\left\| LFT_u(M,\Delta) = M_{22} + M_{21}\Delta(I - M_{11}\Delta)^{-1}M_{12} \right\|_\infty < 1 \tag{4-6}$$

However, note that as suggested in [39] a fictitious performance block of Δ_P can be assumed as shown in Figure 4-5, with appropriate dimensions and $\|\Delta_P\| \le 1$. Therefore, considering Figure 4-5, the robust performance condition, (4-6), can be equivalently considered as a robust stabilization problem with the uncertainty block of $\tilde{\Delta}$ represented in (4-7).

$$\tilde{\Delta} = \{diag[\Delta, \Delta_P]\} \tag{4-7}$$

Note that this happens to be a stabilization problem with respect to the structured uncertainty of $\tilde{\Delta}$, thus yielding (4-8).

$$\mu_\Delta(M) < 1 \tag{4-8}$$

4.4 H_∞ Vs. μ-Synthesis Voltage Controller Design

Mixed sensitivity robust H_∞ design approach along with the inner current feedback loop is used in [35] in order to maintain the stability of the MG when the PFC capacitor bank is added. Following the conventional approach, uncertainty in the effective filter capacitance is assumed to be unstructured and therefore it is modeled as a single lumped 1×1 full block matrix of Δ defined by (4-9) where G_N and G_P are the nominal and perturbed transfer functions, respectively.

$$\Delta(s) = \sigma\left(\frac{G_P - G_N}{G_N}\right) \tag{4-9}$$

$$G_N = \frac{1}{C_f L_f s^2 + C_f (R_f + K_d)s + 1} \tag{4-10}$$

Figure 4-6 shows the standard configuration adopted for H_∞ controller design. $\Delta(s)$ is the plant unstructured uncertainty and the weighting function W_Δ is determined from the worst case $\Delta(s)$ and is selected to lie above σ(Δ) to normalize the uncertainty block (i.e. $\|\Delta\|_\infty<1$).

In Figure 4-6 W_{tr} and W_u are the weighting functions, penalizing the tracking error and controller effort respectively and similar to section 3.2 are suggested to be in the form of (4-11) and (4-12) where k_0=1,ω_0=377rad/s, ζ_0= 0.01, and β=0.001.

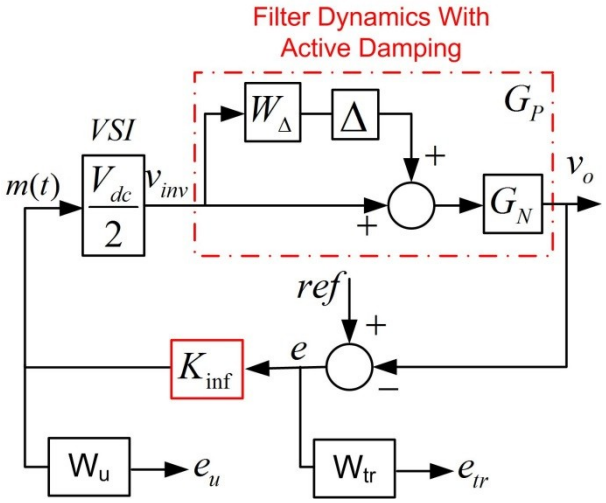

Figure 4-6: Schematic of the closed-loop system with a conventional H_∞ Controller.

$$W_{tr}(s) = \frac{k_0 \omega_0^2}{s^2 + \zeta_0 \omega_0 s + \omega_0^2} \tag{4-11}$$

$$W_u(s) = \beta \tag{4-12}$$

Following the provided design approach, $K_{\inf}(s)$ can be derived as in (4-13). Note that the current feedback from the filter capacitor is adopted with the active damping gain K_d=6 in order to dampen the LC resonant peak.

$$K_{\inf} = \frac{\begin{pmatrix} 8.437*10^4 s^4 + 8.219*10^8 s^3 + \\ 3.347*10^{12} s^2 + 9.293*10^{15} s + 1.956*10^{18} \end{pmatrix}}{\begin{pmatrix} s^5 + 4.254*10^5 s^4 + 2.51*10^9 s^3 + \\ 1.049*10^{13} s^2 + 4.347*10^{14} s + 1.47*10^{18} \end{pmatrix}} \tag{4-13}$$

Although adopting the H_∞ optimization approach, based on singular values minimization, provides stable operation of the system in the presence of the unstructured uncertainties, it leads to conservative solutions where the performance of the perturbed system is degraded and therefore it fails to meet the robust performance criteria. Therefore, in this chapter a more detailed model of the system uncertainties is adopted which provides further knowledge of their structure; thus, making it possible to use the μ-synthesis approach in order to achieve a less conservative robust voltage controller for MG applications.

Figure 4-7 shows the schematic of the closed-loop system with the μ-synthesis controller, where instead of using a lumped unstructured uncertainty block, the uncertainties over the effective filter capacitor (C_f) caused by the addition of C_{pf} as well as the possible filter inductance variations are modeled individually using the multiplicative perturbation method. $W_{\Delta C}$, $W_{\Delta L}$ are the weightings used to normalize the uncertainty blocks assuming C_f varies up to 5 times its nominal value and a 10% deviation on L_f. W_{tr} and W_u are assumed to have the same form as (21) and (22), respectively.

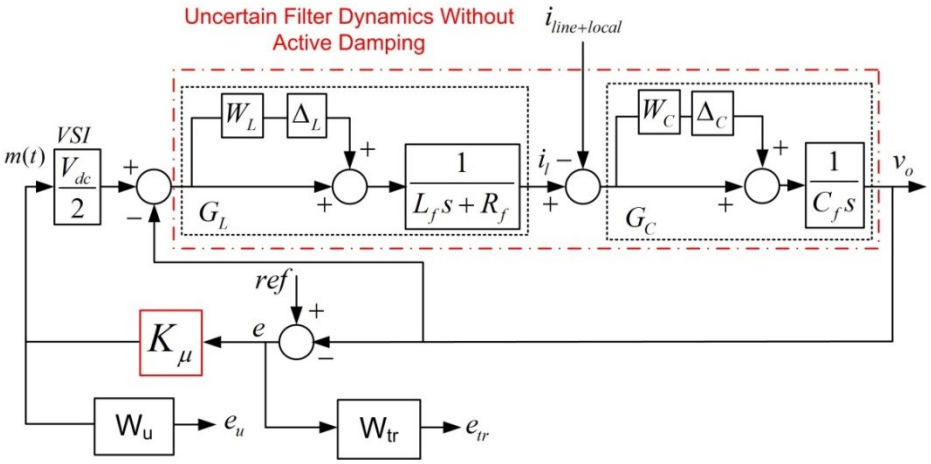

Figure 4-7: Schematic of the closed-loop system with a μ-synthesis controller

Note that the modeling approach in Figure 4-7 provides more information on the structure of the uncertainty block as suggested in (4-14).

$$\Delta = \{diag[\Delta_C, \Delta_L] \,,\ \Delta \in C^{1\times 1}\} \tag{4-14}$$

Considering the same weighting functions as in (4-11) and (4-12), the D-K iteration method is then adopted in order to compute the μ controller. Note that the proposed controller, which is based on structured singular analysis provides a direct voltage control solution where no inner current control is needed for plant stabilization purposes. The controller obtained with this method has a high order; therefore the Hankel-norm model reduction method is applied to reduce its order to 6 as shown in (4-15). In spite of the higher controller order, the proposed controller doesn't adopt an inductor-current feedback controller and doesn't need a capacitor current feedback controller for active damping; therefore, it leads to easier design and implementation as compared to the conventional multi-loop H_∞ controller. Further, the sensor requirements are less, as only the output voltage is used for feedback. To limit the converter current during abnormal conditions, the inductor current is monitored and used to generate a proportional signal to block the pulse-width modulator, which in turns limits the fault current of the converter. This protection feature however does not compromise the advantages of direct voltage control.

$$K_\mu = \frac{\begin{pmatrix} 8.29*10^6 s^5 + 5.79*10^{10} s^4 + 6.06*10^{13} s^3 \\ -4.23*10^{15} s^2 + 7.01*10^{19} s + 1.45*10^{21} \end{pmatrix}}{\begin{pmatrix} s^6 + 3.61*10^5 s^5 + 1.81*10^{10} s^4 + 1.08*10^{14} s^3 \\ +1.55*10^{17} s^2 + 1.65*10^{19} s + 2.16*10^{22} \end{pmatrix}} \tag{4-15}$$

4.4.1 Comparative Analysis

Figure 4-8 shows the robust stability measure when the K_{inf} controller is adopted with an active damping loop. Having enough damping of the LC filter resonance mode is crucial in this case. Figure 4-8 implies that without the inner capacitor-current control loop the system stability is not guaranteed in presence of high capacitive uncertainties and therefore, direct voltage control using H_∞ robust design fails.

Assuming active damping, the nominal and robust performance of the closed-loop system with K_{inf} are shown in Figure 4-9. It can be seen that when there are no perturbations, the closed-loop system achieves nominal performance (μ<1); however it fails to satisfy the robust performance criterion which is required to yield a satisfactory performance level even in presence of plant dynamic uncertainties.

The robust stability and performance measures for the closed loop system with K_μ are shown in Figure 4-10 and Figure 4-11, respectively. The robust stability of the system is inferred from Figure 4-10 where the frequency response of $\mu_\Delta(M_{11})$ is less than 1 over the entire frequency range. Note that this is achieved without adopting any inner inductor or capacitor current loop, which indicates the robust and inherent damping characteristics of the proposed μ-synthesis direct voltage controller. In order to show the difference between the structured and unstructured modeling of the uncertainties, in the same plot, the maximum singular value of the leading 2×2 transfer matrix , $\|M_{11}\|_\infty$,is shown, which characterizes the robust stability with respect to unstructured perturbations. It is seen that the latter is greater than 1 over some frequencies. This means that the robust stability is not preserved if the uncertainty is unstructured. This confirms that if further information is known about the uncertainty structure, structured singular values gives less conservative results as compared to the conventional approach where the uncertainties are lumped together as an unstructured matrix of Δ. Figure 4-11 reveals that both the nominal and robust performance measures are less than 1 when K_μ is applied. This implies that the system not only remains stable in presence of high uncertainties caused by the addition of the PFC capacitor, but also that the μ-based controller would provide satisfactory tracking and disturbance rejection performances in this case.

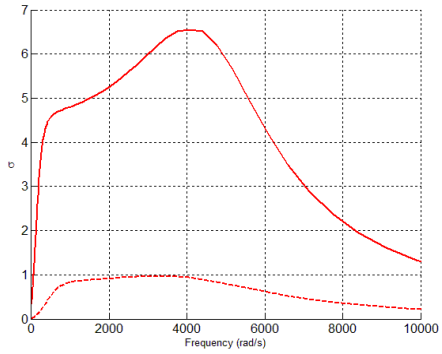

Figure 4-8: Robust stability analysis of K_{inf} without damping (solid) with damping (dashed)

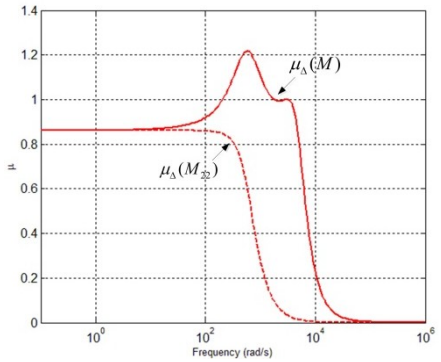

Figure 4-9: Nominal performance (dashed) and robust performance (solid) analysis with K_{inf} control.

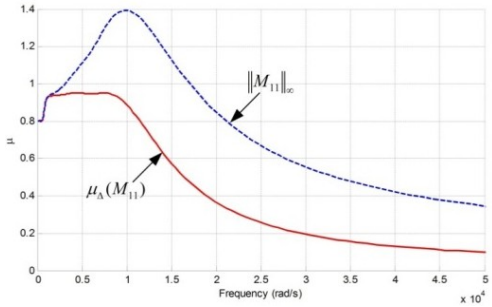

Figure 4-10: Robust stability analysis of K_μ direct voltage control with structured (solid) and unstructured (dashed) uncertainty.

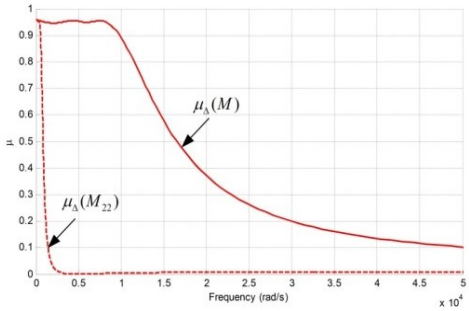

Figure 4-11: Nominal performance (dashed) and robust performance (solid) analysis of proposed K_μ controller.

Figure 4-8 to Figure 4-11 imply that although the H_∞ controller maintain the stability of the closed loop system in presence of the PFC capacitor it yields a limited capacitive uncertainty rejection range, and fails to maintain a satisfactory level of performance within the robustness range. Moreover, adopting this controller requires applying an active damping method. Even then, as was illustrated in Figure 4-3, applying a filter capacitor current feedback cannot fully compensate for the resonance effect caused by connecting the PFC capacitors. The μ-synthesis controller on the other hand, can provide both voltage robust stability and performance without any need for the inner current feedback (damping).

In order to have a better appreciation of the range of the uncertainty that the system remains stable in and also in order to compare the relative stability of the closed loop poles, the characteristic equation of the closed loop system is derived in (4-16), where K_v is the voltage controller transfer function.

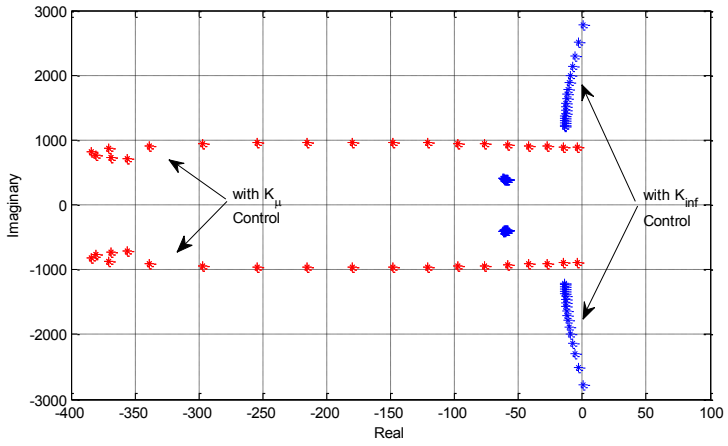

Figure 4-12: Dominant modes of the closed-loop resonant transfer function with K_μ and K_{inf} when C_{PF} is increased

$$G_{Close} = \frac{V_{dc}}{2} / \{C_f C_{pf} L_f L_c s^4 + C_f C_{pf}(L_f R_c + L_c R_f + K_d L_c)s^3 + (C_{pf} L_f + C_{pf} L_c(1+K_v) + C_f C_{pf}(K_d R_c + R_c R_f) + C_f L_f)s^2 + (K_v C_{pf} R_c + K_d C_f + C_{pf}(R_f + R_c) + C_f R_f)s + 1 + K_v\} \quad (4\text{-}16)$$

Figure 4-12 shows how the closed loop dominant poles change when the PFC capacitor increases when $K_{\inf}$ and K_μ controllers are used. The locations of the poles suggest that K_μ provides more damping yielding better performance under the occurrence of uncertainties. It should be noted that $K_{\inf}$ is designed to yield the best performance available. Performance limitation is inherently associated with the unstructured uncertainty construction associated with the H_∞ control approach.

4.5 Evaluation Results

4.5.1 Sample Simulation Results

To evaluate the performance of the proposed control scheme under the operation of a MG system, the test system shown in Figure 4-1 is implemented for time-domain simulations in the Matlab/Simulink environment. Note that the DG1 and DG2 ratings are assumed to be 40 kVA and 20 kVA respectively for this set of simulations; therefore, the droop gains are also updated to match this objective: DG1: m=3e-5 rad/s/W, n=5e-6 and DG2: m=6e-5 rad/s/W, n=1e-5.

First, the effect of the common inductive load at the main feeder is studied; the local load and also the nonlinear load are assumed to be disconnected. A three phase capacitor bank is used to provide 17.3kVAr in order to compensate for the low power factor of the supplied load. This would increase the load power factor from 0.85 lagging to 1.0. In order to have a better appreciation of the proposed direct controller, its performance has been compared to the conventional dual loop decoupled PI controller with feed-forward adopted in [19] as well as robust conventional H_∞ control with active damping.

Figure 4-13(a) shows how each DG unit is supplying active and reactive power via droop control to meet the load demand before and after the connection of the PFC. Figure 4-13 (b) shows the output voltage of DG1 when the PFC capacitor bank is connected at t = 1.76s with the conventional robust H_∞ dual-loop controller applied (the output voltage of the second DG shows similar performance). Due to weak robust stability of the conventional H_∞ controller, the disturbance rejection performance is very poor as shown in Figure 4-13 (b). Figure 4-13 (c)-(d) shows the performance of the system when the dual-loop conventional decoupled PI controller with feed-forward [19] and the single-loop direct-voltage μ-controller are adopted; respectively. The performance comparison reveals that adopting the proposed direct voltage μ-controller can not only maintain the system stability without any inner control loop (i.e. active damping); but can also improve the performance over that of the conventional dual-loop decoupled controller with feed-forward in terms of less voltage oscillation and higher quality of the output voltage.

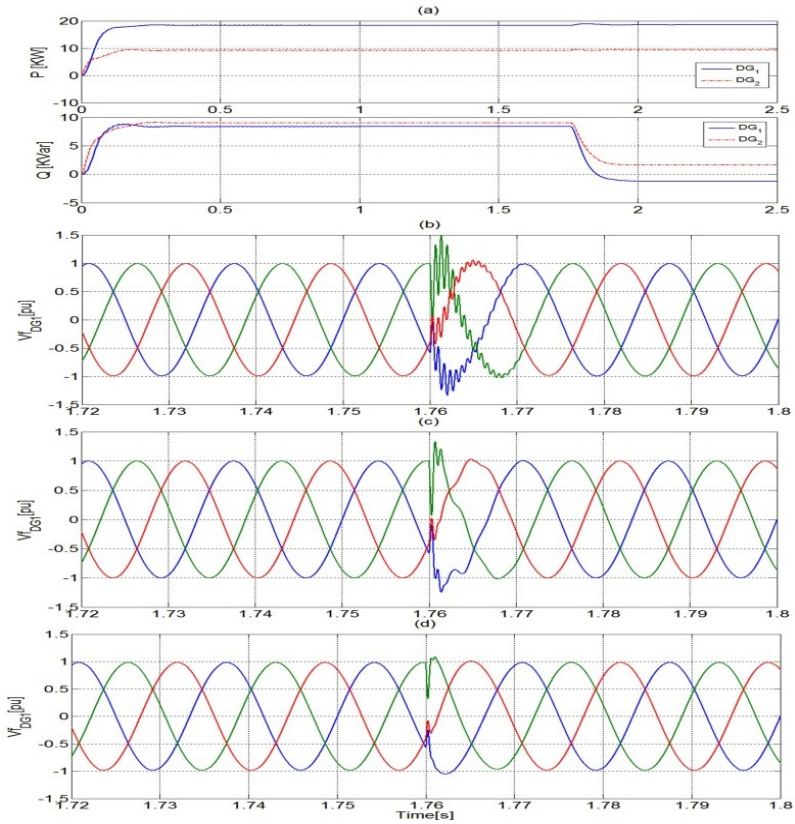

Figure 4-13: (a) Active and reactive power responses of the microgird setup. (b) Output voltage of DG1 when the PFC capacitor is added with dual loop H_∞ control. (c) Output voltage of DG1 when PFC capacitor is added with conventional PI dual-loop control with feed-forward. (d) Output voltage of DG1 when the PFC capacitor is added with the proposed direct voltage μ-control.

In order to investigate the performance of the proposed controller in the presence of local disturbances, the capacitive RLC-type local load (residential capacitive load) shown in Figure 4-1 is connected to DG1 at t=1.76s while the inductive RL-load and the PFC capacitor bank are both connected to the main feeder. Figure 4-14 (a) shows how the demanded active and reactive powers are divided between the two DGs. Because of the capacitive nature of the connected load, the total net reactive power generated by DG unit is negative and it is mainly affecting DG1 due to load proximity to DG1. Figure 4-14 (b), (c) and (d) demonstrate the output voltage of DG1 at the point of common coupling when the conventional robust H_∞ dual-loop control scheme, conventional PI controller and the proposed direct voltage μ-controller are adopted, respectively. The proposed controller yields the best performance in terms of the robust stability and voltage quality.

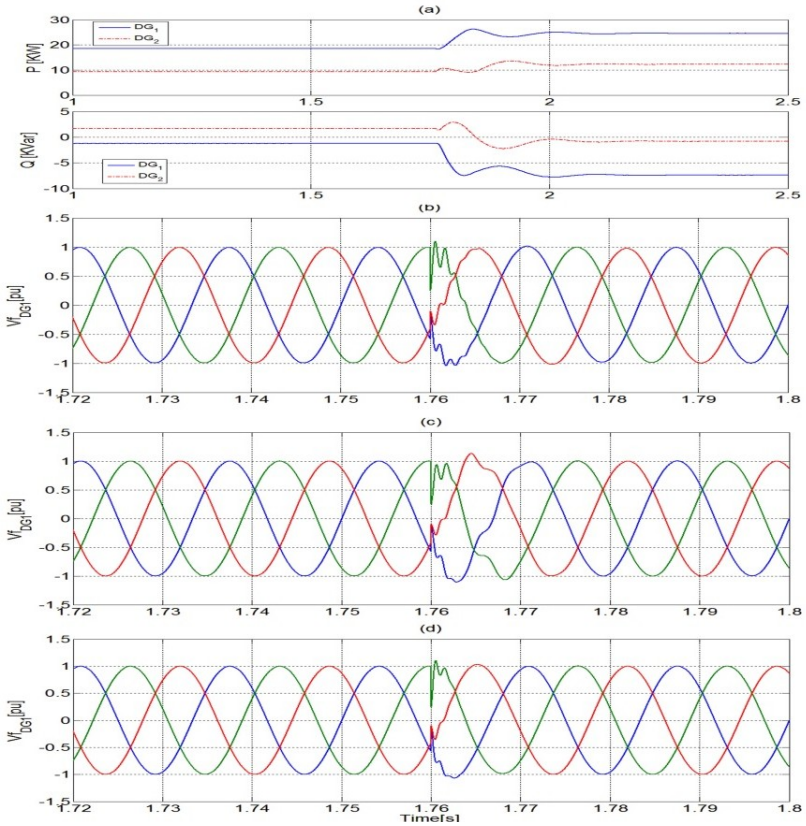

Figure 4-14: (a) Active and Reactive power responses of the micro-gird setup when a capacitive local load is added. (b) DG1 output voltage with dual loop H_∞ control. (c) DG1 output voltage with conventional PI dual-loop control with feed-forward. (d) DG1 output voltage with proposed direct voltage μ-control.

Figure 4-15 shows the performance of DG1 when the nonlinear load is switched on at t = 0.25s under different control structures. Note that the connection of the nonlinear-rectifier load introduces different harmonic distortions which in turn can excite different resonance modes in presence of the PFC capacitor. Therefore, this scenario can be considered as a useful measure to test the performance of the proposed controller in rejecting unknown harmonic disturbances. Figure 4-15 (a) shows the output voltage when the conventional PI dual-loop controller with feed-forward is adopted. As can be seen, although the system remains stable, the voltage quality is highly degraded (THD=9.5%). Figure 4-15 (b) implies that adopting the dual-loop H_∞ voltage controller can also help maintain system stability and in spite of a slight improvement in the voltage quality, the voltage THD is still very high (THD=6.9%). However the best voltage quality in the presence of nonlinear loads can be achieved with the proposed direct voltage μ-controller as shown in Figure 4-15 (c). The voltage THD in this case is 0.33% and 5.7% prior to and after connecting the nonlinear load, respectively.

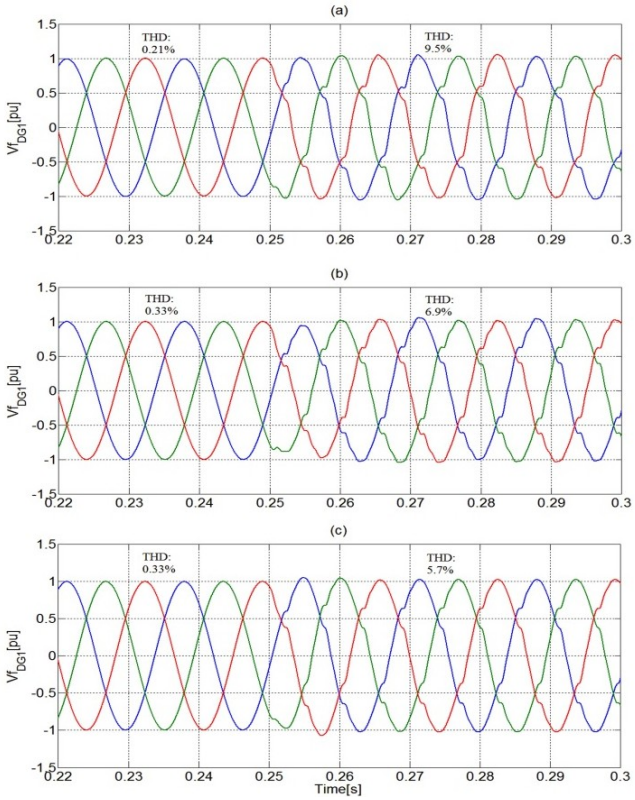

Figure 4-15: DG1 output voltage when the nonlinear load is connected (a) with conventional dual-loop control with feed forward. (b) with H_∞ dual-loop control (c) with proposed direct voltage μ-control

It should be noted that the proposed controller is tested without internal model dynamics at harmonic frequencies to gauge the robustness of the controller under harmonic disturbances. The THD in the output voltage can be further reduced by embedding internal model dynamics in the voltage control structure. This can be achieved by including the same resonance dynamics suggested earlier in (3-20).

4.5.2 Sample Experimental Results

The same experimental setup shown in Figure 3-15 is used to verify the performance of the proposed controller. Figure 4-16 shows the DG power and voltage responses when the R-load is connected. The voltage sag recovers in less than a second. The detailed voltage waveform at the instance of the load connection is also shown in Figure 4-16 (c) verifying the capability of the proposed method to reject load disturbances.

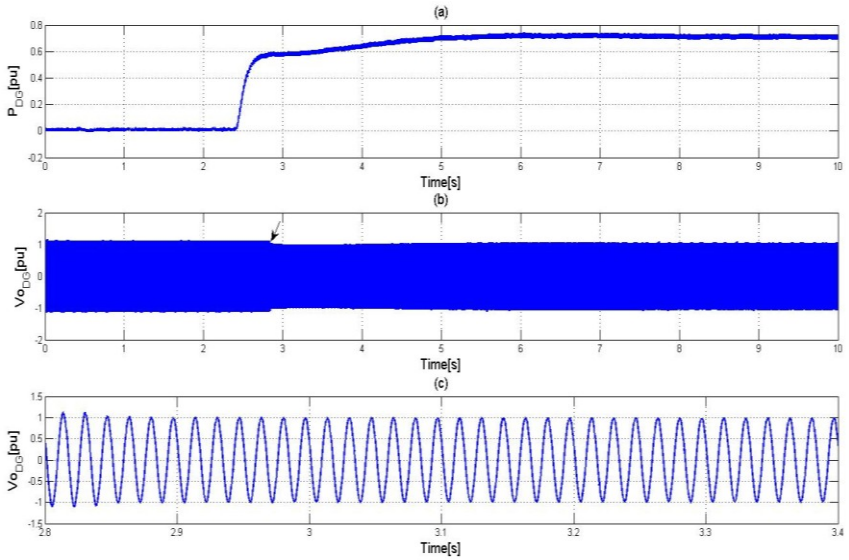

Figure 4-16: Control performance with the proposed μ-control. (a) Power response, (b) phase-*a* voltage response, (c) detailed waveform.

In order to verify the effectiveness of the proposed μ-controller in maintaining a stable operation of the DG units in the presence of highly capacitive loads and PFC capacitor banks, the nominal filter capacitor value is increased by 500% and the response of the proposed method is presented in Figure 4-17. Note that instead of changing the actual filter component, the nominal values adopted for controller design are changed to emulate such a parameter mismatch. As can be seen the μ-controller is capable of maintaining system stability by effectively damping the resonance mode changes caused by the filter capacitor increase. On the other hand however, as mentioned earlier, without enough active damping the H_∞ controller is incapable of maintaining the system stability. Figure 4-18 shows unstable system operation due to the lack of effective damping when the H_∞ controller is adopted with K_d=2.

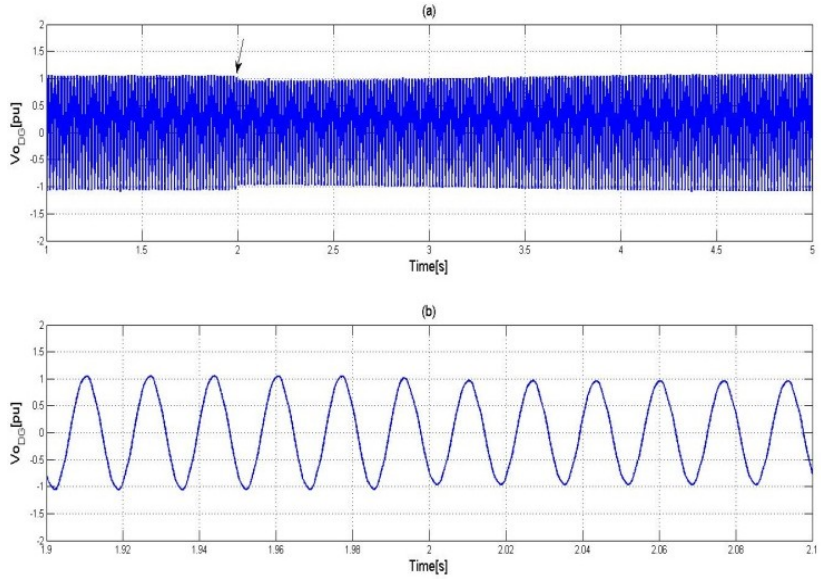

Figure 4-17: System voltage response to a 500% increase in output filter capacitor when the proposed μ-controller is adopted.

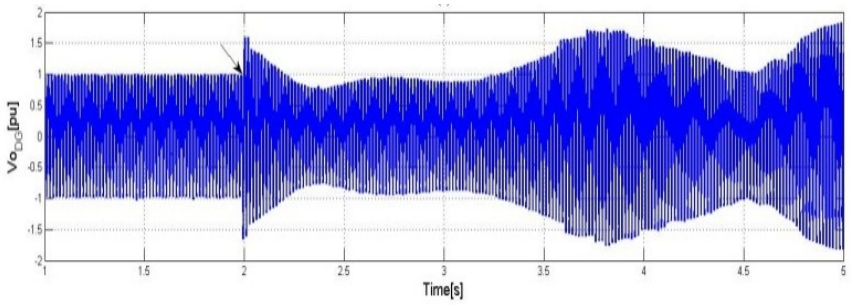

Figure 4-18: System voltage response to a 500% increase in output filter capacitor when the H_∞ controller is adopted with K_d=2.

4.6 Summary and Conclusions

This chapter presented a robust single-loop direct voltage control strategy featuring effective suppression of uncertain resonant modes generated due to PFC capacitors and residential capacitive loads in DG MGs. An improved uncertainty modeling approach has been adopted to facilitate the realization of a robust controller based on structured singular values analysis. The salient features of the proposed controller are 1) robust stability and robust control performance as compared to a conventional H_∞ multi-loop controller, 2) single-loop direct voltage control performance without dedicated active or passive damping, which simplifies the control structure and reduces the sensor requirements, and 3) effective mitigation of uncertain and multiple resonant modes due to PFC or capacitive loads, which in turns enhances the power quality of the MG system. A

theoretical comparative analysis, comparative time-domain simulation studies and experimental results have been presented to show the effectiveness and robustness of the proposed controller in MG applications.

Chapter 5

Robust Direct Current Control of LCL-Filtered DG Units in Grid-Connected and Islanded MGs[4]

In the previous chapters only the stability of voltage controlled units was studied; however several renewable energy entities as well as control units such as active filters are operated in current controlled mode. These units are often interfaced through LCL ac-side filters due to the higher attenuation provided by this type of filter which enables the converter to operate which lower switching frequencies. But it should be noted that the adoption of LCL filtered current controlled units can introduce low- and high-frequency instabilities due to the filter resonance as well as the interactions between the current controller and the grid side impedance [10, 42-45]. The associated undamped resonance peak also limits the open loop gain; thus compromising the controller's bandwidth yielding very slow response times [10]. Further, without resonance damping, the resonance mode can be excited during network or converter disturbances. Several damping solutions were introduced in 1.1.4; however, the limitations of the existing current controlled interfaced converters in providing a high bandwidth single-loop control structure is the main motivation of this chapter by addressing the following objectives:

1. Single loop stabilization with inherent LCL resonance peak damping.
2. Stable system operation under a wide range of grid (or MG) impedance variation. It should be noted that one important aspect of current-controlled operation of DG units is their performance in an isolated MG system where they should continue their stable operation while the voltage is maintained via other dispatchable units [19, 31]. However, the stable operation of such a current-controlled unit can be compromised when connected to a MG system due to the lack of "stiff grid" concept. The possible voltage variations as well as higher line uncertainties in a MG operating regime, call for the adoption of more robust interfaces that can not only work in grid-connected mode but are also able to

[4] A version of this chapter has been published: A. Kahrobaeian, and Y. A.-R. I. Mohamed, "Robust Single-Loop Direct Current Control of LCL-Filtered Converter-based DG Units in Grid-Connected and Autonomous MG Modes", accepted in *IEEE Trans. on Power Electronics*, in press.

maintain system stability when connected to a MG with higher line and voltage uncertainties.

3. Tracking and selective harmonic compensation that provides high disturbance rejection at the fundamental and harmonic frequencies.

It should be noted that in order to meet all the aforementioned objectives the proposed controller should achieve an acceptable trade-off between the controller bandwidth and the stable parameter uncertainty range. Robust control based on structured singular value (μ) minimization [39, 98] is adopted in this chapter to provide less trade-off compared to the conventional H_∞ control.

Robust H_∞ control is reported in many converter-based applications [37, 99, 100]. H_∞-norm minimization approach is reported in [37] to stabilize perturbed LCL-interfaced current controlled DG units where the line parametric uncertainty is modeled as a lumped-sum unstructured block. However, the suggested scheme fails to provide a single-loop structure and still requires the adoption of the inner current active damping loop. Moreover, the proposed interface fails to provide harmonic filtering which is necessary for active filter applications and therefore depends on a voltage grid feed-forward technique for rejecting the grid-side voltage disturbances. Therefore, motivated by the aforementioned limitations, this chapter presents an improved direct single-loop current control scheme based on the structured singular value (μ) minimization approach. Unlike the conventional H_∞-based approach, the proposed interface is shown to be able to maintain perturbed system stability without the application of any additional damping loops. Moreover, the performance of the perturbed system in terms of the grid-voltage and harmonic disturbance rejection can be improved significantly by the adopted method. This is due to the less conservative nature of the μ-synthesis based solution as it takes advantage of the additional structure introduced to the uncertainty block by the performance criteria [98]. In this method, the unstructured uncertainty block adopted in the H_∞ approach is replaced by a structured one as a fictitious uncertainty block associated with the performance criteria is added. It will be shown that the solution achieved by this method can significantly enhance robust performance of the system compared to H_∞-based method. Mathematical and comparative analysis are provided to show the advantages of the proposed μ-synthesis approach over the conventional H_∞ controller in maintaining robust stability as well as good performance. The performance of the proposed controller in mitigating fundamental and harmonic disturbances is

investigated in both grid-connected and MG regimes using time-domain simulation and experimental studies [101].

5.1 Problem statement

In order to study the stability of LCL-interfaced current controlled units in a typical MG system, a non-dispatchable current-controlled unit is assumed to be added to the previously studied typical MG system as shown in Figure 5-1. Without any loss of generality only three DG units are assumed to be connected where DG1 is the current-controlled unit (e.g. PV or wind-based unit) and DG2 and DG3 are considered to be the voltage-controlled (i.e. dispatchable) units introduced earlier in Chapter 4. The line and DG circuit parameters are as follow: S_{base} = 8 kVA, $V(L\text{-}L)_{base}$ = 208 V(LL), DG1 = 10 kVA, 60Hz, V_{dc} = 400V, L_f=1.2mH, C_f= 50μF, r_f= 0.1Ω, L_c = 0.5mH, r_c = 0.1Ω, f_{sw} = 10 kHz, DG2, DG3: V_{dc} = 400V, 8 kVA, L1 = (1+3.2j)%, L2 = (1+3.2j)%, L4 = (3+16j)%, L3 = (0.5+2.6j)%, L5 = (1+0.53)% .

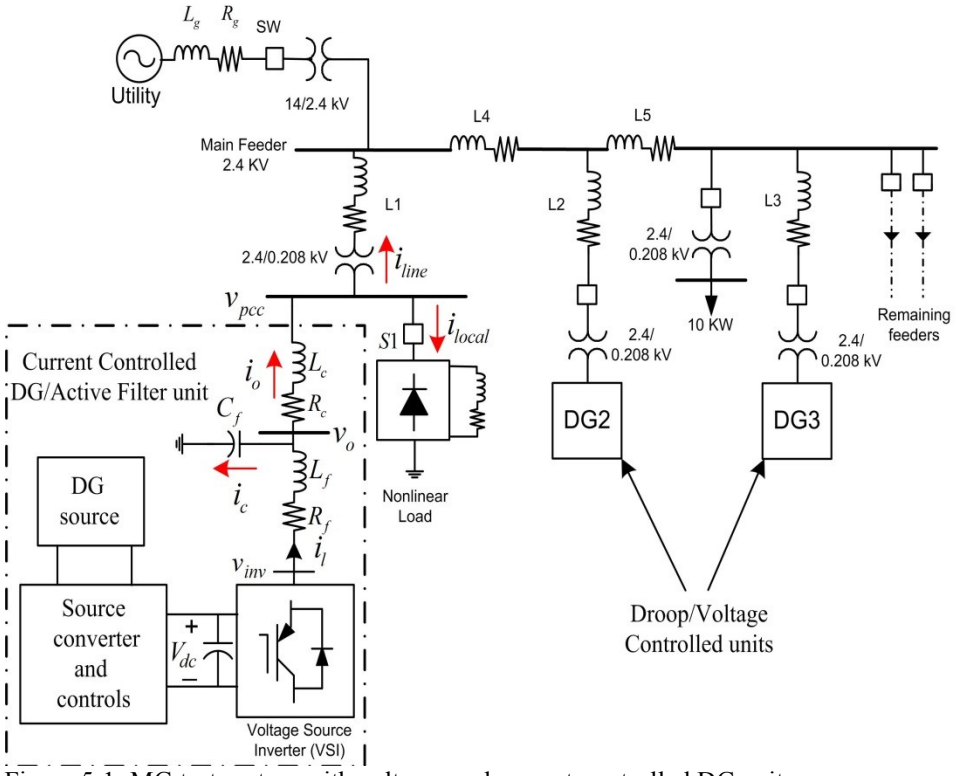

Figure 5-1: MG test system with voltage- and current-controlled DG units.

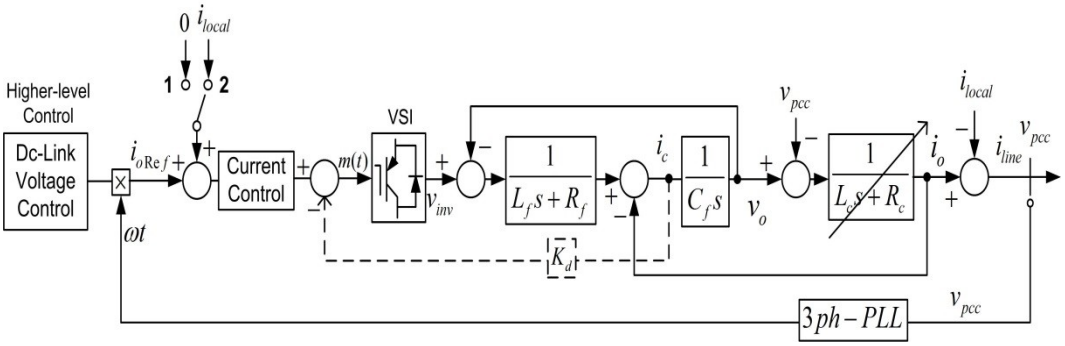

Figure 5-2: Block diagram of the current-controlled DG unit interface with LCL filter.

In grid connected mode, the demanded power is supplied by both the utility and DG units. However once disconnected from the utility, the dispatchable voltage controlled units (i.e. DG 2,3) are responsible for supplying the entire connected load via droop control. In this case, DG1 is considered to inject the maximum power available and therefore can also be considered as a negative load. Note that the dispatchable units of DG2 and DG3 are often operated via frequency and voltage droop strategy as stated in 3.1 and although several studies have reported on their stability in MG applications, very few studies have been done on the stable operation of current controlled units in isolated MG mode. Figure 5-2 shows the open-loop block diagram of the current controlled DG unit (DG1) with an LCL filter where $i_{o\mathrm{Re}f}$, the reference current, is usually calculated by the higher level dc-link voltage control that is in charge of maintaining the dc-link voltage according to the DG source power variations. In many applications, the harmonic current of the local load is also added to the reference current in order to compensate for the local load's harmonics content, resulting in improved grid-side current quality. This provides an excessive feature where the DG unit can operate as a harmonic filter for power quality purposes when needed. However, this requires the current controller to provide high disturbance rejection for the fundamental and selected harmonics.

The additional current feedback loop (from the filter capacitor), which may also be adopted to dampen the LCL filter resonance peak, is shown in Figure 5-2, by the dashed line. However, as will be shown in this chapter, a direct current control scheme is achievable and can eliminate the need for this extra loop and the associated sensor and control requirements. Also note that voltage variations at the point of common coupling form an external source of disturbance and thus should be rejected as much as possible. The open-loop dynamics between the output current and the inverter voltage and the external voltage disturbance can be therefore, derived as (5-1).

$$i_o(s) = \overbrace{\frac{1}{\Gamma(s)}}^{G_{inv}} v_{inv}(s) - \frac{L_f C_f s^2 + C_f (R_f + K_d) s + 1}{\Gamma(s)} v_{pcc}(s) \tag{5-1}$$

$$\Gamma(s) = L_f L_c C_f s^3 + C_f (L_f R_c + L_c (R_f + K_d)) s^2 + ((R_f + K_d) R_c C_f + L_f + L_c) s + (R_f + R_c)$$

Note that without adopting active damping (i.e. K_d=0) The resonance frequencies can be seen in both the i_o/v_{inv} and i_o/v_{pcc} responses in (5-1) and bring the system to instability.

PI and proportional-resonant controller with harmonic compensators (P-HERES) are well established controllers that provide both good tracking and disturbance rejection in dq and stationary frames respectively [43]. As can be seen from the open-loop frequency response of Figure 5-3, without damping the resonance peak, the bandwidth of the current controller will be limited. Therefore, low bandwidth single-loop controllers are suggested in [44, 57] without the need to damp the resonance peak. However, it should be noted that such a solution yields very slow dynamics and compromised harmonic rejection ability as the system bandwidth will be very limited. The aforementioned limitations suggest that damping of the LCL filter resonance peak is essential for both stable and acceptable performance of the current control interface. Achieving a single-loop controller that can provide inherent resonance damping with acceptable dynamics is one of the main objectives of this chapter.

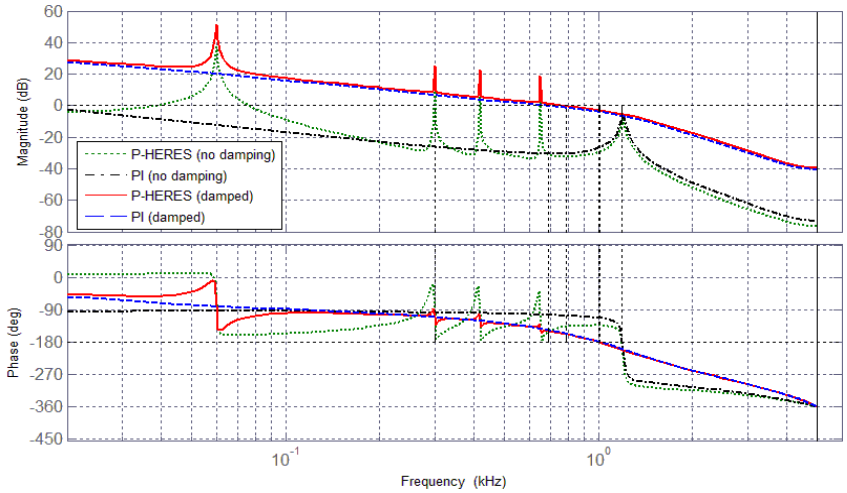

Figure 5-3: Open-loop frequency response with the PI and P-HERES controllers with and without damping

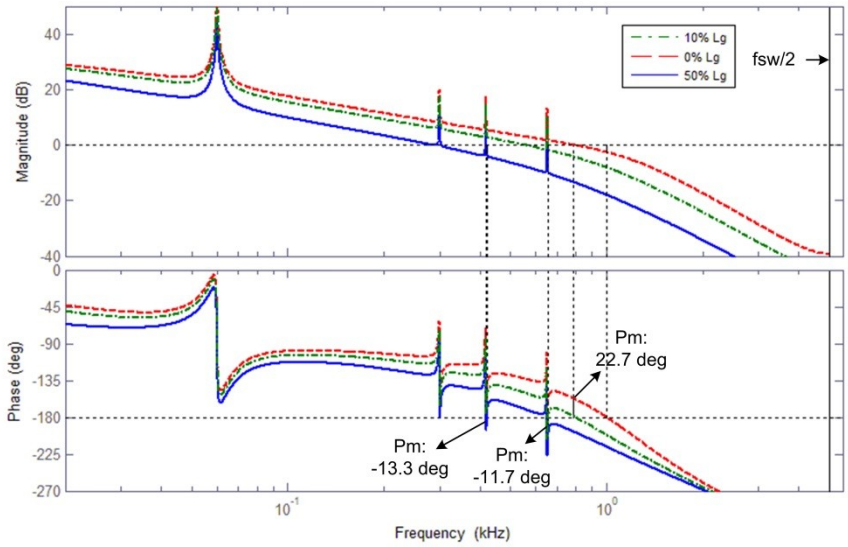

Figure 5-4: The effect of grid inductance variations over the damped frequency response with P-HERES controller

Moreover, even when the inner damping loop is applied, the adoption of harmonic compensators can compromise system stability in presence of line parametric uncertainties. Figure 5-4 shows the variation of the harmonic compensators' resonance frequencies (i.e. 5^{th}, 7^{th} and 11^{th}) with the percentage variation of the grid inductance (a typical weak grid inductance of 5mH is assumed as the base value in this case). As can be seen from Figure 5-4, even with active damping, increasing the line inductance can bring the frequencies of the harmonic compensators outside the bandwidth of the system; thus, leading to instability as the system phase margin becomes negative due to the phase shift at the selected harmonics.

The limitations of the conventional methods in optimizing the number of required sensors, as well as maintaining system stability in the presence of line perturbations call for more optimal and robust solutions. This chapter is seeking a current control approach that not only eliminates the need of the extra inner current loop by providing inherent damping, but also maintains system stability in presence of a high range of line parameter perturbations that may occur during grid connected and/or MG operating modes.

5.2 Suboptimal H_∞-based Current Control

As mentioned in 4.2, the mixed sensitivity H_∞ optimization approach has been adopted in many UPS and DG control applications [19, 37, 59, 99, 100], where the system uncertainties are modeled as an unstructured but bounded perturbation block.

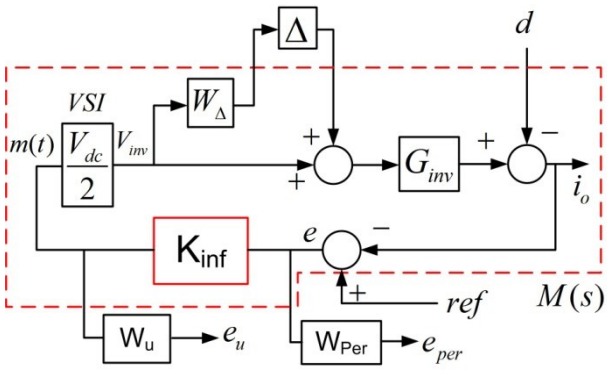

Figure 5-5: Schematic of the closed-loop system with conventional H_∞ controller

Following the modeling approach introduced in 4.2, Figure 5-5 shows the conventional H_∞-based current control problem considering both the performance and stability criteria. In Figure 5-5, $W_\Delta.\Delta$ denotes the lumped-sum uncertainty block defined by the relative deviation of the perturbed system from its nominal value in (5-2) where G_{inv_Nom} and G_{inv} are the nominal and perturbed transfer functions from v_{inv} to i_o, respectively presented earlier in (5-1).

$$\left\| W_\Delta.\Delta \right\|_\infty = \sigma\left(\frac{G_{inv} - G_{inv\_Nom}}{G_{inv\_Nom}}\right) \tag{5-2}$$

Weighting, W_Δ, is introduced to normalize Δ and can be obtained based on the worst case relative system uncertainty frequency response. In order to address the tracking and disturbance rejection objectives, the following weighting function is suggested in the form of (5-3). Where similar to equation (4-11), ω_0 is the fundamental angular frequency, h is the harmonic number, k_h is a constant and ζ is the damping coefficient. The suggested weightings make it possible to implement the controller in the stationary reference-frame. In Figure 5-5 W_u is added to penalize the controller effort where a small value is assigned to fulfill the design convergence condition [98, 102]. Note that the performance parameters are as follow: ω_0=377rad/s, k_1=0.2, k_5=0.05, k_7= k_{11}=.01, ζ= 0.01.

$$W_{Per}(s) = \sum_{h=1,5,7,11} \frac{k_h (h\omega_0)^2}{s^2 + \zeta(h\omega_0)s + (h\omega_0)^2} \tag{5-3}$$

In order to apply the robust control theorem, the control structure of Figure 5-5 can be rearranged to match the standard 2-input, 2-output M-Δ configuration of Figure 4-4. The H_∞-based robust controller, K_{inf}, can then be designed to fulfill the mixed-sensitivity optimization problem of (5-4) which follows the robust stability and performance criteria.

In (5-4), M_{11} models the weighted complementary sensitivity transfer function and M_{22} is the weighted sensitivity transfer function.

$$\left\| \begin{matrix} M_{11} \\ M_{22} \end{matrix} \right\|_{\infty} < 1 \tag{5-4}$$

The feasibility of designing an H_∞-based direct control interface is studied based on (5-4) where no inner current feedback was applied first (i.e. K_d=0). The robust stability and nominal performance measures in this case are later compared to the dual-loop structure. Note that W_Δ should be chosen in a way that (5-5) holds.

$$\left| W_\Delta(j\omega) \right| \geq \max \left| \frac{\Delta G_{inv}(j\omega)}{G_{inv}(j\omega)} \right| \quad \forall \omega \tag{5-5}$$

Figure 5-6 (a)-(b) demonstrates the first order weighting function of W_Δ adopted to normalize the system deviations in both the undamped and damped cases, respectively. The line–side inductance (L_c) is assumed to vary up to 10 times from its nominal value. Note that the resultant weighting functions of the two undamped and damped cases are $W_\Delta = (7.512s+4.996)/(s+2690)$ and $W_\Delta = (0.2684s+0.00733)/(s+367.8)$ respectively.

Figure 5-7 (a) compares the robust stability analysis of these two cases based on the small gain Theorem 1 presented in section 4.2. It can be seen that without adopting the inner damping loop, the presented H_∞-based controller fails to maintain the stability of the perturbed system. However, the robust stability measure of the dual-loop structure suggests that the adoption of the inner damping loop increases the stability margin and therefore, can guarantee the robust stability of the perturbed system over the modeled uncertainty range and can be considered as an option for robust stable operation. This however, is achieved with the cost of performance degradation. Figure 5-7 (b) shows the performance measure of the actively damped H_∞-based controller where can be seen that $\left\| M_{22} \right\|_\infty$ is greater than 1, implying that the performance criteria cannot be met. Moreover, the H_∞-design algorithm fails to achieve robust stability with a single-loop structure for the relatively wide range of modeled line perturbations. This suggests that H_∞-based controllers can either be used for a limited range of system uncertainties or for more relaxed performance objectives. As it will be discussed in the next section, this can be attributed to the conservative nature of suboptimal-H_∞-based solutions where the structure of the uncertainty block is not accounted for.

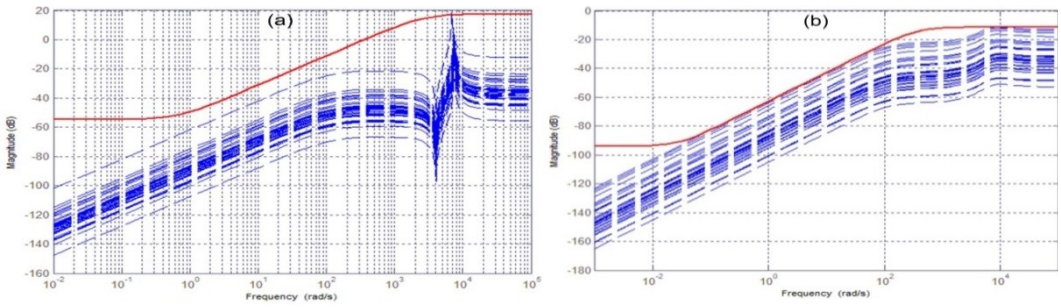

Figure 5-6: System relative uncertainty frequency response (dashed) and the fitted first order W_Δ response (solid): (a) without active damping (K_d=0) (b) with active damping (K_d=10).

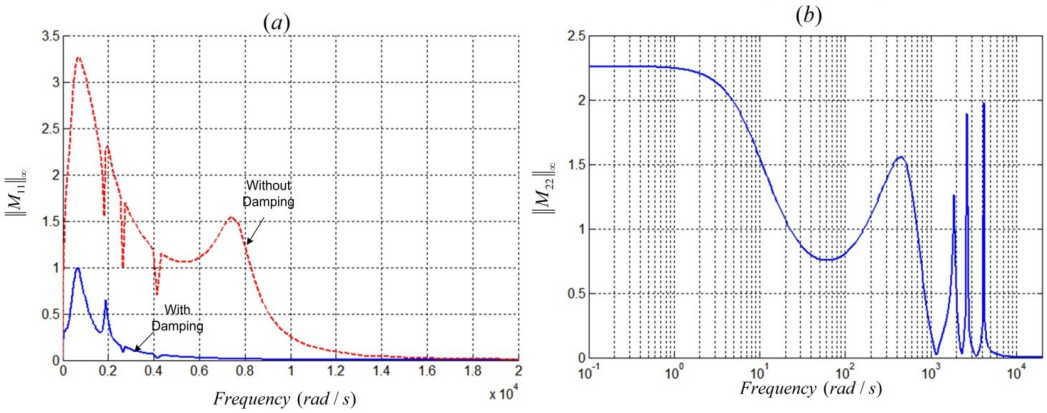

Figure 5-7: (a) Robust stability analysis of K_{inf} without damping (dashed) and with damping (solid). (b) Performance of K_{inf} with damping.

The designed suboptimal-H_∞-based 9th order controller with inner active damping is discretized using the "Tustin" approximation with 10 kHz sampling time. The resulting controller is shown in (5-6).

$$K_{\inf} = \frac{-0.01378z^9 + 0.08736z^8 - 0.2238z^7 + 0.2713z^6 - 0.08614z^5 - 0.1845z^4 + 0.2723z^3 - 0.1678z^2 + 0.05145z - 0.00639}{z^9 - 8.693z^8 + 33.84z^7 - 77.44z^6 + 114.8z^5 - 114.3z^4 + 76.48z^3 - 33.14z^2 + 8.441z - 0.9626} \quad (5\text{-}6)$$

5.3 Direct μ-Synthesis-Based Robust Control

As mentioned in section 4.3, information on the structure of the uncertainties provides less conservative solutions compared to the unstructured case. Considering this extra information can not only increase the stability margin of the perturbed system, it could also improve the performance of the perturbed system. Therefore some structure can be added to the uncertainty block, if a fictitious normalized uncertainty block, Δ_P, is assumed to be connected to the external inputs and outputs of the system as shown in Figure 5-8.

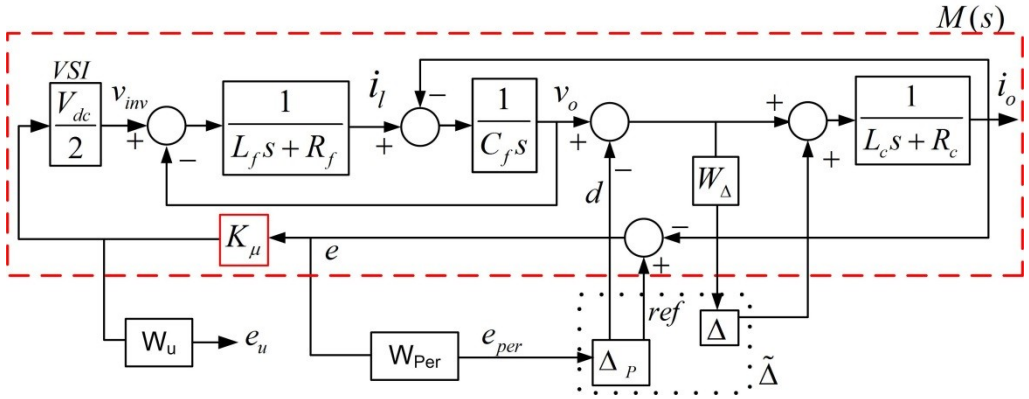

Figure 5-8: Schematic of the closed-loop system with the proposed μ-synthesis controller.

Figure 5-8 shows the closed loop scheme with the proposed μ-synthesis controller where instead of the conventional lump-sum modeling approach, the line inductive uncertainty is modeled in a more detailed fashion using the multiplicative perturbation method. Moreover a certain structure is added to the uncertainty block by introducing the performance associated block of Δ_P as suggested earlier in Figure 4-5. Once again, W_Δ is the weighting used to normalize the line uncertainty that can vary up to 10 times from the nominal value. Note that in order to compare the performance of the proposed μ-synthesis controller with the conventional H_∞-based one, the same performance weighting function as in (5-3) is considered for W_{Per}.

By introducing the new structured uncertainty block of $\tilde{\Delta}$, the μ-synthesis approach can now be applied in order to achieve both robust stability and enhanced performance. the D-K iteration method, provided by Matlab® Robust Control Toolbox [96], is adopted to compute μ and design the controller. Based on the weighted schemes provided in Figure 5-8 and considering the performance parameters to be: $\omega_0 = 377$rad/s, $K_1 = 0.2$, $K_5 = 0.1$, $K_7 = K_{11} = .05$, $\zeta = 0.01$ and $W_\Delta = (0.5802s+0.00047)/(s+132)$. The reduced order μ-synthesis controller $K_\mu(s)$ is designed. Note that the proposed controller, which is based on structured singular analysis, provides a direct current control solution where no inner current control is needed for plant stabilization purposes.

Figure 5-9 shows the robust stability and performance analysis of the proposed controller. Figure 5-9 (a) proves that the less conservative solution achieved through this method, maintains perturbed system stability as $\|M_{11}\|_\infty$ is less than unity.

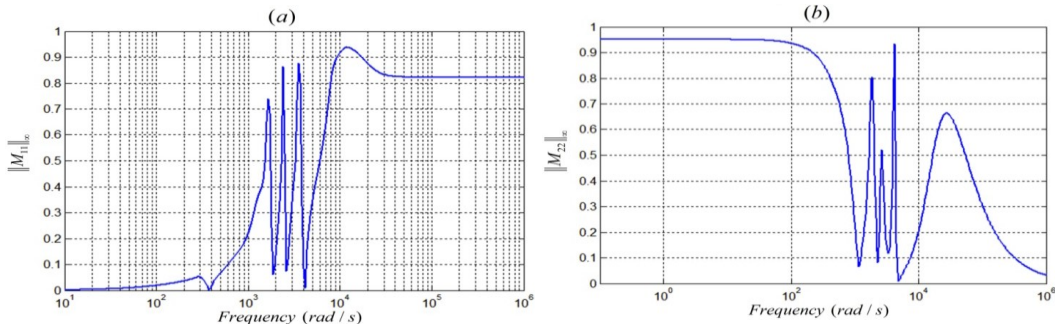

Figure 5-9: (a) Robust stability analysis of K_μ without damping. (b) Performance of K_μ without damping.

In addition, as can be seen from Figure 5-9 (b), the performance of the system is also significantly improved where the sensitivity transfer function is well bounded by the suggested performance criteria (i.e. $\|M_{22}\|_\infty < 1$).

Comparing Figure 5-9 with Figure 5-7 reveals two important facts about the advantages of the proposed robust control strategy over its counterpart conventional: H_∞-based methods:

- Adding structure to the uncertainty block and using structured singular value (μ) analysis results in a direct stabilizing current controller that, unlike the conventional methods, does not require an extra inner-loop damping method to maintain the perturbed system stability for a relatively wide range of line uncertainties.
- Comparing the performance analysis in Figure 5-9 (b) with Figure 5-7 (b) suggests that even with active damping, robust stability in dual-loop H_∞-based controllers is achieved at the cost of compromised performance. However, the proposed direct control method is capable of optimizing both the stability and performance criteria at the same time.

The designed controller is discretized using the "Tustin" approximation with 10 kHz sampling time. The resultant controller is shown in (5-7).

$$K_\mu = \frac{6.625z^{12} - 70.32z^{11} + 329.8z^{10} - 885.5z^9 + 1451z^8 - 1343z^7 + 274.3z^6 + 1026z^5 - 1543z^4 + 1147z^3 - 504.4z^2 + 125.6z - 13.77}{z^{12} - 8.587z^{11} + 32.95z^{10} - 74.06z^9 + 107.1z^8 - 102.7z^7 + 63.55z^6 - 21.95z^5 + 0.4777z^4 + 3.649z^3 - 1.985z^2 + 0.5414z - 0.0682} \quad (5\text{-}7)$$

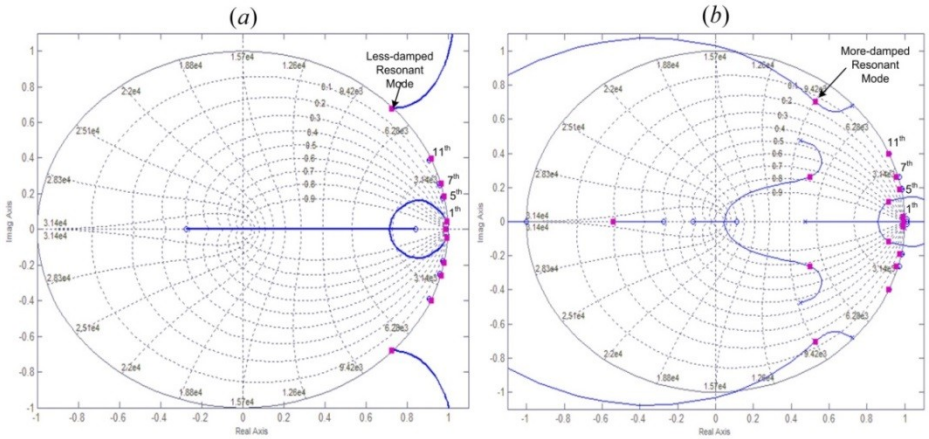

Figure 5-10: Root loci of the discretized system with (a) Conventional single loop P-HERES control (b) Proposed single-loop K_μ control

Also, the root locus of the proposed controller is shown in Figure 5-10 where it is compared to the conventional single-loop proportional-resonant controller with harmonic compensators (P-HERES) presented in [43]. Figure 5-10 confirms the effectiveness of the proposed controller in damping the filter resonance mode using only one current sensor. Note that in the conventional single-loop methods presented in [44, 57, 58] stability margins are limited, and therefore, the loop gain has to be reduced in order to maintain stability. However, the proposed method enables the current controller to achieve higher dynamics since, unlike the conventional single loop controllers, the loop gain is not limited by the undamped resonance mode.

The response time of the proposed controller is compared to the conventional case in Figure 5-11. As can be seen, the proposed method provides better dynamics. It should be noted that these dynamics can be even improved if the parameter uncertainty range considered in the design procedure is reduced due to the inherent trade-off between the robust stability and control performance in the robust control design.

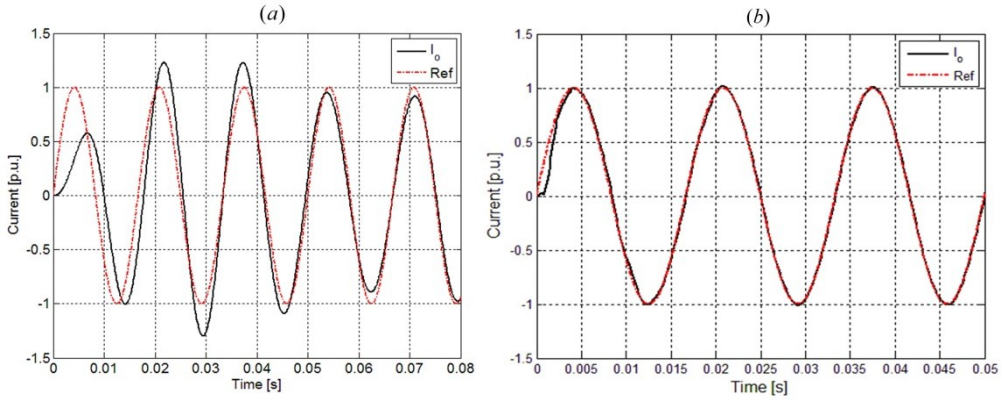

Figure 5-11: System response with (a) Conventional single loop P-HERES control (b) Proposed single loop K_μ control.

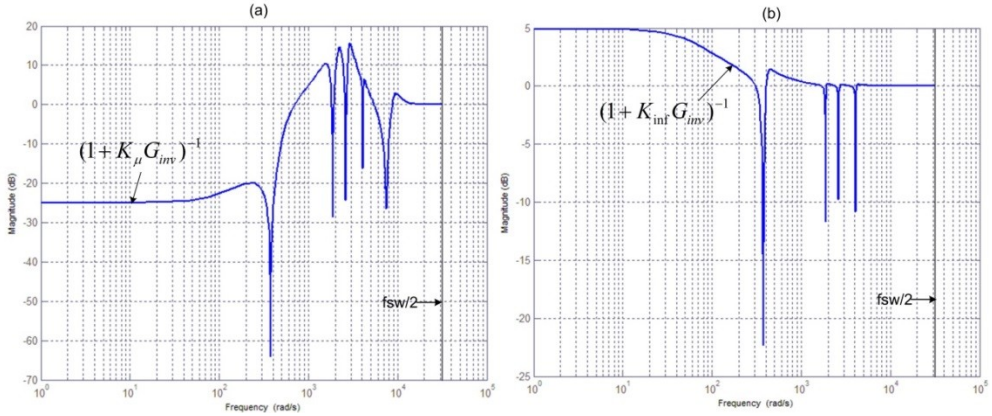

Figure 5-12: The frequency response of system sensitivity transfer function with (a) Single-loop K_μ controller. (b) Dual-loop K_{inf} controller.

In order to have a better appreciation of the advantages of the proposed μ-synthesis single loop control over the conventional dual-loop H_∞-based control, the frequency response of the sensitivity transfer functions in both cases are presented in Figure 5-12 (a),(b). Once again, it should be noted that W_{Per} is suggested to provide minimum tracking error and maximized disturbance rejection for the fundamental disturbances and selected (5^{th},7^{th},11^{th}) harmonics and is assumed to be the same in both the μ-synthesis and suboptimal H_∞ designs in order to have a fair comparison.

As can be seen from Figure 5-12 (a), the proposed single-loop μ-synthesis controller is capable of minimizing the output tracking error for the fundamental and selected harmonics. However, as Figure 5-12 (b) reveals, the performance of the conventional dual-loop H_∞-based controller is compromised. This implies that although the robust stability is achieved as shown in Figure 5-7 (a) by adopting the inner damping loop, the desired performance is not maintained.

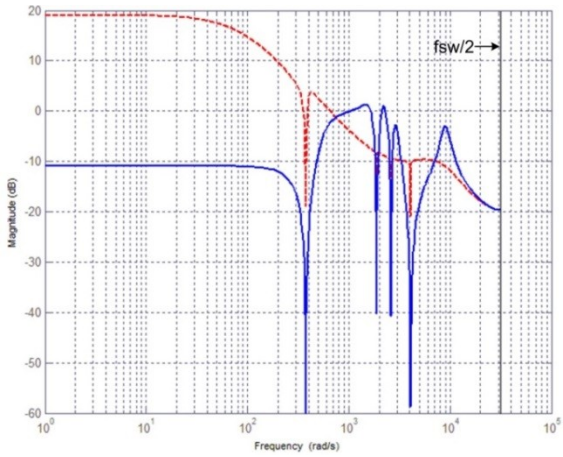

Figure 5-13: The closed-loop frequency response from the external voltage disturbance to the output current with the single-loop K_μ controller (solid) and with dual-loop K_{inf} controller (dashed).

A higher sensitivity transfer function in Figure 5-12 (b) suggests slower dynamics and a compromised disturbance rejection of the conventional H_∞-based method as compared to the proposed scheme.

As suggested in Figure 5-12, the proposed controller is expected to provide higher disturbance rejection as compared to the conventional H_∞-based robust algorithm. This can be verified by comparing the closed-loop frequency responses from the external voltage disturbance (V_{PCC}) to the output current (i_o) in (5-1) for the two cases. The responses are compared in Figure 5-13 where it can be seen that the higher disturbance rejection feature provided by the proposed controller makes the system more robust against external voltage disturbances both in the fundamental frequency and the selected harmonics; therefore, eliminating the need to adopt any feed-forward compensators and reduces the sensor requirements to a minimum (only the grid-side currents are used for feedback control).

5.3.1 Control Design for Lower Switching Frequencies

In order to achieve faster response dynamics, a 10 kHz switching frequency is adopted in this design. However the same design method can be easily followed to design μ-synthesis based robust controllers for lower switching frequency applications. The application of the proposed method for 3 kHz switching frequency is shown here as an example. However it should be noted that the LCL filter parameters should be updated for the new switching frequency based on the following two criteria:

Firstly, in order to effectively dampen the oscillatory modes using a digital damping controller, the sampling frequency, f_{sw}, should satisfy the Nyquist criterion with respect to the parallel resonance frequency. Therefore, the inequality in (5-8) should be satisfied for different system parameters:

$$f_{sw} > \frac{1}{\pi}\sqrt{\frac{L_f + L_c}{C_f L_f L_c}}\,. \tag{5-8}$$

Secondly, it should be noted that as a rule-of-thumb the filter resonance frequency is usually selected around (1/10)th of the switching frequency to ensure high attenuation of the switching harmonics. Therefore, the filter specifications for lower switching frequencies are different. In order to evaluate the performance of the proposed controller using a 3 kHz switching frequency, the LCL filter parameters are updated to provide a resonance frequency of 475 Hz to ensure both good attenuation of the switching harmonics and also a reasonable bandwidth. The following parameters satisfy the aforementioned filter design criteria: L_f= 2 mH, L_c = 1.2 mH, C_f= 150 μF.

Figure 5-14 compares the root-loci plots of the designed system for 10 kHz and 3 kHz respectively. The proposed controller can dampen the filter resonance in both cases while maintaining robust performance under uncertainty in the grid-side inductance.

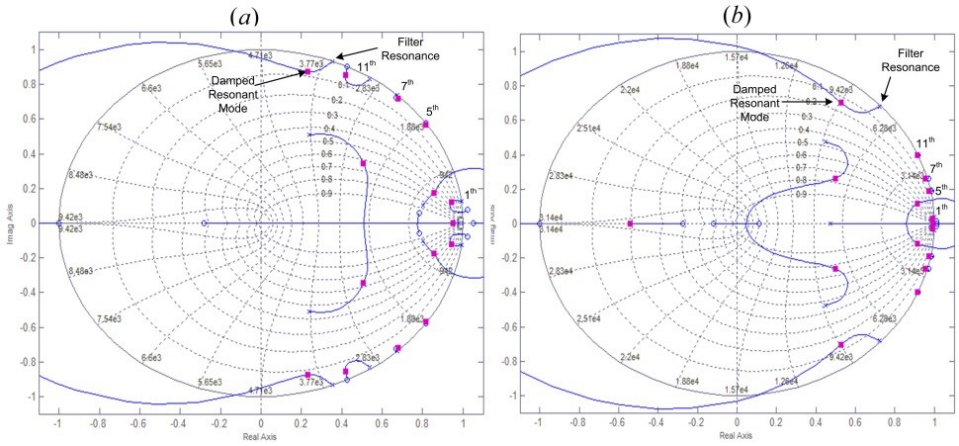

Figure 5-14: Root loci of single loop μ-based controlled system (a) f_{sw}=3 kHz, (b) f_{sw}=10 kHz.

5.4 Evaluation Results

5.4.1 Sample Simulation Results

To evaluate the performance of the proposed control scheme under both grid-connected and MG operating modes, the test system shown in Figure 5-1, adopted from the IEEE standard 399 [88] for low voltage applications, is implemented for time-domain simulation in the Matlab/Simulink environment. The performance of the proposed μ-synthesis current controller is studied in both grid-connected (when the switch SW is on) or MG regime (when the switch SW is off). In order to have a better appreciation of the harmonic compensation capability of the proposed controller, it is assumed that a nonlinear diode-rectifier type load can also be locally connected to DG1 via switch S1. The performance of the proposed μ-synthesis direct controller in maintaining the system stability as well as harmonic compensation is compared to the conventional dual-loop H_∞ schemes in different operating conditions and typical system parameters.

To study the tracking performance as well as the robust stability of the proposed controller in the grid connected mode, Figure 5-15 shows DG1's current response as the grid inductance (L_g) is increased from 0.1mH to 4.5mH at t = 0.6s to emulate a weak grid condition. The local nonlinear load is assumed to be disconnected at this point. The performance of the robustly-designed dual-loop H_∞ and μ-synthesis controllers are also presented in Figure 5-15 (a) and (b), respectively. As can be seen, both controllers are capable of maintaining system stability under weak grid condition. However, it should be noted that in the H_∞ controller, an inner damping loop is adopted whereas the μ-synthesis control provides a direct control solution eliminating the need for extra current sensors and multi-loop control tuning. Moreover, as Figure 5-15 (a) suggests, the response time of the H_∞ controller to the sudden parametric change is higher compared to the μ-synthesis indicating its slower dynamics (i.e. limited bandwidth).

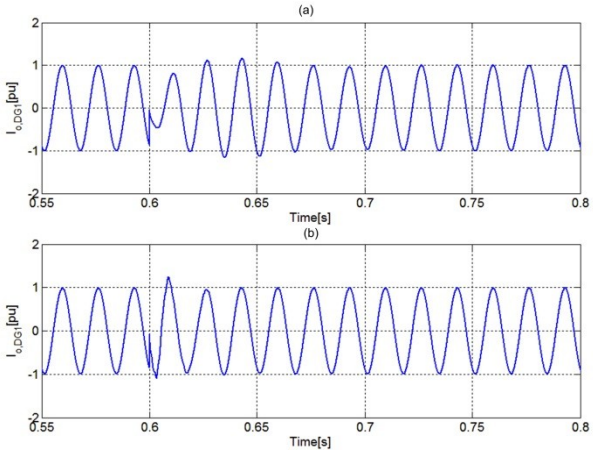

Figure 5-15: Output current of DG1 when Lg is increased from 0.1mH to 4.5mH (a) with H_∞ dual loop control (b) with proposed direct μ-synthesis control.

One of the demanding features in current-controlled units is their ability to compensate for current harmonics caused by the connection of local nonlinear loads. Without compensating for the local nonlinear loads, the harmonic content will be injected to the utility grid which affects the overall system power quality indices. The undesirable local harmonics can be compensated for from the utility side if the same harmonic contents are generated by the DG unit. This can be achieved by adding the local load current to the reference as shown in Figure 5-2. Note that in this case, the DG unit performs as a harmonic filter that cancels out the local nonlinear load harmonics. In order to appreciate the importance of this feature, the local load current is first considered not to be added to the reference current (position "1"in Figure 5-2). Figure 5-16(a), (b) and (c) show the local nonlinear load current as well as the DG output current and the line current, respectively when the current reference is first set to be 0.85 p.u. As can be seen, the connection of the nonlinear load at t = 0.6 s results in a highly distorted current being injected to the grid. The line current quality can be significantly improved by injecting the same local load harmonics via the DG unit in order to cancel them out from the line current. In order to achieve this objective, the controller should however, provide good harmonic compensation (i.e. low sensitivity transfer function) at the selected harmonics. The harmonic compensation ability of the H_∞-based and μ-synthesis controllers are therefore evaluated and compared by injecting the local current to the reference signal (position "2" Figure 5-2).

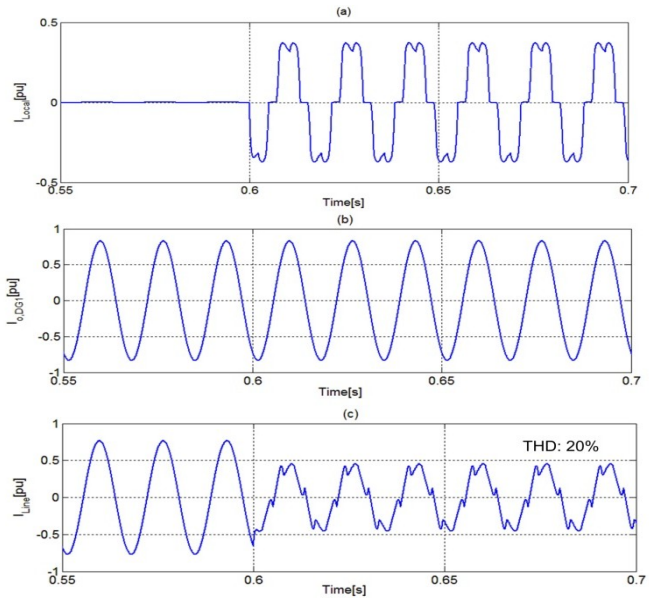

Figure 5-16: Control performance without compensating the local load nonlinear current (a) Nonlinear local load current (b) DG output current (i_o) (c) Line current (I_{Line}).

Figure 5-17 (a),(b) shows the compensated line currents when dual-loop H_∞ and proposed direct μ-synthesis controllers are adopted, respectively. Figure 5-17 reveals the higher harmonic compensation capability of the μ-synthesis controller as the current THD is significantly improved as compared to the H_∞ case. It should be noted that the enhanced line current quality is achieved by the filtering act of the DG unit; therefore, its output current (i_o) is expected to contain the local load harmonic contents in order to filter them out from the line current. Figure 5-18 demonstrates the DG output current that has been generated by the μ-synthesis direct current controlled DG unit in order to compensate for the local load harmonics.

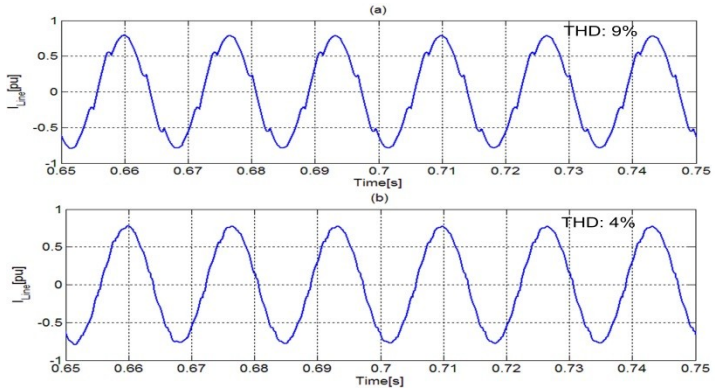

Figure 5-17: Compensated line current (a) with dual-loop H_∞ control (b) with proposed single-loop μ-control.

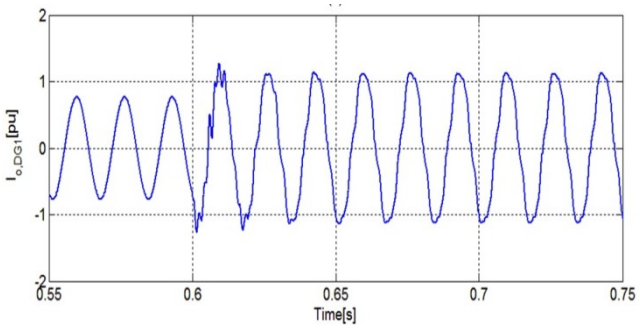

Figure 5-18: DG output current generated to compensate for the local nonlinear load with μ-control.

In order to evaluate the performance of the system during the transition from grid-connected to MG mode, an intentional islanding event is created at t=1s by switching SW off. The local nonlinear load is assumed to be disconnected in this case and the current reference is selected to be 0.88 p.u. resulting in a 7kW output power generated by DG1 in both grid connected and islanded operating modes. However, the droop-voltage controlled units (i.e. DG 2,3) are expected to regulate their output power to match with the local power demand as the system switches to the MG operational mode. Figure 5-19 (a) shows the power generated by each DG unit whereas Figure 5-19 (b)-(c) presents the current responses when the conventional dual-loop H_∞ and proposed direct μ-synthesis controllers are adopted, respectively. Note that by disconnecting the MG system of Figure 5-1 from the grid, the effective line inductance seen by DG1 will change yielding an unstable operation. Figure 5-19 suggests that both dual-loop H_∞ and direct μ-synthesis controllers are capable of maintaining stability as verified by the robust stability analysis earlier in Figure 5-7 and Figure 5-9. It should be noted however, that comparing Figure 5-19 (b) and Figure 5-19 (c) suggests that the dual-loop H_∞ controller has slower dynamics as compared to the proposed direct μ-synthesis based interface during the transition period.

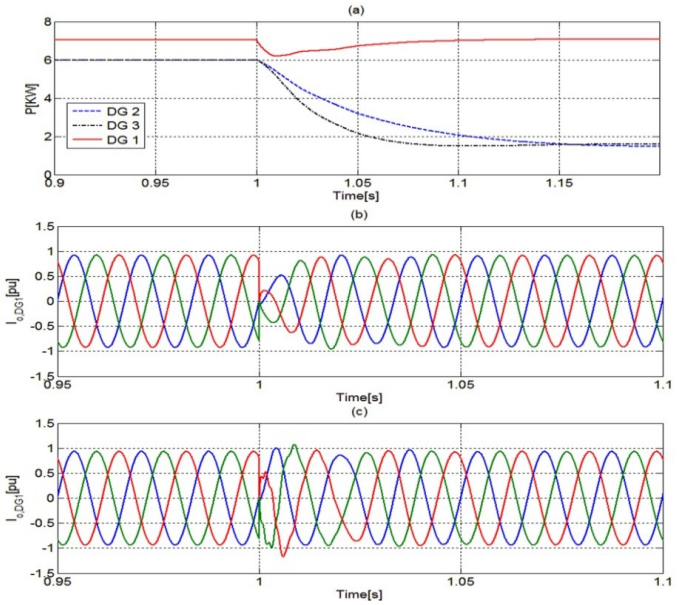

Figure 5-19: The MG system response due to the islanding event (a) power responses (b) DG1 output current with dual-loop H_∞ control (c) DG1 output current with proposed single-loop μ-control.

The presence of nonlinear loads especially in a MG system, can introduce voltage harmonic distortions due to the lack of a stiff grid concept and therefore, the current controlled units' ability to reject selected voltage harmonics from their output current is of outmost importance for the MG stable operational mode. In order to investigate the voltage harmonic rejection of the proposed controller, 0.6% of 5^{th} and 0.2% of 7^{th} harmonic distortions are introduced to the MG voltage. The output current of DG1 in the presence of the voltage harmonic content is compared with the dual-loop H_∞ and μ-synthesis controllers as shown in Figure 5-20 (a) and (b), respectively. Comparing the output current THD in both cases reveals that the proposed μ-synthesis controller demonstrates better voltage harmonic rejection as compared to its counterpart. This agrees with the analysis provided earlier in Figure 5-13.

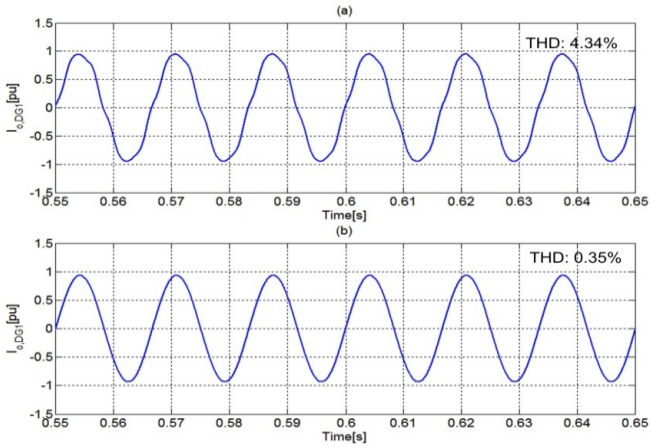

Figure 5-20: The closed-loop output current response when the distorted voltage is applied (a) Dual-loop H_∞ control (b) Proposed single-loop μ-control.

5.4.2 Sample Experimental Results

To validate the presented analysis and proposed control design, a 1.0 kW, 208V, 6 0Hz, laboratory-scale grid-connected converter system is used. A Semi-stack IGBT voltage-source converter is used to interface the DG unit to the utility grid through the output LCL filter. The dSpace1104 control system is used to implement the proposed control scheme in real-time. The pulse-width modulation algorithm is implemented on the slave-processor (TMS320F240-DSP) of the dSPACE controller. The dSPACE1104 interfacing board is equipped with eight digital-to-analogue channels (DAC) and eight analogue-to-digital channels (ADC) to interface the measured signals to/from the control system. The software code is generated by the Real-Time-WorkShop in the Matlab/Simulink® environment. A variable resistive load box is used as the output load. The current and voltage sensors used are HASS 50-S and LEM V 25-400, respectively. The LCL filter parameters are L_f = 1.2mH, C_f = 50μF and L_c = 0.5mH. The converter switching frequency is 10 kHz, which indicates that the proposed controller can be implemented under high switching frequencies. Since the sharp IGBT commutation spikes may impair the current acquisition process, the synchronous sampling technique with a symmetric PWM module is adopted. With this method, the sampling is performed at the beginning of each modulation cycle. Only two current phases are fed-back as the neutral point is isolated. A 3-phase dq-PLL is adopted for grid-synchronization. The proposed controller is compared to the conventional P-HERES controller and single- and dual-loop H_∞ controllers.

Figure 5-21(a) shows the output current response with the proposed direct μ-synthesis controller along with the voltage waveform at the point of common coupling. The voltage THD is 2.5% and its harmonic spectrum is also presented in Figure 5-21 (a). The presence of low-order voltage harmonics makes it possible to evaluate the harmonic disturbance rejection capability of the proposed controller and compare it with the conventional H_∞ and P-HERES controllers. Figure 5-21 (b) and Figure 5-21 (c) present the current and voltage responses when the conventional dual-loop H_∞ and P-HERES controllers are adopted, respectively. Table 5-1 presents the voltage and current low-order harmonic content as well as their THD. Comparing the quality of the output current in the presence of voltage harmonic distortions for different control schemes reveals the improved performance of the μ-synthesis controller in rejecting voltage harmonics. Note that the H_∞ controller fails to provide good disturbance rejection, and therefore, the current THD is the highest. This can be attributed to the fact that in the H_∞ minimization algorithm, robust stability is only achieved (to provide robust performance under grid impedance variation) at the cost of compromised performance as was discussed earlier in section 5.3.

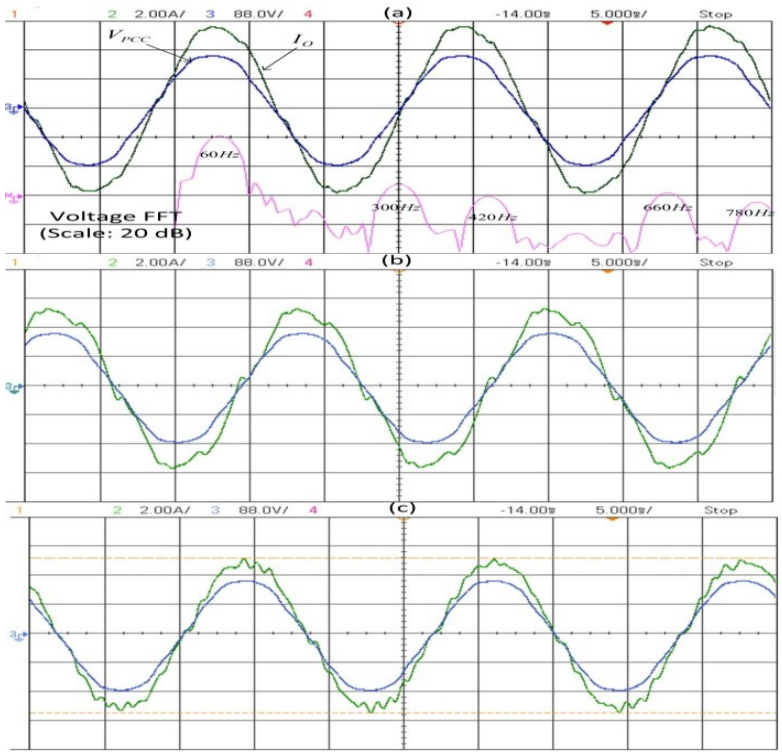

Figure 5-21: Output Current and voltage waveforms with (a) proposed single-loop μ-control (b) dual-loop H_∞ control (c) dual-loop P-HERES control.

Table 5-1: Comparative current THD and harmonic contents in presence of different control algorithms when the grid voltage THD is 2.5%.

	V_{PCC}	Output Current		
		μ-Synthesis	*P-HERES*	H_∞
THD	2.50%	3.80%	4.9%	7.9%
5^{th} (% of Fundamental)	2.13%	3.26%	2.76%	7.47%
7^{th} (% of Fundamental)	0.72%	1.11%	0.76%	2.83%
11^{th} (% of Fundamental)	1.01%	0.77%	3.07%	2.06%

In order to evaluate the robust stability of the proposed controller, the grid-side inductance is increased up to 240% of its nominal value as L_c is replaced with a 1.2mH inductor. Figure 5-22 (a) and (b) show the output current of the perturbed system with μ-synthesis and conventional dual-loop H_∞ control respectively. As can be seen, both controllers are well capable of preserving the stability of the perturbed system. However, once again it should be noted that for H_∞ control, this is achieved at the cost of extra current sensors and an inner damping loop as well as the compromised performance as suggested earlier in Figure 5-21 and Table 5-1. The performance of the dual-loop P-HERES controller is also presented in Figure 5-22 (c) where it can be seen that introducing higher grid-side inductance can significantly reduce the stability margins yielding oscillatory system performance as the harmonic compensators fall out of the crossover frequency. Figure 5-22 (c) clearly shows that even with the adoption of inner damping loops, proportional resonant controller is incapable of maintaining system stability when low-order harmonic compensators are added as expected from Figure 5-4.

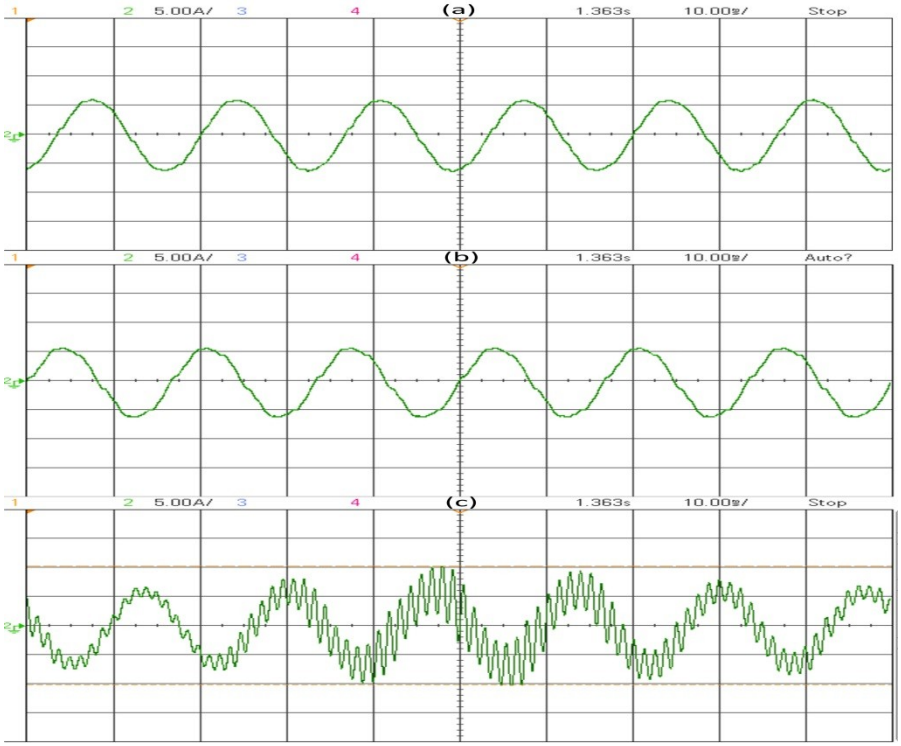

Figure 5-22: The perturbed system output current with (a) proposed single-loop μ-control (b) dual-loop H_∞ control (c) dual-loop P-HERES control.

In order to show the importance of adopting an inner damping loop in the H_∞-based design approach, Figure 5-23 shows the performance of the single-loop H_∞ control when $K_d = 0$ and the line inductance is increased to 1.2 mH. As can be seen in Figure 5-23, prior to changing the line inductance, the controller is capable of maintaining the nominal stability by providing inherent damping as suggested in [59]. However it cannot provide robust stability as expected. Figure 5-24 shows the tracking response of the proposed controller as the reference has been increased at t = 1.135s. As can be seen, the controller shows fast dynamics in responding to the reference step-change indicating the high bandwidth performance of the close-loop system with direct current control and inherent damping of LCL filter resonance.

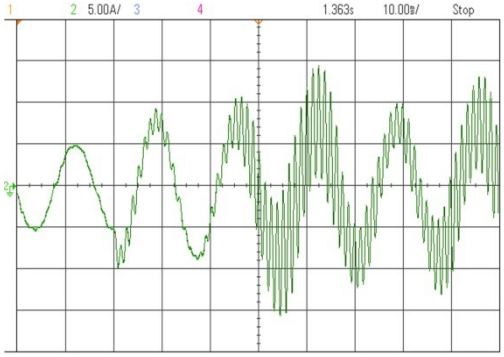

Figure 5-23: the DG Current response when L_c is increased from 0.5 mH to 1.2 mH with the single-loop H_∞ control.

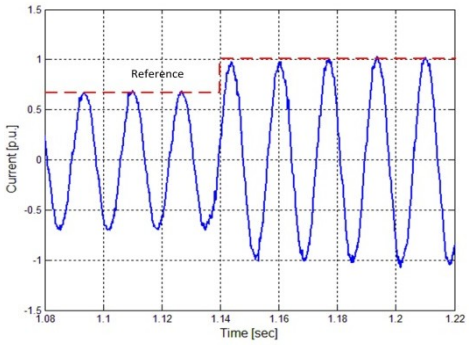

Figure 5-24: the current response of the proposed μ-synthesis controller (solid) to a tracking step change (dashed).

5.5 Summary and Conclusions

This chapter presented a robust single-loop direct current control strategy for LCL-filtered current controlled DG converters that can be used in both grid-connected and islanded MG modes. The proposed method is synthesized based on structured singular value (μ) minimization to maintain stable operation for a wide range of grid-side parametric uncertainties. Unlike the conventional H_∞-based approach, which requires an additional inner damping loop, the less conservative nature of the μ-synthesis-based solution eliminates the need for dual-loop control structures yielding faster dynamics and the need for less number of current sensors. Moreover, introducing the performance criteria in the uncertainty block structure significantly improves the system performance as compared to the conventional H_∞-based controllers. The high disturbance rejection of the proposed scheme at the fundamental and selected harmonics removes the dependency of the current control loop on the feed-forward grid-voltage and also makes it possible for the DG unit to operate as a harmonic filter when connected to nonlinear loads. The proposed controller ensures robust stability and performance under grid impedance variation and/or network configuration in islanded MG operation; therefore, it enhances the stability and performance of the DG units.

Chapter 6

Low-Frequency Oscillations in MV MG Systems with IM Load[5]

The operation of IM loads in droop-controlled converter-based MGs yields special characteristics due to the direct and relatively fast frequency control (e.g. droop control) using the load power. Difficulties occur in the following ways:

1) Electromechanical rotor oscillations in large IMs couple the rotor speed oscillations, which are directly coupled to the supply frequency and the rotor flux dynamics where the rotor-circuit time-constant is large and both the rotor electrical and mechanical dynamics are coupled. Since rotor oscillations yield both mechanical and electrical power oscillations, the output power of individual DG units feeding an IM inherently contains the frequency modes of these oscillations. It should be noted that rotor oscillations are characterized by their low-frequencies (in the range of 0.2Hz to few Hz [64]) and they cannot be effectively filtered by the average power low-pass filters used to extract the average power components in DG units (which are usually designed with a cut-off frequency in the range of few Hz to allow sufficient time-scale separation between cascaded loops and to ensure high power quality measures in the MG). The power-sharing controller in autonomous MGs uses the average output power of each DG unit to modulate the frequency for appropriate power sharing. This mechanism creates a feedback system, where rotor oscillations generate power-angle oscillations via the controlled VSI. Due to the lightly-damped nature of rotor oscillations in large IMs, the feedback system can be subjected to power oscillations and instability even at low values of the static droop gains. It is well known that low-values of static droop gains yield higher stability margins at the cost of inaccurate steady-state power sharing

[5] A version of this chapter has been published: A. Kahrobaeian, and Y. A.-R. I. Mohamed, "Analysis and Mitigation of Low-Frequency Instabilities in Autonomous Medium-Voltage Converter-Based MGs With Dynamic Loads", *IEEE Trans. on Industrial Electronics*, vol.61, no.4, pp.1643,1658, April 2014.

performance when a MG system is feeding static loads. However, this fact might be violated when the MG load has a high penetration of high power IMs; i.e. the MG stability can be challenged even under conservative values of the droop gain coefficients.

2) Unlike the idealized operation of an IM under an infinite-bus condition, in a typical MG system with IMs, active and reactive power oscillations will be coupled.

3) The droop gains in a MG system can vary over a considerable range to optimize the cost and operation aspects of MG via a higher-level management controller [62]. Therefore, system stability should be guaranteed over a wide range of droop gain variations.

Motivated by the aforementioned difficulties, this chapter presents integrated modeling, analysis and stabilization of droop-controlled converter-based MW MGs with IM loads. A detailed small-signal model of a MW droop-controlled MG system with both dynamic and static loads is developed. The model considers the exact 5^{th} order model of the IM load and the 13^{th} order model of VSI-based DG units along with network dynamics. Conventional cascaded voltage and current control loops are considered to model the DG interface. The proposed model accounts for the impact of supply frequency dynamics associated with the droop-control mechanism to accurately link the MG frequency dynamics to the motor dynamics. The complete small-signal model is used to assess the impact of the IM dynamics on the MG stability as compared to the static load case. Participation factor analysis is conducted to identify the contribution of different states to the dominant eigen-values of the MG system with and without the dynamic load. Further, the small-signal model is used to analyze the MG stability under different values of the droop gains. To stabilize the MG system in the presence of IM loads, a two-degree-of-freedom (DOF) active damping controller is proposed to stabilize the newly introduced dominant dynamics. The proposed supplementary active damping controller does not interfere with the steady-state system performance and yields robust control performance under a wide range of droop parameters. A theoretical analysis, time-domain simulation results, and experimental results are used to validate the effectiveness of the proposed scheme [78].

6.1 MG Dynamic Model with Dynamic Load

Figure 6-1 shows a MW MG system based on the IEEE Standard 399 [88]. The system consists of three 2MW dispatchable DG units with two sets of locally connected static loads (Static load1: 1MW, Static load2: 1.5 MW) and a typical 2250hP, 2.4kV, IM connected to the middle feeder. The DG System parameters are given in Appendix A. In the autonomous mode of operation, i.e. when the MG setup is disconnected from the utility grid, DG units are responsible for maintaining the system voltage and frequency along with meeting the total load demands. The reference voltage-vector provided by an outer droop controller is generated by the VSI interface via a closed-loop cascaded voltage and current control loops [7, 103-108]. A small-signal state-space model of the MGs components is developed and presented in the following sub-sections. The modeling approach can be easily extended to include additional DG units and load models.

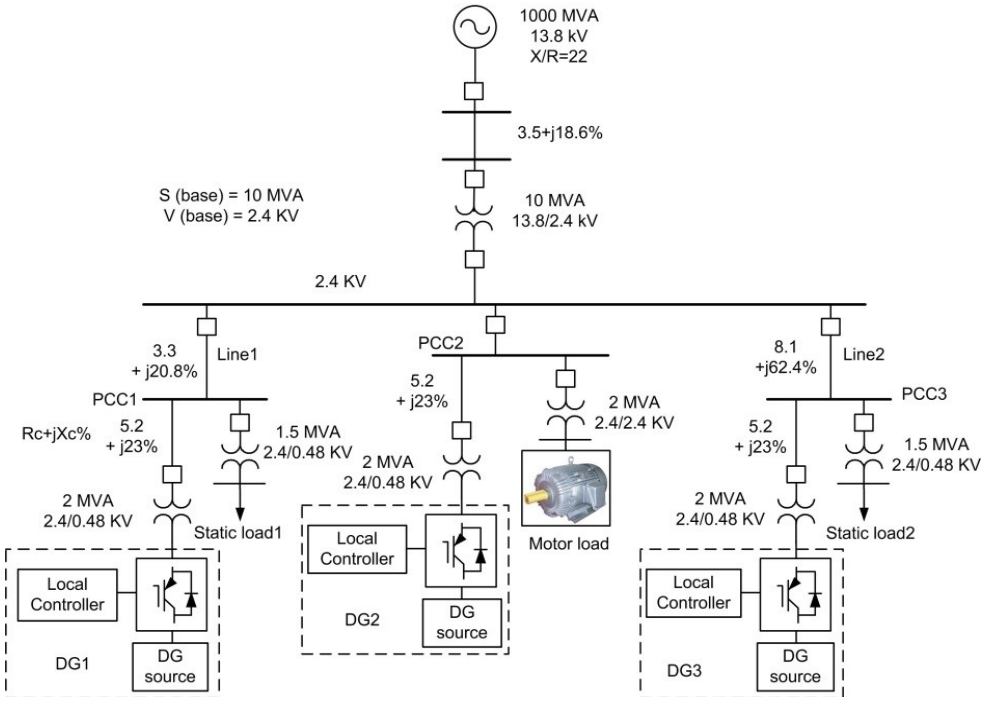

Figure 6-1: MW MG system with IM load.

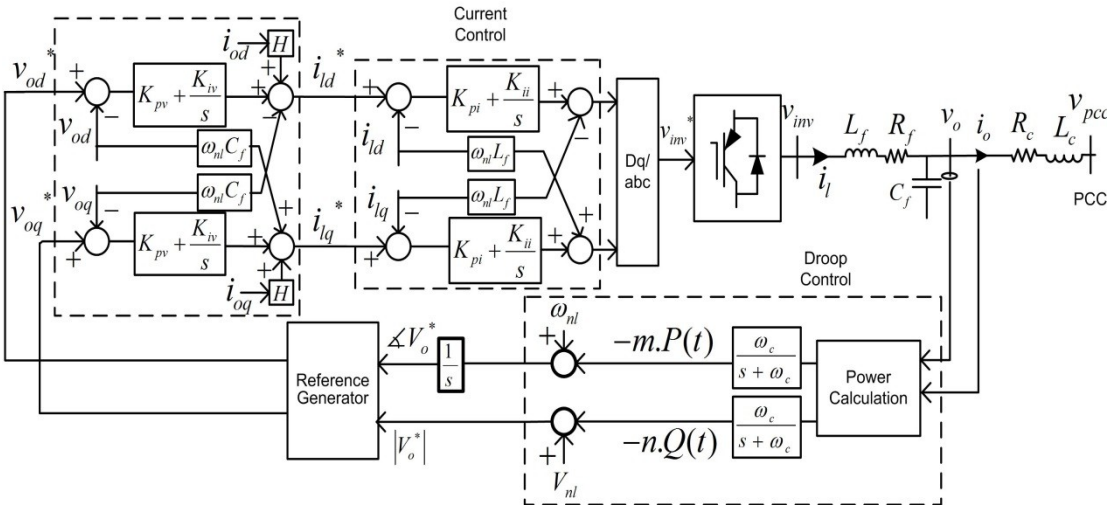

Figure 6-2: HierarchicalDG unit hierarchical control interface.

6.1.1 State-Space Model of a VSI-Based DG Unit

Figure 6-2 shows the complete conventional control system of a typical VSI-based DG unit, which consists of: 1) power sharing control, which sets the voltage phase and magnitude for the inverter output voltage according to the droop settings, 2) a voltage control loop to yield close control characteristics of the output voltage, and 3) an inner current loop to control the filter inductor current, limiting the converter current during abnormal conditions and actively damping the resonance peak of the output LC filter. The power loop consists of the droop controller which allows DG units to share the active and reactive power demand by drooping their output reference voltage frequency and magnitude.

The details of the droop control dynamics are already explained in section 3.1 where it was stated that the adopted average active and reactive power measurements in (6-1) are extracted by a low-pass filter as in (6-2).

$$\omega = \omega_{nl} - mP \;,\; V = V_{nl} - nQ \tag{6-1}$$

$$P = \frac{\omega_c}{s+\omega_c} \times \underbrace{\qquad}_{p(t)} \;,\; Q = \frac{\omega_c}{s+\omega_c} \times \underbrace{\qquad}_{q(t)} \tag{6-2}$$

where v_{od} ,v_{oq}, i_{od}, i_{oq} are the output voltages and currents in the dq reference-frame, respectively, and ω_c is the filter bandwidth.

The voltage and current control loop equations including the conventional PI compensators (with gains K_p and K_i) and the feed-forward gain (H) are listed in (6-3) through (6-6), where the dq reference-frame is assumed to be rotating at the angular speed dictated by the droop controller. Note that the grid-side output current components (i_{od}, i_{oq}) act as external disturbances; therefore they are fed-forward through gain H in order to compensate for their effect.

$$i_{ld}^{*} = K_{pv}(v_{od}^{*} - v_{od}) + K_{iv}\int (v_{od}^{*} - v_{od})dt - \omega_{nl}C_f v_{oq} + Hi_{od} \tag{6-3}$$

$$i_{lq}^{*} = K_{pv}(v_{oq}^{*} - v_{oq}) + K_{iv}\int (v_{oq}^{*} - v_{oq})dt + \omega_{nl}C_f v_{od} + Hi_{oq} \tag{6-4}$$

$$v_{inv,d}^{*} = K_{pi}(i_{ld}^{*} - i_{ld}) + K_{ii}\int (i_{ld}^{*} - i_{ld})dt - \omega_{nl}L_f i_{lq} \tag{6-5}$$

$$v_{inv,q}^{*} = K_{pi}(i_{lq}^{*} - i_{lq}) + K_{ii}\int (i_{lq}^{*} - i_{lq})dt + \omega_{nl}L_f i_{ld} \tag{6-6}$$

where i_{lq} and i_{ld} are the filter currents, all in the dq reference-frame, $v_{inv,d}$ and $v_{inv,q}$ are the inverter output voltages and superscript "*" denotes a reference value.

The current and voltage dynamics for the output LC filter and the point of common coupling (PCC) are given by (6-7) through (6-12), where R_f, L_f, C_f are the per-phase resistance, inductance, and capacitance of the LC filter, respectively, R_c and L_c are the per-phase resistance and inductance of the coupling transformer, respectively, and v_{pccd} and v_{pccq} are the DG bus voltages.

$$\frac{di_{ld}}{dt} = \frac{-R_f}{L_f} i_{ld} + \omega i_{lq} + \frac{1}{L_f}\left(v_{inv,d} - v_{od}\right) \tag{6-7}$$

$$\frac{di_{lq}}{dt} = \frac{-R_f}{L_f} i_{lq} - \omega i_{ld} + \frac{1}{L_f}\left(v_{inv,q} - v_{oq}\right) \tag{6-8}$$

$$\frac{dv_{od}}{dt} = \omega v_{oq} + \frac{1}{C_f}\left(i_{ld} - i_{od}\right) \tag{6-9}$$

$$\frac{dv_{oq}}{dt} = -\omega v_{od} + \frac{1}{C_f}\left(i_{lq} - i_{oq}\right) \tag{6-10}$$

$$\frac{di_{od}}{dt} = \frac{-R_c}{L_c} i_{od} + \omega i_{oq} + \frac{1}{L_c}\left(v_{od} - v_{pccd}\right) \tag{6-11}$$

$$\frac{di_{oq}}{dt} = \frac{-R_c}{L_c} i_{oq} - \omega i_{od} + \frac{1}{L_c}\left(v_{oq} - v_{pccq}\right) \tag{6-12}$$

Since there is more than one DG unit in a MG system, prior to constructing the complete MG state-space model with IM load, all the states should first be transformed to a common reference frame where studying a multi-DG system is possible. This is achieved by arbitrarily assuming the first DG reference frame as the common frame (DQ-frame) to which all the other states should be transferred via the transformation matrix of (6-13), where δ_i is the angle between reference frame of the i-th inverter and the common reference frame (i.e. DG1), and $x_{i,dq}$ and $x_{i,DQ}$ are representing the state values in the aforementioned frames respectively.

$$x_{i,DQ} = \begin{bmatrix} \cos(\delta_i) & -\sin(\delta_i) \\ \sin(\delta_i) & \cos(\delta_i) \end{bmatrix} x_{i,dq} \tag{6-13}$$

A complete state-space model of the DG interface can be obtained by linearizing the differential equations of (6-1) through (6-12) at the system operating point. The complete state-space model of the i-th DG unit interface transferred to the common reference frame using the transformation technique provided in (6-13), can therefore be presented in the form of (6-14) and (6-15).

$$\Delta \dot{x}_{DGi}(t) = A_{DGi}\Delta x_{DGi}(t) + B_{DGi}\Delta v_{pccDQi}(t) + B_{com}\Delta\omega_{com} \tag{6-14}$$

$$\Delta i_{oDQi} = C_{DGi}\Delta x_{DGi}(t) \tag{6-15}$$

$$\Delta x_{DGi} = \begin{bmatrix} \Delta\delta_i & \Delta P_i & \Delta Q_i & \Delta\lambda_{Vdqi} & \Delta\lambda_{Cdqi} & \Delta i_{ldqi} & \Delta v_{odqi} & \Delta i_{odqi} \end{bmatrix}^T \tag{6-16}$$

The state vector is defined as (6-16). Note that $\Delta\lambda_{Vdqi}$ and $\Delta\lambda_{Cdqi}$ in (6-16), are the integrator states of the voltage and current controllers, respectively. The inverter input and output variables are the small-signal bus voltage, Δv_{pccDQi}, and small-signal current, Δi_{oDQ}, which are both expressed in the common reference frame. By linearizing (6-13) and converting the input/output variables from the individual reference frame to the common reference frame, the state, input and output matrices can be derived as (6-17). Further modeling details can be found in [18, 19].

$$
A_{DGi}=\begin{bmatrix}
0 & -m_i & 0 & 0 & 0 & 0 & 0 & 0 & 0 & 0 & 0 & 0 & 0\\
0 & -\omega_c & 0 & 0 & 0 & 0 & 0 & 0 & 0 & 1.5\omega_c I_{odi} & 1.5\omega_c I_{oqi} & 1.5\omega_c V_{odi} & 1.5\omega_c V_{oqi}\\
0 & 0 & -\omega_c & 0 & 0 & 0 & 0 & 0 & 0 & 1.5\omega_c I_{oqi} & -1.5\omega_c I_{odi} & -1.5\omega_c V_{oqi} & 1.5\omega_c V_{odi}\\
0 & 0 & -n_i & 0 & 0 & 0 & 0 & 0 & 0 & -1 & 0 & 0 & 0\\
0 & 0 & 0 & 0 & 0 & 0 & 0 & 0 & 0 & 0 & -1 & 0 & 0\\
0 & 0 & -n_i K_{pv} & K_{iv} & 0 & 0 & 0 & -1 & 0 & -K_{pv} & -\omega_{ni} C_f & H & 0\\
0 & 0 & 0 & 0 & K_{iv} & 0 & 0 & 0 & -1 & \omega_{ni} C_f & -K_{pv} & 0 & H\\
0 & -m_i I_{lqi} & \frac{-n_i K_{pi} K_{pv}}{L_f} & \frac{K_{iv} K_{pi}}{L_f} & 0 & \frac{K_{ii}}{L_f} & 0 & \frac{-K_{pi}-R_f}{L_f} & \omega_o-\omega_{nl} & \frac{-1-K_{pi} K_{pv}}{L_f} & \frac{-\omega_{ni} C_f K_{pi}}{L_f} & \frac{K_{pi} H}{L_f} & 0\\
0 & m_i I_{ldi} & 0 & 0 & \frac{K_{iv} K_{pi}}{L_f} & 0 & \frac{K_{ii}}{L_f} & \omega_o-\omega_{nl} & \frac{-K_{pi}-R_f}{L_f} & \frac{\omega_{ni} C_f K_{pi}}{L_f} & \frac{-1-K_{pi} K_{pv}}{L_f} & 0 & \frac{K_{pi} H}{L_f}\\
0 & -m_i V_{oqi} & 0 & 0 & 0 & 0 & 0 & \frac{1}{C_f} & 0 & 0 & \omega_o & \frac{-1}{C_f} & 0\\
0 & m_i V_{odi} & 0 & 0 & 0 & 0 & 0 & 0 & \frac{1}{C_f} & -\omega_o & 0 & 0 & \frac{-1}{C_f}\\
\frac{1}{L_c'}\begin{pmatrix} V_{bDi}\sin\delta_i \\ -V_{bQi}\cos\delta_i \end{pmatrix} & -m_i I_{oqi} & 0 & 0 & 0 & 0 & 0 & 0 & 0 & \frac{1}{L_c'} & 0 & \frac{-R_c'}{L_c'} & \omega_o\\
\frac{1}{L_c'}\begin{pmatrix} V_{bDi}\cos\delta_i \\ +V_{bQi}\sin\delta_i \end{pmatrix} & m_i I_{odi} & 0 & 0 & 0 & 0 & 0 & 0 & 0 & 0 & \frac{1}{L_c'} & -\omega_o & \frac{-R_c'}{L_c'}
\end{bmatrix}
$$

$$
B_{DGi}=\begin{bmatrix}
0 & \dots & 0 & \frac{-1}{L_c}\cos\delta_i & \frac{-1}{L_c}\sin\delta_i\\
0 & \dots & 0 & \frac{1}{L_c}\sin\delta_i & \frac{-1}{L_c}\cos\delta_i
\end{bmatrix}^T_{13\times 2},\quad B_{com}=[-1 \quad 0 \quad \dots \quad 0]^T_{13\times 1}
\tag{6-17}
$$

$$
C_{DGi}=\begin{bmatrix}
-I_{odi}\sin\delta_i - I_{oqi}\cos\delta_i & 0 & \dots & 0 & \cos\delta_i & -\sin\delta\\
I_{odi}\cos\delta_i - I_{oqi}\sin\delta_i & 0 & \dots & 0 & \sin\delta_i & \cos\delta_i
\end{bmatrix}_{2\times 13}
$$

6.1.2 State-Space Model of the IM

The relation between the IM's stator and rotor voltages and currents can be expressed in the common synchronous rotating reference-frame by (6-18) through (6-21). Note that since fluxes and currents are not independent variables, the IM equations can be written using either of them as state-variables. However, using the voltage equations with currents as state-variables is more suitable for the integration of IM state equations into the complete MG state-space model. Therefore, the relation between the stator and rotor voltage and currents can be given in the common DQ reference-frame [63]

$$
v_{Qs}=r_s i_{Qs}+L_{ss}\frac{di_{Qs}}{dt}+\omega L_{ss} i_{Ds}+L_m\frac{di_{Qr}}{dt}+\omega L_m i_{Dr} \tag{6-18}
$$

$$
v_{Ds}=-\omega L_{ss} i_{Qs}+r_s i_{Ds}+L_{ss}\frac{di_{Ds}}{dt}-\omega L_m i_{Qr}+L_m\frac{di_{Dr}}{dt} \tag{6-19}
$$

$$
v_{Qr}=L_m\frac{di_{Qs}}{dt}+s\omega L_m i_{Ds}+r_r i_{Qr}+L_{rr}\frac{di_{Qr}}{dt}+s\omega L_{rr} i_{Dr} \tag{6-20}
$$

$$v_{Dr} = -s\omega L_m i_{Qs} + L_m \frac{di_{Ds}}{dt} - s\omega L_{rr} i_{Qr} + r_r i_{Dr} + L_{rr} \frac{di_{Dr}}{dt} \tag{6-21}$$

Where L_{ss} and r_s are the stator inductance and resistance, whereas L_{rr} and r_r are the corresponding rotor parameters, L_m, s, and ω are the linkage inductance, rotor slip and the stator supply angular frequency, respectively.

The electromagnetic torque can be expressed in terms of stator and rotor currents as in (6-22) and the relation between torque and the mechanical speed is shown in terms of the motor slip and stator angular speed in (6-23).

$$T_e = \frac{3}{2}.\frac{\rho}{2} L_m (i_{Qs} i_{Dr} - i_{Ds} i_{Qr}) \tag{6-22}$$

$$T_e - T_L = J \frac{d}{dt}((1-s)\omega) \tag{6-23}$$

In (6-22),(6-23), ρ, J and T_L are the number of poles, combined motor and load inertia and the load torque, respectively. The machine parameters are given in Appendix A.

Before linearizing the machine equations, it should be noted that in a MG system, the stator supply frequency ω is governed by the droop equations, and therefore, its small-signal deviations should be accounted for in order to drive a complete and integrated small-signal model. Therefore, the linear differential equations of the induction machine can be presented as (6-24) where the associated matrices are defined in (6-25).

$$\overbrace{\begin{bmatrix} \Delta v_{Qs} \\ \Delta v_{Ds} \\ \Delta v_{Qr} \\ \Delta v_{Dr} \\ \Delta T_L \end{bmatrix}} = F \overbrace{\begin{bmatrix} \Delta i_{Qs} \\ \Delta i_{Ds} \\ \Delta i_{Qr} \\ \Delta i_{Dr} \\ \Delta s \end{bmatrix}} + E \frac{d}{dt} \overbrace{\begin{bmatrix} \Delta i_{Qs} \\ \Delta i_{Ds} \\ \Delta i_{Qr} \\ \Delta i_{Dr} \\ \Delta s \end{bmatrix}} + D_1 \Delta\omega + D_2 \frac{d(\Delta\omega)}{dt} \tag{6-24}$$

Equation (6-24) can be rearranged as in (6-26), where $\Delta\omega$ and $\Delta\dot{\omega}$ can be expressed in terms of MG states.

$$F=\begin{bmatrix} r_s & \omega_0 L_{ss} & 0 & \omega_0 L_m & 0 \\ -\omega_0 L_{ss} & r_s & -\omega_0 L_m & 0 & 0 \\ 0 & s_0\omega_0 L_m & r_r & s_0\omega_0 L_{rr} & -\omega_0 L_m i_{Ds0}-\omega_0 L_{rr} i_{Dr0} \\ -s_0\omega_0 L_m & 0 & -s_0\omega_0 L_{rr} & r_r & \omega_0 L_m i_{Qs0}+\omega_0 L_{rr} i_{Qr0} \\ L_m i_{Dr0} & -L_m i_{Qr0} & -L_m i_{Ds0} & L_m i_{Qs0} & 0 \end{bmatrix}, D_1=\begin{bmatrix} L_{ss} i_{Ds0}+L_m i_{Dr0} \\ -L_{ss} i_{Qs0}-L_m i_{Qr0} \\ s_0 L_m i_{Ds0}+s_0 L_{rr} i_{Dr0} \\ -s_0 L_m i_{Qs0}-s_0 L_{rr} i_{Qr0} \\ 0 \end{bmatrix}$$

$$E=\begin{bmatrix} L_{ss} & 0 & L_m & 0 & 0 \\ 0 & L_{ss} & 0 & L_m & 0 \\ L_m & 0 & L_{rr} & 0 & 0 \\ 0 & L_m & 0 & L_{rr} & 0 \\ 0 & 0 & 0 & 0 & 4J\omega_0/3\rho \end{bmatrix}, D_1=\begin{bmatrix} 0 \\ 0 \\ 0 \\ 0 \\ \dfrac{-4J(1-s_0)}{3\rho} \end{bmatrix} \tag{6-25}$$

$$\Delta\dot{X}_{IM}=(\underbrace{\qquad}_{A_{IM}} \quad {}_{1}+\underbrace{E^{-1}}_{B_{1IM}}\Delta U_{IM}+(\underbrace{\qquad}_{B_{2IM}} \quad \underbrace{\qquad}_{B_{3IM}}\dot{} \tag{6-26}$$

6.1.3 Complete MG State-Space Model

The MG network presented in Figure 6-1 consists of three DG units, line impedances and dynamic and static loads. In order to derive the complete system model where all three DG interfaces as well as the network dynamics are accounted for, the linearized state space model of (6-14)-(6-15) (developed for an individual DG) has been used as a building block along with the network and load dynamics. The network dynamics can be modeled in the form of (6-27) where the associated matrices are defined in (6-28).

$$\Delta\dot{X}_{NET}=A_{NET}\underbrace{\qquad}_{{}_{lineDQ}} \quad {}_{ET}\Delta v_{pccDQ}+B_{2NET}\Delta\omega \tag{6-27}$$

As can be seen in (6-14)-(6-15) and (6-27), the node voltages are considered as the inputs for both the DG interface and also the IM state-space equations. Therefore, in order to integrate the dynamic equations of the induction motor with those of the DG interface, the voltages at the point of common couplings should be well defined. This can be achieved by defining the voltage of the i-th PCC in terms of currents (6-29).

$$B_{1NET}=\begin{bmatrix} \frac{1}{L_{Line1}} & 0 & \frac{-1}{L_{Line1}} & 0 & 0 & 0 \\ 0 & \frac{1}{L_{Line1}} & 0 & \frac{-1}{L_{Line1}} & 0 & 0 \\ 0 & 0 & \frac{1}{L_{Line2}} & 0 & \frac{-1}{L_{Line2}} & 0 \\ 0 & 0 & 0 & \frac{1}{L_{Line2}} & 0 & \frac{-1}{L_{Line2}} \end{bmatrix}, \quad B_{2NET}=\begin{bmatrix} I_{line1Q} \\ -I_{line1D} \\ I_{line2Q} \\ -I_{line2D} \end{bmatrix} \tag{6-28}$$

$$[\Delta V_{PCC,DQ}]=R_N(M_{DG}[\Delta i_{oDQ}]+M_{IM}[\Delta i_{DQs}]+M_{NET}[\Delta i_{lineDQ}]) \tag{6-29}$$

In (6-29), R_N is a 6×6 diagonal matrix whose elements are the resistors defined by the resistive static loads connected to PCC1 and PCC3. Note that for PCC2, a sufficiently large virtual resistor is assumed to be connected in order to have the minimum influence on the analysis. M_{DG}, M_{IM}, and M_{NET} are introduced to map the connection point and lines onto the network nodes. In this case, since the i-th inverter is exactly connected to the i-th node, M_{DG} is a 6×6 unity matrix. M_{IM} is a 6×5 matrix relating the IM connection point into the network nodes. The matrix M_{NET} is filled with +1 or -1 based on whether the given line current is entering or leaving the node. Now, the complete MG small-signal model can be obtained in (6-30) where the associated matrices are defined in (6-31).

$$\begin{aligned} \Delta\dot{x}_{MG} &= A_{MG}\Delta x_{MG}(t) \\ \Delta x_{MG} &= [\Delta x_{DG1}, \Delta x_{DG2}, \Delta x_{DG3}, \Delta x_{NET}, \Delta x_{IM}]_{1\times 48} \end{aligned} \tag{6-30}$$

Note that since the rotor circuit of the induction motor is shorted, the matrix T is used in (6-31) to link only the stator voltage dynamics to the complete MG system.

$$A_{MG}=\begin{bmatrix}\left[A_{DG}+B_{DG}R_N M_{DG}C_{DG}\right]_{39\times 39} & \left[B_{DG}R_N M_{NET}\right]_{39\times 4} & B_{DG}R_N M_{IM}\\ \left[B_{1NET}R_N M_{DG}C_{DG}+B_{2NET}C_{\Delta\omega}\right]_{4\times 39} & \left[A_{NET}+B_{1NET}R_N M_{NET}\right]_{4\times 4} & B_{1NET}R_N M_{IM}\\ \left[B_{1IM}T_{5\times 6}\right]\left[R_N M_{DG}C_{DG}\right]+B_{2IM}C_{\Delta\omega}+B_{3IM}C_{\Delta\omega}A_{DG} & \left[B_{1IM}T_{5\times 6}\right]\left[R_N M_{NET}\right] & A_{IM}+\left[B_{1IM}T_{5\times 6}\right]\left[R_N M_{IM}\right]\end{bmatrix}$$

$$A_{DG}=\begin{bmatrix}A_{DG1}+B_{com}C_{\Delta\omega com} & 0 & 0\\ B_{com}C_{\Delta\omega com} & A_{DG2} & 0\\ B_{com}C_{\Delta\omega com} & 0 & A_{DG3}\end{bmatrix}_{39\times 39},\ B_{DG}=\begin{bmatrix}B_{DG1} & [0]_{13\times 2} & [0]_{13\times 2}\\ [0]_{13\times 2} & B_{DG2} & [0]_{13\times 2}\\ [0]_{13\times 2} & [0]_{13\times 2} & B_{DG3}\end{bmatrix},\ T=\begin{bmatrix}0&0&1&0&0&0\\0&0&0&1&0&0\\0&0&0&0&0&0\\0&0&0&0&0&0\\0&0&0&0&0&0\end{bmatrix},$$

$$C_{DG}=\begin{bmatrix}C_{DG1} & 0 & 0\\ 0 & C_{DG2} & 0\\ 0 & 0 & C_{DG3}\end{bmatrix},\ C_{\Delta\omega}=[0\quad -m_1\quad 0\quad \ldots\quad 0]_{1\times 39} \tag{6-31}$$

6.2 Stability Analysis

Figure 6-3 shows the complete eigenvalue spectrum of the under-study 3-DG MG setup with the parameters presented in Appendix A. Figure 6-3 indicates the frequency-scale separation of the system modes. As can be seen from Figure 6-3, the low frequency modes are the most dominant ones, and therefore the most crucial modes for system stability analysis. Participation factor analysis in [19] suggests that in the case of static loads, these low-frequency modes are mainly influenced by the states of the power sharing loop (i.e. average power and power angle) and the load dynamics do not participate in shaping of these dominant modes in a remarkable way. However, the introduction of motor-type loads in a MG system would introduce new pairs of less-damped eigenvalues that can effectively change the shaping of the system eigenvalues.

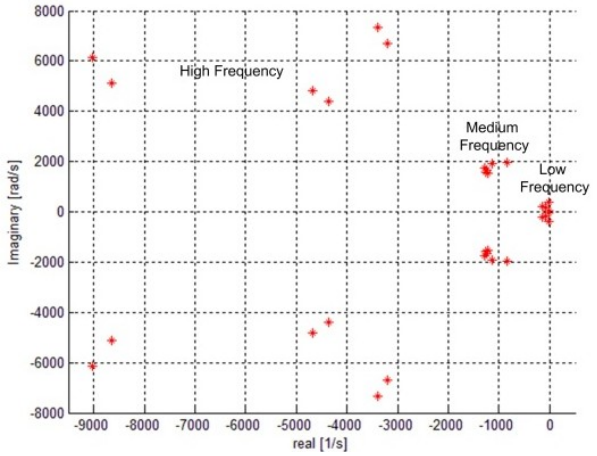

Figure 6-3: The overall eigenvalue spectrum of the MG system with IM load.

Table 6-1: System complex eigenvalues with and without IM and the state participation factors.

m=3e-6	Eigen Values (Dynamic Load)				Eigen Values (Static Load)	
	1,2	3,4	5,6	7,8	1,2	3,4
Real (1/s)	-12.9	-4.41	-11.98	-14.63	-11.78	-14
Im. (rad/s)	±397.67	±25.65	±40	±10.43	±38.33	±20.43
ΔP_1		0.059	0.041	0.074	0.344	0.235
ΔP_2			0.116		0.502	0.072
$\Delta \delta_2$			0.186		1	0.062
ΔP_3		0.275				0.554
$\Delta \delta_3$		0.417			0.0622	1
Δi_{Qs}	1	0.044	0.324	0.168		
Δi_{Ds}	0.835	0.96	0.962	0.963		
Δi_{Qr}	0.97	0.043	0.324	0.167		
Δi_{Dr}	0.802	1	1	1		
Δs			0.036	0.084		

Table 6-1 compares the most dominant oscillatory eigenvalues (with damping of less than -50 s^{-1}) for the study of a MW MG system with an IM load and when the IM load is replaced by an equivalent RL static load model. As can be seen, for a similar set of droop gains, the IM introduces two new less-damped pairs of eigenvalues (i.e. (1,2) and (3,4)).

The participation of each state variable to the listed oscillatory modes is calculated using participation factor analysis and the normalized participation factors greater than 0.01 are listed for both the dynamic and static load cases. Comparing the participation factors reveals that in presence of a motor-type load, the states associated with the IM have a higher impact on system stability as compared to those of the power sharing loop, and therefore, the system stability can be highly affected in presence of such a load.

Figure 6-4 shows the trace of the dominant oscillatory modes of Table 6-1 for the dynamic load case as the droop gain is increased. The almost fixed frequency of the eigenvalues 1, 2 (Eig(1,2)) suggests that they are mainly determined by the stator flux dynamics. Note that the stator flux is composed of both the stator and rotor current components, and therefore they highly participate in Eig(1,2). Moreover, as can be seen from Table 6-1, eigenvalues 1, 2 are not affected by the power sharing dynamics. This agrees with the trace of the modes shown in Figure 6-4 (a) where increasing the droop gains does not affect Eig(1,2). This pair of modes can therefore be ignored for the droop-gain marginal stability analysis as they are almost unaffected by the power control loop parameters.

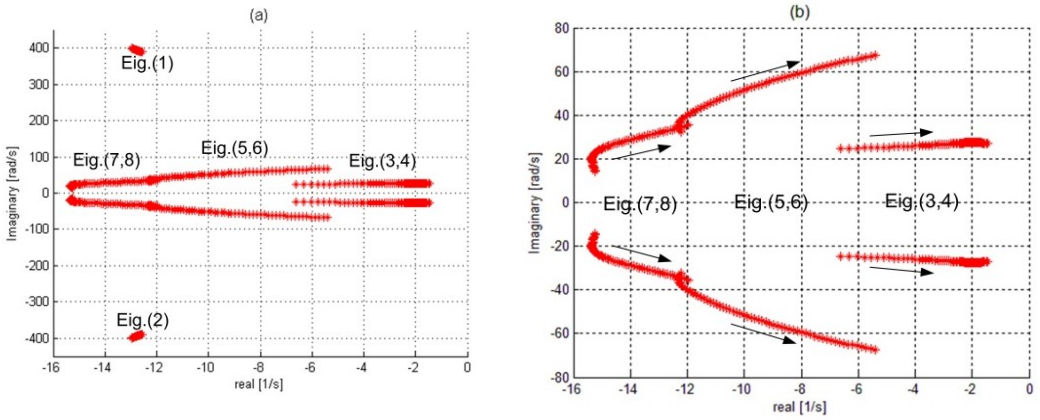

Figure 6-4: (a) Trace of the dominant oscillatory modes when m is increased from 2e-6 to 8e-6 rad/s/W. (b) Magnified trace of eigenvalues (3,4), (5,6), and (7,8).

However, the trace of the rest of eigenvalues in Figure 6-4 (b) suggests that even for lower droop gains, Eig(3,4) show much less damped behavior than the other two pairs yielding a compromised system stability performance even for lower droop gains. It should be noted that in a MG with static loads, low droop gain values contribute to higher stability margins at the cost of inaccurate active power sharing performance. However, the present study indicates that the IM load dynamics induces sensitive modes that can destabilize the MG system even under conservative static droop gains. Moreover, studying the participation factors obtained in Table 6-1, suggests that all the dominant eigenvalue pairs shown in Figure 6-4 (b) are very sensitive to the stator and rotor current D-components. Ignoring the small rotor current components as compared to the stator currents, this means that the system dominant modes are mainly affected by the active power component drawn by the motor. This finding is in line with the well-known fact that controlling the stator current is an effective way to reshape the open-loop IM dynamics, which is the case in IM drive systems [109]. However, in MG applications, the motor currents are not available for stabilization. However, the motor power is shared among remote DG units, which can be used to actively dampen the motor oscillatory performance via remote DG units as proposed in this chapter.

Figure 6-5 compares the trace of the most dominant oscillatory modes for the MG setup with the dynamic load and with its equivalent-power static RL load model, respectively. It can be inferred from Figure 6-5 that the introduction of Eig (3,4), caused by addition of the motor-type load, introduces less-damped eigenvalues yielding a much more oscillatory system response as compared to the static load case. In fact, Eig (3,4)

can be regarded as the source of the added oscillatory response to the system, and therefore, should be considered in stability studies.

Figure 6-6 (c) shows the dominant eigenvalues at different cut-off frequencies (0.8Hz, 1.5Hz, 3.1Hz, and 4.Hz) of the power filter. As can be seen from Figure 6-6 (c), reducing the cut-off frequency does not remove the oscillatory modes as it only reduces their oscillation frequency. Therefore, applying averaging filters with lower cut-off frequencies or even higher order filters will not mitigate the presence of undamped dominant modes as these modes are associated with the dynamics of the motor-type load as well as the power angle oscillations. Furthermore, the power loop bandwidth is mainly dictated by the power-filter and the droop gain. Therefore, there is a strong need to provide additional means to dampen low-frequency oscillations in MGs with IM loads.

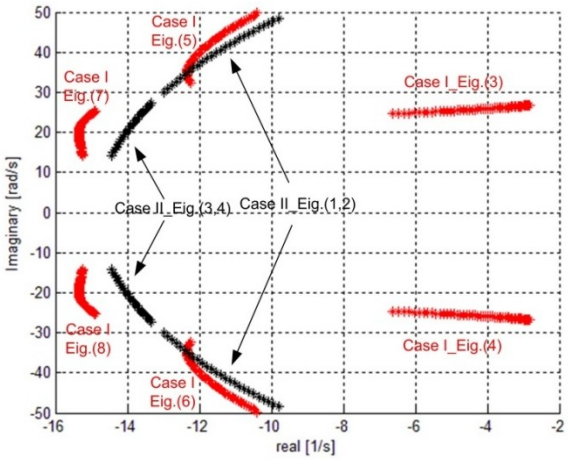

Figure 6-5: Trace of the oscillatory modes when m is increased from 2e-6 to 4.5e-6 rad/s/W with the dynamic load (Case I) with the equivalent static load (Case II).

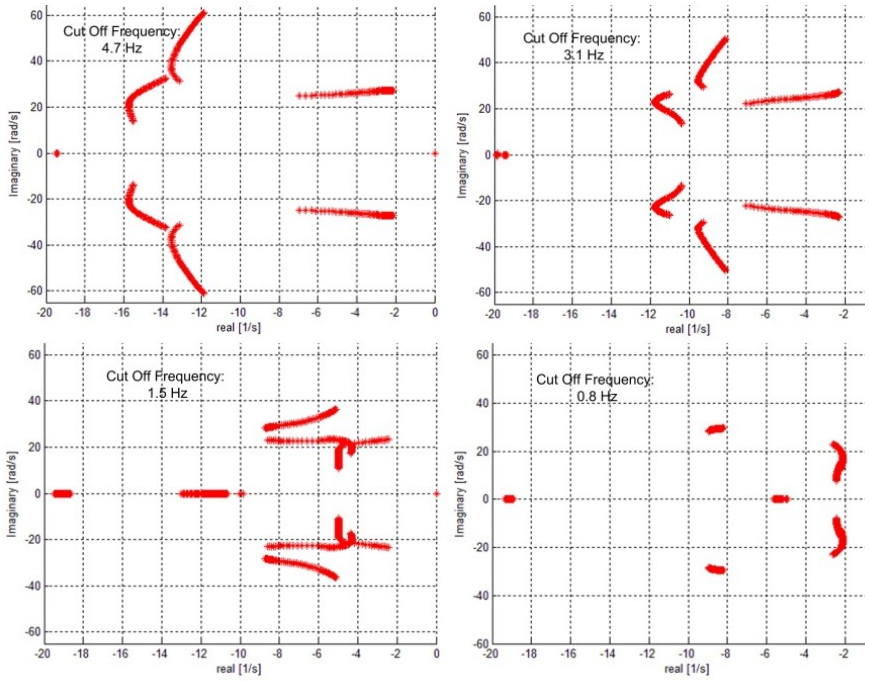

Figure 6-6: Traces of the dominant eigenvalues at different values of the average-power filter cut-off frequency and different droop gains.

6.3 Remote Stabilization Control

As indicated by the participation factor analysis, direct control of stator current remarkably contributes to the damping of these modes (e.g. as in IM drive systems). However, motor currents are not locally available for remote DG units. Further, only local measurements should be used by DG units to realize an autonomous control structure in MGs. However, it can be noted also that the motor active power contains the frequency modes of the electromechanical modes. Therefore, the proposed remote stabilization controller utilizes the average active power of each DG unit as the input signal that contains the frequency content of electromechanical oscillation. In this way, DG units share the stabilizing effort in a remote manner; i.e. by only using the local power signals.

Figure 6-7 shows the proposed 2-DOF active damping strategy which is based on remote compensation of the power swings by introducing a supplementary power angle $\delta_{comp}(s)$ to the original power angle of each converter generated by the active power sharing controller, and a supplementary voltage amplitude $V_{comp}(s)$ to the voltage amplitude generated by the reactive power sharing controller in each DG unit. It should be noted that using the active power in the voltage channel is inspired by the power-

system stabilizer design in conventional synchronous machines, where frequency oscillations are used to inject a damping voltage signal into the output voltage of a synchronous machine via an exciter voltage control [66].

In inverter-based units in MG operation, power oscillations (which are proportional to frequency oscillations) are used to inject a damping signal in the output voltage of the inverter, which has a fast response as compared to conventional synchronous machines. The supplementary signals are added to the power sharing controller as in (6-32),(6-33), where K_1, K_2 and τ are positive design constants.

$$\delta_o(s) = \frac{1}{s}\left(\omega_{nl} - mP(s)\right) - \underbrace{\frac{K_1}{\tau s + 1} P(s)}_{\delta_{comp}(s)} \tag{6-32}$$

$$V_o(s) = \left(V_{nl} - nQ(s)\right) - \underbrace{\frac{K_2 s}{\tau s + 1} P(s)}_{V_{comp}(s)} \tag{6-33}$$

The supplementary terms introduced in (6-32),(6-33) are added to compensate for the power swings caused by the addition of the dynamic load. In other words, the additional oscillations in voltage-angle and amplitude, which are reflected to the active power, will provide internal model control dynamics in each DG unit. According to the internal model control theory, the frequency modes of the disturbances to be eliminated should be included in the stable closed-loop system. Therefore, both the power-angle and the voltage magnitude oscillations can be suppressed by including the proposed feed-forward terms. Since power-angle oscillations cause reactive power and voltage oscillations due to active and reactive power coupling in MG with dynamic loads, the second compensator uses the active power transients to inject a voltage-amplitude damping signal. In addition, the input signal to both compensators is selected as the average power, which has the highest participation to the dominant oscillatory MG modes. It should be noted that the proposed compensators do not interfere with the steady-state power sharing performance and would only appear during the transients yielding less oscillatory responses, as the dc-gain of the power-angle and voltage-amplitude compensators to the frequency and voltage droops dynamics, respectively, are zero.

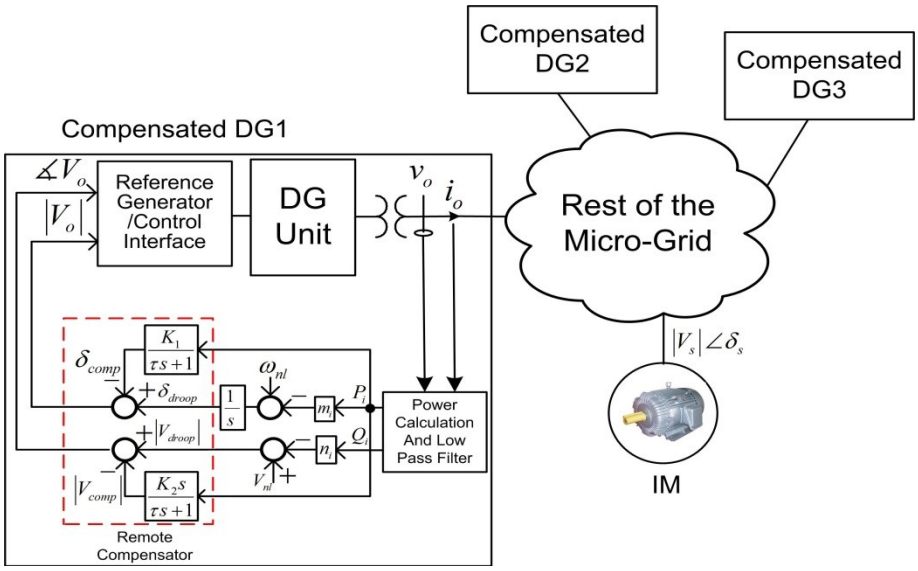

Figure 6-7: Proposed 2-DOF remote stabilization scheme.

The effectiveness of the proposed control scheme is evaluated through small-signal analysis by integrating the new dynamics of the power sharing controller with active damping into the complete MG state-space model. Figure 6-8 (a) shows that the dominant eigenvalues of the compensated system drift to the LHP yielding a less oscillatory performance. As can be seen, the proposed compensated MG remains stable for a larger range of droop gains. Note that higher droop gains provide more accurate power sharing; and therefore having a larger stability margin at high droop gains is very important in MG operation [61]. Further, the drift in the relative stability margins of the compensated MGs are remarkably smaller than the uncompensated system. This feature contributes to the robustness of the stability-based security margins of MGs.

Figure 6-8 (b) compares the system eigenvalue spectrum when the conventional *dP*/*dt*-frequency and *dQ*/*dt*-voltage compensators [110] are adopted. As can be seen, the conventional method is also able to improve the stability of the system; However, the conventional method introduces a set of less-damped high frequency modes compared to the proposed method which will limit the voltage stability as those high frequency oscillations are mainly associated with the voltage dynamics. This reveals the advantage of using the active power measurements instead of the conventional *dQ*/*dt* to drive the compensating voltage signal in high participation of IM loads. The proposed approach is in-line with the participation factor analysis presented in Table 1, where it was shown that the D-axis stator and rotor currents have a high impact over dominant modes.

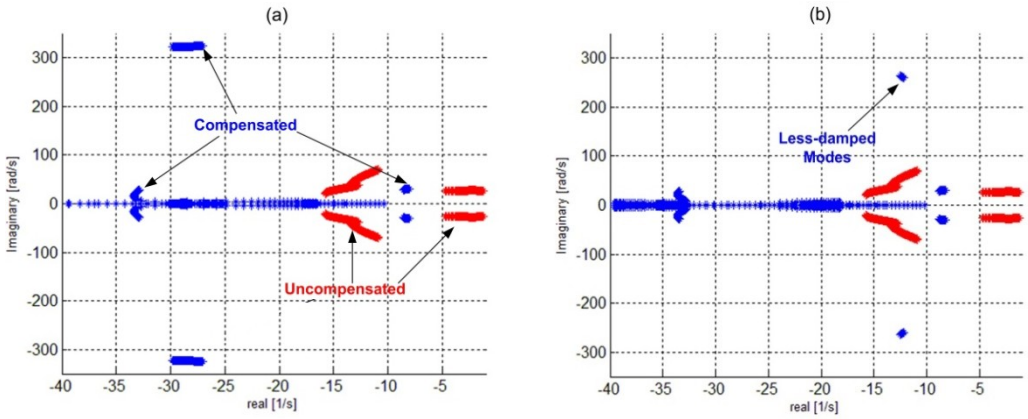

Figure 6-8: (a) Trace of the dominant modes with and without the proposed 2 DOF active compensation controller at a variable droop gain (b) with the conventional *dP*/*dt*-frequency and *dQ*/*dt*-voltage compensators reported in [110].

This implies that using the input active power of the induction motor to generate the compensatory signal is the most effective way to stabilize the system. The presence of the IM load introduces new dynamics to the system which distinguishes this case from the case with static-type loads and their associated conventional stabilization methods. In inverter-based units in MG operation, power oscillations are used to inject a damping signal into the output voltage of the inverter, which has a fast response as compared to conventional synchronous machines. Therefore, the proposed 2-DOF controller offers enhanced damping as compared to the conventional decoupled controller [110].

6.4 Sample Simulation Results

In order to evaluate the performance of the proposed control scheme under the operation of a typical MW MG system, shown in Figure 6-1, it is implemented in time-domain simulations in the Matlab/Simulink® environment. The complete control system of each DG unit is implemented as shown in Figure 6-2. The system and control parameters are given in Appendix A.

Figure 6-9 shows the DG active power responses for the IM and static load scenarios where the IM full-load-torque is applied at $t = 0.8$s from the no-load condition. Figure 6-9 shows the effect of the additional dynamics induced by the IM load as compared to the equivalent static load. As can be seen, the power response shows a much more oscillatory performance as compared to the case with the equivalent static load.

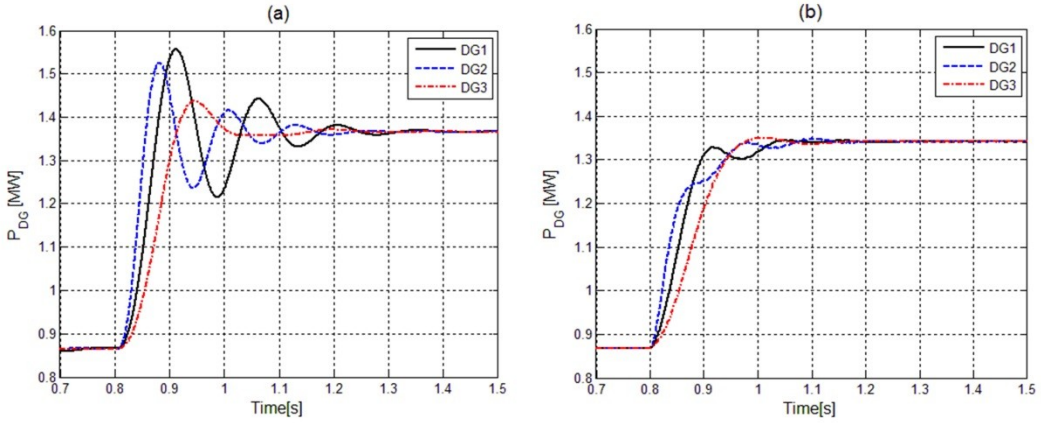

Figure 6-9: Active power response of DG units (a) when the IM is loaded with a1.5 MW mechanical load (b) when the equivalent static load is connected.

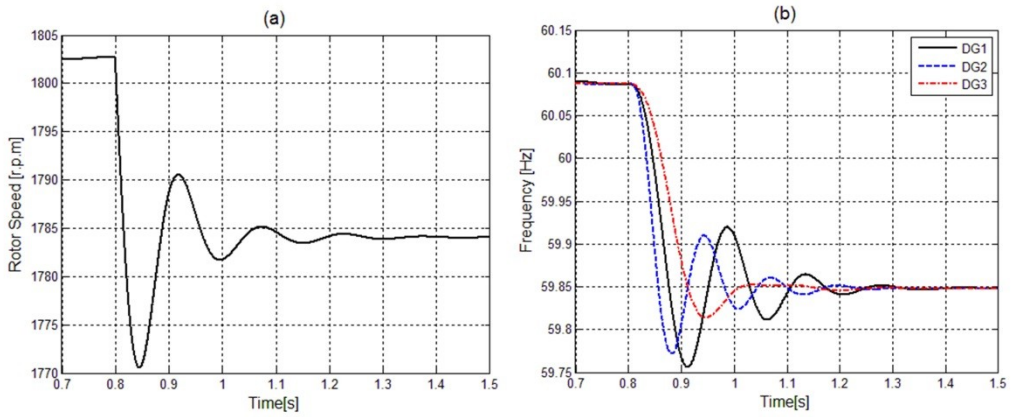

Figure 6-10: (a) Motor speed response (b) DG units output frequency when the IM is fully loaded.

Figure 6-10 (a), (b) show the corresponding motor speed and output frequencies of DG units. Speed oscillations are reflected in the input power of the IM which appears in the system frequency via droop control yielding an additional oscillatory performance as can be seen from Figure 6-10 (b).

The performance of the MG system under a step change of the droop gains is investigated as shown in Figure 6-11 where the droop gains are doubled at t = 0.8s. Figure 6-11 (a) depicts the motor speed, whereas Figure 6-11 (b) shows the stator voltage amplitude. As can be seen, the speed oscillations are reflected in the voltage response due to the active and reactive power coupling and the coupled nonlinear dynamics of the MG system with the IM load. The output voltage vector of the DG units oscillates in both angle and amplitude, and yields oscillatory active and reactive power responses as shown in Figure 6-11 (c) and (d), respectively.

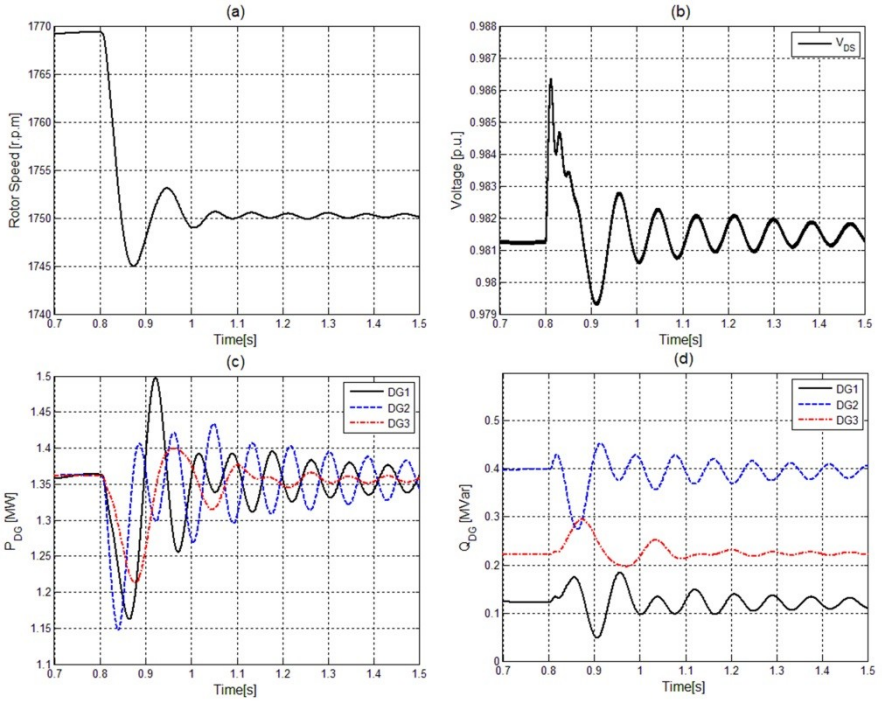

Figure 6-11: (a) The responses of the MG system under the dynamic load when the droop gain is increased from 3e-6rad/s/W to 6e-6rad/s/W (a) the rotor speed (b) the feeder voltage (c) the active power (d) the reactive power.

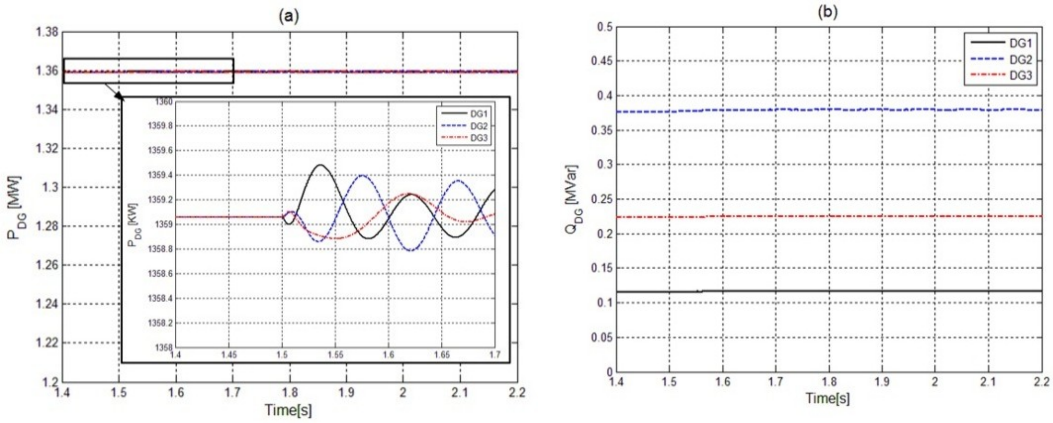

Figure 6-12: Power responses of the MG system with the equvalent static load when the droop gain is increased from 3e-6rad/s/W to 6e-6 at t=1.5s (a) the active power (b) the reactive power.

Figure 6-12 shows the active and reactive power responses for the equivalent static load case. As can be seen, the applied change in the droop gain at t = 1.5s yields damped oscillations with a small-amplitude in the power responses due to the highly damped nature of the poles and the absence of electromechanical oscillations associated with the IM load (e.g. case II in Figure 6-5). Further, the static load doesn't contribute to additional coupling among the active and reactive power responses.

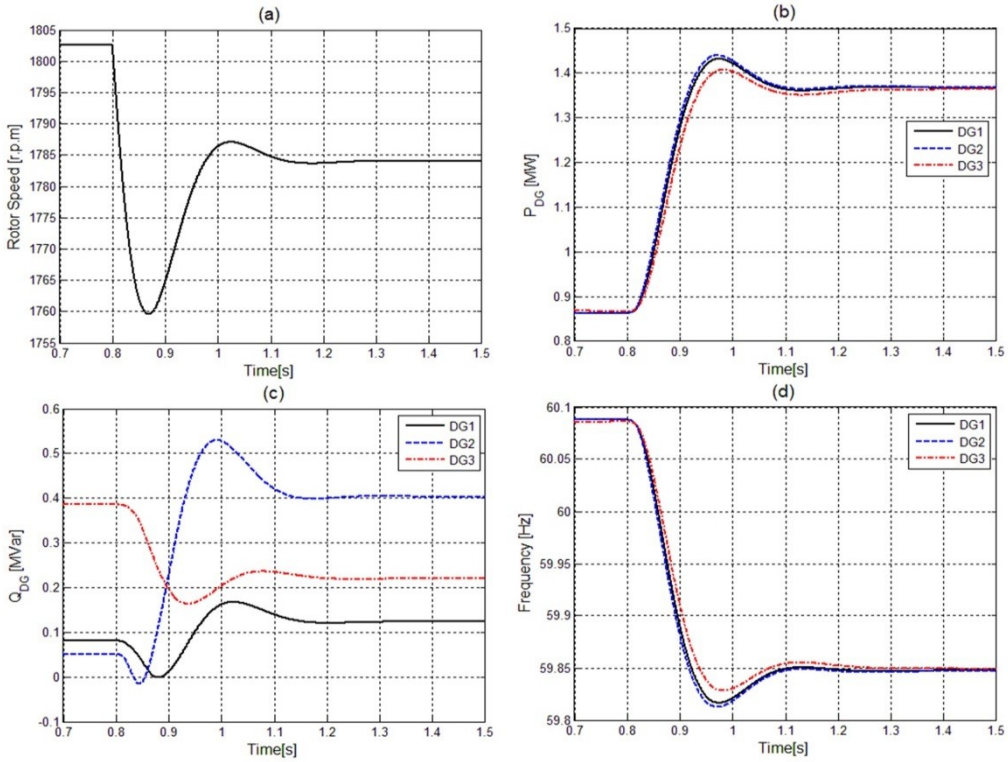

Figure 6-13: System response of the compensated MG when the IM is fully loaded (a) motor speed (b) active power (c) reactive power (d) DG units' output frequencies.

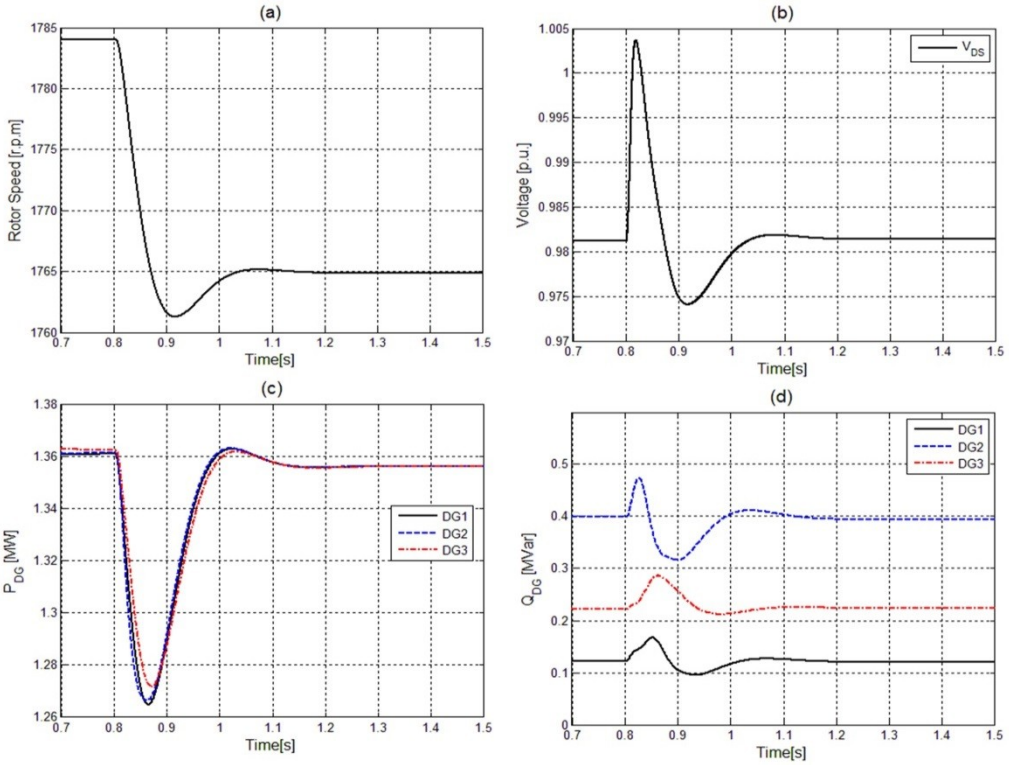

Figure 6-14: System response of the compensated MG when the droop gain is increased (a) the motor speed (b) DG voltage (d-axis component) (c) active power of DG units (d) reactive power of DG units.

The performance of the proposed remote stabilization controller is tested and the results are shown in Figure 6-13 and Figure 6-14. Comparing the responses of the compensated system at the full-load condition, shown in Figure 6-13, to the uncompensated responses (Figure 6-10 and Figure 6-11) proves the effectiveness of the proposed compensator in actively damping the additional oscillatory modes introduced by the induction motor. The proposed compensator is well capable of damping the rotor oscillations yielding damped frequency and power responses of all DG units. Further, the dynamic coupling among the active and reactive power response is remarkably attenuated. The damped response resembles that of an equivalent static load, which confirms the fact that if the rotor oscillatory modes are damped, the circuit-based steady-state behavior of the IM load dominates its dynamics

Figure 6-14 shows the performance of the compensated system when the droop gains are increased from 3e-6 rad/s/W to 6e-6 rad/s/W. Comparing Figure 6-14 to Figure 6-11 clearly reveals the remarkable stable performance of the compensated MG system in presence of the dynamic load. This suggests that the proposed active damping is well capable of actively cancelling the additional angle and voltage amplitude oscillations introduced at the DG terminals. It should be noted that the proposed active damping controller shows excellent performance in the presence of large power angle disturbances (e.g. step change of the full-load torque, and large step changes in the static droop gains). This feature shows the robustness of the proposed damping controller at different operating points and at small- and large-signal based disturbances.

6.5 Sample Experimental Results

As the rotor dynamics are lightly damped in large IM loads; therefore, rotor and power oscillations are yielded in a droop-controlled MG feeding the IM load even with small changes in the droop gains (or under load/network disturbances). However, the rotor oscillations can be excited even in small motors with a large input disturbance in the supply frequency (e.g. large variation in the droop coefficients) [63, 111]. In this way, rotor oscillations will be naturally yielded and will be reflected to the power sharing loop. This approach is used to construct a low-voltage setup that mimics the performance of large motors in terms of the presence of rotor oscillations. When the proposed controller is applied, rotor oscillations can be mitigated and accordingly, MG stability can be preserved under a wide-range of droop parameters.

(a) (b)

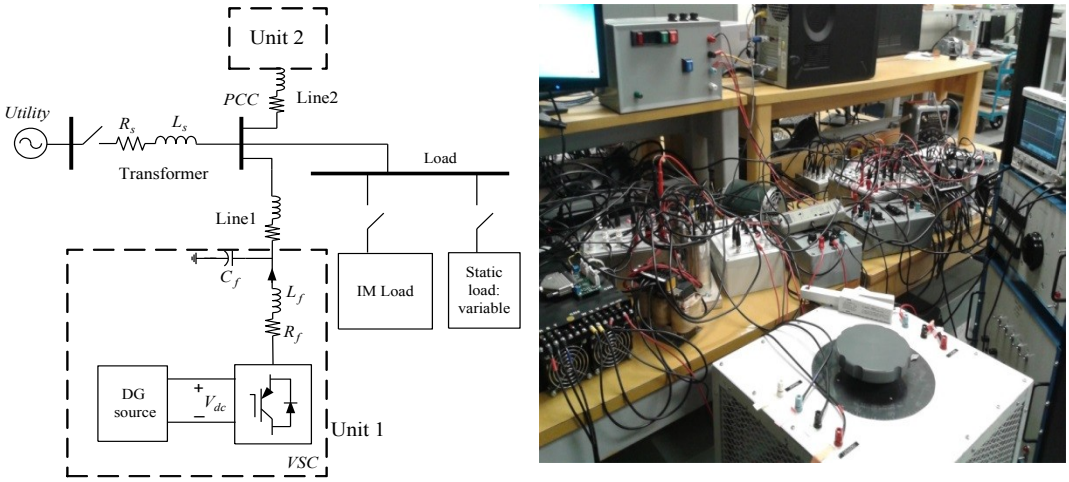

Figure 6-15: Laboratory setup. (a) Schematic diagram of the test system. (b) A view of the test system.

Therefore, to validate the presented analysis, a laboratory-scale 1.0 kVA, 208 V, 60 Hz, MG system, shown in Figure 6-15, is used. The utility gird is disconnected from the MG via an islanding breaker. A Semikron®-Semi-stack IGBT voltage-source converter is used to interface two DG units to the MG system. The dSpace1104 control system is used to implement the proposed control scheme in real-time. The PWM algorithm is implemented on the slave-processor (TMS320F240-DSP) of the dSPACE controller. A 3-phase, 200 V, 1780 rpm induction motor is connected to the MG to represent the dynamic load type whereas a variable resistive load box is used as a static load. Both loads form a composite load (i.e. dynamic and static load). The sampling/switching frequency is intentionally decreased to 2 kHz, in order to mimic the MV-range converters. The current and voltage sensors used are HASS 50-S and LEM V 25-400, respectively. A QD200 speed encoder with a resolution of 2048 lines and a quadrature output of 5V-RS422A-Line-Driver is used to measure the IM speed. The LC ac-side filter parameters are L_f= 0.6 mH and C_f= 50 μF. The lines parameters are 0.1 Ω and 0.5 mH. The MG is tested in the islanded mode of operation where the power sharing function is used.

In order to observe the low-frequency oscillations, the droop gain is increased by a factor of 100; thus, bringing the dominant modes closer to the RHP. Figure 6-16 shows the output current waveforms of both DG units and the common load voltage at the droop gain condition.

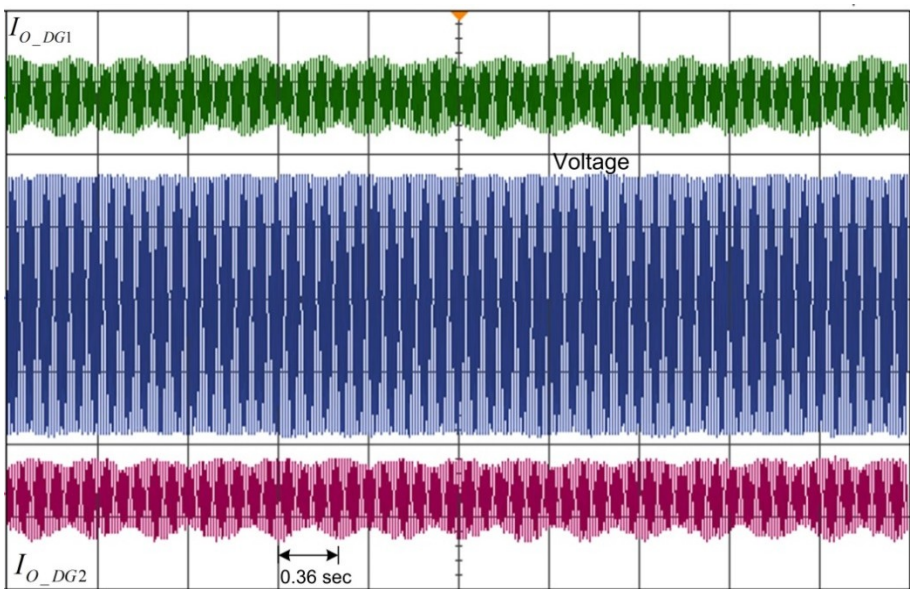

Figure 6-16: DG units' current and voltage responses under high droop gain (with 1 p.u. peak values).

As can be seen from Figure 6-16, exciting the system by increasing the droop gain results in low frequency (2-4 Hz) current oscillations, which is in line with the analytical findings from the eigenvalue analysis. Note that in Figure 6-16 the voltage waveform quality is maintained. This agrees with the previously presented participation factor analysis where the motor input current has the highest participation in the most dominant eigenvalues (i.e. Eigs.3,4). Therefore, the low-frequency oscillations mainly affect the DG current response as expected.

Figure 6-17 shows the associated active and reactive power responses of DG units. The presence of the low-frequency power oscillations leads to circulating power among parallel inverters, which reduce the system stability margins by overloading the DG units. Figure 6-18 shows the active and reactive power sharing errors with conventional droop control and under a step change in the load power at t = 6s. In order to show the effect of the motor load on the aforementioned low-frequency oscillations, the motor load was replaced by an equivalent static load while the same droop gain step change was applied. Figure 6-19 shows DG1 power response in this case. This result is in-line with the theoretical analysis (Figure 6-5), where dominant eigenvalues with a static load possess relatively high damping even under higher values of the droop gains.

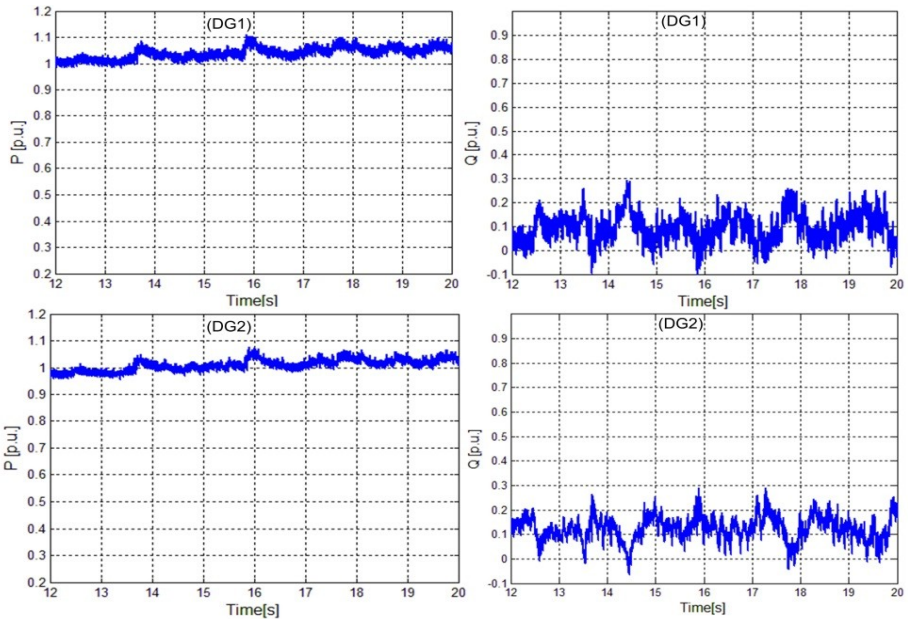

Figure 6-17: DG units active and reactive power responses with a high droop gain.

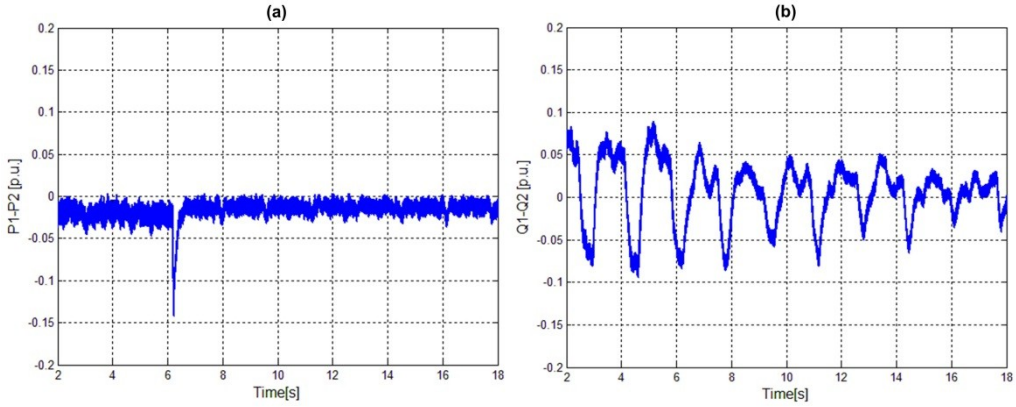

Figure 6-18: Active and reactive power sharing errors among DG units with a step load change.

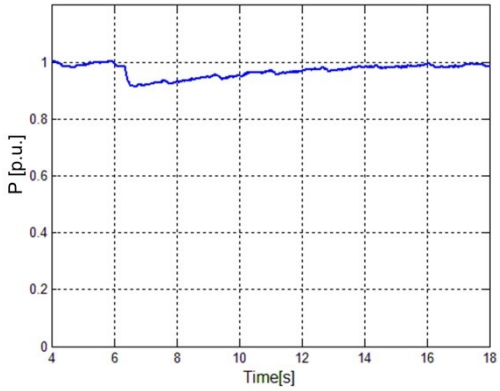

Figure 6-19: DG1 output power response to the droop gain step change when the dynamic load is replaced by the equivalent static-type.

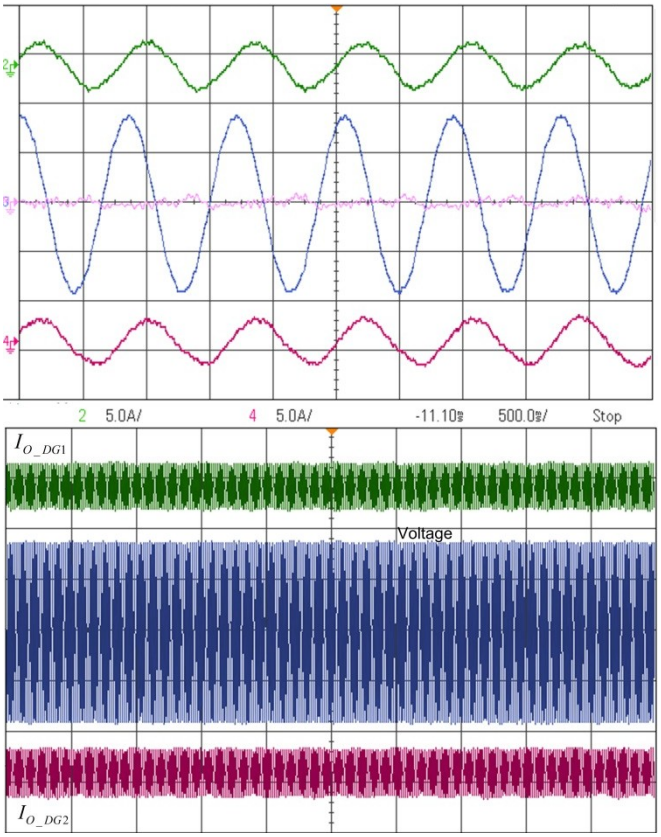

Figure 6-20: Compensated output current and voltage responses with a high droop gain (with 1 p.u. peak values).

The performance of the proposed compensator is also tested under the high droop gain case, and the results are reported in Figure 6-20 and Figure 6-21. The output currents of the DG units and the voltage at the common load are shown in Figure 6-20. The voltage is closely regulated, whereas accurate sharing is achieved with almost zero circulating current. On the longer time-scale, the low-frequency oscillations are mitigated by the proposed compensator.

The active and reactive power responses are shown in Figure 6-21. As can be seen, the use of the compensating angle and the voltage signals, as presented in Figure 6-21, can effectively dampen the low frequency oscillations yielding higher stability margins even with high values of droop gains.

Figure 6-22 shows the DG active and reactive power sharing errors with the proposed compensated droop control and under a step change in the load power at t = 2s. As compared to the conventional droop control performance shown in Figure 6-17, the proposed controller leads to a damped transient response and reduces the circulating currents associated with power oscillations.

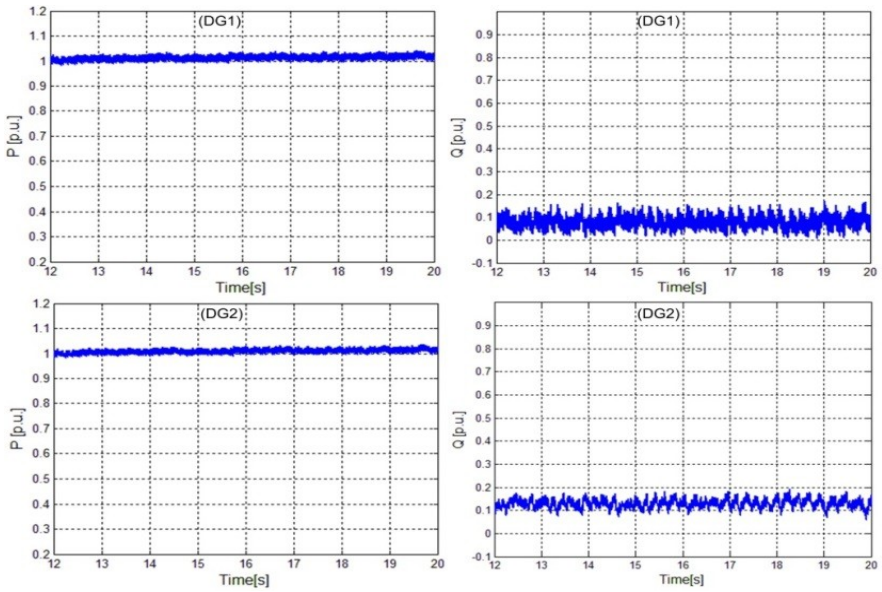

Figure 6-21: Compensated DG output active and reactive responses at high droop gain.

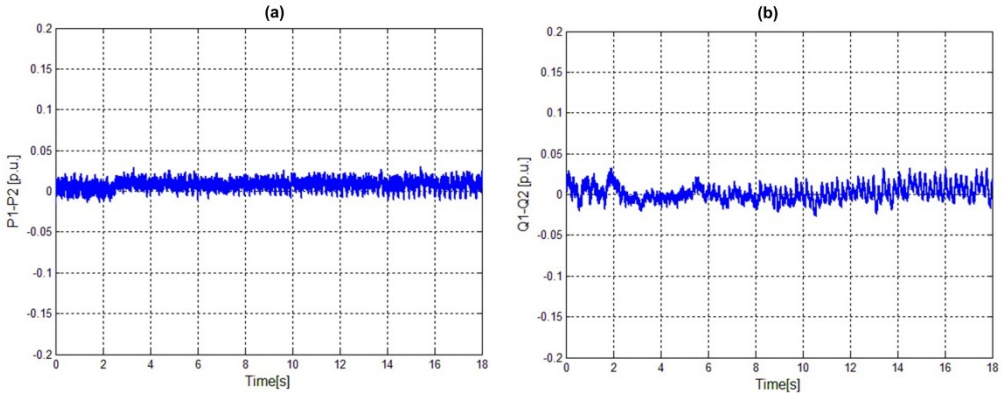

Figure 6-22: Compensated DG units active and reactive power sharing errors with a step load change.

6.6 Summary and Conclusions

This chapter addressed low-frequency oscillations in converter-based MGs with dynamic loads. A complete small-signal model of a typical MW MG with a typical dynamic load (IM load) has been developed. Small-signal stability analysis has revealed that the electromechanical rotor oscillations of a large IM is the source of lightly damped dynamics (low-frequency modes) in MW MG systems yielding an oscillatory frequency and voltage performance even under conservatively selected low droop gains. The participation factor analysis presented in the chapter shows that in the presence of large motor-type loads, the dominant MG eigenvalues are highly sensitive to the motor dynamics and droop gains. It is shown that the active power drawn by the induction

motor is highly participatory in shaping the lightly-damped system eigenvalues. This finding has been used to design a simple and effective two-DOF active damping strategy, which is based on remote compensation of the power swings. The proposed active damping controller introduces a transient supplementary power angle and voltage magnitude signals to effectively dampen MG frequency and voltage oscillations without affecting the steady-state power sharing characteristics. The proposed active damping controller shows robust performance under large-signal MG dynamics, such as a large variation in motor slip during the motor startup, full-load torque step disturbance, and large voltage dips associated with motor startup. Further, the proposed active damping controller facilitates the use of an extended range of static droop gains, which is essential to optimize the economic and technical aspects of MG operation during different operating conditions. A theoretical analysis, simulations and experimental results have been presented to validate the effectiveness of the proposed scheme.

Chapter 7

Networked-based Distributed Control of MG Systems [6]

The power stability of traditional droop-controlled MGs was significantly improved by the power angle feed-forward control method proposed in Chapter 3 and Chapter 6. However, the traditional droop control's inherent failure in providing accurate reactive power sharing, minimal frequency/voltage drift and its poor dynamic performance and subsequent instabilities under high droop gains has motivated the adoption of networked-based secondary and tertiary control schemes [7, 21, 82-85]. However, the proposed structures do not provide a framework to optimize power sharing among the DG units. Moreover the effect of communication delay in such networked-based systems has not been studied in [7, 21, 82-85]. A communication-based inverter control scheme has been proposed in [112] where the system stability is enhanced through supplementary control signals. The proposed method eliminates the inaccurate reactive power sharing problem when the communication is adopted. When the network is not available, the system can easily work in its autonomous droop-based mode. However, a clear procedure to design the controller coefficients is not provided. More importantly, two major drawbacks are noted in this structure: firstly, the frequency drops are not eliminated in the proposed method due to the presence of the frequency and voltage droop loops. Secondly, in the proposed power sharing method in [112], the supplementary frequency and voltage signals are not generated in a distributed manner; hence making system stability sensitive to the communication delays. Note that despite of the adoption of the decentralized traditional droop scheme, which enables continuing operating when the network is shut down, the supplementary signals are generated in a centralized manner which makes all the power measurements used as the necessary feedback signals subject to transmission delays; thus, compromised system stability is yielded even under relatively small delays.

Motivated by the aforementioned reasons, an enhanced networked-based control structure is needed not only to eliminate the frequency deviations, power sharing errors,

[6] A version of this chapter has been published: A. Kahrobaeian, and Y. A.-R. I. Mohamed, "Networked-based Hybrid Distributed Power sharing and Control for Islanded MG Systems", *IEEE Trans. on Power Electronics*, in press.

and stability concerns associated with conventional droop control in MGs, but also to yield 1) improved MG dynamic performance, 2) minimized active/reactive power sharing errors under unknown line impedances, and 3) high reliability and robustness against network failures or communication delays. This chapter proposes a new hybrid distributed networked-based power control scheme that addresses the aforementioned problems in a distributed manner. The new method consists of a set of distributed power regulators (DPRs) that are located at each DG unit to ensure perfect tracking of the optimized set points assigned by the centralized energy management unit. The average power measurements are transmitted to the energy management unit (EMU) to calculate the share of each unit of the total power demand based on a pre-defined optimization criteria. However, it should be noted that unlike [112], only the power set points sent by the EMU are subjected to any possible communication delays. In the proposed method, the distributed nature of the power regulators allows them to adopt the delay-free local power measurements as the required feedback signals. Therefore, the proposed structure provides great robustness against communication delays as it provides a hybrid solution between the optimization provided by the centralized EMU and the reliability that is made possible through the distributed power regulators that can simply convert to autonomous droop controllers in the absence of communication.

One of the main challenges in designing the power regulators is the multi-input multi-output nature of the networked-based MG systems which highly couples the power dynamics. Therefore a general and computationally-efficient state-space model of the proposed networked-controlled MG is developed. The developed model captures the most dominant modes of the system which makes it a very suitable model for stability- and delay-dependent analysis in MG systems with large number of generation units. The developed state-space model is later used in a pole placement technique in order to design the power controllers to ensure both stable operation and good tracking dynamics. Using the developed state-space model, a delay-dependent stability analysis is provided to verify the robustness of the proposed controller in presence of communication delay.

7.1 Hybrid Distributed Energy Management Control

Figure 7-1 shows the proposed networked-based hybrid distributed control scheme for a typical MG where n DG units are assumed to be connected to a network of passive elements and loads.

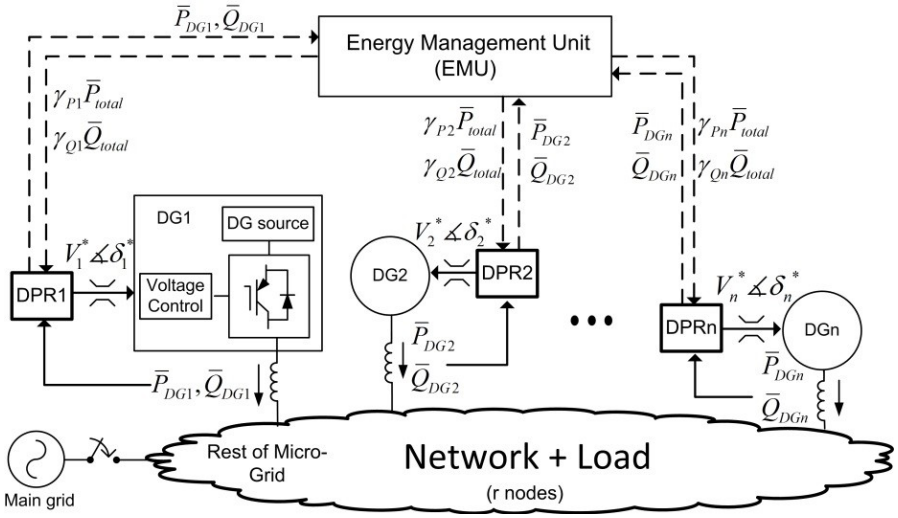

Figure 7-1: Networked-based hybrid distributed energy management control for MG systems.

In the scheme of Figure 7-1, the average active and reactive powers generated by each DG unit are transmitted to the centralized EMU in order to calculate the total power demand and then allocate the optimized power generation level to each DG unit (i.e. $\gamma_{Pi}\ \bar{P}_{\text{total}}$, $\gamma_{Qi}\ \bar{Q}_{total}$, where γ_{Pi} , γ_{Qi} show the desired share of the real and reactive power generated by the i^{th} DG unit respectively, and $\bar{P}_{total}$ and $\bar{Q}_{total}$ are the total MG average active and reactive powers, respectively). The desired active and reactive power set points are then sent to the local DPRs to be tracked by each unit.

As can be seen from Figure 7-1, DPR units decide the reference voltage amplitude and angle values that should be generated by each unit subsequently. Proportional-integral (PI) controllers, described by (7-1) and (7-2), are implemented in each DPR in order to achieve active and reactive power sharing objectives dictated by the EMU, where ω_{nl} and V_{nl} are the no-load frequency and voltage of each individual unit respectively, $\bar{P}_{DGi}$, $\bar{Q}_{DGi}$ are the average active and reactive power of the i^{th} DG unit, m_{Pi} , K_{Pi} are active power-sharing controller gains, n_{Qi} , K_{Qi} , are reactive power-sharing controller gains, s is the Laplace operator, $\delta_{DGi}^{\ *}$ is the command angle of DG unit i, and $V_{DGi}^{\ *}$ is the command voltage magnitude of the i^{th} DG unit. It should be noted that the summation of γ_{Pi} is 1 and similarly the summation of γ_{Qi} is 1. Note that the average active and reactive powers adopted in (7-1) and (7-2) are assumed to be extracted by means of the low-pass filter introduced earlier in (6-2).

$$\delta_{DGi}^{\ *}(t) = \omega_{nl}t + (m_{Pi}\int . + K_{Pi}) \times (\gamma_{Pi}.\bar{P}_{tot} - \bar{P}_{DGi}) \tag{7-1}$$

$$V_{DGi}^{*} = V_{nl} + (n_{Qi}\int . + K_{Qi}) \times (\gamma_{Qi}.\bar{Q}_{tot} - \bar{Q}_{DGi}) \quad (7\text{-}2)$$

It should be noted that the powers allocated by the EMU can be decided based on any cost- or loss- minimization algorithm [73-76]. The details of such algorithms are out of the scope of this chapter as this chapter focuses on the development and analysis of a networked-based framework to improve the flexibility of the existing control structures in order to implement such methods. Moreover, the frequency deviations are well known to be the major disadvantage of the traditional frequency-droop method and despite the accurate active power sharing achieved at the cost of a frequency drop, the desired reactive power sharing is not possible when only the traditional voltage-droop is adopted [18, 19, 78]. On the contrary, the proposed control structure enables the MG to achieve the desired power sharing while maintaining the steady-state frequency constant (i.e. 60 Hz). The voltage drops due to the reactive power sharing in this case can also be reduced significantly compared to the traditional droop algorithm. This is due to the fact that the integrator terms in the PI controllers in DPR units guarantee the tracking of both the assigned active and reactive power set points; therefore, the frequency and voltage amplitudes in (7-1) and (7-2) are maintained close to their nominal values.

One of the issues that should be considered in a networked control system is its reliability and whether it is able to operate when the network is not available. When no power reference is sent from the EMU, the distributed nature of the proposed scheme allows the system to switch to an enhanced communication-less droop control algorithm where m_{Pi} and K_{Qi} act as the frequency and voltage droop gains, respectively; hence, deciding the power sharing ratios. Note that once the control structure switches to the communication-less mode, n_{Qi} should be set to zero in order to ensure that each DG unit contributes to the reactive power generation and avoid the unnecessary integrating action in this mode. As can be seen from Figure 7-1, voltage limiters are adopted at the output stage of each power regulator to maintain voltage levels while the communicated data is delayed. When the communication network is no longer available (i.e. $\gamma_{Pi} = \gamma_{Qi} = 0$) and n_{Qi} is set to zero, (7-1) and (7-2) can be rewritten as in (7-3), (7-4) to derive the conventional droop control equations.

$$\delta_{DGi}^{*}(t) = \omega_{nl}t - (m_{Pi}\int . + K_{Pi}) \times \bar{P}_{DGi} \quad (7\text{-}3)$$

$$V_{DGi}^{*} = V_{nl} - K_{Qi} \times \bar{Q}_{DGi} \quad (7\text{-}4)$$

Note that in (7-3), the product of K_{Pi} and $\bar{P}_{DGi}$ introduces a supplementary power angle that can greatly improve the MG stability margin as reported Chapter 3.

7.2 Dynamic Model of the Networked-Based Power Sharing System

As suggested in Chapter 6, it is well-established that the MG system modes are separated into high-, medium- and low-frequency clusters where the participation analysis in [19, 78], confirms that the dominant low-frequency modes are mainly dictated by the power sharing dynamics. Therefore, since the emphasis of this chapter is on the dynamic performance modeling and stability analysis of the proposed power sharing controller, and in order to avoid the unnecessary higher order models, only the power dynamics are considered in the analytical study. The closed-loop cascaded voltage controller dynamics is hence simplified by a first order low pass filter presented in (7-5) where the closed-loop dynamics of the voltage-controlled DG unit is modeled by a low-pass filter with a time-constant "τ". Note that this assumption simply assumes that the output voltage angles (δ_{DGi}) and amplitudes (V_{DGi}) will follow their reference values (i.e. δ_{DGi}^{*} and V_{DGi}^{*}) within a bandwidth of τ which will be dictated by the inner voltage controller loop.

$$V_{DGi}\angle \qquad\qquad \angle \qquad (7\text{-}5)$$

In order to derive a computationally-efficient small-signal model that captures the dominant dynamics of a MG system with large number of DG units, e.g. similar to the system shown in Figure 7-1, the equivalent set of system admittances should first be derived. Figure 7-1 suggests that there are "n" generating nodes; therefore, it can be assumed that there are "r" remaining nodes which include nodes between the grid lines as well as the connecting points of the loads. Note that the grid admittance matrix is known and the loads can also be represented by their admittance parameters [113]. Therefore, (7-6) can be written to present the relation between the nodal currents and voltages, where the subscript n is used to denote DG nodes and r is used for the remaining nodes. The represented admittance parameters are complex values which represent the resistive and inductive nature of loads and line parameters. However, in order to model the proposed power sharing scheme of Figure 7-1, the interest is mainly on the generation

nodes; therefore, V_r can be eliminated from (7-6) based on the Kron reduction method [113] yielding (7-7).

$$\begin{bmatrix} I_n \\ \cdots \\ 0 \end{bmatrix} \begin{bmatrix} Y_{nn} & \vdots & & \bar{V}_n \\ \cdots & & \cdots & \cdots \\ Y_{nn} & \vdots & & V_r \end{bmatrix} \tag{7-6}$$

$$I_n = \underbrace{\qquad\qquad}_{Y_{eq}} \tag{7-7}$$

The parameters of the reduced matrix ,Y_{eq}, in (7-7) can be represented as the sum of conductance and susceptance (i.e: $Y_i = G_{ij} + j\, B_{ij}$). Equation (7-7) suggests that the network matrix can be reduced to include the DG nodes only. Note that the injected active and reactive powers by each unit can be expressed as (7-8) and (7-9).

$$p_{DGi} = 3\times[V_{DGi}{}^2 G_{ii} + \sum_{\substack{j=1 \\ j\neq i}}^{n} V_{DGi} V_{DGj} (B_{ij} \sin\delta_{ij} + G_{ij} \cos\delta_{ij})] \tag{7-8}$$

$$q_{DGi} = 3\times[-V_{DGi}{}^2 B_{ii} + \sum_{\substack{j=1 \\ j\neq i}}^{n} V_{DGi} V_{DGj} (G_{ij} \sin\delta_{ij} - B_{ij} \cos\delta_{ij})] \tag{7-9}$$

where δ_{ij} shows the relative angle between the i^{th} and j^{th} DG units (i.e. δ_i-δ_j) and G_{ii}, B_{ii} represent the diagonal elements of the reduced network matrix of Y_{eq} while the off diagonal elements are presented by G_{ij} and B_{ij}. Equations (7-8) and (7-9) can be linearized at the system operating points, δ_{0ij}, V_{DG0ij}, yielding (7-10),(7-11):

$$\Delta p_{DGi} = \sum_{j=1}^{n} (\frac{\partial p_{DGi}}{\partial V_{DGj}} \Delta V_{DGj}) + \sum_{\substack{j=1 \\ j\neq i}}^{n} (\frac{\partial p_{DGi}}{\partial \delta_{ij}} \Delta\delta_{ij}) \tag{7-10}$$

$$\Delta q_{DGi} = \sum_{j=1}^{n} (\frac{\partial q_{DGi}}{\partial V_{DGj}} \Delta V_{DGj}) + \sum_{\substack{j=1 \\ j\neq i}}^{n} (\frac{\partial q_{DGi}}{\partial \delta_{ij}} \Delta\delta_{ij}) \tag{7-11}$$

Equations (7-10) and (7-11) suggest that in order to derive the overall state-space model of the networked-based MG system presented in Figure 7-1, one should derive the linearized equations in (7-1)-(7-5) in a way that ΔV_{DGi} and $\Delta\delta_{ij}$ are included in the states. Moreover, the integrator states expressed in (7-12) and (7-13) are defined to fully account for the DPR controller dynamics:

$$\Delta\lambda_{Pi}(t) = \int (\gamma_{Pi} \cdot \sum_{i=1}^{n} \bar{P}_{DGi} - \Delta\bar{P}_i) \tag{7-12}$$

$$\Delta\lambda_{Qi}(t) = \int (\gamma_{Qi} \cdot \sum_{i=1}^{n} \bar{Q}_{DGi} - \Delta\bar{Q}_i) \tag{7-13}$$

Considering the voltage controller dynamics of (7-5) in (7-1) and (7-2) results in (7-14),(7-15).

$$\Delta\dot{\delta}_i = \frac{m_{Pi}}{\tau}(\Delta\lambda_{Pi}) + \frac{K_{Pi}}{\tau}(\gamma_{Pi} \cdot \sum_{i=1}^{n} \bar{P}_{DGi} - \Delta\bar{P}_i) - \frac{\Delta\delta_i}{\tau} \quad \text{for } i=1,...,n \tag{7-14}$$

$$\Delta\dot{V}_i = \frac{n_{Qi}}{\tau}(\Delta\lambda_{Pi}) + \frac{K_{Qi}}{\tau}(\gamma_{Qi} \cdot \sum_{i=1}^{n} \bar{Q}_{DGi} - \Delta\bar{Q}_i) - \frac{\Delta V_i}{\tau} \quad \text{for } i=1,...,n \tag{7-15}$$

As suggested in (7-10),(7-11), it is desired to express (7-14) in terms of the relative angle deviations. Moreover, it should be noted that the relative angle deviations are not independent from each other and can be expressed by means of (n-1) set of independent angles. Without the loss of generality, the angle of the n^{th} converter is assumed to be the reference angle in this chapter; hence, the relative angle between any two inverters can be illustrated as (7-16).

$$\Delta\delta_{ij} = \Delta\delta_{in} - \Delta\delta_{jn} \tag{7-16}$$

Therefore, (7-14) can be rewritten in terms of (n-1) independent relative angles between each DG unit with respect to the angle of the n^{th} inverter (i.e. $\Delta\delta_{in}$ for i =1,2,…,n-1). To achieve this objective, one has to subtract the associated i^{th} equation in (7-16) from the n^{th} one to derive (7-17).

$$\Delta\dot{\delta}_{in} = \frac{m_{Pi}}{\tau}(\Delta\lambda_{Pi} - \Delta\lambda_{Pn}) + \frac{K_{Pi}}{\tau}((\gamma_{Pi} - \gamma_{Pn}) \cdot \sum_{i=1}^{n} \bar{P}_{DGi} - (\Delta\bar{P}_i - \Delta\bar{P}_n)) - \frac{\Delta\delta_{in}}{\tau} \quad \text{for } i=1,...,n\text{-}1 \tag{7-17}$$

In order to complete the state-space model, $\Delta\bar{P}_i$, $\Delta\bar{Q}_i$ should also be included in the system states resulting in (7-18),(7-19).

$$\Delta\dot{\bar{P}}_{DGi} = -\omega_c \bar{P}_{DGi} + \omega_c (\sum_{j=1}^{n} (\frac{\partial p_{DGi}}{\partial V_{DGj}} \Delta V_{DGj}) + \sum_{\substack{j=1 \\ j\neq i}}^{n} (\frac{\partial p_{DGi}}{\partial \delta_{ij}} \Delta\delta_{ij})) \quad \text{for } i=1,...,n \tag{7-18}$$

$$\Delta\dot{\bar{Q}}_{DGi} = -\omega_c \bar{Q}_{DGi} + \omega_c \left(\sum_{j=1}^{n} \left(\frac{\partial q_{DGi}}{\partial V_{DGj}} \Delta V_{DGj}\right) + \sum_{\substack{j=1 \\ j\neq i}}^{n} \left(\frac{\partial q_{DGi}}{\partial \delta_{ij}} \Delta\delta_{ij}\right)\right) \quad \text{for } i=1,...,n \tag{7-19}$$

Once again, the relative angles in (7-18),(7-19) need to be expressed with respect to the n^{th} inverter which has been selected as the reference. Therefore, by substituting (7-16) in (7-18) and (7-19) the following expressions can be found:

$$\begin{aligned}\Delta\dot{\bar{P}}_{DGi} &= -\omega_c \bar{P}_{DGi} + \omega_c \sum_{j=1}^{n} \overbrace{\left[3\times\left(2\times V_{DGi}G_{ii} + \sum_{\substack{j=1 \\ j\neq i}}^{n} V_{DGj}\left(B_{ij}\sin\delta_{ij} + G_{ij}\cos\delta_{ij}\right)\right)\right]}^{} \Delta V_{DGj} \\ &+ \omega_c \sum_{\substack{j=1 \\ j\neq i}}^{n} \overbrace{\left[3\times\left(\sum_{\substack{j=1 \\ j\neq i}}^{n} V_{DGi}V_{DGj}\left(B_{ij}\cos\delta_{ij} - G_{ij}\sin\delta_{ij}\right)\right)\right]}^{\Delta\delta_{in}-\Delta\delta_{jn}} \Delta\delta_{ij} \quad \text{for } i=1,...,n\end{aligned} \tag{7-20}$$

$$\begin{aligned}\Delta\dot{\bar{Q}}_{DGi} &= -\omega_c \bar{Q}_{DGi} + \omega_c \sum_{j=1}^{n} \overbrace{\left[3\times\left(-2\times V_{DGi}B_{ii} + \sum_{\substack{j=1 \\ j\neq i}}^{n} V_{DGj}\left(G_{ij}\sin\delta_{ij} - B_{ij}\cos\delta_{ij}\right)\right)\right]}^{} \Delta V_{DGj} \\ &+ \omega_c \sum_{\substack{j=1 \\ j\neq i}}^{n-1} \overbrace{\left[3\times\left(\sum_{\substack{j=1 \\ j\neq i}}^{n} V_{DGi}V_{DGj}\left(G_{ij}\cos\delta_{ij} + B_{ij}\sin\delta_{ij}\right)\right)\right]}^{\Delta\delta_{in}-\Delta\delta_{jn}} \Delta\delta_{ij} \quad \text{for } i=1,...,n\end{aligned} \tag{7-21}$$

where the coefficients α_{Pij} , β_{Pij} , α_{Qij} , β_{Qij} depend on the linearized active and reactive power expressions shown in (7-18),(7-19). Considering the presented linearized equations, the small-signal state-space model of the proposed networked controlled MG system can be derived as (7-22) where Δx_{MG} consists of (6n-1) state variables including $\Delta\bar{P}_i, \Delta\bar{Q}_i, \Delta\lambda_{Pi}, \Delta\lambda_{Qi}, \Delta V_i$ (for i =1,2,..,n) as well as $\Delta\delta_{in}$ (for i =1,2,..,n-1).

$$\Delta\dot{x}_{MG}(t) = A_{MG}\Delta x_{MG}(t) \tag{7-22}$$

In order to conduct the delay-dependent stability analysis of the proposed controller and show its robustness in presence of communication delays, the small-signal model of (7-22) is expanded to consider a cumulative communication delay time ,τ_d, in the power set points sent by the EMU. Note that the communication delay affects the set points received by the DPRs (i.e. $\gamma_i P_{tot}$,$\gamma_i Q_{tot}$) as the power set points are determined by the

transmitted power measurement from each DG unit. However, it is important to note that the power feedback signals expressed in (7-1),(7-2) are measured locally in each distributed power regulator and, therefore, can be considered delay-free. Therefore, the delay-dependent MG dynamics can be given by (7-23) where A_{MG_Aut} and A_{MG_com} are listed in (7-24),(7-25).

$$\Delta \dot{x}_{MG}(t) = A_{MG\_Aut}\Delta x_{MG}(t) + A_{MG\_com}\Delta x_{MG}(t-\tau_d) \tag{7-23}$$

$$A_{aut} = \begin{bmatrix} -\omega_c(I)_{n\times n} & (0)_{n\times n} & (0)_{n\times n} & (0)_{n\times n} & \omega_c \times \begin{pmatrix} \alpha_{P11} & \cdots & \\ \vdots & \ddots & \vdots \\ \alpha_{Pn1} & \cdots & \end{pmatrix}_{n\times n} \times \begin{pmatrix} \sum_{j\neq 1}^{n}\beta_{P1j} & -\beta_{P12} & \cdots & -\beta_{P1(n-1)} \\ -\beta_{P21} & \sum_{j\neq 2}^{n}\beta_{P2j} & \cdots & -\beta_{P2(n-1)} \\ \vdots & \cdots & \cdots & \vdots \\ -\beta_{P(n)1} & \cdots & -\beta_{P(n)(n-2)} & -\beta_{P(n)(n-1)} \end{pmatrix}_{n\times n-1} \\ (0)_{n\times n} & -\omega_c(I)_{n\times n} & (0)_{n\times n} & (0)_{n\times n} & \omega_c \times \begin{pmatrix} \alpha_{Q11} & \cdots & \\ \vdots & \ddots & \vdots \\ \alpha_{Qn1} & \cdots & \end{pmatrix}_{n\times n} \times \begin{pmatrix} \sum_{j\neq 1}^{n}\beta_{Q1j} & -\beta_{Q12} & \cdots & -\beta_{Q1(n-1)} \\ -\beta_{Q21} & \sum_{j\neq 2}^{n}\beta_{Q2j} & \cdots & -\beta_{Q2(n-1)} \\ \vdots & \cdots & \cdots & \vdots \\ -\beta_{Q(n)1} & \cdots & -\beta_{Q(n)(n-2)} & -\beta_{Q(n)(n-1)} \end{pmatrix}_{n\times n-1} \\ -(I)_{n\times n} & (0)_{n\times n} & (0)_{n\times n} & (0)_{n\times n} & (0)_{n\times n} & (0)_{n\times n-1} \\ (0)_{n\times n} & -(I)_{n\times n} & (0)_{n\times n} & (0)_{n\times n} & (0)_{n\times n} & (0)_{n\times n-1} \\ (0)_{n\times n} & \begin{pmatrix} -\frac{K_{Q1}}{\tau} & \cdots & \\ \vdots & \ddots & \vdots \\ 0 & \cdots & \end{pmatrix}_{n\times n} & (0)_{n\times n} & (0)_{n\times n} & \begin{pmatrix} \ddots & \vdots & \\ \cdots & I & \cdots \\ & \vdots & \ddots \end{pmatrix}_{n\times n} & (0)_{n\times n-1} \\ \begin{pmatrix} -\frac{K_{P1}}{\tau} & 0 & \cdots & \\ 0 & -\frac{K_{P2}}{\tau} & \cdots & \\ \vdots & \cdots & \cdots & \vdots \\ 0 & \cdots & & \end{pmatrix}_{n-1\times n} & \begin{pmatrix} \ddots & \vdots & \\ \cdots & 0 & \cdots \\ & \vdots & \ddots \end{pmatrix}_{n-1\times n} & (0)_{n-1\times n} & (0)_{n-1\times n} & \frac{-1}{\tau}(I)_{n-1\times n-1} & \end{bmatrix}$$

(7-24)

$$A_{sh}=\begin{bmatrix} (O)_{n\times n} & (O)_{n\times n} & (O)_{n\times n} & (O)_{n\times n} & (O)_{n\times n} & (O)_{n\times n-1} \\ (O)_{n\times n} & (O)_{n\times n} & (O)_{n\times n} & (O)_{n\times n} & (O)_{n\times n} & (O)_{n\times n-1} \\ \begin{pmatrix}\gamma_{P1} & \cdots \\ \vdots & \ddots & \vdots \\ \gamma_{Pn} & \cdots\end{pmatrix}_{\times n} & (O)_{n\times n} & (O)_{n\times n} & (O)_{n\times n} & (O)_{n\times n} & (O)_{n\times n-1} \\ (O)_{n\times n} & \begin{pmatrix}\gamma_{Q1} & \cdots \\ \vdots & \ddots & \vdots \\ \gamma_{Qn} & \cdots\end{pmatrix}_{\times n} & (O)_{n\times n} & (O)_{n\times n} & (O)_{n\times n} & (O)_{n\times n-1} \\ (O)_{n\times n} & \begin{pmatrix}\frac{K_{Q1}}{\tau}(\gamma_{Q1}) & \cdots & \gamma_{Q1} \\ \vdots & \ddots & \vdots \\ \frac{K_{Qn}}{\tau}\gamma_{Qn} & \cdots & \gamma_{Qn})\end{pmatrix}_{n\times n} & (O)_{n\times n} & (O)_{n\times n} & (O)_{n\times n} & (O)_{n\times n-1} \\ \begin{pmatrix}\frac{K_{P1}}{\tau}(\gamma_{P1}-\gamma_{Pn}) & \cdots & \cdot(\gamma_{P1}-\gamma_{Pn}) \\ \vdots & \ddots & \vdots \\ \frac{K_{Pn-1}}{\tau}(\gamma_{Pn-1}-\gamma_{Pn}) & \cdots & \cdot(\gamma_{Pn-1}-\gamma_{Pn})\end{pmatrix}_{n-1\times n} & (O)_{n-1\times n} & (O)_{n-1\times n} & (O)_{n-1\times n} & (O)_{n-1\times n-1} \end{bmatrix}$$

(7-25)

7.3 Design and Stability Analysis of a 4-DG Networked-Controlled MG System

In order to have a better appreciation of the proposed scheme and design of the controllers, the proposed state-space model of (7-23) is developed for a 4-DG MG system with 4 loads shown in Figure 7-2. The MG system is studied in its islanded operational mode by assuming it is disconnected from the utility grid by having switch "SW" open.

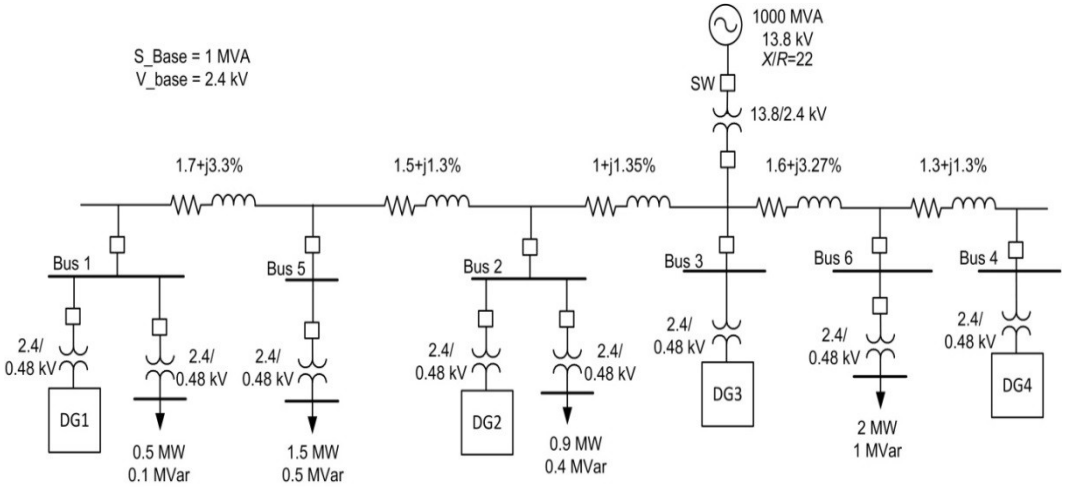

Figure 7-2: Networked controlled 4-DG sample MG system.

The proposed communication-based distributed control system of Figure 7-1 is implemented for the presented case study by sending the averaged output active and reactive powers at each DG to the EMU where the optimized output power sharing ratios are selected and sent back to the DPRs located at the vicinity of each DG entity. The state space-based modelling approach presented in section 7.2 is adopted in order to design the PI controller gains in DPRs in a way that both the dynamic performance and the system stability criteria are met. Note that considering the multi-input multi-output nature of the proposed networked-based control, classical PI tuning methods cannot be used to design the compensators. Therefore, the pole placement technique has been adopted.

7.3.1 With Negligible Communication Delay

The state space model of the MG test system of Figure 7-2 can be derived using the generalized modeling approach presented in (7-23) while the communication delay is initially assumed to be zero (i.e. $\tau_d = 0$). Note that in order to simplify the resulting state-space model, the controller gains in (7-1),(7-2) are assumed to be equal for all the DG units. The DG units in Figure 7-2 are initially assumed to supply equal shares of active and reactive power. Therefore, the associated operating condition can be found using load flow analysis. The resulting operating points as well as other system parameters are presented in Appendix B. The small-signal state-space model of Figure 7-2 can then be derived as (7-26) where the state vector is depicted in (7-27).

$$\Delta \dot{x}_{4DG}(t) = (A_{4DG\_Aut} + A_{4DG\_com})\Delta x_{4DG}(t) \tag{7-26}$$

$$\Delta x_{4DG} = [\Delta \bar{P}_1 \ \ldots \ \Delta \bar{P}_4 \ \ \Delta \bar{Q}_1 \ \ldots \ \Delta \bar{Q}_4 \ \ \Delta \lambda_{P1} \ \ldots \ \Delta \lambda_{P4} \ \ \Delta \lambda_{Q1} \ \ldots \ \Delta \lambda_{Q4} \ \ \Delta V_1 \ \ldots \ \Delta V_4 \ \ \Delta \delta_{14} \ \ \Delta \delta_{24} \ \ \Delta \delta_{34}] \tag{7-27}$$

As stated earlier, it is a well-established fact that if the voltage/current control loops are well-designed to preserve medium- and high-frequency stability, the system dynamics are mainly dictated by the low-frequency modes associated with power sharing controllers [19, 78]. Therefore, only PI power controller gains are expected to shape the most dominant eigenvalues of the system. This finding agrees with the detailed MG analysis, with power sharing voltage control, and the current control loops presented in [19, 78].

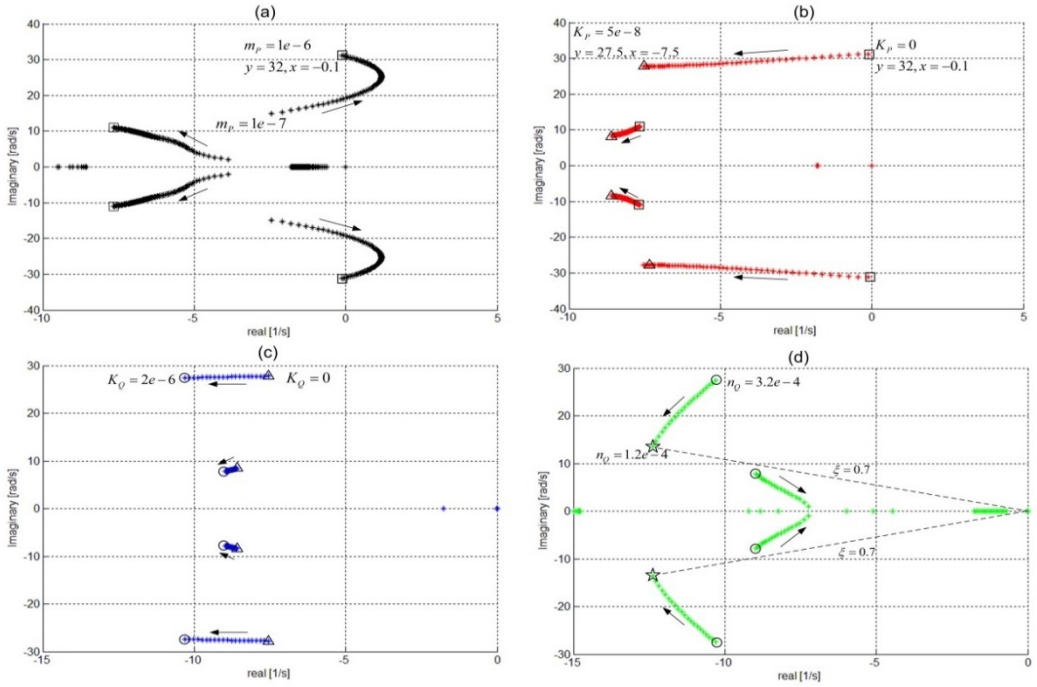

Figure 7-3: System eigenvalue spectrum when (a) $K_P = K_Q = 0$, $n_Q = 3.2e-4$ and m_P changes from 1e-7 to 1e-6 (b) $K_Q = 0$, $n_Q = 3.2e-4$, $m_P = 1e-6$ and K_P changes from 0 to 5e-8 (c) $n_Q = 3.2e-4$, $m_P = 1e-6$, $K_P = 5e-8$ and K_Q changes from 0 to 2e-6 (d) $m_P = 1e-6$, $K_P = 5e-8$, $K_Q = 2e-6$ and n_Q changes from 3.2e-4 to 1.2e-4.

In order to show the effect of the proportional and integral power sharing gains in shaping the dominant modes, initially the proportional gains in (7-1),(7-2) are assumed to be zero (i.e. $K_P = K_Q = 0$) and the reactive power integral gain, n_Q, is considered to be fixed at 3.2e-4 initially. Figure 7-3 (a) shows the dominant eigenvalue spectrum as the active power integral gain, m_P, is increased while n_Q is constant. As can be seen from Figure 7-3 (a), without adopting proportional gains in (7-1) and (7-2), increasing m_P leads to instability. Note that it is desired to be able to operate the system at higher gains in order to enhance power sharing dynamics as well as reducing power sharing errors. Figure 7-3 (b) shows that the least stable mode in Figure 7-3 (a), associated with m_P = 1e-6 (denoted by "□"), can be shifted to the LHP by increasing K_P. Even higher damping as well as higher damping ratios can be provided by increasing K_Q as depicted in Figure 7-3 (c). Although the most stable pairs of modes in Figure 7-3 (c) show high damping, their damping ratio (ζ) can be further improved to match the desired value to provide good tracking response times. Figure 7-3 (d) shows how the dominant modes can be relocated to provide enough damping as well as fast dynamics by readjusting n_Q. (The dominant oscillatory modes are marked by the stars in Figure 7-3 (d)). Note that the validity of the derived model is later verified in section V via the simulated power responses.

7.3.2 With Non-Negligible Communication Delay

One of the major challenges facing networked-based control algorithms is the effect of communication delays on the stability of such systems. However, unlike the fully centralized methods, the distributed nature of the DPRs in the proposed scheme helps the system to maintain its stability in the presence of communication delays. This is due to the fact that in the proposed method, the EMU only provides the power reference values to the local DPRs, which in return will be tracked using the delay-free local measurements. Therefore, since the centralized EMU is not directly responsible for the power regulation, any possible communication delays between the EMU and the DG units (either from or to the entities) will only delay achieving the desired power flow while the DPRs continue to operate in their previous conditions during the delay period. Please note that although having delayed reference values can affect the desired optimized operating points, the stability margins will not be affected as compared to the fully centralized case where the voltage and angle references are directly generated by the EMU in a fully centralized manner [112].

Figure 7-4 compares the effect of the communication delay in the proposed control structure with the case of a fully centralized networked-controlled scheme where the power regulation is assumed to be done directly from the centralized controller (as in [112]). Figure 7-4 (a) shows the proposed system eigenvalue spectrum when the communication delay is assumed to be as big as 1000 ms. As can be seen, the proposed scheme remains stable in presence of high communication delays and the dominant oscillatory modes, which are marked by the stars (achieved through the aforementioned pole placement technique) are not affected (compare with Figure 7-3 (d)). Note that this was expected considering that in the proposed structure only the reference values (sent from EMU) can be affected by the communication delays and the local feedback signals used in the DPRs are considered delay-free due to the distributed nature of these regulators (they are located at the vicinity of each entity); thus, this will not compromise system stability. The advantage of the distributed nature of the proposed scheme over its centralized counterpart is better reflected in Figure 7-4 (b) where it is shown that instability can occur with delay values as small as 24 ms.

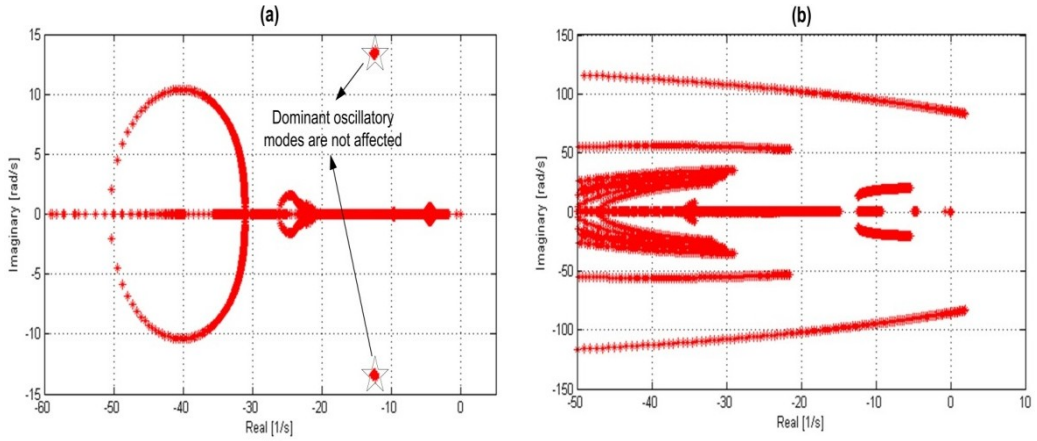

Figure 7-4: System eigenvalue spectrum in presence of communication delay with (a) the proposed distributed method when τd increases from zero to 1000 ms (b) the centralized method when τd increases from 0 to 24 ms.

It should be noted that typical communication delays can be in the order of 100ms to 200ms [114]; therefore, robustness against communication delays is crucial to facilitate effective and reliable networked-controlled systems.

7.4 Simulation Results

7.4.1 Model Verification

In order to validate the accuracy of the proposed small-signal based model derived in (7-26), the performance of the proposed networked-based control system is implemented for time-domain simulation using the Matlab/Simulink environment. Figure 7-6 shows the active and reactive power responses when the control gains are selected to be K_P=K_Q=0, n_Q=3.2e-4 and m_P=*1e-6*. Note that this is associated with the eigenvalues marked with "□" in Figure 7-3 (a) where the dominant system modes are almost located on the $j\omega$ axis with the angular frequency of 32 rad/s. As can be seen from Figure 7-6 (a) and (b), the frequency of the oscillations can be calculated to agree with the one achieved through the small-signal based state space model.

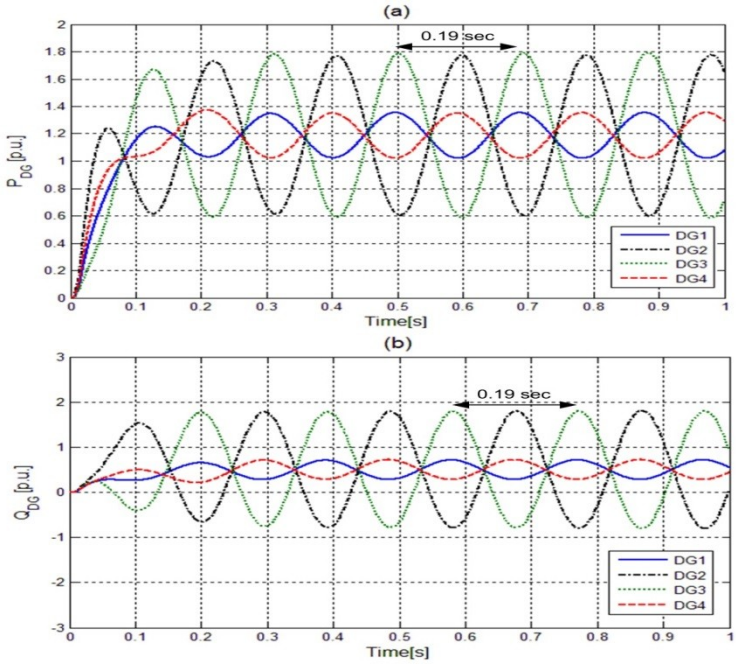

Figure 7-5: System responses when K_P=K_Q=0, n_Q=3.2e-4 and m_P= 1e-6 (a) Active power (b) Reactive power.

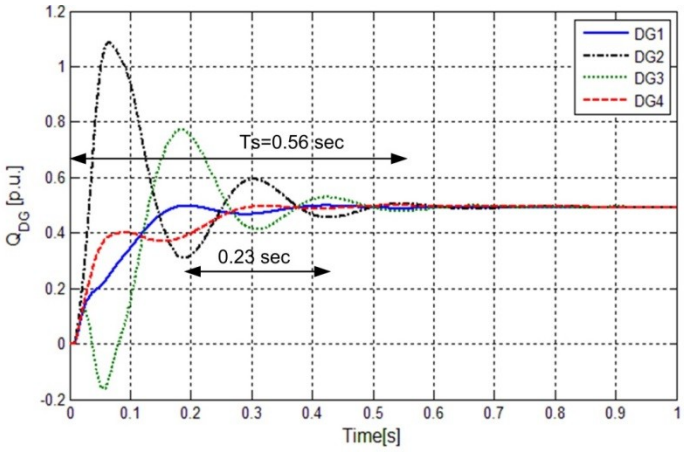

Figure 7-6: Reactive power responses when K_P=5e-8,K_Q=0, n_Q=3.2e-4 and m_P= 1e-6.

Moreover the effect of the proportional gain of K_P (as shown in Figure 7-3 (b)) is also evaluated through the power responses provided in Figure 7-6. The frequency of the least damped oscillations shown in Figure 7-6 is observed to be 27.3 rad/s which agrees with the dominant modes marked by Δ in Figure 7-3 (b). Moreover, the settling time of the power response is also shown in Figure 7-6 which almost agrees with the estimation achieved from the eigenvalue analysis. The estimated settling time is evaluated to be (4/7.5=0.53 s) based on the dominant modes presented in Figure 7-3 (b). Note that this estimation closely agrees with the simulation results of Figure 7-6.

7.4.2 Controller Verification

By following the design procedure of Figure 7-3, the system responses are expected to be well damped with minimal oscillations in order to agree with the location of the dominant oscillatory modes presented in Figure 7-3 (d) (marked by the start signs). Figure 7-7 depicts the system responses with the designed power regulators. Note that for this set of simulations, the active and reactive powers are assumed to be shared equally between the four DGs; thus, $\gamma_{P,Q,1}$ to $\gamma_{P,Q,4}$ are assumed to be equal (i.e. 0.25). As can be seen, the selected coefficients for the PI power controllers which are calculated based on the small-signal-based eigenvalue analysis show well-damped responses as expected.

As mentioned earlier, one of the advantages of the proposed power control framework is the flexibility that it provides in assigning different operating points based on an optimization criteria (e.g. MG operating cost minimization, optimized ancillary services, etc.). Figure 7-8 shows the performance of the proposed system when the active power set points sent from the EMU are changed at t = 3s so that DG1 and DG2 provide 30% of the active and reactive power demands while the remaining two units contribute 20% each. This can be simply achieved by updating $\gamma_{P,Q,1}$,$\gamma_{P,Q,2}$, $\gamma_{P,Q,3}$ and $\gamma_{P,Q,4}$ to be 0.3, 0.3, 0.2 and 0.2 respectively. Figure 7-8 (a),(b) show the active and reactive power responses. As can be seen, the power provided by each DG unit can be adjusted only by changing the power sharing ratios inside the EMU. Note that, unlike the conventional droop scheme this can be achieved without changing the local controller's droop gains. The voltage amplitude and frequency variations, as depicted in Figure 7-8 (c),(d) respectively, are bounded. When the communication network is down, the power sharing strategy will switch to the droop control where the voltage and frequency droop gains suggest how the powers should be shared. Figure 7-9 depicts the power response when the communication network is disabled at t = 2 s. Equal droop coefficients for all DG units suggest that both active and reactive powers are desired to be shared equally between the entities. However, as can be seen from Figure 7-9 (a),(b), although the conventional frequency droop strategy of (5) is well capable of sharing the active power equally among the two DGs, voltage droop fails to reduce the reactive power sharing error to zero.

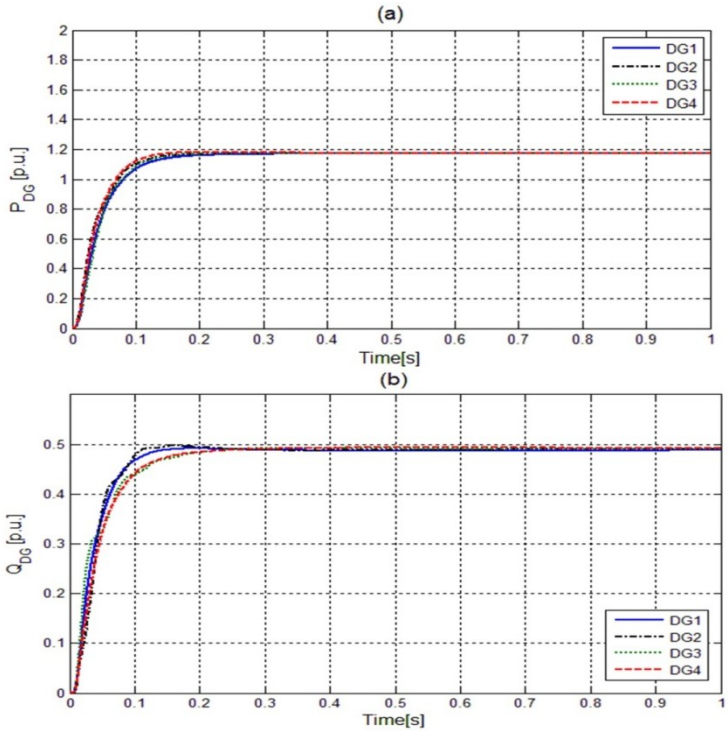

Figure 7-7: System responses when K_P=5e-8, K_Q=2e-6, n_Q=1.2e-4 and m_P=1e-6 (a) Active power (b) Reactive power.

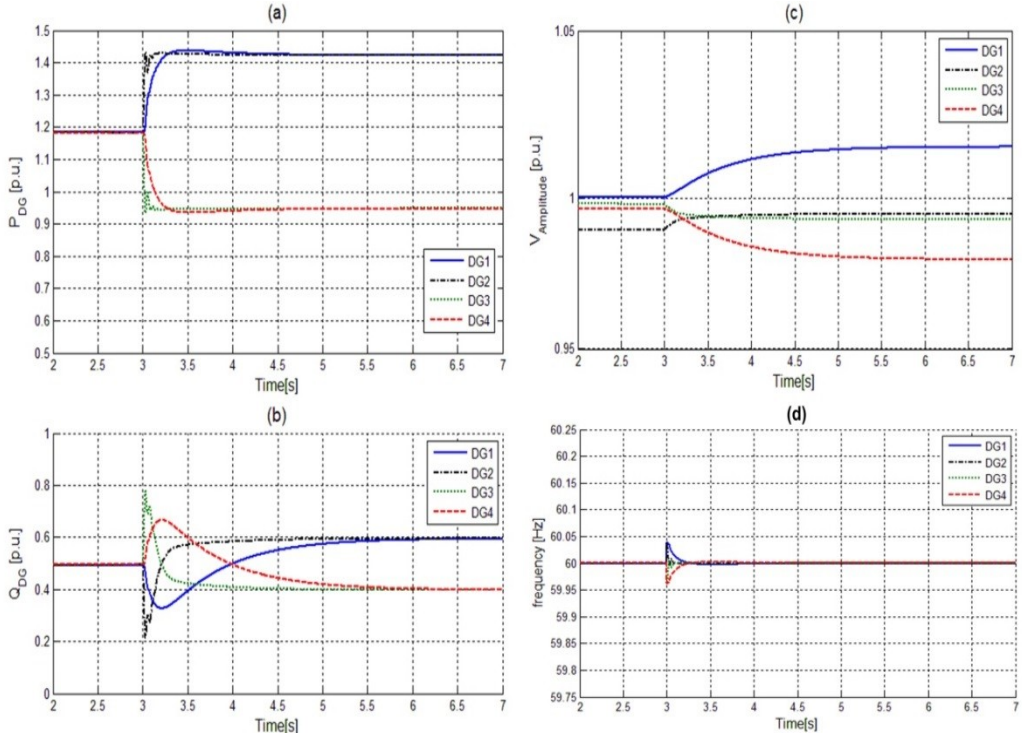

Figure 7-8: Performance of the proposed algorithm when the power reference values are changed at t = 3 s (a) Active power (b) Reactive power (c) Voltage amplitudes (d) Output frequencies.

The inaccurate reactive power sharing is a well-known drawback of autonomous droop control, especially when the line inductances greatly differ from each other. Note that in the conventional droop strategy, better reactive power sharing can only be achieved by adopting higher voltage droop gains yielding compromised stability. Therefore, there is always a tradeoff between the system stability and accurate reactive power sharing when the conventional droop strategy is applied. The DG frequency responses are also depicted in Figure 7-9 (c) where it can be seen that in spite of the perfect active power sharing achieved by the conventional droop strategy, this comes at the cost of frequency deviations.

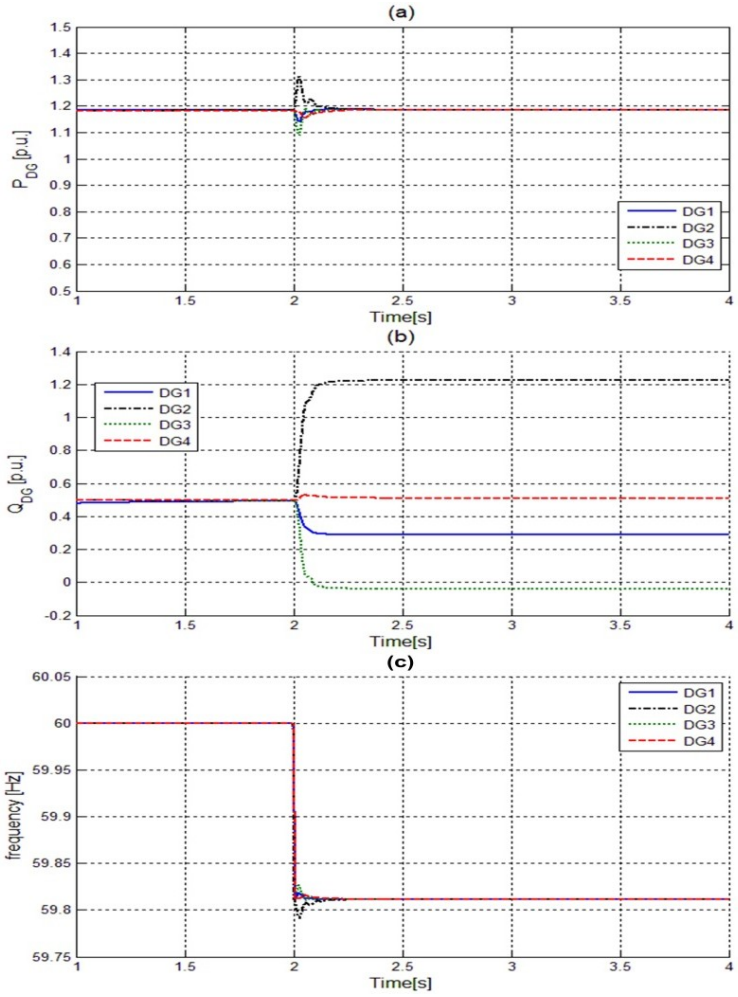

Figure 7-9: Transition of the the proposed algorithm to conventional droop control (a) Active power (b) Reactive power (c) Output frequencies.

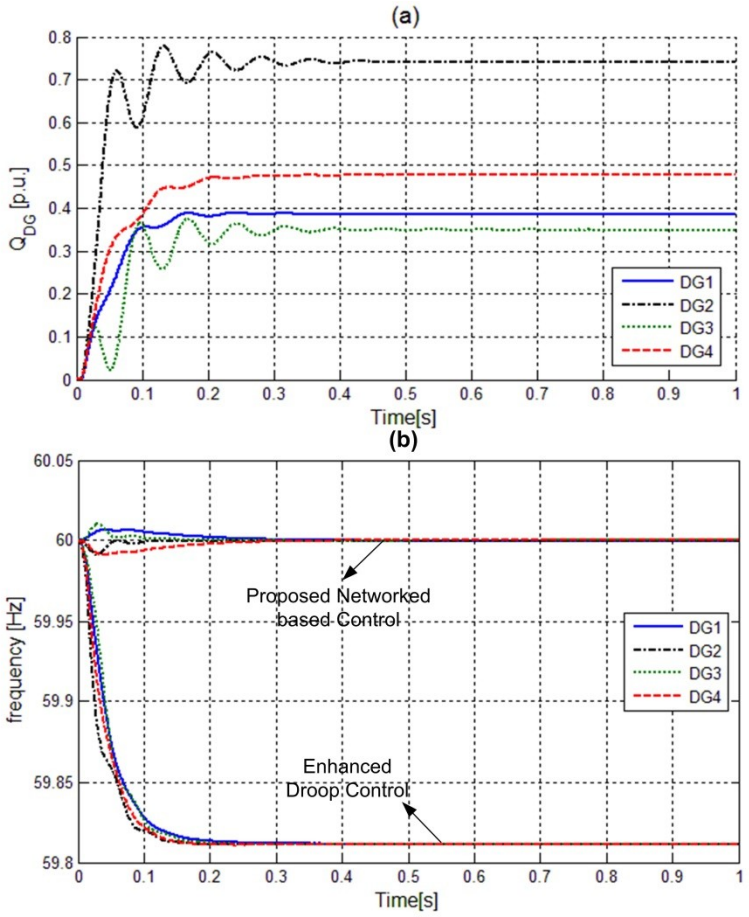

Figure 7-10: (a) Reactive power response of the enhanced droop control (b) Comparing the frequency response of the enhanced droop control with the proposed method.

As mentioned earlier, the reactive power sharing performance can be enhanced by increasing the droop gains but this will compromise system stability as confirmed by the eigenvalue analysis provided in [18, 19, 61, 78]. However, [61] suggest that introducing the derivative of the averaged powers as an supplementary control signal in the droop controllers dynamics can highly enhance the system stability margins; thus, enabling the adoption of higher droop gains yielding reduced reactive power sharing errors. Figure 7-10 (a) shows the reactive power responses achieved by adopting the auxiliary control signal presented in [61]. Although the reactive power sharing is improved, further minimization of the error is not achievable without violating the stability criteria as suggested by the oscillations in Figure 7-10 (a). Moreover, as can be seen from Figure 7-10 (b), the frequency deviation issue is still not alleviated.

As suggested in the introduction, the drawbacks of the autonomous power sharing methods in maintaining accurate reactive power sharing and minimal frequency deviations has encouraged the adoption of the networked-based algorithms. However as

stated earlier the adoption of fully centralized structures makes these methods highly sensitive communication delays. The following section evaluates the advantages of the proposed distributed control structure in maintaining the stability of the delayed systems as suggested by the analysis in Figure 7-4.

7.4.3 Delayed System Performance

Figure 7-11(a), (b) show the active and reactive power responses of the fully centralized control scheme in the presence of a 24 ms communication delay. Note that in a fully centralized system where the voltage amplitude and angle references are directly generated by the centralized EMU, as can be seen from Figure 7-11, the communication delay yields instability as suggested by the eigenvalue analysis shown in Figure 7-4 (b). Note that the frequency of the oscillations (90 rad/s) closely agrees with the small signal analysis of Figure 7-4 (b).

However by distributing the power regulators as suggested in Figure 7-1, the system stability can be greatly increased. Once again note that this is due to the fact that the feedback power signals used to regulate power in each DPR is directly adopted from the local measurements, and therefore unlike fully centralized methods, the feedback signals can be assumed to be delay free and therefore only power reference values ($\gamma_i P_{tot}$,$\gamma_i Q_{tot}$) will be affected by any communication delays. This implies that achieving the desired power set points will be held up for the delay period without compromising its stability. In this case, the presence of communication delays will only appear as a time-scale shift in the system responses as suggested by Figure 7-12(a) which depicts the delayed system responses to changes in the power sharing ratios in EMU at t = 3s. The active power sharing ratios decided by EMU are updated at t = 3s so that DG1 and DG2 provide 30% of the demand each while the remaining two units contribute 20% each. However the reactive power sharing ratios are not changed. As can be seen from Figure 7-12 (a), (b) the communication delay between the EMU and the local DPRs result in a delayed achievement of the updated objectives. Note that unlike [112] the stability of the system is not compromised due to the fact that the delay does not affect the local feedback measurements (used by the local DPRs) and will only reflect on the reference signals; thus, shifting the response times.

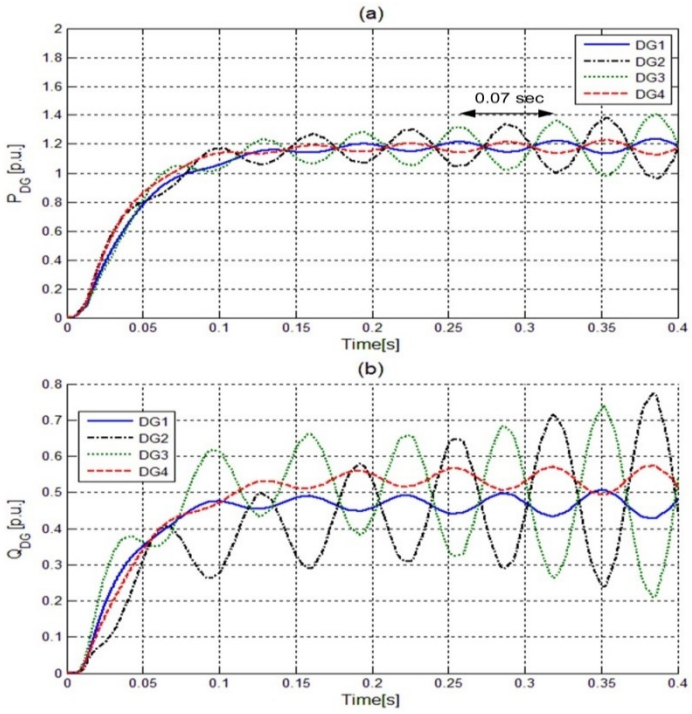

Figure 7-11: System responses of the enhanced control approach presented in [14] in presence of 24 ms of communication delay (a) Active power (b) Reactive power.

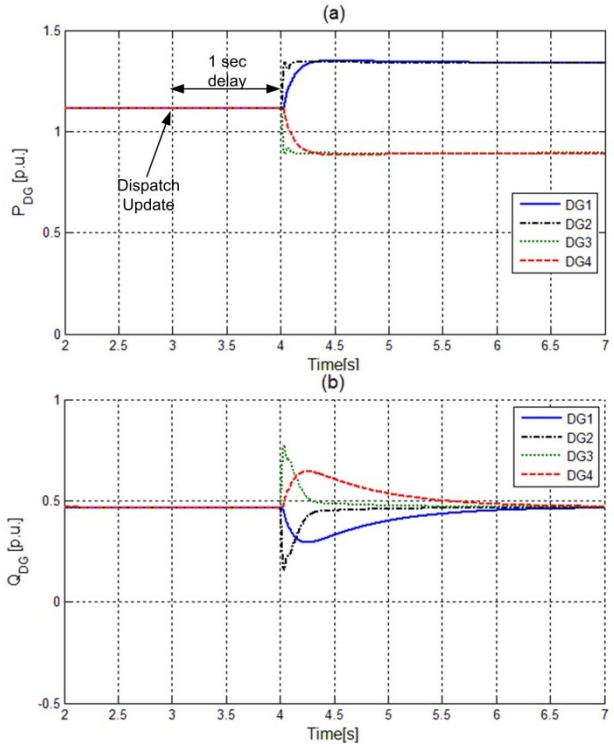

Figure 7-12: System responses of the proposed method when the power reference values are changed at t=3 s and a 1000 ms communication delay is adopted (a) Active power (b) Reactive power.

7.5 Experimental Results

The performance of the proposed algorithm is tested experimentally using a 1.0 kVA 208 V, 60 Hz laboratory scale 2-DG MG setup similar to the one described in section 6.5. Figure 7-13 shows the schematic diagram of the adopted experimental setup where two Semikron®-Semi-stack IGBT voltage-source converters are used to interface the two units to the MG system. Individual dSpace1104 control systems are adopted to implement the local DPR units at each DG entity in real-time. The software code is generated by the Real-Time-WorkShop in a Matlab/Simulink® environment. Without the loss of generality, the dSpace unit connected to DG1 is considered as the EMU. The sampling/switching frequency is considered to be 10 kHz. The output LC filter parameters are considered as L_f = 1.2 mH and C_f = 50 μF. The line parameters are considered to be: Line1 = 1.2 mH, Line2 = 0.5 mH. An inductive common load is considered to be connected in order to demonstrate the effectiveness of the proposed method in providing accurate reactive power sharing. The proposed networked-based control scheme is then implemented to ensure accurate active and reactive power sharing among the two DG units despite of the highly different line inductances. Figure 7-14 shows the output currents of each unit as well as the current sharing error and the load voltage waveform. As can be seen from Figure 7-14, the proposed method is well capable of sharing the power equally among the two DGs.

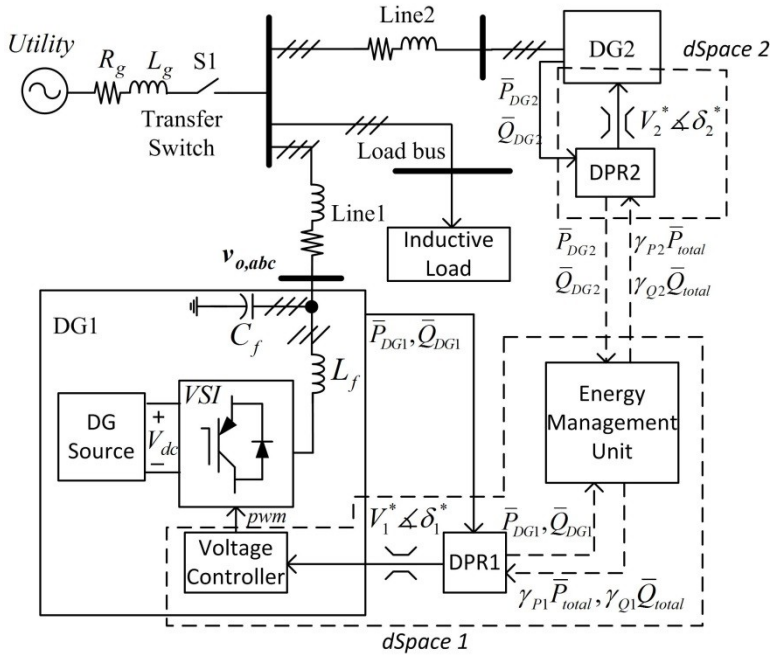

Figure 7-13: Schematic diagram of the laboratory setup

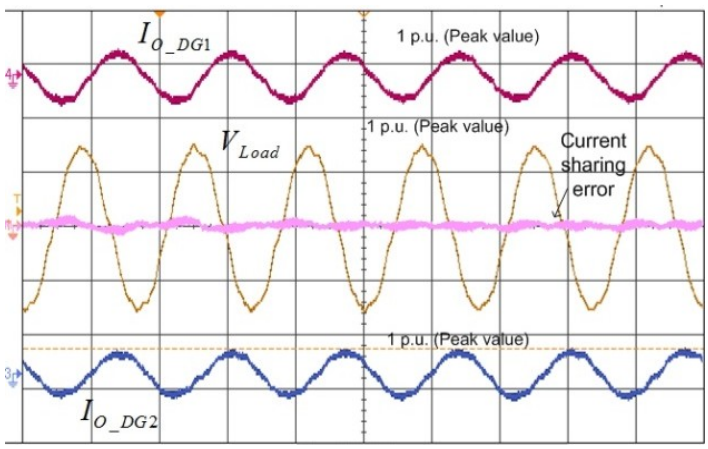

Figure 7-14: DG1 and DG2 output currents, load voltage and the current sharing error when the active and reactive powers are shared equally.

Once again the flexibility of the proposed method in operating the DG units in different power conditions is tested by assigning different active power set points using the EMU. Figure 7-15 (a),(b) show the active and reactive power responses as γ_{P1} , γ_{P2} are updated to 0.25 and 0.75 at t = 4 s, respectively. Note that the reactive power set points are kept constant (i.e. $\gamma_{Q1} = \gamma_{Q2} = 0.5$). The DG1 frequency and voltage deviations are also presented in Figure 7-15 (c) and (d) respectively. Figure 7-15 verifies that the proposed control scheme provides a suitable framework to interactively update the generated power by each DG unit based on any pre-defined optimization criteria.

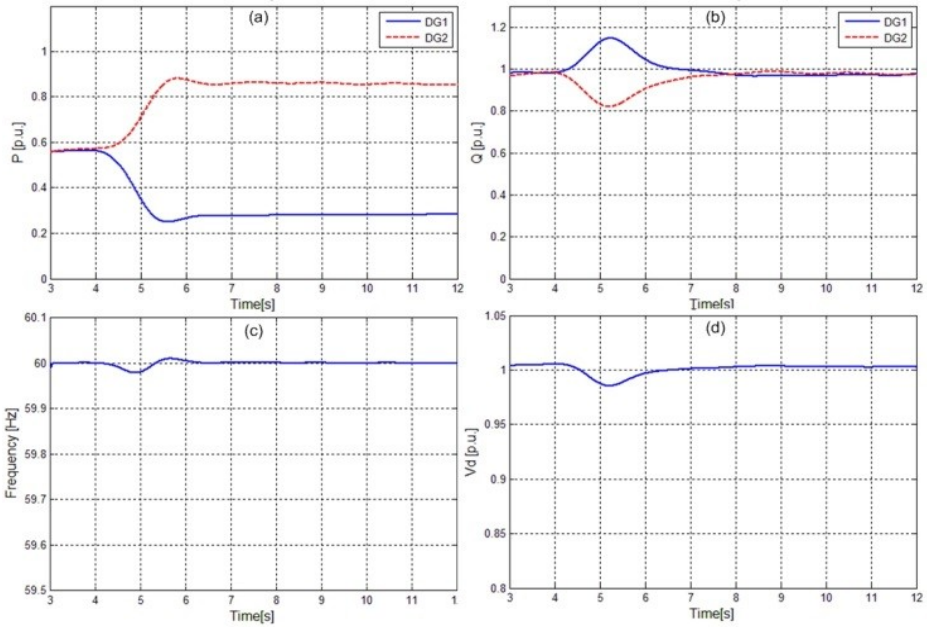

Figure 7-15: Measured performance of the proposed algorithm when the active power reference values are changed to γ_{P1} = 0.25 and γ_{P2} = 0.75 (a) Active power (b) Reactive power (c) DG1 output frequency (d) Load voltage amplitude.

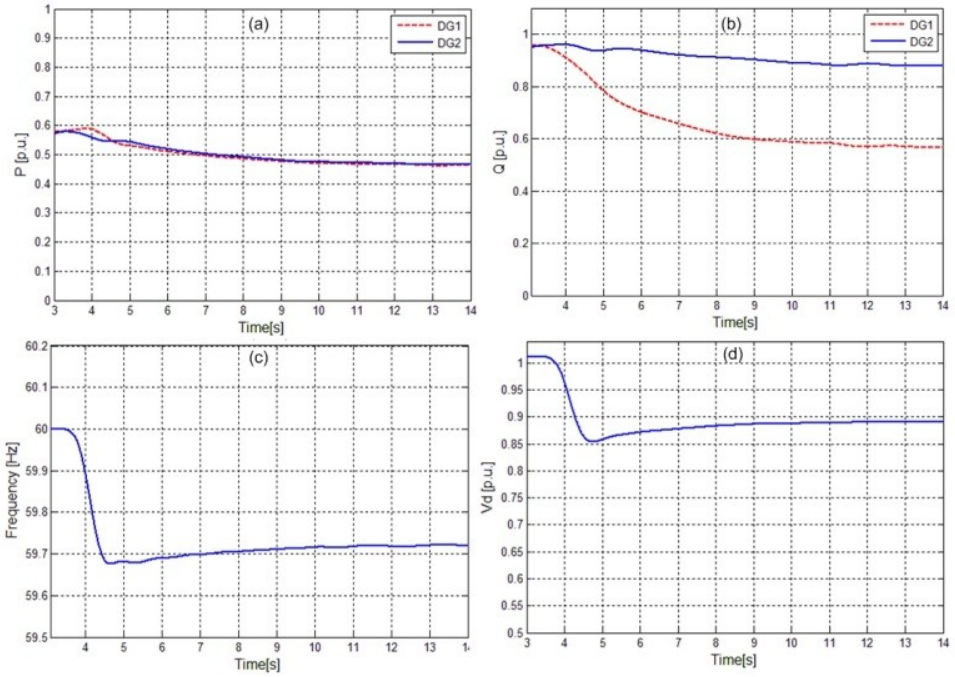

Figure 7-16: Performance of the proposed algorithm when the network gets disconnected (a) Active power (b) Reactive power (c) DG1 output frequency (d) Load voltage amplitude.

The performance of the proposed networked-based control scheme is compared with the conventional droop strategy in Figure 7-16 as the network is disabled at t=3s; thus, the power sharing control algorithm is switched to traditional droop. Once again, in Figure 7-16 the active and reactive power demands are assumed to be shared equally among the two DG units. As can be seen from Figure 7-16 (a), the active power can still be shared equally as the system loses communication. However, Figure 7-16 (c) suggests that the frequency level cannot be maintained when the communication is lost. Moreover, despite of the voltage drop caused by the droop action subsequent to the loss of communication, the reactive power values supplied by each unit are not equal anymore. Note that due to the voltage drop caused by droop action, the total power demand is reduced in Figure 7-16 (a) and (b).

7.6 Summary and Conclusions

This chapter presented a networked-based control strategy that enables optimized operation of the MG systems based on the operational objectives decided by the EMU. The distributed power regulators adopted in the proposed scheme help the DG units follow the decided objectives without violating either stability or the performance criteria. The proposed control strategy eliminates the reactive power sharing errors associated

with the conventional droop control without compromising system stability. Moreover, the frequency deviations are compensated for using the communicated signals. The hybrid distributed structure of the proposed method provides great robustness against communication delays as well as high reliability when the network is shut down. A generalized modeling approach that captures the dominant dynamics of a MG system is developed and adopted in order to shape the dominant system modes, yielding desired performance and stability objectives. Delay-dependent stability analysis is performed to verify the robustness of the proposed method in the presence of communication-delays. A theoretical analysis and several comparative simulation and experimental results are presented to validate the effectiveness of the proposed scheme.

Chapter 8

Active Synchronization and Power Flow Control of Interconnected MGs [7]

The distributed control power sharing scheme proposed in Chapter 7 provides accurate reactive power sharing and minimal frequency drift compared to the traditional droop. Moreover, it facilitates the implementation of optimization/power sharing algorithms without violating the stability criteria. However, as mentioned in section 1.1.6, in order to realize the adoption of MG systems as the building block of future active distribution systems, coordination issues such as power-tie control between different interconnected MG entities as well as their active synchronization prior to their connection, should be addressed.

Therefore, this chapter aims to propose a secondary control structure that can extend the existing networked-based control scheme of Chapter 7 to be adopted for the coordination of multiple interconnected MG systems. The resulting hierarchical distributed control scheme should therefore be able to not only maintain the power sharing framework proposed in Chapter 7, but also provide a higher-level active synchronization and power-tie control feature between the MGs without interfering with their inner power sharing loops.

In the proposed hierarchical method, the most inner control loop consists of the DPRs suggested in Chapter 7 that are located within the vicinity of each dispatchable DG unit. Note that the power regulators at this level ensure perfect tracking of the optimized set points assigned by the local MG dispatch centre. The average power measurements are transmitted to the dispatch centre to calculate the share of each unit of the total power demand based on pre-defined local optimization criteria. The distributed nature of the power regulators allows them to adopt the delay-free local power measurements as the required feedback signals.

[7] A version of this chapter has been submitted to *IEEE Trans. on Power Systems*.

A higher-level synchronization and power-tie control unit is then designed to minimize voltage and phase differences between two MGs prior to their connection and to regulate the power flow between the two entities. The power-tie set points can be decided by the upper level-control centre either based on supply/demand estimations or any global cost- or loss-minimization algorithms [62, 73-77]. Note that the auxiliary synchronizing and power-tie control signals generated by the proposed method are sent to the dispatch centre to ensure that the control effort is shared among the DG units without violating the local power sharing objectives. Therefore, the hierarchical structure of the proposed method provides great flexibility in adopting both local and global optimization algorithms. A detailed analysis and the design process for all controllers are provided. Detailed time-domain simulation results are presented to show the validity and effectiveness of the proposed controller.

8.1 MG-Based Active Distribution System

Figure 8-1 shows sample MG clusters that can be interactively connected or disconnected from each other or from the utility grid. When disconnected from the utility grid, the MG clusters can be assumed to include the neighboring DG entities and loads in order to construct a supply-adequate-based structure [72]. Without the loss of generality, MGs 1 and 2 are considered as the test clusters in this chapter. MG1 consists of two dispatchable DG units and the local load while two dispatchable entities and a non-dispatchable PV unit as well as the local load are included in MG2. Although the clusters can be designed based on a long-term probabilistic planning study [72] to provide adequate supply for their local loads, the power flow among the MGs should also be controlled in real-time to provide higher reliability and optimum operation and to overcome the uncertain nature of generation and loads within each MG. In Figure 8-1, the power generated by the PV unit is assumed to vary between 0 and 200kW; therefore, the tie-line power flow command should be updated by the supervisory controller to compensate for the variations.

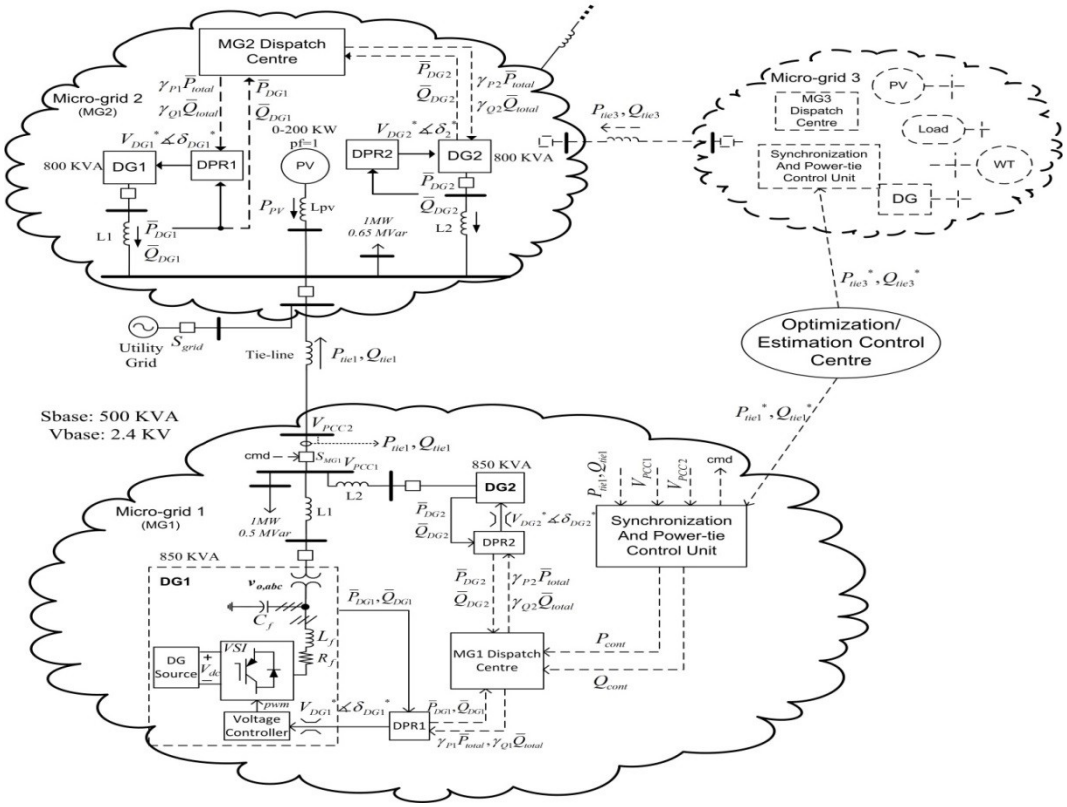

Figure 8-1: Hierarchical distributed energy management and synchronization control for multiple MG systems.

Note that several load- or cost-estimation algorithms can be adopted in the optimization/estimation control centre [73-76]. The details of such algorithms are out of the scope of this chapter since the goal of this research is to provide a control framework that improves the flexibility of the existing MG control structures in order to implement such methods. In the test system of Figure 8-1, the power generation level of MG2 is subject to change due to the presence of the non-dispatchable PV unit. A tie-line power flow control strategy is therefore to be suggested in order to enable the import or export of power to and from the second MG. However, prior to the connection of the two MGs, proper synchronization process should be implemented in order to minimize the voltage and phase deviations at the point of common coupling. Note that each DG unit inside MG1 should contribute in both synchronization and power-tie control efforts based on its local desired power sharing criteria, and therefore the power sharing objectives should not be violated through the process. Figure 8-1 shows the proposed networked hierarchical scheme in which the communicated signals are depicted by dashed lines. As shown in Figure 8-1, active synchronization and power-tie control between the two MGs is achieved by generating the appropriate control signals (P_{cont} and Q_{cont}) which are sent to

the MG dispatch centre to be shared among all the dispatchable entities based on the local power sharing objectives. It should be noted that P_{cont} and Q_{cont} are only non-zero during the regulation process and once the synchronization or power-tie objectives are met, they will go to zero.

The details of the power sharing mechanism inside each MG were discussed in Chapter 7 where it was elaborated that the average active and reactive powers generated by each dispatchable DG unit are transmitted to the MG dispatch centre in order to calculate the total generated power and then allocate the optimized power generation level to each DG i.e. $\gamma_{Pi}\ \bar{P}_{\text{total}}$, $\gamma_{Qi}\ \bar{Q}_{total}$, where γ_{Pi}, γ_{Qi} show the desired share of the real and reactive power generated by the i^{th} dispatchable unit respectively, and $\bar{P}_{\text{total}}$ and $\bar{Q}_{total}$ are the total average active and reactive power generated by the dispatchable units respectively. The desired active and reactive power set points are then sent to the local DPRs to be tracked by each unit. As can be seen from Figure 8-1, DPR units decide the reference voltage amplitude and angle values that should be generated by each unit subsequently. PI controllers can be designed and implemented in each DPR to achieve active and reactive power sharing objectives using the state space modeling approach provided in section 7.2

Power-tie control and synchronization units are introduced in order to complete the hierarchical control interface. Figure 8-2 shows the details of the proposed hierarchical networked-based control structure implemented on the 2-DG system of MG 1. The proposed scheme facilitates the implementation of the aforementioned objectives such as active synchronizations, tie-line power flow control as well as the local accurate and optimized power sharing (earlier introduced in Chapter 7).

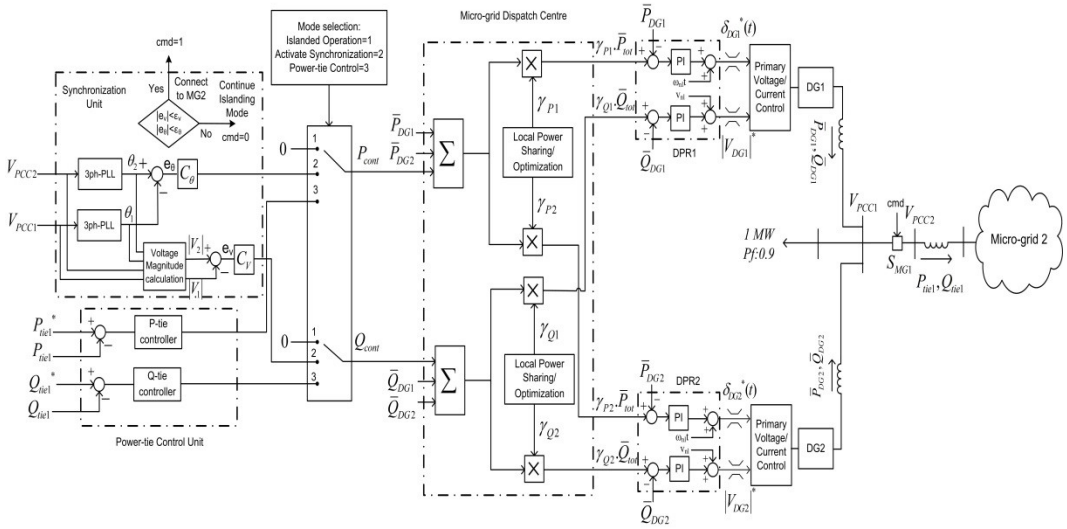

Figure 8-2: The proposed hierarchical control structure.

As shown in Figure 8-2, the MG can operate in 3 modes:

Mode 1: When the switch between the two MGs, S_{MG1}, is off the MG continues to operate in islanded mode where the auxiliary power control signals (P_{cont},Q_{cont}) are set to zero. In this case, the local demand is shared between the two DG units based on the desired local power sharing objectives. The PI regulators at each DPR, which were characterized by (7-1) and (7-2), guarantee accurate active and reactive power sharing among the entities. Note that this mode was discussed in detail in Chapter 7.

Mode 2: When the MG is to be connected to the neighboring MG (or grid), the synchronization process is activated. The auxiliary active and reactive power control signals are then generated to minimize the phase and voltage differences respectively. Note that the synchronization effort is also shared among the DG units based on the rating/optimization criteria decided by the dispatch unit. Phase and voltage controllers (C_θ , C_V) are to be designed to achieve this goal. Controller design is presented in Section 8.2.2.

Mode 3: When phase/voltage errors are smaller than a pre-defined tolerance, S_{MG1} is turned on to connect the two MGs, and the power flow control is then activated to regulate the tie-line power between them. The references (P_{tie1}^* and Q_{tie1}^*) are decided by the higher level control centre based on the load and generation estimations in both MGs. The appropriate P-tie and Q-tie controllers are designed in Section 8.2.2 to provide well-damped power flow responses.

8.2 Controllers Design

8.2.1 DPR Controllers

The small-signal state-space based pole placement technique introduced in 7.2 is adopted to design the local PI controllers in each DPR. The small-signal state-space model of each of the 2-DG networked controlled MG subsystems presented in Figure 8-1, can therefore be derived as in (8-1) following the general modeling approach presented in section 7.2.

$$\Delta\dot{x}_{MG} = A_{MG}\Delta x_{MG}(t) \tag{8-1}$$

$$\Delta x_{MG} = [\Delta\bar{P}_{DG1} \quad \Delta\bar{P}_{DG2} \quad \Delta\bar{Q}_{DG1} \quad \Delta\bar{Q}_{DG2} \quad \Delta\lambda_{P1} \quad \Delta\lambda_{P2} \quad \Delta\lambda_{Q1} \quad \Delta\lambda_{Q2} \quad \Delta V_{DG1} \quad \Delta V_{DG2} \quad \Delta\delta_{12}] \tag{8-2}$$

Note that A_{MG} is given by (8-3) where the parameters are explained in 7.2.

$$A_{MG} = \begin{bmatrix} -\omega_c(I)_{2\times2} & (O)_{2\times2} & (O)_{2\times2} & (O)_{2\times2} & \omega_c\times\begin{pmatrix}\alpha_{P11} & \alpha_{P12}\\ \alpha_{P21} & \alpha_{P22}\end{pmatrix}_{2\times2} & \omega_c\times\begin{pmatrix}\beta_{Q11}\\ \beta_{Q21}\end{pmatrix}_{2\times1} \\ (O)_{2\times2} & -\omega_c(I)_{2\times2} & (O)_{2\times2} & (O)_{2\times2} & \omega_c\times\begin{pmatrix}\alpha_{Q11} & \alpha_{Q12}\\ \alpha_{Q21} & \alpha_{Q22}\end{pmatrix}_{2\times2} & \omega_c\times\begin{pmatrix}\beta_{Q11}\\ \beta_{Q21}\end{pmatrix}_{2\times1} \\ \begin{pmatrix}-1+\gamma_{P1} & \gamma_{P1}\\ \gamma_{P2} & -1+\gamma_{P2}\end{pmatrix} & (O)_{2\times2} & (O)_{2\times2} & (O)_{2\times2} & (O)_{2\times2} & (O)_{2\times1} \\ (O)_{2\times2} & \begin{pmatrix}-1+\gamma_{Q1} & \gamma_{Q1}\\ \gamma_{Q2} & -1+\gamma_{Q2}\end{pmatrix}_{2\times2} & (O)_{2\times2} & (O)_{2\times2} & (O)_{2\times2} & (O)_{2\times1} \\ (O)_{2\times2} & \begin{pmatrix}\frac{K_{Q1}(-1+\gamma_{Q1})}{\tau} & \frac{K_{Q1}}{\tau}\gamma_{Q1}\\ \frac{K_{Q2}}{\tau}\gamma_{Q2} & \frac{K_{Q2}(-1+\gamma_{Q1})}{\tau}\end{pmatrix}_{2\times2} & (O)_{2\times2} & \begin{pmatrix}\frac{n_{Q1}}{\tau} & 0\\ 0 & \frac{n_{Q2}}{\tau}\end{pmatrix} & \frac{-1}{\tau}(I)_{2\times2} & (O)_{2\times1} \\ \begin{pmatrix}\frac{K_{P1}(-1+\gamma_{P1}-\gamma_{P2})}{\tau} & \frac{K_{P2}(-1+\gamma_{P1}-\gamma_{P2})}{\tau}\end{pmatrix}_{1\times2} & (O)_{1\times2} & \begin{pmatrix}\frac{m_{P1}}{\tau} & -\frac{m_{P2}}{\tau}\end{pmatrix}_{1\times2} & (O)_{1\times2} & (O)_{1\times2} & \frac{-1}{\tau} \end{bmatrix} \tag{8-3}$$

The pole placement technique is then adopted to design the power regulators of (7-1),(7-2) for each one of the 2-DG MG entities shown in Figure 8-1 similar to section 7.3. Note that the initial operating condition adopted for the model linearization and other system parameters are given in Appendix C. Figure 8-3 shows the design procedure adopted for tuning the power regulators' coefficients. Figure 8-3 (a) shows the dominant eigenvalue spectrum as the active power integral gain, m_P, is increased, while n_Q is kept constant and the proportional gains are assumed to be zero initially. As can be seen from Figure 8-3 (a), without adopting proportional gains in Figure 8-3, increasing m_P leads to instability.

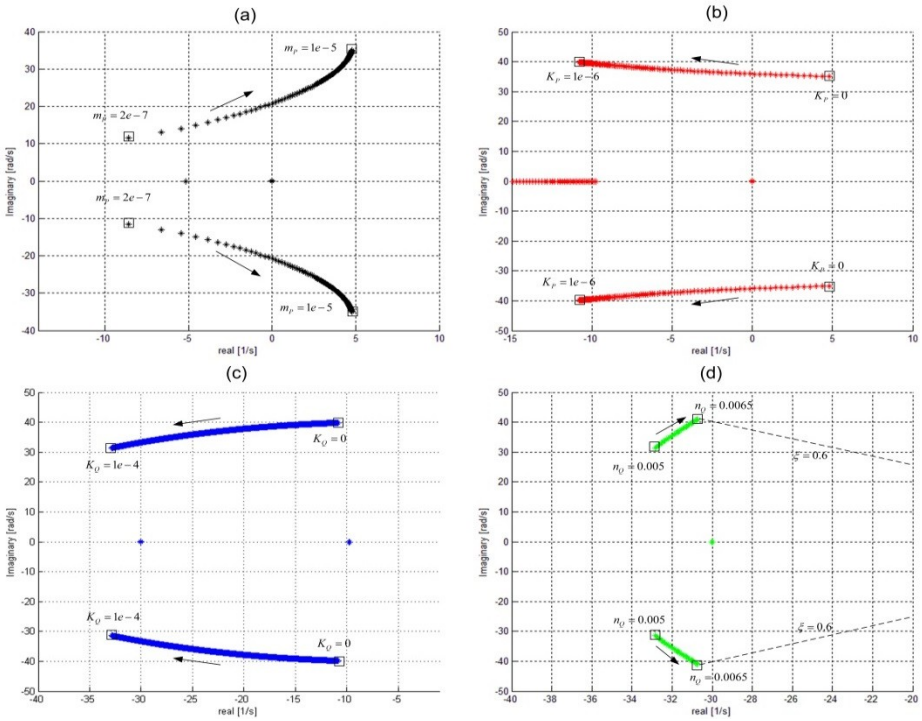

Figure 8-3: System eigenvalue spectrum of MG1 when (a) K_P=K_Q=0, n_Q=5e-3 and m_P changes from 2e-7 to 1e-5 (b) K_Q=0,n_Q=5e-3, m_P=1e-5 and K_P changes from 0 to 1e-6 (c) n_Q=5e-3, m_P=1e-5, K_P=1e-6 and K_Q changes from 0 to 1e-4 (d) m_P=1e-5, K_P=1e-6, K_Q=1e-4 and n_Q changes from 5e-3 to 6.5e-3.

Note that it is desirable to be able to operate the system with higher gains in order to enhance power sharing dynamics as well as reduce power sharing errors. Figure 8-3 (b) shows that the most unstable mode in Figure 8-3 (a) associated with m_P=1e-5, can be shifted to the LHP by increasing K_P. Even higher damping as well as higher damping ratios can be provided by increasing K_Q as depicted in Figure 8-3 (c). Although the most stable pair of modes in Figure 8-3 (c) show high damping, their damping ratio ζ can be further improved in order to match the desired value of ζ=0.6 which is selected to provide good tracking response times. Figure 8-3 (d) shows how the dominant modes can be relocated to provide enough damping as well as fast dynamics by readjusting n_Q.

8.2.2 Active Synchronization and Power-Tie Control

Connecting MG1 to MG2 calls for minimizing its voltage and angle differences with the neighboring MG at their point of common coupling prior to their connection. In the proposed active synchronization scheme, this is achieved by sending auxiliary active and reactive power control signals (P_{cont} and Q_{cont}) to the dispatch centre at MG1 so all of its DG units will contribute to the synchronization effort without violating the power sharing

ratios. The auxiliary power control signals sent by the synchronization unit provide the necessary voltage and frequency deviations to achieve minimal amplitude and phase error prior the connection of the two entities. As shown in Figure 8-2, the synchronization mode is activated when the MG is operating in mode 2. The same concept can be used to regulate the power flow between the two MGs subsequent to their connection by adjusting the angle and voltage of MG1 at its point of common coupling with respect to MG2 by generating appropriate P_{cont} and Q_{cont} signals (this is shown as mode 3 in Figure 8-2). However, in order to design the synchronizing controllers as well as the power flow regulators presented in Figure 8-2, one should first derive the linearized system transfer functions considering P_{cont} and Q_{cont} as the input signals while the voltage amplitude and angle deviations at the point of common coupling ($\Delta|V_{PCC1}|$ and $\Delta\delta_{PCC1}$) are considered to be the outputs. Once again this can be achieved by deriving the state-space model of the overall system considering the aforementioned input and output signals; however, this task might be time consuming especially when the number of DG units is increased.

Alternatively, a system identification-based method is adopted in order to estimate the linearized transfer functions when MG1 is disconnected from the neighboring unit. It should be noted that system identification method based on the frequency-response are more tailored to power system studies as it eliminates the need for detailed system parameters (as compared to eigenvalue analysis), and it can be used in field testing using frequency-response measurements. Figure 8-4 shows the injected test signal as P_{cont} and Q_{cont} when the two MGs are disconnected. The small signal angle and voltage deviations ($\Delta|V_{PCC1}|$ and $\Delta\delta_{PCC1}$) at the point of common coupling are then measured and a low order plant transfer function is estimated using the system identification Matlab Toolbox.

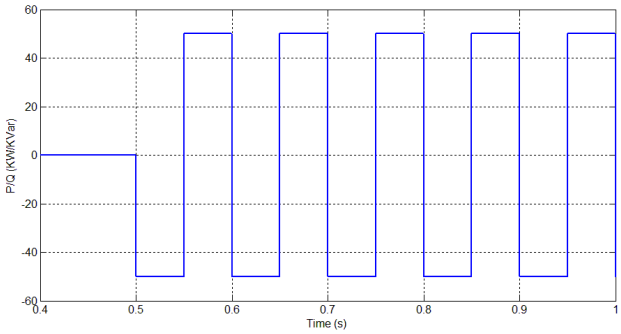

Figure 8-4: The injected P_{cont} and Q_{cont} test signals.

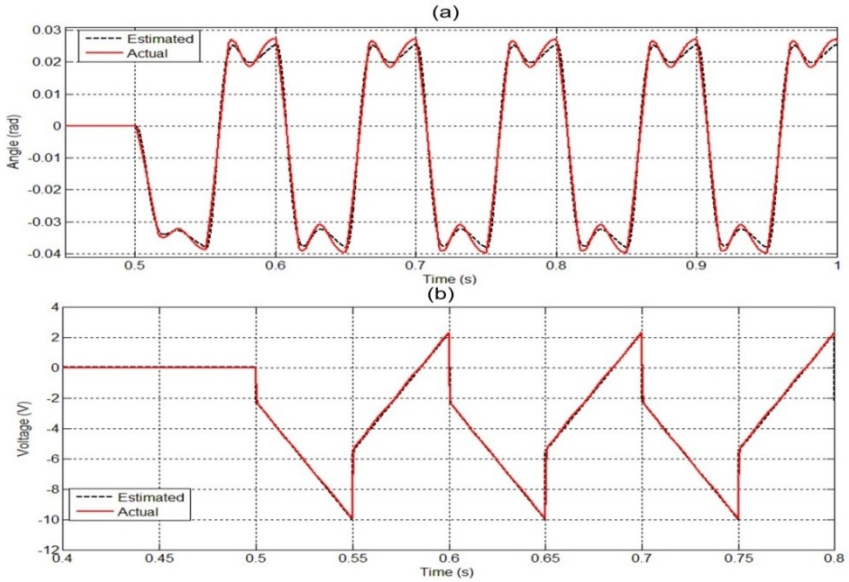

Figure 8-5: the estimated and actual (a) Angle and (b) Voltage deviations at the point of common coupling due to the application of the test signals in Figure 8-4.

The accuracy of the estimated transfer function is shown in Figure 8-5 (a) where the actual angle deviation is compared with the estimated one. Equation (8-4) shows the 3rd-order identified transfer function between P_{cont} and $\Delta\delta_{PCC1}$. The parameters are given in Appendix C.

$$G_{\delta} = \frac{\Delta\delta_{PCC1}}{\Delta P_{cont}} = \frac{K_{P\delta}(1+T_{z\delta}s)}{s(1+2\xi T_{w\delta}\ s+(T_{w\delta}s)^2)(1+T_{p\delta}s)} \tag{8-4}$$

Similarly by applying the same test signal of Figure 8-4 as for Q_{cont}, the voltage amplitude deviations ($\Delta|V_{PCC1}|$) at the point of common coupling are measured and a 1st-order transfer function in the form of (8-5) is used. Figure 8-5 (b) verifies that the estimated signal matches the actual one quite well.

$$G_V = \Delta\,|V_{PCC1}|\,/\Delta Q_{cont} = K_{PV}\ (1+T_{zV}s)/(1+T_{pV}s) \tag{8-5}$$

Using the estimated transfer functions of (8-4) and (8-5) we are now able to design the synchronizing controllers of C_v and C_θ shown in Figure 8-2 via loop shaping method. Prior to designing these controllers, let us derive the linearized transfer functions between P_{cont} and P_{tie1} as well as Q_{cont} and Q_{tie1} respectively. The active and reactive power flow between the two MGs can be expressed by (8-6) and (8-7).

$$P_{tie} = 3\times[-V_{PCC1}{}^2 G_{tie} + V_{PCC1}V_{PCC2}(B_{tie}\sin\delta_{PCC12} + G_{tie}\cos\delta_{PCC12})] \tag{8-6}$$

$$Q_{tie} = 3[V_{PCC1}{}^2 B_{tie} + V_{PCC1} V_{PCC2} (G_{tie} \sin \delta_{PCC12} - B_{tie} \cos \delta_{PCC12})] \quad (8\text{-}7)$$

Note that in the test system of Figure 8-1, the voltage and angle differences between MG1 and 2 are only assumed to be controlled by MG1; therefore, $\Delta|V_{PCC2}|$ and $\Delta\delta_{PCC2}$ can be considered to be zero. Moreover, considering the inductive tie-line, the active power flow can be assumed to be mainly associated with the angle deviations while the voltage deviations are affecting the reactive power flow.

Therefore, (8-8),(8-9) yield a scaled version of the same transfer functions in (8-4) and (8-5). Note that K_δ and K_v in (8-8),(8-9) are dependent on the operating conditions and are listed in Appendix C.

$$\frac{\Delta P_{tie}}{\Delta P_{cont}} = 3V_{PCC1} V_{PCC2} . (B_{tie} \cos(\delta_{0PCC12}) - G_{tie} \sin(\delta_{0PCC12})) \frac{\Delta \delta_{PCC1}}{\Delta P_{cont}} = K_\delta G_\delta \quad (8\text{-}8)$$

$$\frac{\Delta Q_{tie}}{\Delta Q_{cont}} = 3(2V_{PCC1} . B_{tie} + V_{PCC2} (G_{tie} \sin(\delta_{0PCC12}) - B_{tie} \cos(\delta_{0PCC12})) . (\frac{\Delta |V_{PCC1}|}{\Delta Q_{cont}}) = K_v G_v \quad (8\text{-}9)$$

Equations (8-8),(8-9) reveal that once the synchronizing controllers of C_v and C_θ are designed for the estimated plants of (8-4) and (8-5), the same controllers can be scaled by K_δ^{-1} and K_V^{-1} to be adopted as the power flow regulators. Note that K_δ^{-1} and K_V^{-1} can be calculated based on the desired power flow range and the associated voltage and angle conditions at the points of common coupling. The loop shaping method is used to design the angle and voltage controllers. Figure 8-3 suggests that the power associated dominated modes show very slow dynamics (30-40 rad/s considering the design specifications provided in Figure 8-3 (d)). Therefore, the hierarchical structure of the proposed control scheme of Figure 8-2 asks for the design of low bandwidth synchronizing and power-tie controllers which comply with the slow dynamics of the inner control loops. The desired loop bandwidths are therefore assumed to be 10 rad/s and 5 rad/s for the angle and voltage open loop frequency responses, respectively. Note that different bandwidths are considered to provide a frequency-scale separation between the active and reactive power synchronizing controllers. This will enhance the decoupling between the angle- and voltage-related synchronization dynamics. The designed synchronizing angle and voltage controllers are given by (8-10) and (8-11).

$$C_\delta = \frac{937730.938(s + 4.265e4)(s + 2.4e-4)(s^2 + 74.18s + 1.781e4)}{s(s + 9.602)(s^2 + 5677 * s + 3.723e7)} \quad (8\text{-}10)$$

$$C_V = 1.106e5(s+0.03634)/(s^2+68.99s) \tag{8-11}$$

The resulting loop-gain frequency responses are also presented in Figure 8-6 and Figure 8-7 respectively where it can be seen that the desired loop bandwidths are achieved. The frequency location of the controllers' zeroes and poles that are designed to achieve the desired bandwidth are also shown in the responses.

Note that as suggested in (8-8),(8-9), the following controllers can be then adopted for power-tie flow control purposes, where K_δ and K_v are given in Appendix C.

$$P_{\_tie\_controler} = C_\delta / K_\delta \tag{8-12}$$

$$Q_{\_tie\_controler} = C_V / K_V \tag{8-13}$$

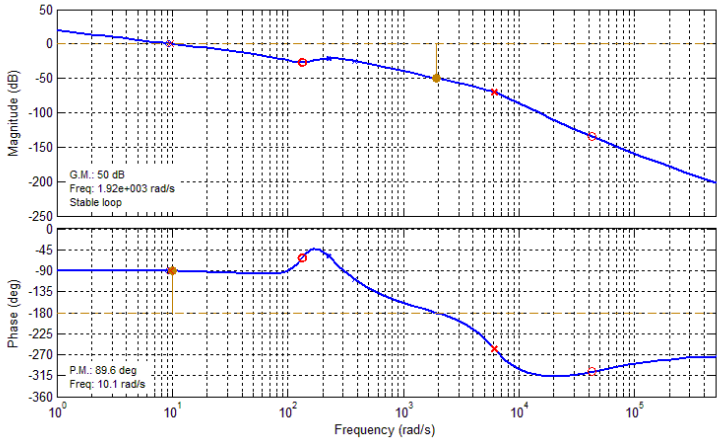

Figure 8-6: Frequency response of $G_\delta.C_\delta$.

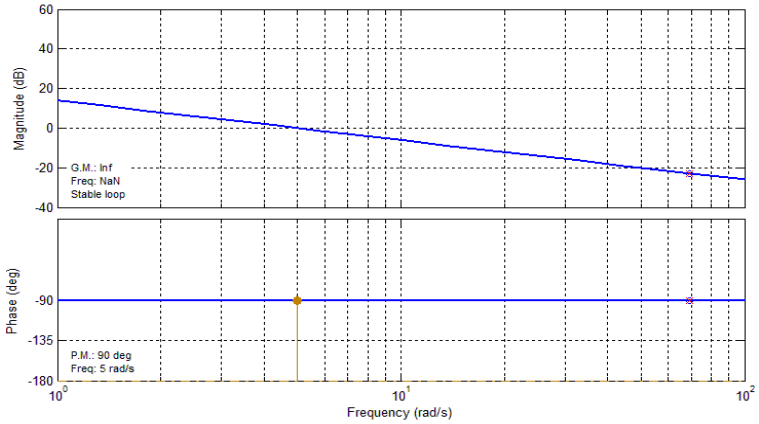

Figure 8-7: Frequency response of *Gv.Cv*.

8.3 Evaluation Results

To show the effectiveness of the proposed hierarchical control structure in synchronization and power flow control between MGs, the two MGs shown in Figure 8-2 which were initially assumed to operate in their islanded modes, are to be connected. The voltage and angle levels in MG1 are different from MG2 prior to their connection. Note each MG in Figure 8-2 consists of two dispatchable units while a PV unit with variable power generation level (0-0.4 p.u.) is included in MG2. For the first set of simulations, the PV unit is assumed to be generating 200kW (0.4p.u.) at unity power factor. The synchronization process is then started at t = 1s by activating mode 2 in MG1. Note that without the loss of generality, only MG1 is used for the synchronization and power control purposes. Once operating in mode 2, the voltage and phase errors are constantly reduced and as soon as they become smaller than a pre-defined tolerance, the two MGs are connected, and the operational mode should be changed into mode 3 in order to control the power flow between the two MGs.

Figure 8-8(a),(b) show the voltage and angle differences between the two MGs across the switch S_{MG1} prior and after its connection respectively ($|V_{PCC1}|$-$|V_{PCC2}|$, δ_{PCC1}-δ_{PCC2}). The errors are reduced using the proposed controllers until they are smaller than the tolerance. This is achieved at t = 2.15s when the two MGs are connected. Figure 8-9 (a) shows the tie-line power between the two MGs after connection. The active/reactive power flow is controlled via MG1 as it is operating in mode 3. The line current is also shown in Figure 8-9 (b).

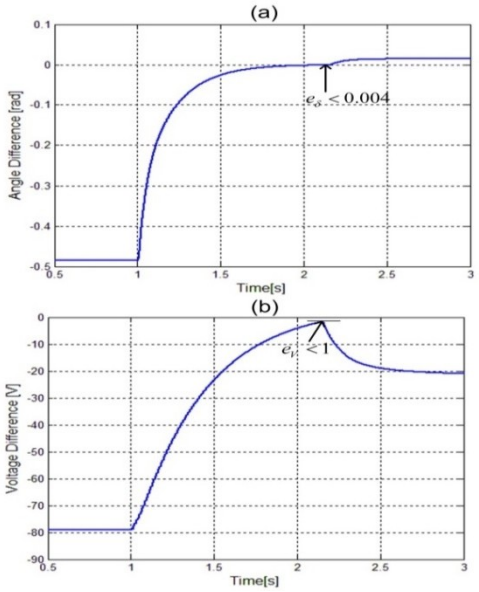

Figure 8-8: (a) the phase error (δ_{PCC1}-δ_{PCC2}) and (b) the voltage error ($|V_{PCC1}|$-$|V_{PCC2}|$) at the PCC.

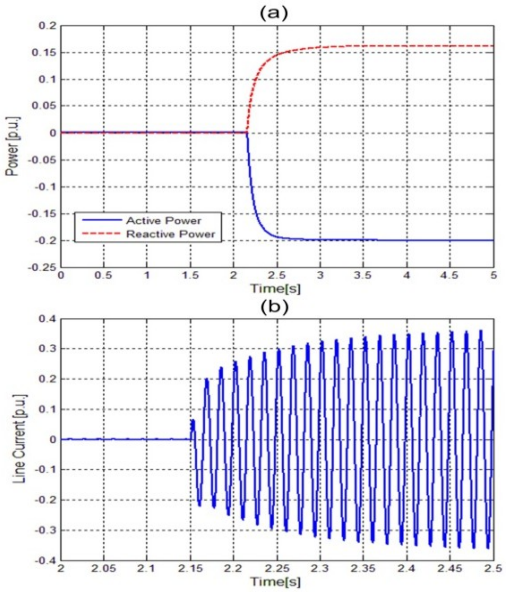

Figure 8-9: (a) Active and reactive power-tie flow from MG1 to MG2 (b) the line current.

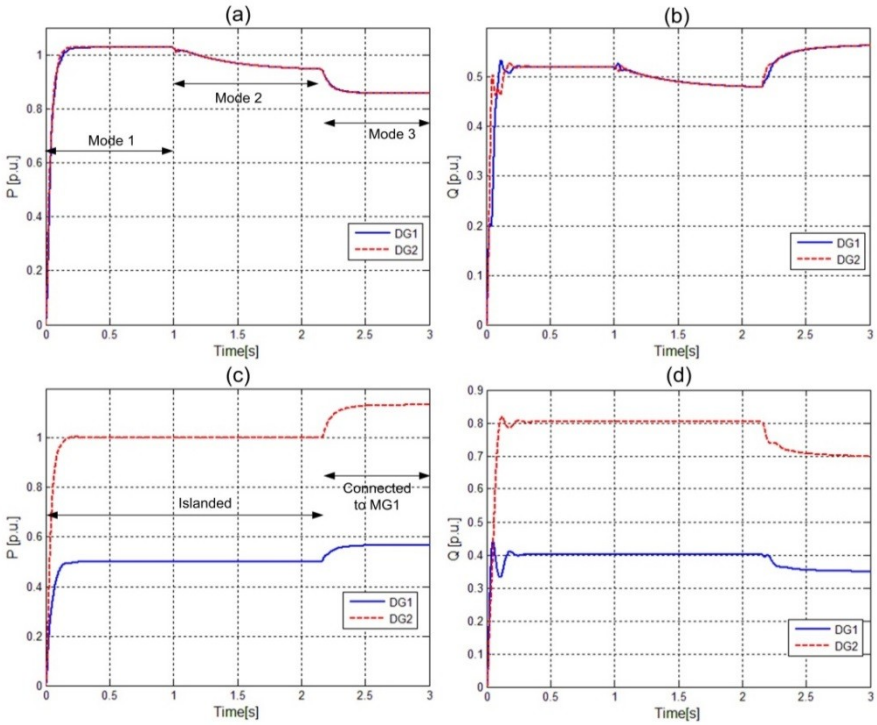

Figure 8-10: The DG units power responses when the two MGs are connected at t = 2.15s in (a),(b) MG1 and (c),(d) MG2.

The active and reactive power responses generated by the dispatchable units in each MG are also shown in Figure 8-10. Note that in order to show the flexibility of the proposed control scheme in sharing the power demand between the DG units in each MG based on their local power sharing objectives, the active and reactive powers are decided

to be shared equally between the two DGs inside MG1 while the share of DG1 in MG2 is assumed to be half of DG2. Note that these sharing ratios are chosen arbitrarily and can be updated based on a local cost optimization algorithm decided inside the MG dispatch centre. As can be seen from Figure 8-10, prior, during and after the activation of the synchronization process, the power demands in both MGs are shared among the entities as desired. However, note that once the synchronization process is activated at t = 1s, the voltage level in MG1 is reduced to match that in MG2 (as suggested in Figure 8-8(b)). Therefore, the active and reactive power consumptions associated with the adopted RL load model are slightly reduced in MG1 during the synchronization interval. After the connection of the two MGs, the power flow control algorithm is activated (mode 3). At this point, considering the excessive active power generated by the PV entity (0.4 p.u.), the tie-active power reference is set to -0.2 p.u in order to enable MG1 to import active power from the neighboring cluster. This can be seen in Figure 8-10(a),(c) as the active power generated by the dispatchable units are reduced and increased in MG1 and MG2, respectively. However, the reactive power demand in MG2 is considered to be higher and therefore, MG1 is expected to contribute to the inductive load located in the second MG by exporting 80 kVar (0.16 p.u.) reactive power.

As suggested in Figure 8-10(b),(d), this will result in an increase in the generated reactive power level in MG1 yielding to reduced reactive power generation by the DG units in MG2. The well-damped power responses verify the effectiveness of the proposed power control design methods adopted for both inner loop (DPR) and outer loop (synchronization/power-tie control) at different power levels. As stated earlier, the synchronization and power flow control is achieved via generating the appropriate auxiliary power signals (P_{cont}, Q_{cont}). These signals are shown in Figure 8-11(a). As expected, these signals are generated only temporarily to adjust the angle and voltage levels and once the desired operating point is achieved, they converge to zero. The V_{PCC1} voltage waveforms at the moment of connection of the two MGs (t = 2.15s) are also shown in Figure 8-11(b). Figure 8-12(a) shows the frequency deviation caused in MG1 due to the injection of the auxiliary P_{cont} signal. The temporary frequency deviations are used to minimize the phase error during the synchronization process. Note that the steady-state frequency is maintained at 60 Hz through the adoption of the distributed power sharing algorithm as discussed in Chapter 7.

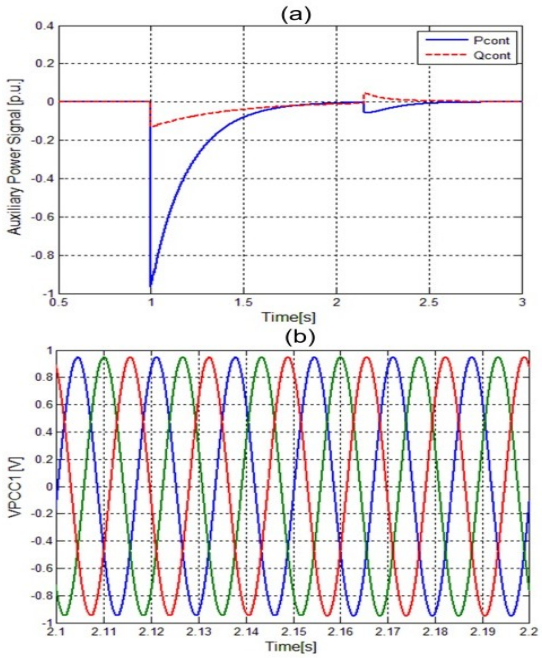

Figure 8-11: (a) P_{cont} and Q_{cont} auxiliary signals (b) The V_{PCC1} voltage waveforms at the moment of connection of the two MGs.

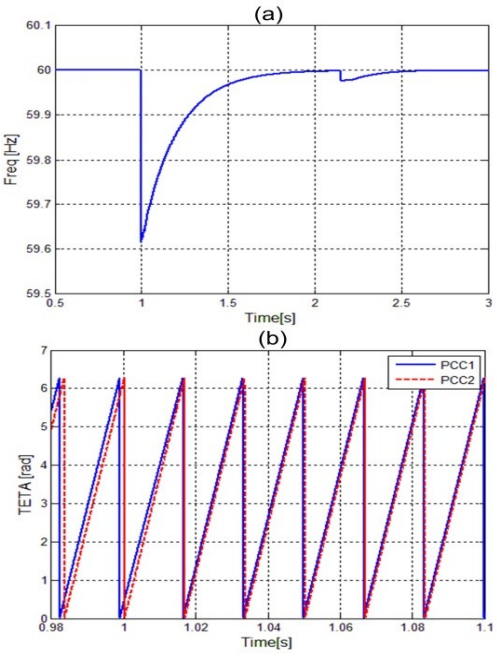

Figure 8-12: (a) MG1 frequency deviation for synchornization purpose (b) The effect of frequency transients on the output of MG1's 3-phase PLL.

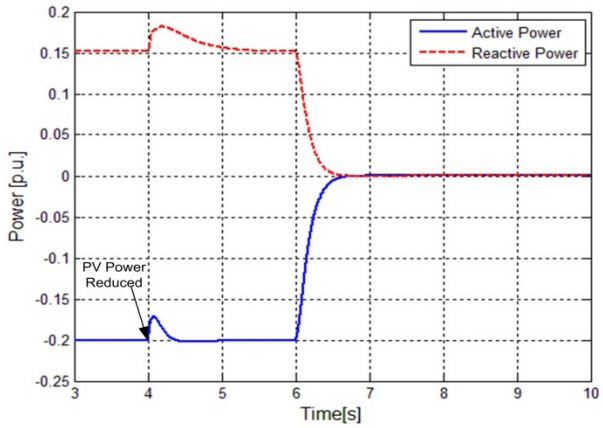

Figure 8-13: Active and reactive power-tie from MG1 to MG2 when P_{PV} is changes from 0.4 to 0.2 p.u. at t = 4s and when P_{tie} and Q_{tie} are set to zero at t = 6s.

The effect of frequency transients on the output of MG1's 3-phase PLL is shown in Figure 8-12 (b) where it is compared with the PLL output from V_{PCC2} of Figure 8-2. It can be seen that the initial phase miss-match is reduced due to the frequency transient generated by the synchronization unit. Moreover, it should be noted that transient frequency deviations are necessary to control the power-tie flow when the two MGs are connected to each other. This can be seen at t = 2.15s in Figure 8-12(a) where a slight

frequency deviation is generated in order to adjust δ_{PCC1} with respect *to* δ_{PCC2} to achieve the desired power flow.

One of the main objectives of the proposed control structure is to enable power transfer between the two MGs based on the generation/demand estimation provided by the higher level Optimization/Estimation control centre. In order to show this feature, the power generated by the PV unit located in MG2 is assumed to be reduced from 0.4 to 0.2 p.u. at t = 4s. This variation in the power generation is then assumed to be estimated by the optimization/estimation control centre at t = 6s. Therefore, it is decided that MG1 should no longer import any power from MG2; thus, the power-tie level is set to zero in order to maintain the PV generation for MG2 local demand. Figure 8-13 shows the active and reactive power-tie values. As can be seen prior to changing the power-tie reference to zero, the power-tie values are maintained at their initial levels despite of the change in the PV generation level. At t = 6s both active and reactive power flows are set to zero; thus, the remaining power generated by the PV unit is only used to supply MG2.

Figure 8-14 shows the power responses of the dispatchable units in MG1 and MG2 to the PV generation decrease and the subsequent power-tie correction. The adopted power sharing ratios in each MG are the same as before. As shown in Figure 8-14(c), once the PV power generation is reduced, it should be compensated for by the remaining two dispatch-able DG units in MG2 in order to maintain the power-tie level. However at t = 6s, the power-tie is decided to be reduced to zero yielding an active power generation increase in MG1 due to the fact that no power is imported anymore (Figure 8-14 (a)). Note that the reactive power generation level in MG1 is decreased due to the fact that no more reactive power is exported from MG1 anymore (Figure 8-14 (b)). This will result in a reactive power generation increase in MG2 as seen in Figure 8-14 (d).

The direction of the power flow between the two MGs can also be controlled by the power-tie control unit. In this set of simulations, the power-tie is initially assumed to be zero while the generated active power by the PV unit in MG2 is 0.2 p.u. However, the PV generation level is assumed to further reduce to zero at t = 4s. The power-tie level is then updated by the Estimation/Optimization control centre to match the new conditions at t = 6s by allocation +0.2 p.u. active power to be exported from MG1 to MG2 at unity power factor.

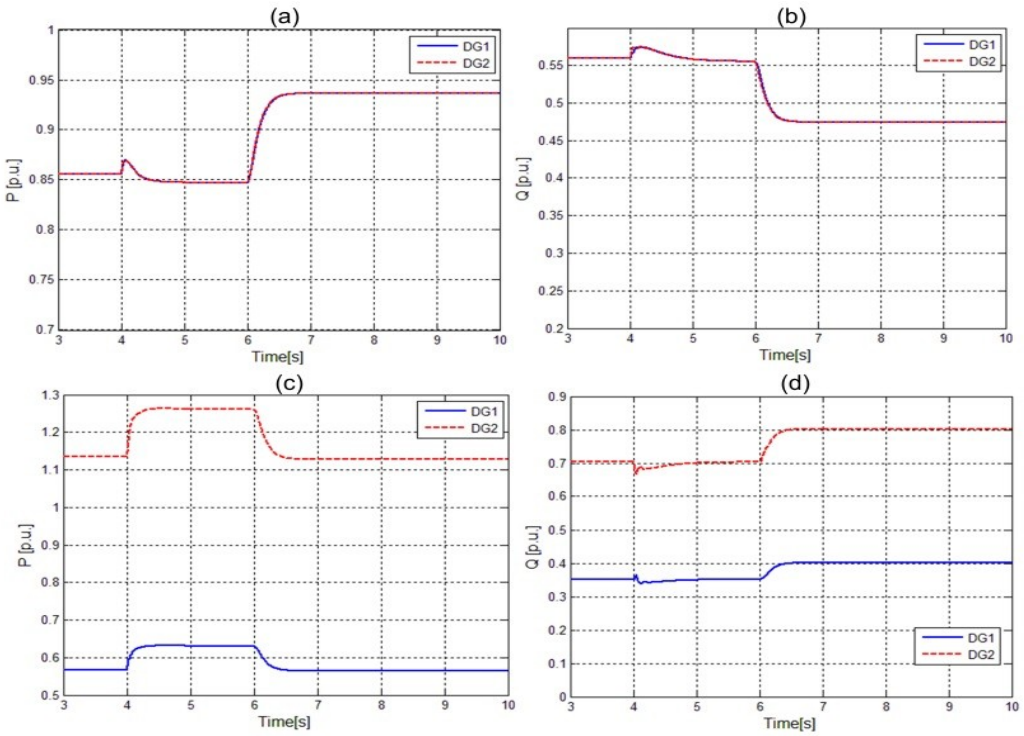

Figure 8-14: The DG units power responses when P_{PV} is changed from 0.4 to 0.2 p.u. at t = 4s and when P_{tie} is increased from -0.2 p.u. to 0 at t = 6s. in (a),(b) MG 1 and (c),(d) MG 2.

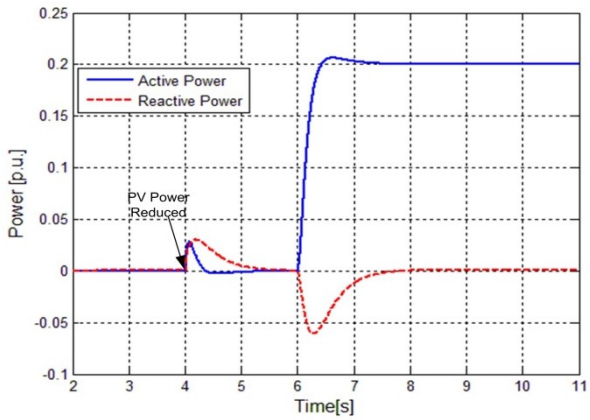

Figure 8-15: Active and reactive power-tie from MG1 to MG2 when P_{PV} is changes from 0.2 p.u. to 0 at t = 4s and when P_{tie} is increased from 0 to 0.2 p.u. at t = 6s.

Figure 8-15 shows the power-tie dynamics where it can be seen that after the PV generation level is reduced and prior to updating the power-tie values by the upper level control centre, the power-tie values are maintained at zero. However at t = 6s, it is decided to export 0.2 p.u. from MG1 in order to compensate for the generation shortage at the neighboring MG entity. Note that the reactive power flow is maintained at zero to show the decoupling achieved by the controller.

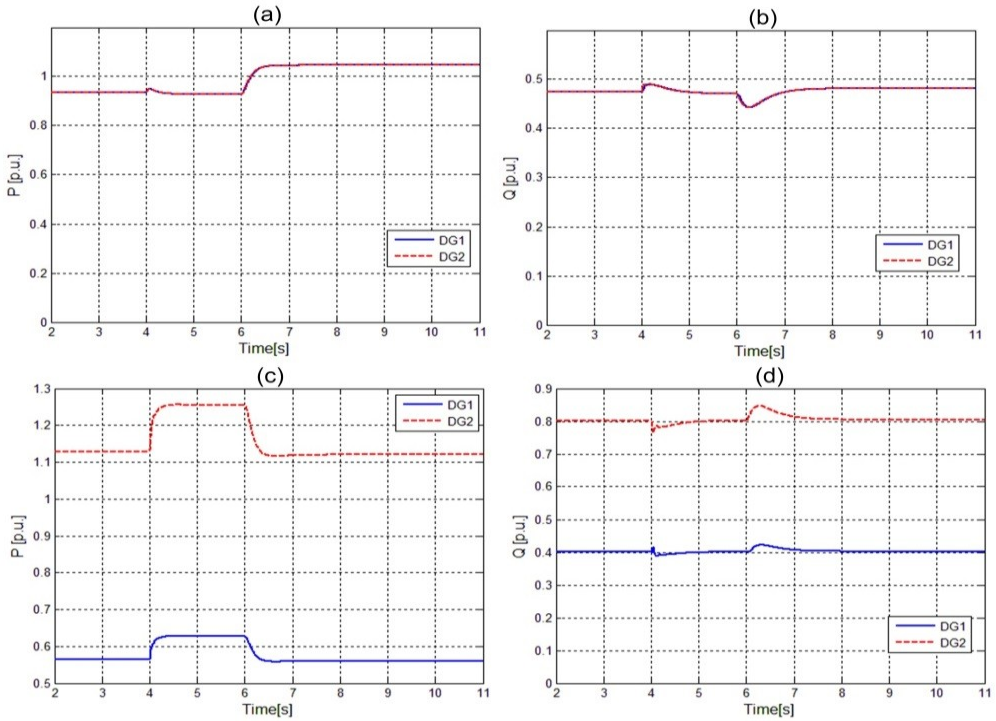

Figure 8-16: The DG units power responses when P_{PV} is changes from 0.2 p.u. to 0 at t = 4s and when P_{tie} is increased from 0 to 0.2 p.u. at t = 6s. in (a),(b) MG 1 and (c),(d) MG 2.

The power responses of the dispatchable DG units in both MG1 and MG2 are shown in Figure 8-16.(a),(b) and Figure 8-16 (c),(d) respectively. As P_{PV} is reduced to zero at t = 4s, the power generated by the DG units in MG2 are increased to supply the local demand. However, as can be seen from Figure 8-16 (a),(c) at t = 6s the power is imported by MG2 and therefore the power levels are reduced back to their initial values whereas the power generated by the DG entities in MG1 are increased. Note that since Q_{tie1}^{*} is set to zero, the reactive power levels are maintained at their values.

8.4 Summary and Conclusions

A comprehensive distributed control framework for power sharing, active synchronization and power-flow control among multiple interconnected MGs is presented in this chapter. The proposed control structure not only eliminates the frequency deviations, power sharing errors, and stability concerns associated with conventional droop control in MGs, but also yields: 1) improved MG dynamic performance, 2) minimized active/reactive power sharing errors, and 3) active synchronization and power-tie control between interconnected MGs without interfering with the inner power sharing

loops. A theoretical analysis and detailed simulation results are presented to show the effectiveness of the proposed control structure.

Chapter 9

Conclusion

9.1 Research Summary and Contributions

The main goal of this research is to develop novel converter-level and system-level control interfaces that can guarantee stable and high quality operation of MG systems as the future building block of active distribution systems. Such interfaces should provide robust stability and performance of the DG entities and MGs under challenging uncertain nature of distribution systems. Therefore the research objectives of this thesis are identified to address several stability and coordination challenges facing MG systems. In order to achieve these research objectives, several novel control algorithms at both the converter-level and system-level were introduced.

Under the smart grid environment, DG units should be included in the system operational control framework, where they can be used to enhance system reliability by providing backup generation in isolated mode, and to provide ancillary services (e.g. voltage support and reactive power control) in the grid-connected mode. To meet these requirements, an interactive DG interface for flexible MG operation in the smart distribution system environment was proposed in Chapter 2. The proposed interface utilizes a fixed power-voltage-current cascaded control structure to minimize control function switching and is equipped with internal model control structure to maximize the disturbance rejection performance within the DG interface. The proposed control system facilitates flexible and robust DG operational characteristics such as 1) voltage or reactive power regulated operation (PV-Bus or PQ-Bus) in the grid-connected mode, 2) regulated power control in autonomous MG mode, 3) smooth transition between autonomous and grid connected mode and vice versa, 4) reduced voltage distortion under nonlinear loading conditions, and 5) robust control performance under islanding detection delays. Evaluation results are presented to demonstrate the flexibility and effectiveness of the proposed controller.

It was discussed in Chapter 3 that in the conventional hierarchical DG control interfaces as well as the structure introduced in Chapter 2, the voltage and power-angle

interaction dynamics between the DG converters and the rest of a MG system are not accounted for in the design procedure. Therefore a system-oriented design approach was suggested to be adopted in order to provide control system robustness against system-level interactions without strict knowledge of complete MG system dynamics. To achieve this, the MG system is modeled by a dynamic equivalent circuit, which might include uncertainties induced due to MG impedance variation and interactions with the equivalent MG bus-voltage. The equivalent MG model along with local load interactions and uncertainties are augmented with the DG interface power circuit model to develop a robust H_∞ voltage controller. To account for power angle interaction dynamics, an angle feed-forward control approach is adopted, where the angle of the equivalent MG bus, as seen by each DG units, is estimated and used for feed-forward control. Unlike conventional droop controllers, the proposed scheme yields a two-degree-of-freedom controller, resulting in stable and smooth power sharing performance over a wide range for the static droop gain and also at different loading conditions. A theoretical analysis and comparative simulation and experimental results are presented to demonstrate the robustness and effectiveness of the proposed control scheme.

It was discussed in Chapter 4 that the adoption of PFC capacitors and residential capacitive loads in MGs can introduce severe voltage stability issues due to the uncertain nature of the associated resonance peaks. Therefore, unlike the conventional H_∞-based control design, an improved uncertainty modeling approach was suggested to facilitate the realization of a robust controller based on structured singular values (μ) analysis. The resultant direct voltage controller does not require any additional passive or active damping loops. This feature reduces the sensor requirements in the DG interface controller and enhances the bandwidth characteristics of the closed-loop voltage-controlled converter. Mathematical and comparative analyses are provided to show the advantages of the proposed μ-synthesis controller over the conventional H_∞ controller in maintaining robust stability as well as robust performance of the MG in the presence of parameter uncertainties and uncertain resonant peaks caused by connection of PFC capacitors. Systematic design approach for the proposed controller is presented. Time-domain simulation studies and comparative experimental results are presented to show the effectiveness and robustness of the proposed controller in MG applications.

Chapter 5 presented a robust direct single-loop current control scheme based on the structured singular value (μ) minimization approach for LCL-filtered current controlled

distributed generation converters in grid-connected and isolated MG modes. Unlike the conventional H_∞-based approach, the proposed interface maintains perturbed system stability, under a wide range of grid (or MG) impedance variations, without the application of any additional damping loops. Moreover, the performance of the perturbed system in terms of grid-voltage and harmonic disturbance rejection can be improved significantly by the adopted method. This is due to the less conservative nature of the μ-synthesis based solution as it takes advantage of the additional structure introduced to the uncertainty block by the performance criteria. The salient features of the proposed controller are 1) single-loop direct current control of LCL-filtered converters with inherent damping of the LCL filter resonance without any need for additional damping loops, 2) robust stability and active damping performances by mitigating the LCL resonance under wide range of grid (or MG) impedance variation, 3) improving the performance of the current controller by removing its dependency on the grid-voltage feed-forward loop by providing high disturbance rejection feature against fundamental and harmonic voltage disturbances. 4) computationally-efficient fixed-order structure with minimum sensor requirements (only grid-side currents are needed for feedback control). A comparative theoretical analysis, time-domain simulation results and experimental test results are presented to show the effectiveness of the proposed control scheme.

In Chapter 6, the dynamics of medium-voltage MG systems was studied under the presence of MW motor type loads. It was noted that in most of the MG stability analysis in the literature, only static type load models were adopted. However the highly-nonlinear IM dynamics that couple the active power, reactive power, voltage and supply frequency dynamics challenge the stability of MV droop-controlled MGs. Therefore, to fill in this gap, a detailed small-signal model of a typical MV droop-controlled MG system –based on IEEE Standard 399 - with both dynamic and static loads is developed. The proposed model accounts for the impact of supply frequency dynamics associated with the droop-control scheme to accurately link the MG frequency dynamics to the motor dynamics. The analysis suggests that the adoption of IM loads introduces new oscillatory modes that are mainly associated with the slow electromechanical rotor dynamics. Participation factor analysis is performed to identify the DG parameters with highest contribution yielding to a two-degree-of-freedom active damping controller that can effectively stabilize the new oscillatory dynamics. The proposed supplementary active damping controller does not interfere with the steady-state performance and yields a robust control

performance under a wide range of droop parameters, and robust damping performance at small- and large-signal disturbances. Theoretical analysis, simulation and experimental results are presented to show the effectiveness of the proposed control scheme.

Although the stability challenges associated with the conventional autonomous control scheme can be mitigated to some extent via the adoption of the converter-level control interfaces proposed in Chapter 3 –Chapter 6. However, as discussed in Chapter 7, in order to fully address the frequency deviation, reactive power sharing error and stability concerns associated with conventional autonomous droop control, new networked-based control strategies are required. Therefore a new hybrid distributed networked-based power control scheme is provided in Chapter 7 that provides 1) improved MG dynamic performance, 2) minimized active/reactive power sharing errors under unknown line impedances, and 3) high reliability and robustness against network failures or communication delays. The distributed nature of the proposed scheme as well as its low-bandwidth communication system requirements allow it to provide great robustness against communication delays and network failures. Further, a pole placement technique is adopted to design the distributed power regulators adopted in the proposed method by adoption of a generalized and computationally efficient modeling approach that captures the dominant dynamics of a MG system thus, allowing effective controller tuning. Comparative simulation and experimental results are presented to show the validity and effectiveness of the proposed controller.

In Chapter 8, a comprehensive coordinating control system is proposed to realize the smart grid paradigm where the power can flow between the clusters of distributed generation MG systems. The proposed hierarchical control structure which benefits from the distributed structure suggested in Chapter 7, not only captures the advantages of the previously introduced hybrid networked-based control structure but also yields active synchronization and power-tie control between interconnected MGs without interfering with the inner power sharing loops. A theoretical analysis and detailed simulation results are presented to show the effectiveness of the proposed control structure.

9.2 Directions for Future Work

In continuation of this work, the following subjects are suggested for future studies:

- In MG systems, energy storage capability of the system should be significantly enhanced by proposing both converter- and system-level control algorithms.
- Analytical software tools are needed to be developed in order to study the overall static and dynamic stability of wide area converter-dominated distributed power systems.
- Optimization algorithms should be designed and tested using the control framework introduced in Chapters 7 and 8 in order to provide lower energy losses and higher reliability through active monitoring and power-tie regulation among clusters of MGs and the utility grid in a sustainable manner.
- Wide area stabilization of converter dominated multi-MG systems is required by proposing real-time cooperative control algorithms which can effectively increase marginal stability.
- The rapid expansion of communication networks has brought the future vision of smart grids where sharing information among distributed entities can introduce new levels of intelligence to the existing power system. Therefore future research plans should investigate the network protocols and requirements for the realization of such a vision.

Bibliography

[1] "IEEE Recommended Practice for Interconnecting Distributed Resources with Electric Power Systems Distribution Secondary Networks," *IEEE Std 1547.6-2011,* pp. 1-38, 2011.

[2] "Smart Grid: An Introduction," the U.S. Department of Energy, 2009.

[3] E. M. Lightner and S. E. Widergren, "An Orderly Transition to a Transformed Electricity System," *Smart Grid, IEEE Transactions on,* vol. 1, pp. 3-10, 2010.

[4] K. Moslehi and R. Kumar, "A Reliability Perspective of the Smart Grid," *Smart Grid, IEEE Transactions on,* vol. 1, pp. 57-64, 2010.

[5] G. T. Heydt, "The Next Generation of Power Distribution Systems," *Smart Grid, IEEE Transactions on,* vol. 1, pp. 225-235, 2010.

[6] A. Timbus, M. Liserre, R. Teodorescu, P. Rodriguez, and F. Blaabjerg, "Evaluation of Current Controllers for Distributed Power Generation Systems," *Power Electronics, IEEE Transactions on,* vol. 24, pp. 654-664, 2009.

[7] J. M. Guerrero, J. C. Vasquez, J. Matas, L. G. de Vicuna, and M. Castilla, "Hierarchical Control of Droop-Controlled AC and DC Microgrids; A General Approach Toward Standardization," *Industrial Electronics, IEEE Transactions on,* vol. 58, pp. 158-172, 2011.

[8] M. Liserre, R. Teodorescu, and F. Blaabjerg, "Multiple harmonics control for three-phase grid converter systems with the use of PI-RES current controller in a rotating frame," *Power Electronics, IEEE Transactions on,* vol. 21, pp. 836-841, 2006.

[9] Y. A. R. I. Mohamed, E. F. El-Saadany, and M. M. A. Salama, "Adaptive Grid-Voltage Sensorless Control Scheme for Inverter-Based Distributed Generation," *Energy Conversion, IEEE Transactions on,* vol. 24, pp. 683-694, 2009.

[10] M. Liserre, R. Teodorescu, and F. Blaabjerg, "Stability of photovoltaic and wind turbine grid-connected inverters for a large set of grid impedance values," *Power Electronics, IEEE Transactions on,* vol. 21, pp. 263-272, 2006.

[11] T. Erika and D. G. Holmes, "Grid current regulation of a three-phase voltage source inverter with an LCL input filter," *Power Electronics, IEEE Transactions on,* vol. 18, pp. 888-895, 2003.

[12] D. Min, M. N. Marwali, J. Jin-Woo, and A. Keyhani, "Power Flow Control of a Single Distributed Generation Unit," *Power Electronics, IEEE Transactions on,* vol. 23, pp. 343-352, 2008.

[13] K. Hyosung, Y. Taesik, and C. Sewan, "Indirect Current Control Algorithm for Utility Interactive Inverters in Distributed Generation Systems," *Power Electronics, IEEE Transactions on,* vol. 23, pp. 1342-1347, 2008.

[14] Y. Zhilei, X. Lan, and Y. Yangguang, "Seamless Transfer of Single-Phase Grid-Interactive Inverters Between Grid-Connected and Stand-Alone Modes," *Power Electronics, IEEE Transactions on,* vol. 25, pp. 1597-1603, 2010.

[15] G. Fang and M. R. Iravani, "A Control Strategy for a Distributed Generation Unit in Grid-Connected and Autonomous Modes of Operation," *Power Delivery, IEEE Transactions on,* vol. 23, pp. 850-859, 2008.

[16] Y. A. R. I. Mohamed and A. A. Radwan, "Hierarchical Control System for Robust Microgrid Operation and Seamless Mode Transfer in Active Distribution Systems," *Smart Grid, IEEE Transactions on,* vol. 2, pp. 352-362, 2011.

[17] F. Katiraei, M. R. Iravani, and P. W. Lehn, "MG autonomous operation during and subsequent to islanding process," *Power Delivery, IEEE Transactions on,* vol. 20, pp. 248-257, 2005.

[18] Y. A. R. I. Mohamed and E. F. El-Saadany, "Adaptive Decentralized Droop Controller to Preserve Power Sharing Stability of Paralleled Inverters in Distributed Generation Microgrids," *Power Electronics, IEEE Transactions on,* vol. 23, pp. 2806-2816, 2008.

[19] N. Pogaku, M. Prodanovic, and T. C. Green, "Modeling, Analysis and Testing of Autonomous Operation of an Inverter-Based Microgrid," *Power Electronics, IEEE Transactions on,* vol. 22, pp. 613-625, 2007.

[20] Y. Wei, C. Min, J. Matas, J. M. Guerrero, and Q. Zhao-ming, "Design and Analysis of the Droop Control Method for Parallel Inverters Considering the Impact of the Complex Impedance on the Power Sharing," *Industrial Electronics, IEEE Transactions on,* vol. 58, pp. 576-588, 2011.

[21] A. Mehrizi-Sani and R. Iravani, "Potential-Function Based Control of a Microgrid in Islanded and Grid-Connected Modes," *Power Systems, IEEE Transactions on,* vol. 25, pp. 1883-1891, 2010.

[22] J. A. Peas Lopes, C. L. Moreira, and A. G. Madureira, "Defining control strategies for MicroGrids islanded operation," *Power Systems, IEEE Transactions on,* vol. 21, pp. 916-924, 2006.

[23] M. C. Chandorkar, D. M. Divan, and R. Adapa, "Control of parallel connected inverters in standalone AC supply systems," *Industry Applications, IEEE Transactions on,* vol. 29, pp. 136-143, 1993.

[24] R. Majumder, G. Ledwich, A. Ghosh, S. Chakrabarti, and F. Zare, "Droop Control of Converter-Interfaced Microsources in Rural Distributed Generation," *Power Delivery, IEEE Transactions on,* vol. 25, pp. 2768-2778, 2010.

[25] A. Seon-Ju, P. Jin-woo, C. Il-Yop, M. Seung-Il, K. Sang-hee, and N. Soon-Ryul, "Power-Sharing Method of Multiple Distributed Generators Considering Control Modes and Configurations of a Microgrid," *Power Delivery, IEEE Transactions on,* vol. 25, pp. 2007-2016, 2010.

[26] M. N. Marwali and A. Keyhani, "Control of distributed generation systems-Part I: Voltages and currents control," *Power Electronics, IEEE Transactions on,* vol. 19, pp. 1541-1550, 2004.

[27] G. Weiss, Z. Qing-Chang, T. C. Green, and L. Jun, "H∞ repetitive control of DC-AC converters in microgrids," *Power Electronics, IEEE Transactions on,* vol. 19, pp. 219-230, 2004.

[28] H. Karimi, E. J. Davison, and R. Iravani, "Multivariable Servomechanism Controller for Autonomous Operation of a Distributed Generation Unit: Design

and Performance Evaluation," *Power Systems, IEEE Transactions on,* vol. 25, pp. 853-865, 2010.

[29] Y. A. R. I. Mohamed and E. F. El-Saadany, "A Control Scheme for PWM Voltage-Source Distributed-Generation Inverters for Fast Load-Voltage Regulation and Effective Mitigation of Unbalanced Voltage Disturbances," *Industrial Electronics, IEEE Transactions on,* vol. 55, pp. 2072-2084, 2008.

[30] H. Karimi, A. Yazdani, and R. Iravani, "Robust Control of an Autonomous Four-Wire Electronically-Coupled Distributed Generation Unit," *Power Delivery, IEEE Transactions on,* vol. 26, pp. 455-466, 2011.

[31] A. Kahrobaeian and Y. A. R. I. Mohamed, "Interactive Distributed Generation Interface for Flexible MG Operation in Smart Distribution Systems," *Sustainable Energy, IEEE Transactions on,* vol. 3, pp. 295-305, 2012.

[32] L. Kojovic, "Impact DG on voltage regulation," in *Power Engineering Society Summer Meeting, 2002 IEEE*, 2002, pp. 97-102 vol.1.

[33] P. Brady, C. Dai, and Y. Baghzouz, "Need to revise switched capacitor controls on feeders with distributed generation," in *Transmission and Distribution Conference and Exposition, 2003 IEEE PES*, 2003, pp. 590-594 vol.2.

[34] R. C. Dugan and R. C. Dugan, *Electrical power systems quality*, 2nd ed. New York: McGraw-Hill, 2003.

[35] L. Yun Wei, D. M. Vilathgamuwa, and L. Poh Chiang, "Robust Control Scheme for a Microgrid With PFC Capacitor Connected," *Industry Applications, IEEE Transactions on,* vol. 43, pp. 1172-1182, 2007.

[36] L. Tzann-Shin, S. J. Chiang, and C. Jhy-Ming, "Hinf loop-shaping controller designs for the single-phase UPS inverters," *Power Electronics, IEEE Transactions on,* vol. 16, pp. 473-481, 2001.

[37] Y. Shuitao, L. Qin, F. Z. Peng, and Q. Zhaoming, "A Robust Control Scheme for Grid-Connected Voltage-Source Inverters," *Industrial Electronics, IEEE Transactions on,* vol. 58, pp. 202-212, 2011.

[38] M. Aten and H. Werner, "Robust multivariable control design for HVDC back to back schemes," *Generation, Transmission and Distribution, IEE Proceedings-,* vol. 150, pp. 761-767, 2003.

[39] J. C. Doyle, "Structured uncertainty in control system design," in *Decision and Control, 1985 24th IEEE Conference on*, 1985, pp. 260-265.

[40] J. Doyle, "Analysis of Feedback-Systems with Structured Uncertainties," *Iee Proceedings-D Control Theory and Applications,* vol. 129, pp. 242-250, 1982.

[41] R. Turner, S. Walton, and R. Duke, "Robust High-Performance Inverter Control Using Discrete Direct-Design Pole Placement," *Industrial Electronics, IEEE Transactions on,* vol. 58, pp. 348-357, 2011.

[42] I. J. Gabe, V. F. Montagner, and H. Pinheiro, "Design and Implementation of a Robust Current Controller for VSI Connected to the Grid Through an LCL Filter," *Power Electronics, IEEE Transactions on,* vol. 24, pp. 1444-1452, 2009.

[43] Y.A-R. I. Mohamed, "Suppression of Low-and High-Frequency Instabilities and Grid-Induced Disturbances in Distributed Generation Inverters," *Power Electronics, IEEE Transactions on,* vol. 26, pp. 3790-3803, 2011.

[44] J. Dannehl, C. Wessels, and F. W. Fuchs, "Limitations of Voltage-Oriented PI Current Control of Grid-Connected PWM Rectifiers With LCL Filters," *Industrial Electronics, IEEE Transactions on,* vol. 56, pp. 380-388, 2009.

[45] R. Teodorescu, F. Blaabjerg, M. Liserre, and P. C. Loh, "Proportional-resonant controllers and filters for grid-connected voltage-source converters," *IEE Proceedings-Electric Power Applications,* vol. 153, pp. 750-762, 2006.

[46] M. H. Bierhoff and F. W. Fuchs, "Active damping for three-phase PWM rectifiers with high-order line-side filters," *Industrial Electronics, IEEE Transactions on,* vol. 56, pp. 371-379, 2009.

[47] J. Dannehl, F. W. Fuchs, S. Hansen, and P. B. Thøgersen, "Investigation of active damping approaches for PI-based current control of grid-connected pulse width modulation converters with LCL filters," *Industry Applications, IEEE Transactions on,* vol. 46, pp. 1509-1517, 2010.

[48] Y. Tang, P. C. Loh, P. Wang, F. H. Choo, and F. Gao, "Exploring inherent damping characteristic of LCL-filters for three-phase grid-connected voltage source inverters," *Power Electronics, IEEE Transactions on,* vol. 27, pp. 1433-1443, 2012.

[49] G. Shen, D. Xu, L. Cao, and X. Zhu, "An improved control strategy for grid-connected voltage source inverters with an LCL filter," *Power Electronics, IEEE Transactions on,* vol. 23, pp. 1899-1906, 2008.

[50] X. Wang, X. Ruan, S. Liu, and C. K. Tse, "Full feedforward of grid voltage for grid-connected inverter with LCL filter to suppress current distortion due to grid voltage harmonics," *Power Electronics, IEEE Transactions on,* vol. 25, pp. 3119-3127, 2010.

[51] E. Twining and D. G. Holmes, "Grid current regulation of a three-phase voltage source inverter with an LCL input filter," *Power Electronics, IEEE Transactions on,* vol. 18, pp. 888-895, 2003.

[52] M. Malinowski and S. Bernet, "A Simple Voltage Sensorless Active Damping Scheme for Three-Phase PWM Converters With an LCL Filter," *Industrial Electronics, IEEE Transactions on,* vol. 55, pp. 1876-1880, 2008.

[53] W. Eric and P. W. Lehn, "Digital Current Control of a Voltage Source Converter With Active Damping of LCL Resonance," *Power Electronics, IEEE Transactions on,* vol. 21, pp. 1364-1373, 2006.

[54] J. Dannehl, F. W. Fuchs, and P. B. Thøgersen, "PI state space current control of grid-connected PWM converters with LCL filters," *Power Electronics, IEEE Transactions on,* vol. 25, pp. 2320-2330, 2010.

[55] G. Shen, X. Zhu, J. Zhang, and D. Xu, "A new feedback method for PR current control of LCL-filter-based grid-connected inverter," *Industrial Electronics, IEEE Transactions on,* vol. 57, pp. 2033-2041, 2010.

[56] J. Dannehl, M. Liserre, and F. W. Fuchs, "Filter-Based Active Damping of Voltage Source Converters With LCL filter," *Industrial Electronics, IEEE Transactions on,* vol. 58, pp. 3623-3633, 2011.

[57] R. Teodorescu, F. Blaabjerg, M. Liserre, and A. Dell'Aquila, "A stable three-phase LCL-filter based active rectifier without damping," in *Industry*

Applications Conference, 2003. 38th IAS Annual Meeting. Conference Record of the, 2003, pp. 1552-1557.

[58] Y. Jinjun, D. Shanxu, and L. Bangyin, "Stability Analysis of Grid-Connected Inverter With LCL Filter Adopting a Digital Single-Loop Controller With Inherent Damping Characteristic," *Industrial Informatics, IEEE Transactions on,* vol. 9, pp. 1104-1112, 2013.

[59] B. Bahrani, M. Vasiladiotis, and A. Rufer, "High-Order Vector Control of Grid-Connected Voltage Source Converters with LCL-Filters," *Industrial Electronics, IEEE Transactions on,* vol. PP, pp. 1-1, 2013.

[60] E. A. A. Coelho, P. C. Cortizo, and P. F. D. Garcia, "Small-signal stability for parallel-connected inverters in stand-alone AC supply systems," *Industry Applications, IEEE Transactions on,* vol. 38, pp. 533-542, 2002.

[61] R. Majumder, B. Chaudhuri, A. Ghosh, R. Majumder, G. Ledwich, and F. Zare, "Improvement of Stability and Load Sharing in an Autonomous Microgrid Using Supplementary Droop Control Loop," *Power Systems, IEEE Transactions on,* vol. 25, pp. 796-808, 2010.

[62] E. Barklund, N. Pogaku, M. Prodanovic, C. Hernandez-Aramburo, and T. C. Green, "Energy Management in Autonomous Microgrid Using Stability-Constrained Droop Control of Inverters," *Power Electronics, IEEE Transactions on,* vol. 23, pp. 2346-2352, 2008.

[63] P. C. Krause, O. Wasynczuk, S. D. Sudhoff, and P. C. Krause, *Analysis of electric machinery and drive systems*, 2nd ed. New York: IEEE Press, 2002.

[64] B. M. Nomikos and C. D. Vournas, "Investigation of induction Machine contribution to power system oscillations," *Power Systems, IEEE Transactions on,* vol. 20, pp. 916-925, 2005.

[65] P. Waide and C. Brunner, "Energy-efficiency policy opportunities for electric motor-derived systems. IEA (International Energy Agency)," 2011.

[66] P. Kundur, N. J. Balu, and M. G. Lauby, *Power system stability and control*. New York: McGraw-Hill, 1994.

[67] "Standard load models for power flow and dynamic performance simulation," *Power Systems, IEEE Transactions on,* vol. 10, pp. 1302-1313, 1995.

[68] L. Pereira, D. N. Kosterev, P. Mackin, D. Davies, J. Undrill, and Z. Wenchun, "An interim dynamic induction motor model for stability studies in the WSCC," *Power Systems, IEEE Transactions on,* vol. 17, pp. 1108-1115, 2002.

[69] F. P. De Mello and J. W. Feltes, "Voltage oscillatory instability caused by induction motor loads," *Power Systems, IEEE Transactions on,* vol. 11, pp. 1279-1285, 1996.

[70] G. Diaz, C. Gonzalez-Moran, J. Gomez-Aleixandre, and A. Diez, "Composite Loads in Stand-Alone Inverter-Based Microgrids; Modeling Procedure and Effects on Load Margin," *Power Systems, IEEE Transactions on,* vol. 25, pp. 894-905, 2010.

[71] A. A. A. Radwan and Y. A. R. I. Mohamed, "Stabilization of Medium-Frequency Modes in Isolated Microgrids Supplying Direct Online Induction Motor Loads," *Smart Grid, IEEE Transactions on,* vol. PP, pp. 1-13, 2013.

[72] S. A. Arefifar, Y. A. I. Mohamed, and T. H. M. El-Fouly, "Supply-Adequacy-Based Optimal Construction of Microgrids in Smart Distribution Systems," *Smart Grid, IEEE Transactions on,* vol. 3, pp. 1491-1502, 2012.

[73] M. Fathi and H. Bevrani, "Adaptive Energy Consumption Scheduling for Connected Microgrids Under Demand Uncertainty," *Power Delivery, IEEE Transactions on,* vol. 28, pp. 1576-1583, 2013.

[74] E. Handschin, F. Neise, H. Neumann, and R. Schultz, "Optimal operation of dispersed generation under uncertainty using mathematical programming," *International Journal of Electrical Power & Energy Systems,* vol. 28, pp. 618-626, 2006.

[75] C. A. Hernandez-Aramburo, T. C. Green, and N. Mugniot, "Fuel consumption minimization of a microgrid," *Industry Applications, IEEE Transactions on,* vol. 41, pp. 673-681, 2005.

[76] A. Khodaei and M. Shahidehpour, "Microgrid-Based Co-Optimization of Generation and Transmission Planning in Power Systems," *Power Systems, IEEE Transactions on,* vol. 28, pp. 1582-1590, 2013.

[77] F. D. Galiana, F. Bouffard, J. M. Arroyo, and J. F. Restrepo, "Scheduling and Pricing of Coupled Energy and Primary, Secondary, and Tertiary Reserves," *Proceedings of the IEEE,* vol. 93, pp. 1970-1983, 2005.

[78] A. Kahrobaeian and Y. A. R. I. Mohamed, "Analysis and Mitigation of Low-Frequency Instabilities in Autonomous Medium-Voltage Converter-Based Microgrids With Dynamic Loads," *Industrial Electronics, IEEE Transactions on,* vol. 61, pp. 1643-1658, 2014.

[79] H. Karimi, H. Nikkhajoei, and R. Iravani, "Control of an Electronically-Coupled Distributed Resource Unit Subsequent to an Islanding Event," *Power Delivery, IEEE Transactions on,* vol. 23, pp. 493-501, 2008.

[80] J. M. Guerrero, H. Lijun, and J. Uceda, "Control of Distributed Uninterruptible Power Supply Systems," *Industrial Electronics, IEEE Transactions on,* vol. 55, pp. 2845-2859, 2008.

[81] R. Majumder, B. Chaudhuri, A. Ghosh, R. Majumder, G. Ledwich, and F. Zare, "Improvement of stability and load sharing in an autonomous microgrid using supplementary droop control loop," in *Power and Energy Society General Meeting, 2010 IEEE*, 2010, pp. 1-1.

[82] M. Savaghebi, A. Jalilian, J. C. Vasquez, and J. M. Guerrero, "Secondary Control Scheme for Voltage Unbalance Compensation in an Islanded Droop-Controlled Microgrid," *Smart Grid, IEEE Transactions on,* vol. 3, pp. 797-807, 2012.

[83] A. Pantoja and N. Quijano, "A Population Dynamics Approach for the Dispatch of Distributed Generators," *Industrial Electronics, IEEE Transactions on,* vol. 58, pp. 4559-4567, 2011.

[84] Q. Shafiee, J. M. Guerrero, and J. C. Vasquez, "Distributed Secondary Control for Islanded Microgrids-A Novel Approach," *Power Electronics, IEEE Transactions on,* vol. 29, pp. 1018-1031, 2014.

[85] Q. Shafiee, C. Stefanovic, T. Dragicevic, P. Popovski, J. Vasquez, and J. Guerrero, "Robust Networked Control Scheme for Distributed Secondary Control

of Islanded MicroGrids," *Industrial Electronics, IEEE Transactions on,* vol. PP, pp. 1-1, 2013.

[86] A. Bidram and A. Davoudi, "Hierarchical Structure of Microgrids Control System," *Smart Grid, IEEE Transactions on,* vol. 3, pp. 1963-1976, 2012.

[87] C. Changhee, J. Jin-Hong, K. Jong-Yul, K. Soonman, P. Kyongyop, and K. Sungshin, "Active Synchronizing Control of a Microgrid," *Power Electronics, IEEE Transactions on,* vol. 26, pp. 3707-3719, 2011.

[88] "IEEE Recommended Practice for Industrial and Commercial Power Systems Analysis (Brown Book)," *IEEE Std 399-1997,* pp. 1-488, 1998.

[89] "IEEE Draft Guide for Design, Operation, and Integration of Distributed Resource Island Systems with Electric Power Systems," *IEEE P1547.4/D11, March 2011,* pp. 1-55, 2011.

[90] M. Morari, "Robust Process-Control," *Abstracts of Papers of the American Chemical Society,* vol. 197, pp. 57-Iaec, Apr 9 1989.

[91] Y. A. R. I. Mohamed, "Mitigation of Converter-Grid Resonance, Grid-Induced Distortion, and Parametric Instabilities in Converter-Based Distributed Generation," *Power Electronics, IEEE Transactions on,* vol. 26, pp. 983-996, 2011.

[92] X. Wilsun, Z. Guibin, L. Chun, W. Wencong, W. Guangzhu, and J. Kliber, "A Power Line Signaling Based Technique for Anti-islanding Protection of Distributed Generators: Part I: Scheme and Analysis," in *Power Engineering Society General Meeting, 2007. IEEE*, 2007, pp. 1-1.

[93] M. A. Redfern, O. Usta, and G. Fielding, "Protection against loss of utility grid supply for a dispersed storage and generation unit," *Power Delivery, IEEE Transactions on,* vol. 8, pp. 948-954, 1993.

[94] M. Green and D. J. N. Limebeer, *Linear robust control*, Dover ed. Mineola, N.Y.: Dover Publications, Inc., 2012.

[95] A. Kahrobaeian and Y. A. I. Mohamed, "Suppression of Interaction Dynamics in DG Converter-Based Microgrids Via Robust System-Oriented Control Approach," *Smart Grid, IEEE Transactions on,* vol. 3, pp. 1800-1811, 2012.

[96] G. Balas, R. Chiang, A. Packard, and M. Safonov, "Robust Control Toolbox User's Guide. The MathWorks," *Inc., Natick, MA,* 2006.

[97] A. Kahrobaeian and Y. A. I. Mohamed, "Direct Single-Loop mu-Synthesis Voltage Control for Suppression of Multiple Resonances in Microgrids with Power-Factor Correction Capacitors," *Smart Grid, IEEE Transactions on,* vol. 4, pp. 1151-1161, 2013.

[98] S. Skogestad and I. Postlethwaite, "Multivariable feedback control: analysis and design," *New York,* 1996.

[99] T.-S. Lee, S.-J. Chiang, and J.-M. Chang, "H∞ loop-shaping controller designs for the single-phase UPS inverters," *Power Electronics, IEEE Transactions on,* vol. 16, pp. 473-481, 2001.

[100] M. Aten and H. Werner, "Robust multivariable control design for HVDC back to back schemes," in *Generation, Transmission and Distribution, IEE Proceedings-*, 2003, pp. 761-767.

[101] A. Kahrobaeian and Y. A-R. I. Mohamed, "Robust Single-Loop Direct Current Control of LCL-Filtered Converter-based DG Units in Grid-Connected and Autonomous Microgrid Modes," *Power Electronics, IEEE Transactions on,* vol. PP, pp. 1-1, 2014 (in press): DOI: 10.1109/TPEL.2013.2294876.

[102] F. M. Callier and C. A. Desoer, *Linear system theory*: Springer-verlag, 1991.

[103] A. Chaouachi, R. M. Kamel, R. Andoulsi, and K. Nagasaka, "Multiobjective Intelligent Energy Management for a Microgrid," *Industrial Electronics, IEEE Transactions on,* vol. 60, pp. 1688-1699, 2013.

[104] V. C. Gungor, L. Bin, and G. P. Hancke, "Opportunities and Challenges of Wireless Sensor Networks in Smart Grid," *Industrial Electronics, IEEE Transactions on,* vol. 57, pp. 3557-3564, 2010.

[105] I. J. Balaguer, L. Qin, Y. Shuitao, U. Supatti, and P. Fang Zheng, "Control for Grid-Connected and Intentional Islanding Operations of Distributed Power Generation," *Industrial Electronics, IEEE Transactions on,* vol. 58, pp. 147-157, 2011.

[106] T. L. Vandoorn, J. D. M. De Kooning, B. Meersman, J. M. Guerrero, and L. Vandevelde, "Voltage-Based Control of a Smart Transformer in a Microgrid," *Industrial Electronics, IEEE Transactions on,* vol. 60, pp. 1291-1305, 2013.

[107] D. De and V. Ramanarayanan, "Decentralized Parallel Operation of Inverters Sharing Unbalanced and Nonlinear Loads," *Power Electronics, IEEE Transactions on,* vol. 25, pp. 3015-3025, 2010.

[108] R. M. Kamel, A. Chaouachi, and K. Nagasaka, "Three Control Strategies to Improve the Microgrid Transient Dynamic Response During Isolated Mode: A Comparative Study," *Industrial Electronics, IEEE Transactions on,* vol. 60, pp. 1314-1322, 2013.

[109] M. Bertoluzzo, G. Buja, and R. Menis, "Direct torque control of an induction motor using a single current sensor," *Industrial Electronics, IEEE Transactions on,* vol. 53, pp. 778-784, 2006.

[110] J. M. Guerrero, J. Matas, L. G. de Vicuna, M. Castilla, and J. Miret, "Wireless-Control Strategy for Parallel Operation of Distributed-Generation Inverters," *Industrial Electronics, IEEE Transactions on,* vol. 53, pp. 1461-1470, 2006.

[111] H. A. Toliyat and G. B. Kliman, *Handbook of electric motors*, 2nd ed. New York: Marcel Dekker, 2004.

[112] L. Hao, C. Bong Jun, Z. Weihua, and S. Xuemin, "Stability Enhancement of Decentralized Inverter Control Through Wireless Communications in Microgrids," *Smart Grid, IEEE Transactions on,* vol. 4, pp. 321-331, 2013.

[113] P. M. Anderson, A. A. Fouad, and Institute of Electrical and Electronics Engineers., *Power system control and stability*, 2nd ed. Piscataway, N.J.: IEEE Press ; Wiley-Interscience, 2003.

[114] F. Milano and M. Anghel, "Impact of Time Delays on Power System Stability," *Circuits and Systems I: Regular Papers, IEEE Transactions on,* vol. 59, pp. 889-900, 2012.

Appendix A

Parameters of the Simulated Study System in Chapter 6

The MG test system parameters and operating conditions adopted in Figure 6-1 are as follow:

- Base Value: S(base) = 10 MVA, V(base) = 2.4 kV
- DG Parameters: 2 MVA, L_f = 0.6mH, C_f = 50μF, R_f = 0.1Ω, f_{sw} = 2 kHz, ω_c = 10 rad/s, K_{pv} = 0.05, K_{iv} = 365, K_{pi} = 1.5, K_{ii} = 250, H = 0.75, f_{nl} = 60.5Hz, m_1 = m_2 = m_3 = 3e-6 rad/s/W
- Network Parameters: Rc+jXc: (5.2+23j)%, Line1: (3.3+20.8j)%, Line2: (8.1+62.4j)%
- Load parameters: Static load1: 1MW, Static load2: 1.5 MW. Motor load: 2250 HP, 2.4 kV, 60 Hz, r_s = 0.029 Ω, L_{ss} = 35.2 mH, r_r = 0.022 Ω, L_{rr} = 35.2 mH, L_m = 34.6 mH, J_{noload} = 12.77 kg.m^2, $J_{\text{full\_load}}$ = 63.87 kg.m^2, ρ = 4, T_L = 7964.04 N.m.
- Compensator Parameters: K_1 = 7e-7, K_2 = 1.5e-5, τ = 0.001.

Appendix B

Parameters of the Simulated Study System in Chapter 7

The MG test system parameters and operating conditions adopted in Figure 7-2 are as follow:

- **Base Value:** S_{base} = 1MVA, $V(L\text{-}L)_{base}$ = 2.4kV
- **Initial operating point:** $\bar{P}_{DG1} = \bar{P}_{DG2} = \bar{P}_{DG3} = \bar{P}_{DG4}$ = 1.18 p.u. , $\bar{Q}_{DG1} = \bar{Q}_{DG2} = \bar{Q}_{DG2} = \bar{Q}_{DG4}$ =0.49 p.u., V_{DG1} = 1, V_{DG2} = 0.99 , V_{DG3}=0.998 , V_{DG4} = 0.996, δ_1 = 0, δ_2 = -.0075, δ_3 = -.0016, δ_4 = -.01037 ($\gamma_{P,Q,I}$ = 0.25).
- **Power Regulator Parameters:** K_P = 5e-8, K_Q = 2e-6, n_Q = 1.2e-4 and m_P = 1e-6, ω_{nl} = 120π rad/s, ω_c = 30 rad/s, V_{nl} = 1 p.u.
- **DG Parameters:** V_{DC} = 800 V, L_f = 1.2mH, C_f = 50μF, R_f = 0.1 Ω, f_{sw} = 10 kHz, Voltage controller's bandwidth: 530Hz, current controller's bandwidth: 1.1 kHz, τ: 5e-6 s.

Appendix C

Parameters of the Simulated Study System in Chapter 8

The MG test system parameters and operating conditions adopted in Figure 8-1 are as follow:

Base Value: S(base) = 0.5 MVA, V(base) = 2.4kV

- **MG1**: Initial conditions (pu): $\bar{P}_{DG1} = \bar{P}_{DG2} = 1.02$ $\bar{Q}_{DG1} = \bar{Q}_{DG2} = 0.52$, $V_1 = 1.055$, $\delta_{0(12)} = 0.02278$, $V_2 = 1.045$, ($\gamma_{MG1,P,Q,1} = \gamma_{MG1,P,Q,2} = 0.5$) L1: (0.043+0.0392j)pu , L2: (0.043+0.016j)pu.
- **MG2:** Initial conditions (pu): $\bar{P}_{DG1} = 0.5$, $\bar{P}_{DG2} = 1.0$, $\bar{Q}_{DG1} = 0.4$, $\bar{Q}_{DG2} = 0.8$,$V_1 = 0.98$, $\delta_{12} = 0.02298$, $V_2 = 1.01$, ($\gamma_{MG1,P,Q,1} = 1/3$, $\gamma_{MG1,P,Q,2} = 2/3$), L1: (0.043 +0.0392j) p.u., L2: (0.043+0.016j)p.u., L_{pv}: (0.0086+0.00327i)p.u.
- **Power Regulator Parameters:** $m_P = 1e\text{-}5$, $K_P = 1e\text{-}6$, $K_Q = 1e\text{-}4$ and $n_Q = 6.5e\text{-}3$, $\omega_{nl} = 120\pi$ rad/s, $\omega_c = 30$ rad/s, $V_{nl} = 1$ p.u.
- **DG Parameters:** $L_f = 1.2$mH, $C_f = 50\mu$F, $R_f = 0.1\Omega$, Voltage controller's bandwidth: 530 Hz, current controller's bandwidth: 1.1 kHz, Tie-Line: (0.0043+0.0654j) p.u.
- **Synchronization and Power-tie controller:** $K_{P\delta} = 4.9755e\text{-}6$, $\zeta = 0.48067$, $T_{z\delta} = 0.10868$, $T_{w\delta} = 0.0044343$, $T_{p\delta} = 0.002629$, $K_{PV} = 0.085806$, $T_{zV} = 0.014495$, $T_{pV} = 27.5187$, $K_\delta = 3.5834$, $K_V = 3.8382$.